325
12-13-63

ORNL-3499, Vol I
UC-34 – Physics
TID-4500 (23rd ed.)

NEUTRON PHYSICS DIVISION
ANNUAL PROGRESS REPORT
FOR PERIOD ENDING AUGUST 1, 1963

OAK RIDGE NATIONAL LABORATORY
operated by
UNION CARBIDE CORPORATION
for the
U.S. ATOMIC ENERGY COMMISSION

DISCLAIMER

Printed in USA. Price: $3.00 Available from the
Office of Technical Services
U. S. Department of Commerce
Washington 25, D. C.

ORNL-3499, Vol I

Contract No. W-7405-eng-26

NEUTRON PHYSICS DIVISION
ANNUAL PROGRESS REPORT,
For Period Ending August 1, 1963

E. P. Blizard, Director
A. D. Callihan, Associate Director
F. C. Maienschein, Associate Director

DATE ISSUED

DEC 10 1963

OAK RIDGE NATIONAL LABORATORY
Oak Ridge, Tennessee
operated by
UNION CARBIDE CORPORATION
for the
U. S. ATOMIC ENERGY COMMISSION

THIS PAGE

WAS INTENTIONALLY

LEFT BLANK

PREFACE

For the first time since its inception in 1955, the Neutron Physics Division is issuing its annual progress report in two volumes, not because of the size of the report but to aid the reader who normally will be interested in only one of our two major programs. In the very broadest sense these programs may be classified as a low-energy neutron physics program and a high-energy radiation shielding program; however, as will be apparent from the contents of the report, the research effort of the division is not so clearly separable.

It is the so-called low-energy program that is reported here in Volume I, with the first chapter, "Nuclear and Reactor Physics," largely consisting of papers from our cross-section study program. This program is designed to provide neutron cross sections for reactor calculations. These methods are now so accurate that it is not sufficient to supply data from cross-section measurements alone; it is now necessary to interpolate on the basis of nuclear structure theory. This theory is being developed and is being tested both against neutron cross-section measurements and against inherently more accurate measurements of charged-particle cross sections. Measurements of neutron and charged-particle cross sections carried out in this Division are so used.

The second chapter, "Critical Experiments," collects the papers describing work performed both with basic critical assemblies and with reactor cores. Chapter 3, "Reactor Shielding," for the most part consists of papers reporting shielding investigations in conjunction with civil or military defense and shielding studies for the Space Nuclear Auxiliary Power program.

Two chapters that are new to the annual report this year are Chapter 4, "Radiation Shielding Information Center," which describes the initial efforts of RSIC to collect, evaluate, and disseminate information on radiation shielding, and Chapter 5, "Mathematics and Computer Programs." The latter is new only in the sense that the papers on mathematics and computer programs are collected in one chapter, rather than being dispersed under other chapter headings.

Chapter 6, "Radiation Detector Studies (I)," consists of papers which discuss methods for measuring low-energy radiations; its counterpart for high-energy radiations is included in Volume II. Chapter 7, "Water Desalination Studies – Theoretical," presents the small (but vital) fraction of a large Laboratory program that is located in the Neutron Physics Division.

Chapters 8, 9, and 10, titled "High-Energy Radiation Shielding Calculations," "Measurements of Radiations from High-Energy Proton Interactions," and "Radiation Detector Studies (II)," respectively, will be found in Volume II.

THIS PAGE

WAS INTENTIONALLY

LEFT BLANK

TABLE OF CONTENTS AND SUMMARY

1. NUCLEAR AND REACTOR PHYSICS

2. CRITICAL EXPERIMENTS

3. REACTOR SHIELDING

4. RADIATION SHIELDING INFORMATION CENTER

5. MATHEMATICS AND COMPUTER PROGRAMS

6. RADIATION DETECTOR STUDIES (I)

1. Nuclear and Reactor Physics

THIS PAGE

WAS INTENTIONALLY

LEFT BLANK

1.1. MEASUREMENT OF α, THE RATIO OF THE NEUTRON CAPTURE CROSS SECTION TO THE FISSION CROSS SECTION, OF U^{235} IN THE NEUTRON ENERGY REGION FROM 4 ev TO 2 kev[1,2]

G. deSaussure, L. W. Weston, R. Gwin, J. E. Russell,[3] and R. W. Hockenbury[3]

Introduction

The initiation of a program of experiments intended to measure the value of α, the ratio of the neutron capture cross section to the fission cross section, over a wide range of energies was previously reported.[4,5] This paper discusses the measurements for U^{235} over the neutron energy range 4 ev to 2 kev. Results obtained for the energy range 12 to 690 kev are presented in Sec. 1.2.

Experimental Procedure

The technique employed for the measurements of α in the range 4 ev $< E_n <$ 2 kev is based upon the use of a multiplate U^{235} fission chamber located at the center of a large tank of liquid scintillator.[5] The absorption of a neutron by the U^{235} of the fission chamber is accompanied by the emission of capture or fission gamma rays, according to the nature of the event following the absorption, which are detected with high efficiency in the scintillator. If a fission event occurs, the fission fragments are simultaneously detected by the fission chamber. Thus the ratio of capture events to fission events can be computed from the ratio of the scintillator counts not in coincidence with a fission chamber count to the scintillator counts in coincidence with a fission chamber count. Suitable corrections for background and efficiency must be applied.

Pulsed neutrons were produced in a target bombarded by electron bursts from the Rensselaer Polytechnic Institute linear electron accelerator. The neutron energies were measured by time-of-flight techniques.

Results

The results of these measurements are shown in Figs. 1.1.1 through 1.1.5, each covering a different energy range and each containing three curves. The upper curve represents the relative fission rate and the middle curve the relative capture rate. These rates are the product of the appropriate macroscopic cross section multiplied by the neutron flux at the sample. The neutron flux was roughly measured and found to be proportional to E^x per unit time of flight, where $x = 0.71 \pm 0.25$. The absolute value of α, shown in the lowest curve, is obtained by dividing the capture rate by the fission rate and is independent of the neutron flux.

The values of α obtained in the present work have been used to compute values of η of U^{235},

---

[1] Summary of a paper to be submitted for publication in *Nuclear Science and Engineering*.

[2] The indispensable contributions of R. D. Smiddie, Instrumentation and Controls Division, to the progress of these experiments are gratefully acknowledged. Appreciation is also expressed to M. M. Chiles, I and C Division, who designed and constructed the fission chambers; to G. S. Petit, Oak Ridge Gaseous Diffusion Plant, who electroplated the fission-chamber foils and tested the homogeneity of the deposits by α counting and weighting; to N. W. Hill and J. H. Todd, I and C Division, who designed and constructed the electronic circuit; and to R. Fullwood and D. Kraus, Rensselaer Polytechnic Institute, who assisted in the operation of the accelerator.

[3] Rensselaer Polytechnic Institute, Troy, N.Y.

[4] G. deSaussure *et al.*, *Neutron Phys. Div. Ann. Progr. Rept. Sept. 1, 1961*, ORNL-3191, p 177.

[5] G. deSaussure *et al.*, *Neutron Phys. Div. Ann. Progr. Rept. Sept. 1, 1962*, ORNL-3360, p 51.

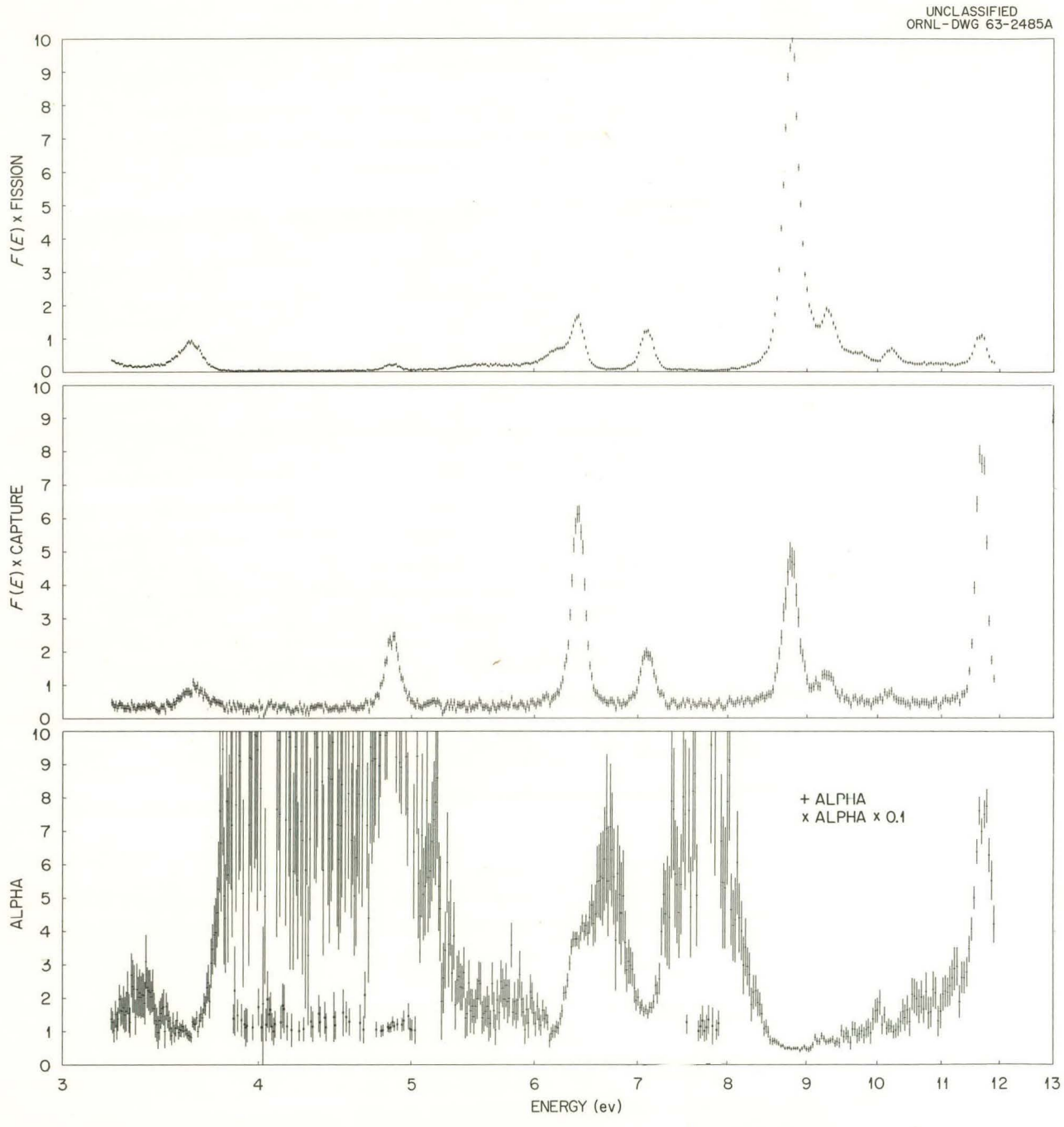

Fig. 1.1.1. Fission Rate, Capture Rate, and α of U^{235} vs Neutron Energy: 4 ev $\leqq E_n \leqq$ 12 ev. The fission rate and capture rate are plotted on the same arbitrary scale; α is plotted in absolute values.

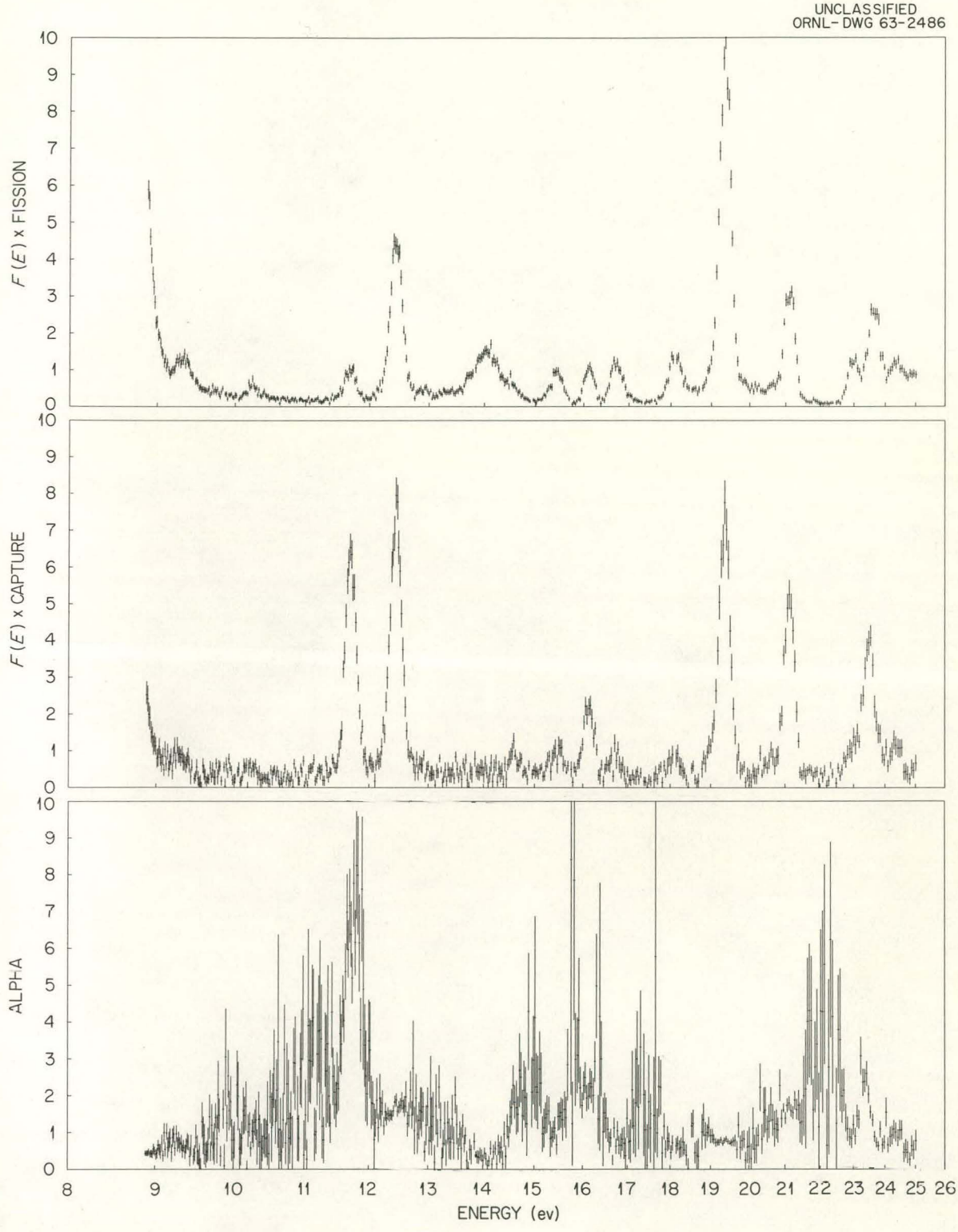

Fig. 1.1.2. Fission Rate, Capture Rate, and α of U^{235} vs Neutron Energy: 9 ev $\leq E_n \leq$ 25 ev. The fission rate and capture rate are plotted on the same arbitrary scale; α is plotted in absolute values.

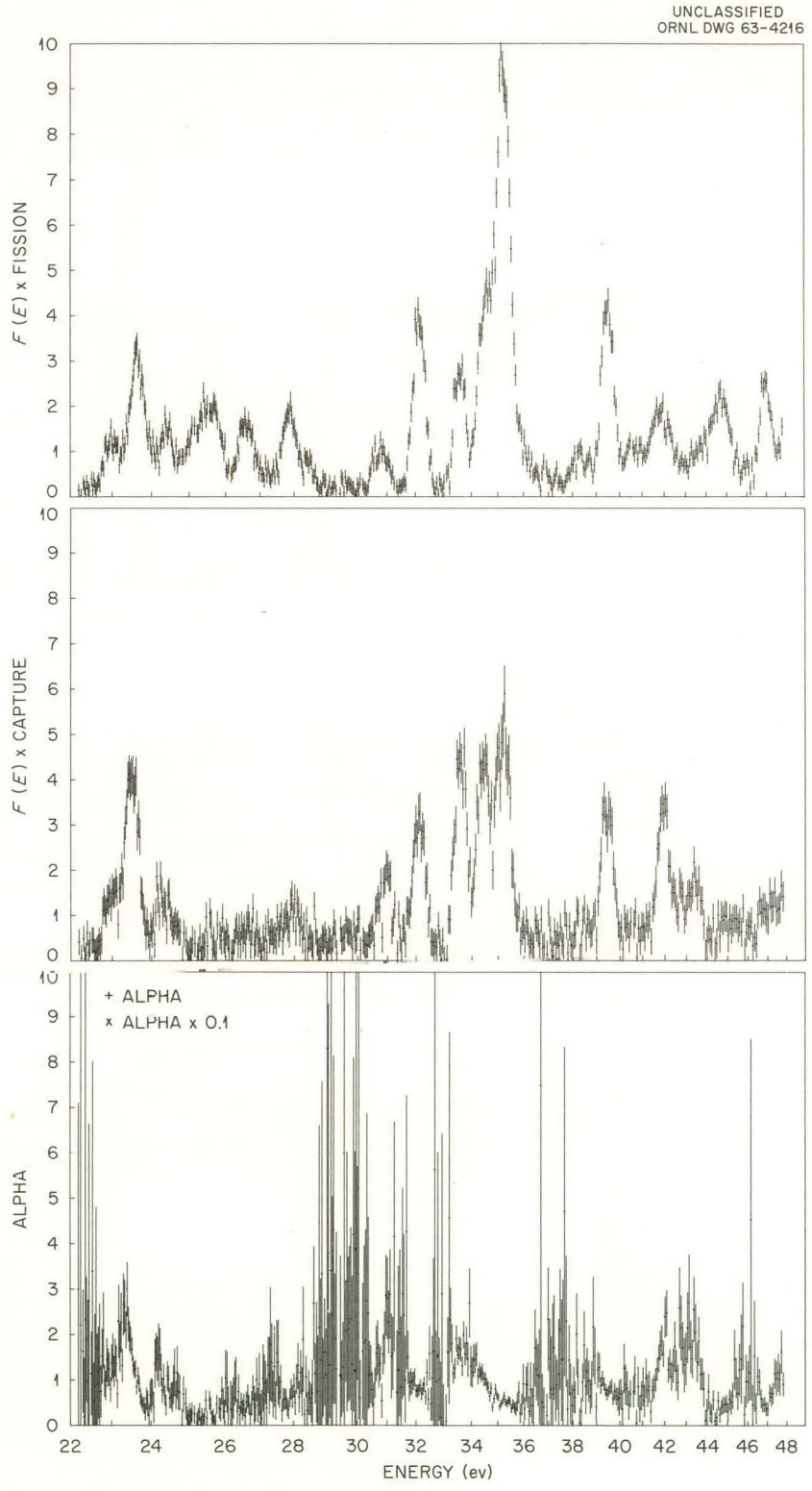

Fig. 1.1.3. Fission Rate, Capture Rate, and α of U^{235} vs Neutron Energy: 22 ev $\leq E_n \leq$ 48 ev. The fission rate and capture rate are plotted on the same arbitrary scale; α is plotted in absolute values.

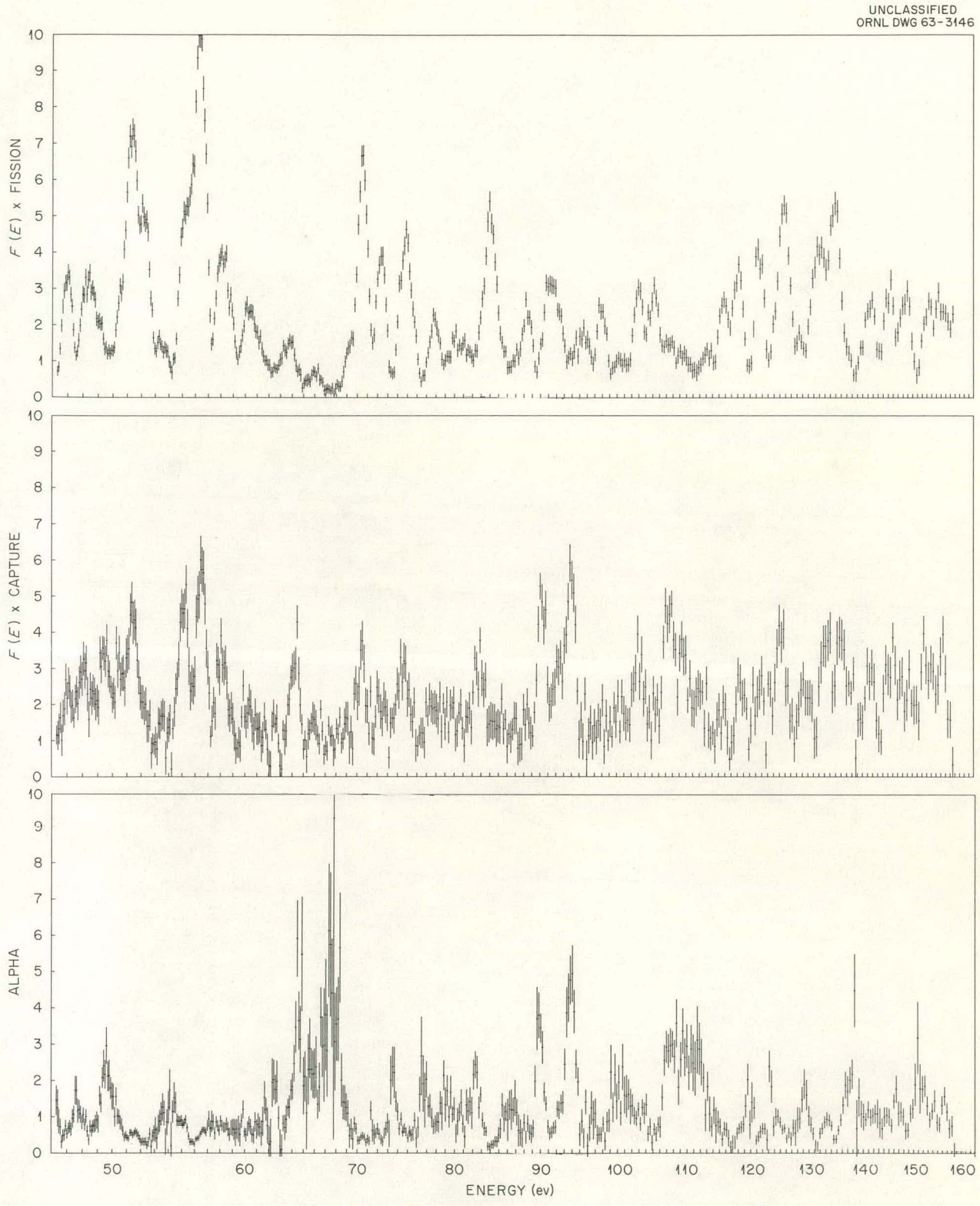

Fig. 1.1.4. Fission Rate, Capture Rate, and α of U^{235} vs Neutron Energy: 49 ev $\leq E_n \leq$ 160 ev. The fission rate and capture rate are plotted on the same arbitrary scale; α is plotted in absolute values.

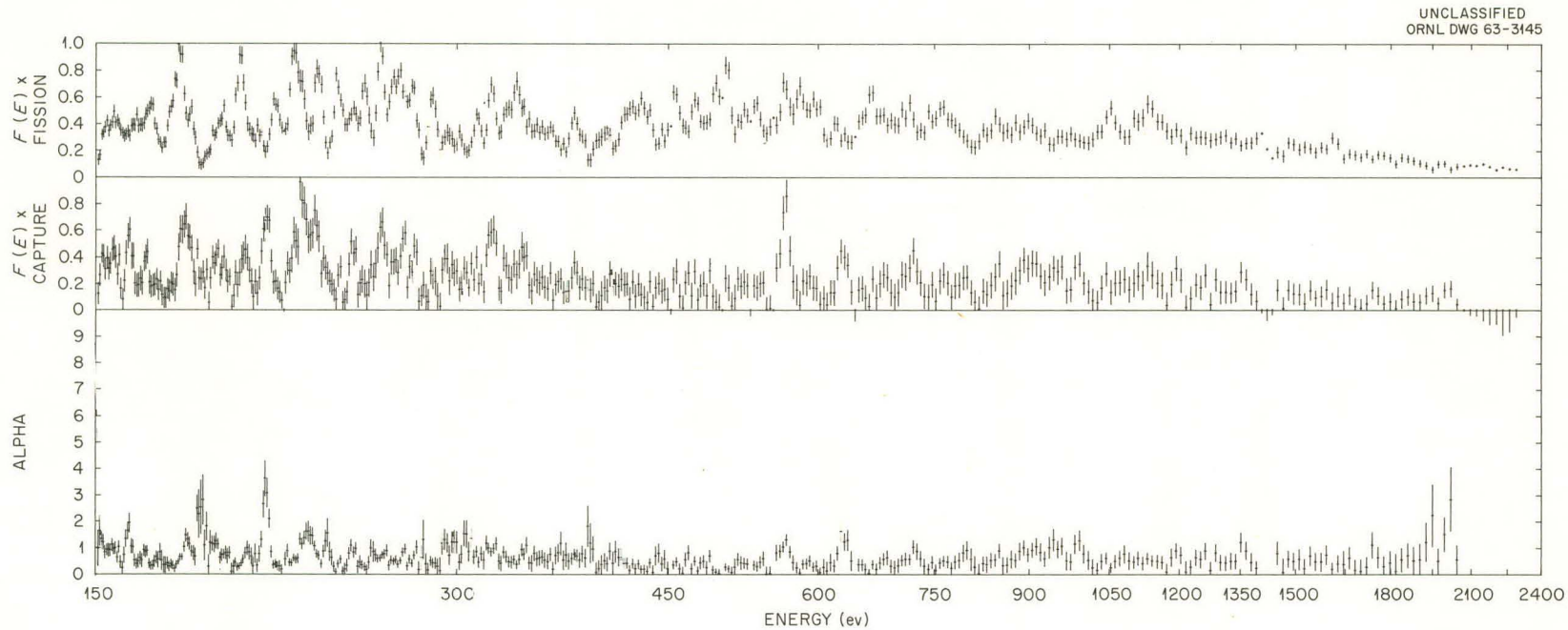

Fig. 1.1.5. Fission Rate, Capture Rate, and α of U^{235} vs Neutron Energy: 150 ev $\leq E_n \leq$ 2 kev. The fission rate and capture rate are plotted on the same arbitrary scale; α is plotted in absolute values.

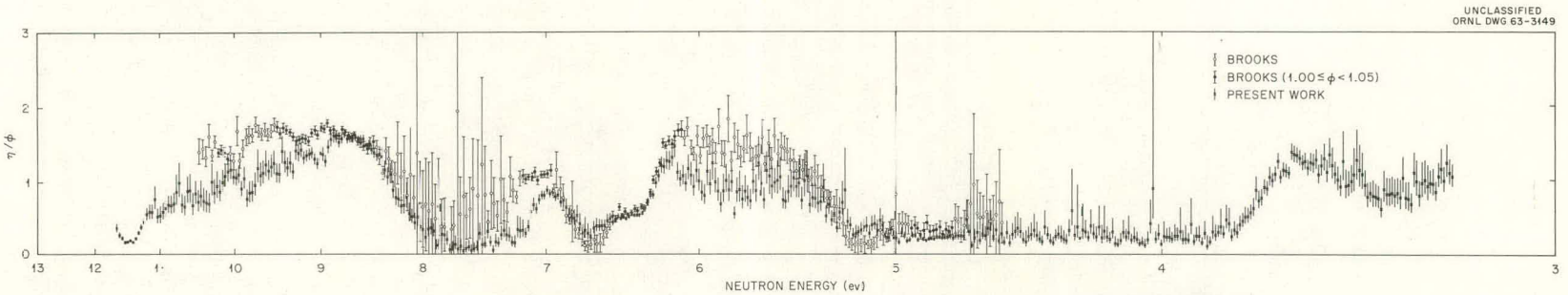

Fig. 1.1.6. Value of η as a Function of Neutron Energy: 3 ev $\leq E_n \leq$ 11 ev. The quantity ϕ is a factor representing an uncertainty in the work of Brooks.

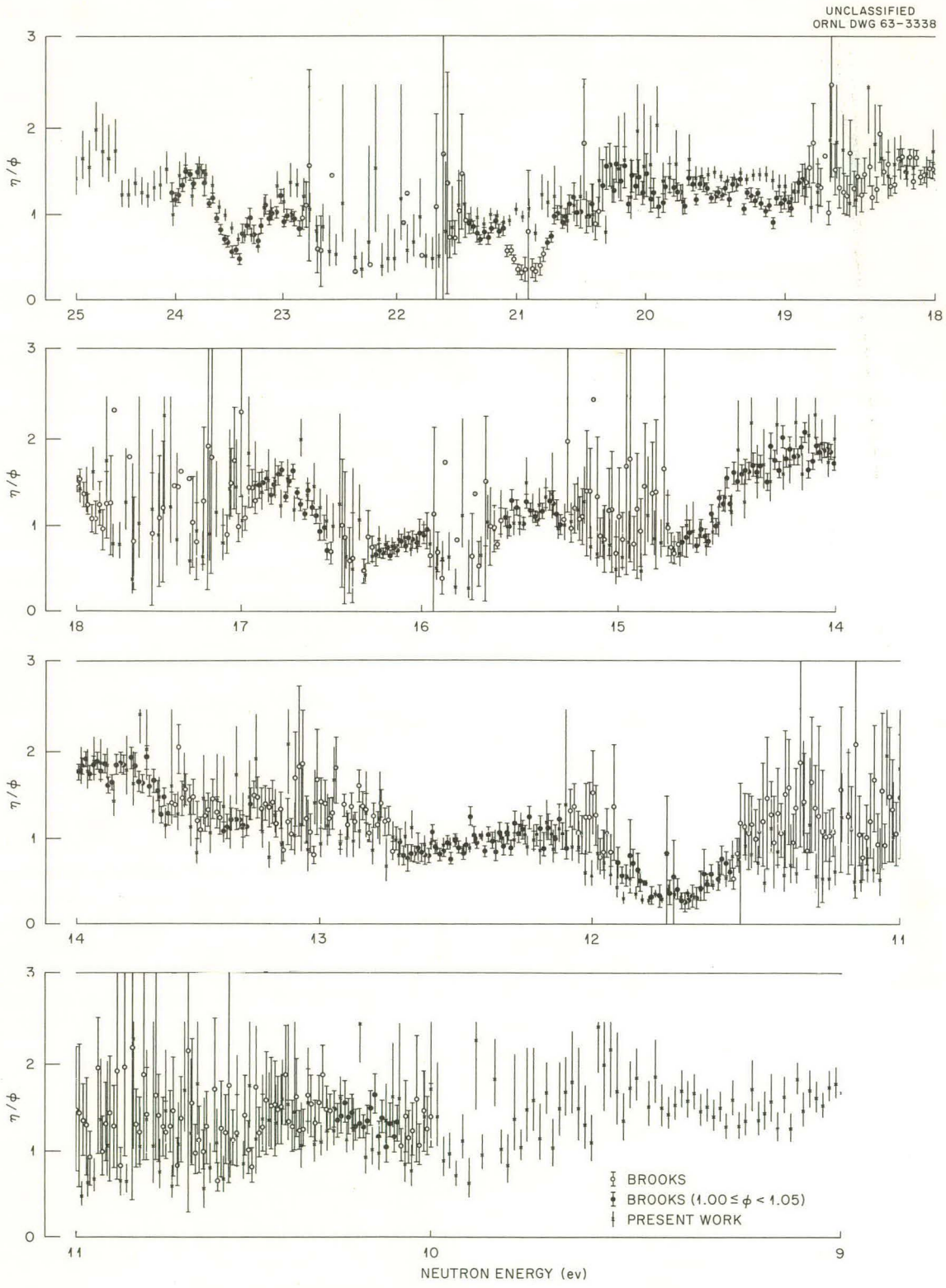

Fig. 1.1.7. Value of η as a Function of Neutron Energy: 9 ev $\leqq E_n \leqq$ 25 ev. The quantity ϕ is a factor representing an uncertainty in the work of Brooks.

the yield of fission neutrons per absorption over the energy range from 4 to 25 ev. For this calculation ν, the number of neutrons emitted per fission, was taken to be 2.43. The calculated values are compared with a direct measurement of η vs energy by Brooks[6] in Figs. 1.1.6 and 1.1.7, and the agreement is found to be fairly good.

Precision of Measurements

The instrumental energy resolution was between 1.6 and 2%. The main contribution to the energy uncertainty was the flight path uncertainty, 0.8%, resulting mostly from the large sample thickness (fission chamber length) of 20 cm for the total flight path of 25 m. The time uncertainty varied from 16 to 90 nsec/m but remained much smaller than the flight path uncertainty up to 1 kev. A 10% uncertainty exists in the absolute value of α, associated with an uncertainty in the efficiency of the detector, but is not included in the errors shown on the figures. The relative value of α at any two energies is not affected by this uncertainty.

[6]F. D. Brooks, p 131 in *Neutron Time of Flight Methods* (ed. by J. Spaepen), European Atomic Energy Community (EURATOM), Brussels, 1961.

1.2. MEASUREMENT OF α, THE RATIO OF THE NEUTRON CAPTURE CROSS SECTION TO FISSION CROSS SECTION, OF U^{235} AT kev NEUTRON ENERGIES[1]

L. W. Weston, G. deSaussure, and R. Gwin

Introduction

The measurement of α of U^{235} for incident neutron energies in the range 12 to 690 kev (see Sec. 1.1 for discussion of measurements at lower energies) employed a technique developed by Diven *et al.*[2,3] In this technique a pulsed beam of neutrons is allowed to strike a U^{235} sample placed at the center of a large liquid scintillator loaded with gadolinium. A capture event in the sample is characterized by a scintillator pulse due to a single fast cascade of gamma rays in coincidence with the beam pulse. A fission event is characterized by a prompt pulse due to fission gamma rays followed a few microseconds later by additional pulses produced by gamma rays resulting from fission neutrons that have been thermalized in the scintillator material and captured by the gadolinium. The major difference between the experiments of Diven *et al.* and the present experiment is that in these measurements time-of-flight techniques were used to determine neutron energies below 100 kev.

Experimental Arrangement

Figure 1.2.1 shows the general experimental arrangement, and Fig. 1.2.2 is a block diagram of the electronics. The ORNL 3-Mv pulsed Van de Graaff was used to produce neutrons by the $Li^7(p,n)Be^7$ reaction. The Li^7 target was placed outside the scintillator tank, 97 cm from the U^{235} sample, and a collimator of Li^6-loaded paraffin was positioned to shield the scintillator liquid from direct target neutrons. The sample was

[1]The invaluable and continuing contributions of R. D. Smiddie, Instrumentation and Controls Division, to the success of these experiments are gratefully acknowledged.

[2]J. C. Hopkins and B. C. Diven, *Nucl. Sci. Eng.* **12**, 169 (1962).

[3]B. C. Diven, J. Terrell, and A. Hemmendinger, *Phys. Rev.* **109**, 144 (1958).

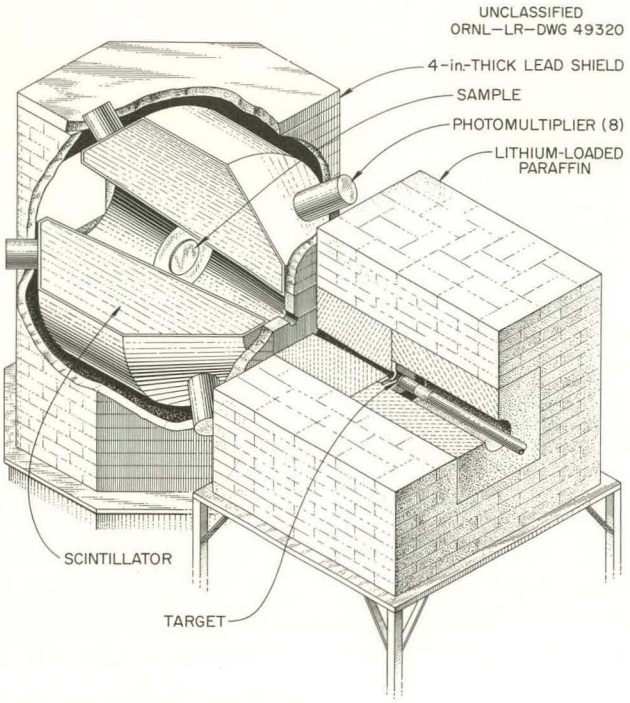

Fig. 1.2.1. Experimental Arrangement Using Large Liquid Scintillator.

located at the center of the scintillator tank[4] and consisted of twenty $2\frac{1}{8}$-in.-diam by 0.01-in.-thick disks of metallic uranium, 97.5% U^{235}, 1.6% U^{234}, 0.08% U^{236}, and 0.73% U^{238}, spaced 0.1 in. apart. Each disk weighed 10 g. The scintillator liquid contained 16 g of gadolinium 2-ethylhexoate per liter of solution.

The energies of the neutrons striking the target were established by using monoenergetic neutrons above 100 kev and at 30 kev, while for all energies below 100 kev the neutron energy was established by measuring the time of flight of the neutrons from the Li^7 target to the sample. Time-of-flight techniques were also used to discriminate against background for measurements with monoenergetic neutrons.

The neutrons produced in the Li^7 target passed through the collimator system and struck the U^{235} sample. The prompt gamma rays emitted in either a capture event or a fission event were detected by the liquid scintillator. The voltage pulse, called the prompt pulse, developed by the scintillator and the associated electronics was used to determine the time of the event in the sample (see Fig. 1.2.2) and thus the energy of the neutron producing the event. Considerations of the signal-to-background ratio led to the use of a pulse-height bias corresponding to the absorption of a 2.75-Mev gamma ray in the scintillator. Pulses having a voltage less than the bias were not analyzed. Two microseconds after a prompt pulse was detected a circuit was activated to inspect for pulses resulting from the capture of neutrons in the gadolinium. A detailed examination of the probability of detecting fission neutrons in the gadolinium of the liquid scintillator led to the use of a 32-μsec inspection time as well as the use of a pulse-height bias corresponding to the absorption of 1.9-Mev gamma rays in the scintillator. In those cases where a pulse was detected in the 32-μsec inspection interval the time-of-flight signal presented to the analyzer (see Fig. 1.2.2) was stored in the second half of the analyzer memory. The time-of-flight signal was stored in the first half of the analyzer memory in the absence of a pulse during the 32-μsec inspection interval.

A typical example of the time-of-flight data is shown in Fig. 1.2.3. The open-circle points were obtained with a lead sample, calculated to have the same macroscopic scattering cross section as the U^{235} sample, substituted for the U^{235}.

Data Analysis

The relation used to determine the value of α from the time-of-flight data was

$$\alpha = \frac{SF_f}{SF_c} \frac{\gamma[1 - C_0(1 - P_T)] - [C_0(1 - P_T)]}{(1 - P_T) - \gamma P_T}, \quad (1)$$

where

γ = the ratio of events not followed by delayed pulses to events followed by delayed pulses,

C_0 = the probability that no delayed pulses would be detected following a fission event (= 0.125 ± 0.007),

P_T = the probability that a random background pulse would occur during the 32-μsec gate (= ~5%),

[4]This is the 1.2-m-diam tank described by J. H. Gibbons *et al.*, *Phys. Rev.* **122**, 182 (1961).

UNCLASSIFIED
ORNL-LR-DWG 74434

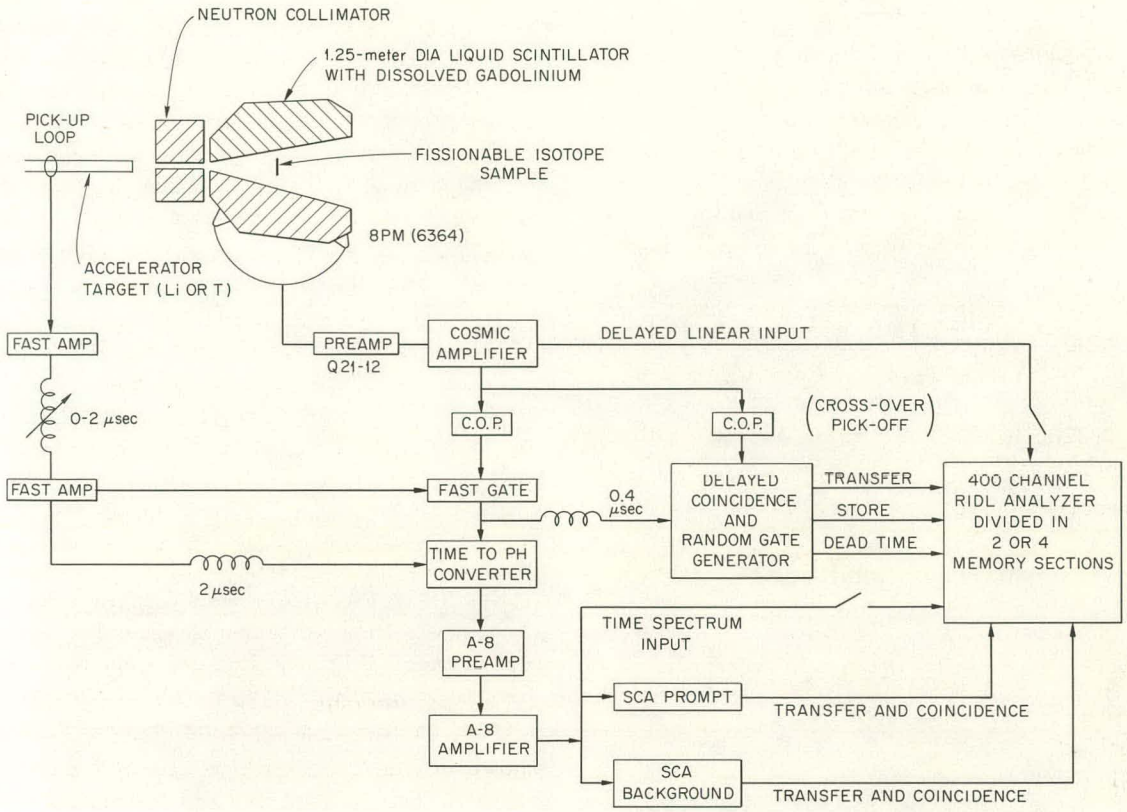

Fig. 1.2.2. Block Diagram of Electronics for Gadolinium-Loaded Scintillator Experiment.

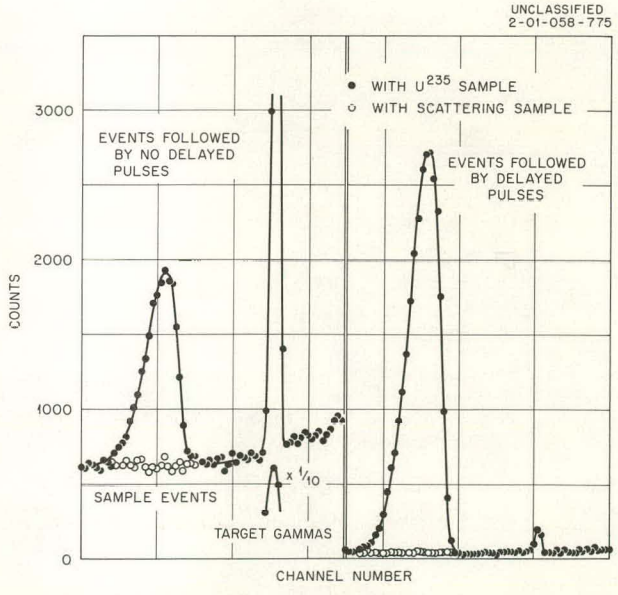

Fig. 1.2.3. Time-of-Flight Spectrum for 30-kev Neutrons on U^{235}.

SF_f/SF_c = the spectral fraction ratio, that is, the ratio of the fraction of fission pulses detected above the electronic bias to the fraction of capture pulses detected above the bias (= 1.14 ± 0.08).

For runs with monoenergetic neutrons, γ was taken to be the ratio of the area under the time-of-flight peak characterized by no delayed events to the area under the peak characterized by delayed events. For time-of-flight runs, a channel-by-channel ratio or the sum-over-a-few-channels ratio was used. A difficulty was encountered in this procedure in that there appeared to be a slight (~4 nsec) shift in time between events due to capture and those due to fission. This is not completely understood, but is probably due in part to the energy imparted to the scintillator by the scattering of fission neutrons, which occurs a few nanoseconds after the prompt-fission gamma rays are emitted.

The probability C_0 was measured by replacing the U^{235} sample by a fission chamber[5,6] containing ~5 g of U^{235}. Whenever a fission fragment was detected by the chamber during a burst of target neutrons, the 32-μsec gate was opened to detect gamma-ray pulses caused by capture of fission neutrons by the gadolinium. A possible error in C_0 due to the probability of a fission neutron causing additional fissions in the fission chamber being different from that for a thick sample was minimized by the multiplate design of the thick sample. It has been estimated that this difference caused no more than a 1% error in C_0.

The probability P_T was measured during the α experiments by generating a 32-μsec gate at random time and searching for gamma-ray pulses in the scintillator.

The spectral fraction ratio SF_f/SF_c was established by a study of pulse-height spectra of events at 30 and 600 kev. Figure 1.2.4 shows pulse-height spectra resulting from capture and fission events. The fission gamma-ray spectrum was extended to zero energy by observing coincidences between fission-chamber and scintillation-tank pulses. The capture gamma-ray spectrum was extrapolated to zero energy with the help of Monte Carlo calculations by Macklin.[7]

[5]G. deSaussure *et al., Neutron Phys. Div. Ann. Progr. Rept. Sept. 1, 1961,* ORNL-3193, p 177.

[6]G. deSaussure *et al., Neutron Phys. Div. Ann. Progr. Rept. Sept. 1, 1962,* ORNL-3360, p 51.

Results

Results of the experiment are given in Table 1.2.1 and compared with some results of Hopkins and Diven in Fig. 1.2.5. Agreement with previous results is seen to be good. The results include a correction for the contamination of the sample by U^{238} and other isotopes. This correction (<3%)

[7]R. L. Macklin, private communication.

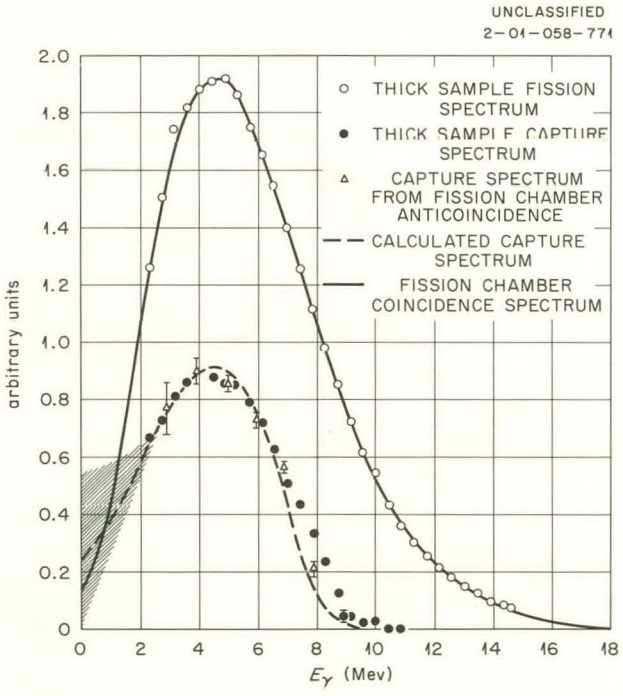

Fig. 1.2.4. Gamma-Ray Pulse-Height Spectra Resulting from Neutron Capture and Fission in U^{235}.

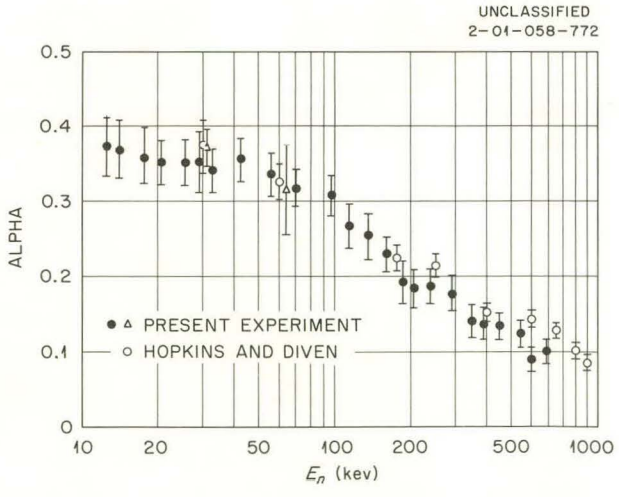

Fig. 1.2.5. Alpha as a Function of Incident Neutron Energy from 12 to 690 kev.

was done by assuming all the contaminants to have the same capture cross section as U^{238}. The error introduced by this assumption is not expected to exceed 1%.

The dominant errors in the present results are due to the uncertainty in the spectral fraction (7%), the uncertainty in C_0 ($\geq$4%), and the statistical counting errors.

Table 1.2.1. Experimental Values of α for U^{235} for kev Neutron Energies

Neutron Energy (kev)	α	Neutron Energy (kev)	α
12.3 ± 0.8	0.368 ± 0.040	115.0 ± 11.5	0.264 ± 0.030
14.0 ± 0.9	0.364 ± 0.040	136.0 ± 10.5	0.251 ± 0.030
17.5 ± 1.2	0.354 ± 0.040	160.0 ± 10.0	0.226 ± 0.023
20.5 ± 1.5	0.347 ± 0.031	185.0 ± 9.7	0.189 ± 0.028
25.5 ± 2.0	0.347 ± 0.031	205.0 ± 9.5	0.182 ± 0.025
29.4 ± 10.0	0.348 ± 0.039	240.0 ± 9.3	0.186 ± 0.023
30.0 ± 10.0[a]	0.372 ± 0.026	295.0 ± 9.1	0.175 ± 0.023
32.5 ± 2.7	0.339 ± 0.030	350.0 ± 9.0	0.139 ± 0.022
42.0 ± 3.7	0.352 ± 0.030	390.0 ± 8.8	0.136 ± 0.021
56.0 ± 5.5	0.333 ± 0.030	450.0 ± 8.7	0.132 ± 0.019
64.0 ± 15.0[a]	0.315 ± 0.060	540.0 ± 8.6	0.122 ± 0.018
70.0 ± 7.8	0.313 ± 0.025	600.0 ± 8.5	0.087 ± 0.018
96.0 ± 10.0	0.304 ± 0.025	690.0 ± 8.4	0.097 ± 0.018

[a]Measurements with fission-chamber technique: G. deSaussure *et al.*, *Neutron Phys. Div. Ann. Progr. Rept. Sept. 1, 1962*, ORNL-3360, p 51.

1.3. AN INVESTIGATION OF THE FEASIBILITY OF MEASURING α BY UTILIZING THE DIFFERENCE IN THE TOTAL ENERGIES OF PHOTONS EMITTED IN A FISSION EVENT AND A CAPTURE EVENT[1]

R. Gwin, G. deSaussure, L. W. Weston, E. Haddad,[2] and W. M. Lopez[2]

Introduction

Section 1.1 describes the measurement of α of U^{235} by a method in which a fission chamber containing a relatively large quantity of the fissile isotope U^{235} is located in a large scintillator tank. The extension of this method to measurements of α of U^{233} or Pu^{239} creates severe

[1]The indispensable contributions of R. D. Smiddie, Instrumentation and Controls Division, to the progress of these experiments are gratefully acknowledged.

[2]General Atomic, San Diego, Calif.

problems owing to pileup pulses produced by alpha particles in a fission chamber containing those isotopes. Therefore the feasibility of an alternate method, which does not require a fission chamber containing a large amount of the fissile isotope, has been experimentally tested.[3]

Theory

The logic of this type of experiment has been detailed previously.[4,5] Briefly, the method depends on the difference between the pulse-height distribution resulting from the absorption of capture gamma rays in a large scintillation detector and that resulting from the absorption of fission gamma rays. In the case of a gamma-ray cascade resulting from a capture event, the energy is fixed by the binding energy of the neutron – about 6.3 Mev for U^{235} and U^{233}. For gamma rays resulting from fission events, the total energy is not constant and in a fraction of the fission events is greater than 6.3 Mev. For a system with good summing properties for coincident gamma rays and good pulse-height resolution, the pulse-height distribution resulting from fission events extends to larger pulse heights than the distribution resulting from capture events. Thus, above a certain pulse height, called the "high bias," the gamma-ray events detected in such a system following a neutron interaction with a sample will result from fissions only. If the shape of the pulse-height distribution produced by fission gamma rays is known, the total number of fission events can be determined from a measurement of the number of gamma-ray events producing a pulse height above the high bias. The number of capture events is then given by the total number of gamma-ray events below the high bias less the number of fission events below the high bias. The shape of the pulse-height distribution due to fission events can be determined from measurements with a fission chamber containing a small amount of the fissile isotope.

Experimental Results

The gamma-ray detector for the present work was the large liquid scintillator described by Haddad.[3] From the results which follow, it appears that this detector has sufficiently good summing properties and pulse-height resolution to be useful in such experiments.

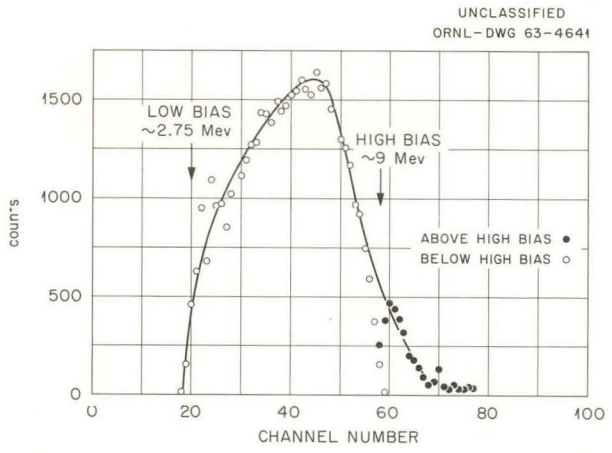

Fig. 1.3.1. Capture-Gamma-Ray Spectrum from the 11.65-ev Resonance of U^{235}.

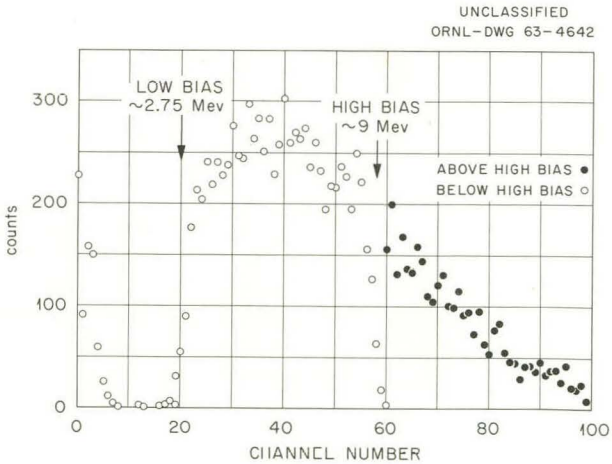

Fig. 1.3.2. Fission-Gamma-Ray Spectrum from the 11.65-ev Resonance of U^{235}.

[3]These experiments were performed at the LINAC facility at General Atomic. For a description of the facility see: E. Haddad *et al., Radiative Capture Cross Section Measurements*, GA-3874 (Mar. 1, 1963).

[4]G. deSaussure *et al., Neutron Phys. Div. Ann. Progr. Rept. Sept. 1, 1962*, ORNL-3360, p 51.

[5]B. C. Diven and J. C. Hopkins, p 407 in *Neutron Time-of-Flight Methods* (ed. by J. Spaepen), European Atomic Energy Community (EURATOM), Brussels, 1961.

Figures 1.3.1 and 1.3.2 show the pulse-height distributions for capture and fission events, respectively, in the 11.65-ev resonance of U^{235}.

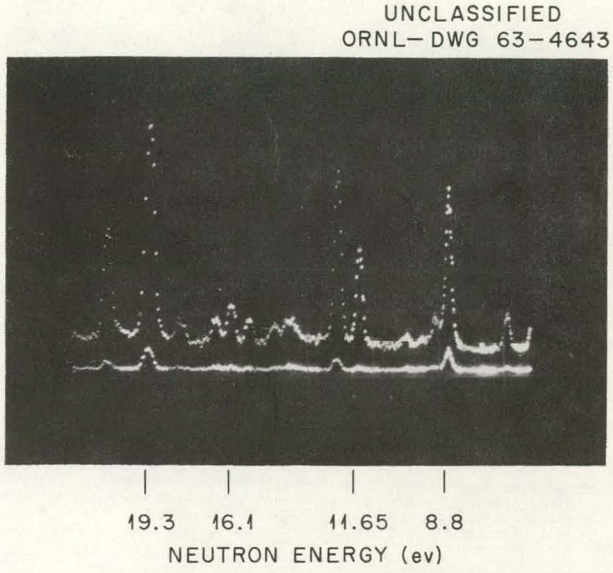

Fig. 1.3.3. Typical Time-of-Flight Spectrum for U^{235}: Relative Gamma-Ray Count Rate in Scintillator vs Neutron Energy. Upper curve, below high bias; lower curve, above high bias.

For this resonance the value of α is about 9. Inspection of the data shows that approximately 15% of the fission gamma rays produce pulse heights that are above the maximum pulse height produced by a capture gamma ray; similar results would be expected for U^{233}. A typical time-of-flight spectrum for U^{235} is shown in Fig. 1.3.3, covering the neutron energy range from roughly 6 to 21 ev. The upper curve represents the gamma-ray events falling between a high bias of $\sim$9 Mev and a low bias of $\sim$2.75 Mev. The lower curve represents the gamma-ray events which were above the high bias. It can be seen that for the 11.65-ev resonance identified on the figure very few counts were observed above the high bias compared with the number of counts below the high bias. This shows, qualitatively, that α is relatively large ($\sim$9) in this resonance.

Conclusion

Although the data obtained in these tests have not been further analyzed, it appears that the method should be given detailed consideration for the measurement of α of U^{233} and Pu^{239}.

1.4. VALIDITY OF THE DWBA FOR INELASTIC SCATTERING FROM NUCLEI[1]

F. G. Perey and G. R. Satchler[2]

It had been suggested that the distorted wave Born approximation (DWBA) used for analyzing inelastic scattering of alpha particles and nucleons is poor because of the strong coupling between the ground state and one or more excited states and that the set of coupled Schrodinger equations for these states should be solved exactly. It had also been suggested that if the coupling strength is expressed in terms of the collective model, DWBA is adequate only for deformations $\beta \leq 0.2$ for medium-energy (10- to 20-Mev) protons scattering from medium-weight nuclei. The data presented[1] substantiate the validity of DWBA, when applied consistently, in a considerably wider range. Also, the study gives additional support to the use of the simple DWBA in other reactions such as stripping, even when the inelastic scattering is known to be strong.

[1]Abstract of paper published in *Phys. Letters* 5(3), 212 (1963).

[2]Physics Division.

1.5. OPTICAL MODEL ANALYSIS OF PROTON ELASTIC SCATTERING IN THE RANGE OF 9 TO 22 Mev[1]

F. G. Perey

Thirty-five elastic-scattering angular distributions have been analyzed with the optical model using least-squares criteria for incident proton energies between 9 and 22 Mev. An increase of the real well depth as a function of mass number that was observed is explained[1] by the presence of a nuclear symmetry term in the potential and by the momentum dependence of the potential. The calculations are in good agreement with the polarization and reaction cross-section data. Formulas were derived for obtaining the values of the parameters of the optical model as a function of mass number and energy.

[1]Abstract of paper published in *Phys. Rev.* 131, 745 (1963)

1.6. FLUCTUATIONS IN THE EXCITATION FUNCTION FOR ELASTIC AND INELASTIC SCATTERING OF PROTONS FROM Ni^{62}

J. K. Dickens, F. G. Perey, and R. J. Silva[1]

Fluctuations in the excitation functions for elastic and inelastic scattering of protons from Ni^{62} have been observed. A 100-μg/cm^2-thick target with a 25-μg-thick carbon backing was bombarded with the proton beam of the ORNL tandem Van de Graaff. Scattered particles were detected with silicon surface-barrier detectors at 60 and 90° from the beam direction; measurements were taken every 4 kev for a range of about 100 kev at energies of 4.0 and 8.0 Mev. At these energies the target was approximately 5.8 and 3.6 kev thick, respectively. The results of the measurements are shown in Figs. 1.6.1 and 1.6.2.

At 90°, the energy of protons elastically scattered from the carbon backing of the target was too close to that of protons inelastically scattered from the 1.172-Mev level of Ni^{62} for the fluctuations in the excitation function of the inelastically scattered protons to be extracted. When the excitation function of the carbon-scattered protons alone was monitored, however, it was found, as was expected, that there were no fluctuations in the excitation function of the protons elastically scattered from carbon. (Only a slow increase due to carbon buildup on the target under proton bombardment was observed, the rate of accumulation being about 0.3 μg/hr.) Thus the fluctuations observed were due to the nickel. They appeared to be uncorrelated in the elastic and inelastic channels and also uncorrelated for elastic scattering at 60 and 90°. The widths of the fluctuations were approximately 10 to 15 kev. If these fluctuations are associated with the finite widths of the compound nuclear states,[2] then these states have approximate lifetimes of 10^{-19} sec.

[1]Chemistry Division.

[2]T. Ericson, *Phys. Rev. Letters* 5, 430 (1960).

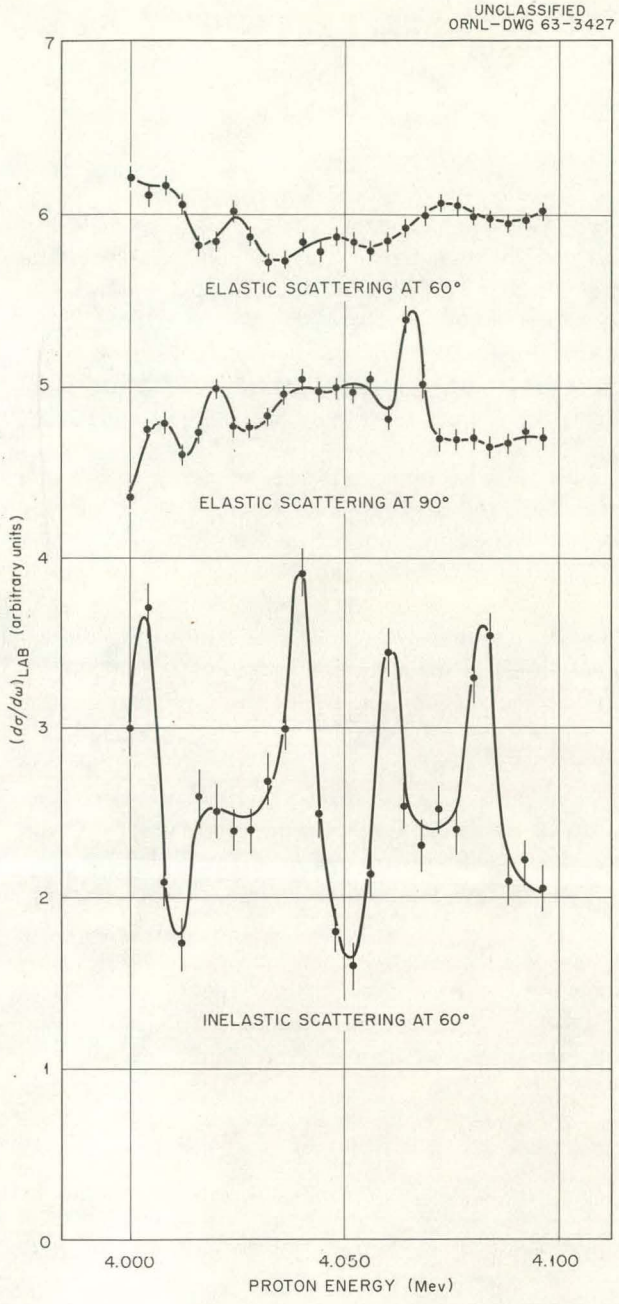

Fig. 1.6.1. Elastic and Inelastic Scattering of Protons from Ni^{62} at 60 and 90° for Proton Energies Between 4.0 and 4.1 Mev at Intervals of 4 kev. Target approximately 5.8 kev thick.

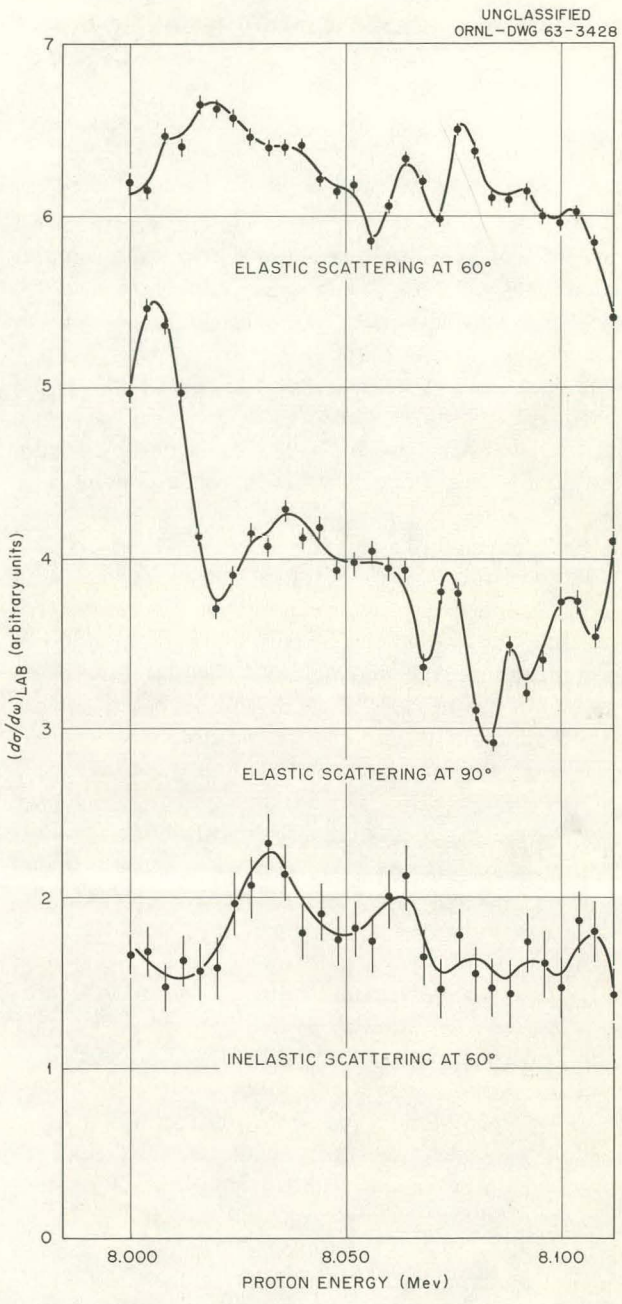

Fig. 1.6.2. Elastic and Inelastic Scattering of Protons from Ni^{62} at 60 and 90° for Proton Energies Between 8.0 and 8.1 Mev at Intervals of 4 kev. Target approximately 3.6 kev thick.

1.7. ELASTIC AND INELASTIC SCATTERING OF PROTONS BY THE EVEN-EVEN GERMANIUM ISOTOPES

J. K. Dickens, F. G. Perey, and R. J. Silva[1]

Current interest in the collective states of nuclei has prompted measurements of the angular distributions of 11-Mev protons inelastically scattered by the first 2^+ excited states of the even-even stable isotopes Ge^{70}, Ge^{72}, Ge^{74}, and Ge^{76}. The angular distributions of the protons elastically scattered by the isotopes were also obtained. In addition, several new levels in Ge^{70}, Ge^{74}, and Ge^{76} were observed and the positions of the 3^- collective states determined for all four nuclei.

In general, the experimental method for this work is the method common to all of our charged-particle cross-section experiments (see, for example, Secs. 1.9 and 1.12). The 11-Mev proton beam from the ORNL tandem Van de Graaff is directed into an evacuated scattering chamber, where it strikes the target and is then collected in a Faraday cup. The target is always oriented $+45°$ with respect to the beam line for forward-angle measurements and $-45°$ with respect to the beam line for backward-angle measurements. The data are normalized at between 90 and 100°. A counter permanently positioned at $-90°$ is used to assist in beam monitoring. The pulses corresponding to elastic events recorded by this "90° counter" are monitored by a scaler.

Scattered charged particles are detected by solid-state counters of both the surface-barrier and lithium-drifted type. The pulses from the particle detector are amplified by standard laboratory electronic equipment and are stored in an RIDL 400-channel analyzer. Dead-time losses in the analyzer, which are kept at less than 10%, are monitored by measuring the number of 90° counter (elastic) pulses in coincidence with the blocking pulse from the analyzer.

The output of the pulse-height analyzer (punched paper tape) is immediately transferred to magnetic computer tape and is simultaneously printed by the high-speed printer by using the Control Data 160A computer in the High Voltage Laboratory. In addition to recording the number of counts in each channel, the printout includes the running sums for each channel, that is, the number of counts up to and including the channel recorded. When sufficient spectra have been transferred to magnetic tape, a program written for the Control Data 1604 computer prepares them for plotting by CALCOMP. A precision plot is obtained for each spectrum; a typical spectrum is illustrated in Fig. 1.7.1.

Groups associated with the reactions of interest are identified, and the total counts and background counts for each group are obtained at each angle. Because this part of the data reduction is somewhat subjective, no satisfactory computer routine has been developed to perform this task. However, the remainder of the calculation is straightforward and a computer routine finishes the data reduction. The cross sections obtained are printed out, punched on cards in a format suitable for several theoretical computer routines, and plotted by CALCOMP. The plot output of this program is illustrated by Fig. 1.7.2.

Four of the five targets used in this experiment consisted of a layer of the separated isotope deposited on a carbon backing, each being ~ 200 $\mu g/cm^2$ thick. The fifth target consisted of natural germanium and was used to obtain the relative cross sections of inelastic proton scattering by the first 2^+ levels. Thus, cross sections for proton scattering by the heavier isotopes have been calculated relative to the proton scattering by Ge^{70}, but absolute cross sections have not yet been determined. The cross section for elastic scattering by Ge^{70} at 20° has been chosen as that predicted by a general optical model calculation (see Sec. 1.5).

The four angular distributions obtained for elastically scattered protons are illustrated in Fig. 1.7.3, and those for protons inelastically scattered by the first 2^+ excited state in each isotope are shown in Fig. 1.7.4. In Fig. 1.7.3 a pronounced change is evident in the shape of the angular distribution from the lightest to the heaviest isotope; no change in shape is displayed in the angular distributions for the inelastically scattered protons. The somewhat smaller relative cross sections for inelastic scattering by the

[1]Chemistry Division.

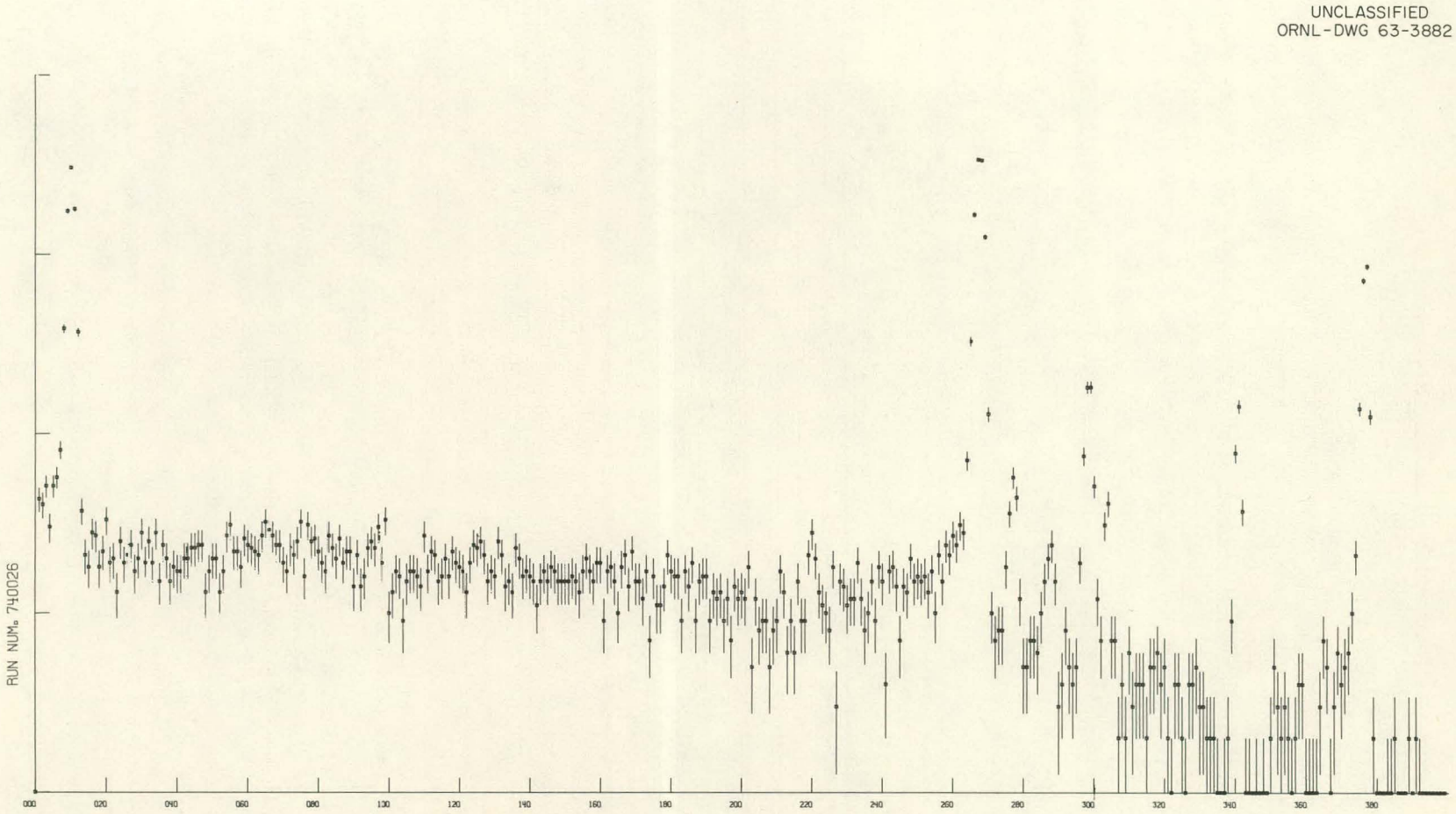

Fig. 1.7.1. Typical Pulse-Height Spectrum Obtained from Plotting Routine: Spectrum of 11-Mev Protons Scattered by Ge^{74} at 110°.

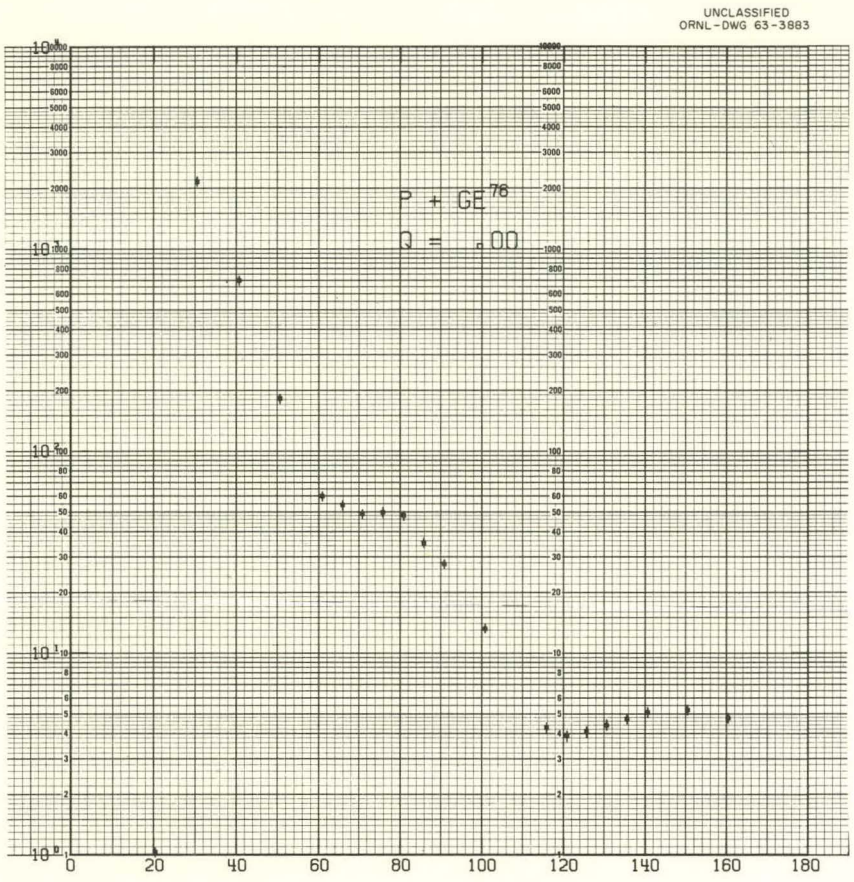

Fig. 1.7.2. Example of Output from the Plotting Routine of the Cross-Section Calculation Code: Differential Cross Sections for Elastic Scattering of 11-Mev Protons by Ge^{76}. The point at 20° would be off the top of the graph and has been folded over.

0.835-Mev level of Ge^{72} (if not associated with the normalizing factor) may be related to the closing of a neutron subshell at $N = 40$.

In addition to the previously reported energy levels at 1.04, 1.21, and 2.4 Mev in Ge^{70}, levels at 1.76, 2.24, and 2.61 Mev were observed. No new levels in Ge^{72} were seen up to an excitation energy of 3.05 Mev. In Ge^{74} the excitations of all levels reported by Eichler *et al.*[2] were seen except that of the level at 1.71 Mev. This is due to the solid-state-counter escape peak (see Sec. 1.13). A strong excitation of a new level at 2.61 Mev was also observed for Ge^{74}. In Ge^{76}, in addition to known levels at 0.567 and 1.12 Mev, levels at 1.45 and 2.82 Mev were observed.

Angular distributions are being obtained for the higher levels in these isotopes and are being analyzed with the use of the distorted-wave Born approximation formalism. Although the analysis is not complete, the positions of the 3^- collective states of the four isotopes can be identified: 2.61 Mev in Ge^{70}, 2.51 Mev in Ge^{72}, 2.61 Mev in Ge^{74}, and 2.82 Mev in Ge^{76}. Except for the 2.51-Mev level in Ge^{72}, none of these states had been observed before. The magnitude and shape of the angular distributions allow them to be definitely identified as collective 3^- levels.

[2]E. Eichler *et al.*, *Nucl. Phys.* **35**, 625 (1962).

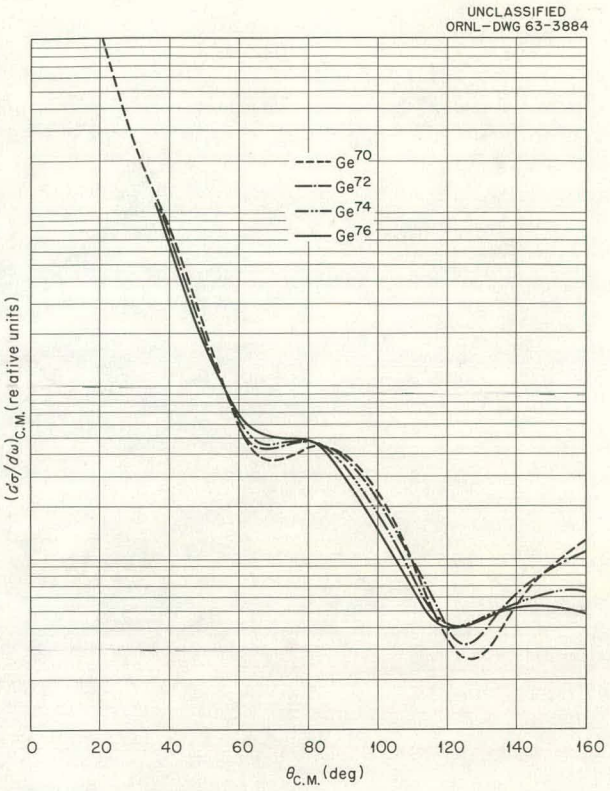

Fig. 1.7.3. Angular Distributions for Elastic Scattering of 11-Mev Protons by Ge^{70}, Ge^{72}, Ge^{74}, and Ge^{76}.

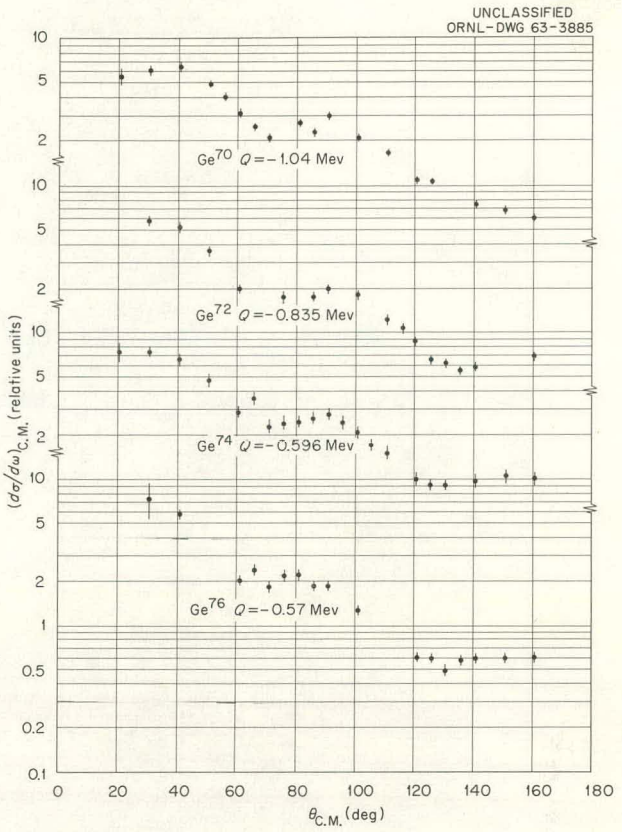

Fig. 1.7.4. Angular Distributions for Inelastic Scattering of 11-Mev Protons by the First 2^+ Excited States of the Four Even-Even Isotopes of Germanium.

Figure 1.7.5 shows the angular distributions obtained for protons inelastically scattered by these 3^- levels in Ge^{70} and Ge^{72}. For Ge^{72} the 3^- assignment to the 2.51-Mev level contradicts the previous assignment of 2^+ by Brun *et al.*[3] from the study of the decay of As^{72}. The 3^- levels show very little change in excitation energy through the range of the isotopes; this fact is characteristic of the near-constancy of the octopole vibration energy for most elements and aids in the identification of these states.

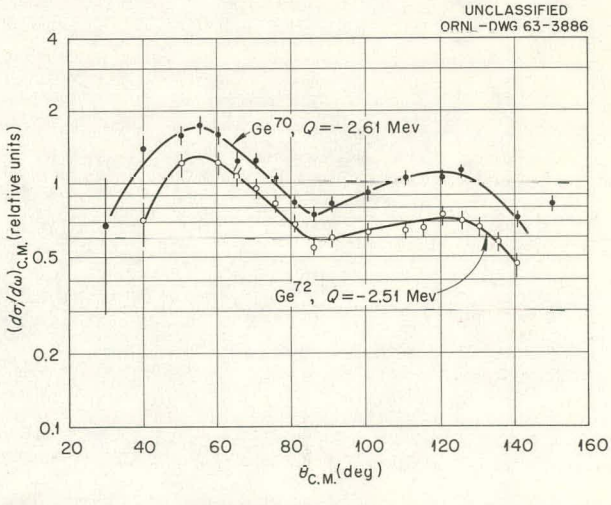

Fig. 1.7.5. Angular Distributions for Inelastic Scattering of 11-Mev Protons by the 3^- Collective States of Ge^{70} and Ge^{72}. The lines are included as guides and do not represent theoretical calculations.

[3] E. Brun, J. J. Kraushaar, and W. E. Meyerhof, *Phys. Rev.* **102**, 808 (1956).

1.8. EXCITED-CORE MODEL OF ODD-A NUCLEI AND THE $Cu^{63}(p,p')$ REACTIONS[1]

F. G. Perey, R. J. Silva,[2] and G. R. Satchler[3]

Differential inelastic scattering cross sections were measured for 11-Mev protons on Cu^{63} and Ni^{62}. It is shown[1] that such measurements are useful in checking predictions of the excited-core model. The scattering from the four lowest states of Cu^{63} is similar to the scattering from the first 2^+ collective state of Ni^{62}, implying that these four levels probably arise from the coupling of a $p_{3/2}$ proton to the 2^+ collective state in Ni^{62}.

[1]Abstract of paper published in *Phys. Letters* **4**, 25 (1963).

[2]Chemistry Division.

[3]Physics Division.

1.9. INELASTIC SCATTERING OF PROTONS FROM Cu^{63} AND Cu^{65} AND THE EXCITED-CORE MODEL

J. K. Dickens, F. G. Perey, and R. J. Silva[1]

A model for odd-A nuclei in which the single odd particle (or hole) is in excess of a closed shell has been considered by Lawson and Uretsky.[2] In this model the ground state of the odd nucleus is obtained by coupling the odd particle to the 0^+ ground state of the even-even core. Excited states are obtained by coupling the odd particle in the same state to the 2^+ first excited state of the even-even core. For the cases of Cu^{63} and Cu^{65}, a $p_{3/2}$ proton is coupled to Ni^{62} and Ni^{64}, respectively, giving rise to a multiplet of excited states having spins of $\frac{1}{2}$, $\frac{3}{2}$, $\frac{5}{2}$, and $\frac{7}{2}$. To lowest order, this multiplet is degenerate, with an energy equal to the core excitation energy; however, residual interactions between the nucleon and the core will split the multiplet. The model predicts that the "center of gravity" of the multiplet remains unchanged. That is, if I_0 is the spin of the ground state of the odd nucleus and E_c and I_c are the energy and spin of the state in the core, respectively, then

$$\sum_I E_I(2I+1) = (2I_0+1)(2I_c+1)E_c \ .$$

A further consequence of this model is that the intensity of excitation of the member of the multiplet with spin I should be $(2I+1)/[(2I_0+1)\times(2I_c+1)]$ times the intensity of excitation of the corresponding state of spin I_c in the even core nucleus. In addition, the angular momentum transfer during inelastic scattering by a member of the multiplet equals I_c, even when conservation of angular momentum allows other values. Thus, the shapes of the angular distributions for scattering of protons by members of the multiplet and by the excited state of the core should be similar.

To test these predictions, measurements were made of the inelastic scattering of 11-Mev protons by Cu^{63} and Cu^{65} and by the respective core nuclei Ni^{62} and Ni^{64}. [Although reported elsewhere (see Sec. 1.8), the results of the measurements on Ni^{62} and Cu^{63} are presented here for comparison with the data from Ni^{64} and Cu^{65}.] The general experimental details are discussed in another paper (Sec. 1.7). For this experiment

[1]Chemistry Division.

[2]R. D. Lawson and J. L. Uretsky, *Phys. Rev.* **108**, 1300 (1957); a more general treatment for which the odd nucleon is in a $p_{1/2}$ or $s_{1/2}$ shell is given by A. deShalit, *Phys. Rev.* **122**, 1530 (1961).

~1-mg/cm^2-thick enriched targets of each isotope were used; the overall resolution of the detection system (f.w.h.m.) was about 40 kev and all proton groups of interest were easily resolved.

Figure 1.9.1 illustrates the angular distributions of protons inelastically scattered by the first 2^+ state of Ni^{62} and the first five excited states of Cu^{63}. Angular distributions for protons scattered by the first four levels of Cu^{63} are similar to one another and to that for the 2^+ state of Ni^{62}. The angular distribution of the fifth excited state, however, is quite different. The spins of the first two states of Cu^{63} are known[3] to be $\frac{1}{2}$ and $\frac{5}{2}$. If spins of $\frac{7}{2}$ and $\frac{3}{2}$ are assigned to the third and fourth states, respectively, the "center of gravity" is 1168 kev, in excellent agreement with the energy 1172 kev of the first 2^+ excited state of Ni^{62}. The sum of the differential cross sections at 40° for the first four levels of Cu^{63} is 7.4 mb/steradian, only 10% lower than the value 8.2 mb/steradian measured for the 2^+ state of Ni^{62}.

The Cu^{65}-Ni^{64} analysis is not so clearcut since an unambiguous choice cannot be made for the $\frac{3}{2}$ member of the multiplet of Cu^{65} using the model. A spin assignment of $\frac{1}{2}^{(-)}$, based on the absence of any observed beta transition from

[3] J. B. Cummings *et al.*, *Phys. Rev.* **120**, 2128 (1960).

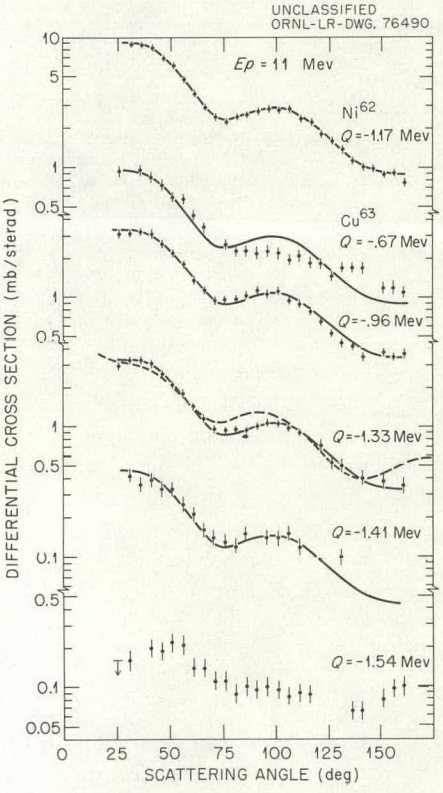

Fig. 1.9.1. Angular Distributions of Inelastically Scattered Protons by the First Excited State of Ni^{62} and the First Five Excited States of Cu^{63}. The solid lines show the shape of the Ni^{62} angular distribution; the dashed curve is the result of preliminary distorted wave Born approximation calculation with angular momentum transfer of 2.

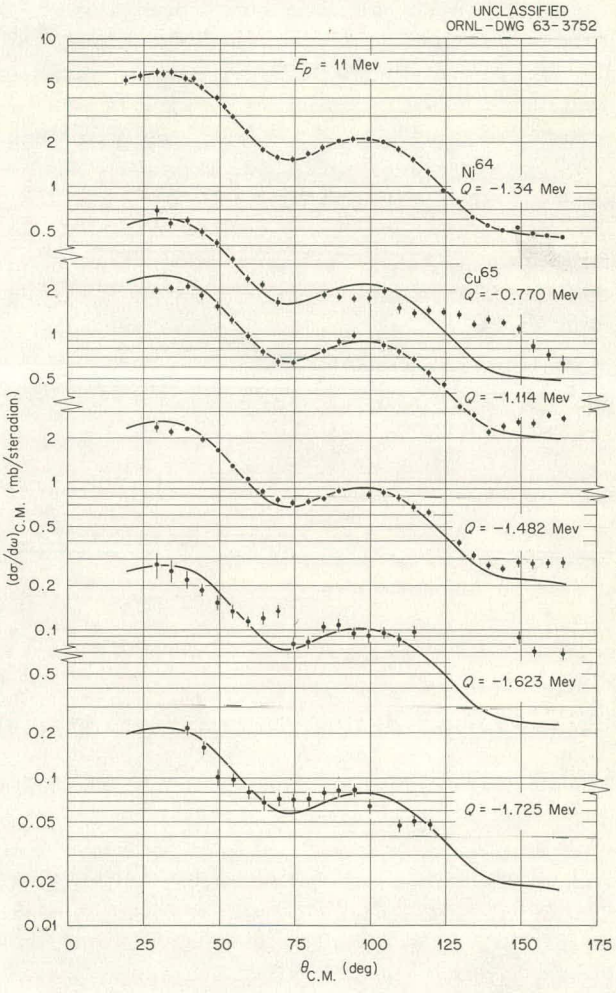

Fig. 1.9.2. Angular Distributions of Inelastically Scattered Protons by the First 2^+ State of Ni^{64} and the First Five Excited States of Cu^{65}. The solid lines give the shape of the Ni^{64} angular distribution in each case.

Ni^{65} or Zn^{65}, has been proposed[4] for the first excited state of Cu^{65}. This assignment tends to be substantiated by the fact that for the spin $\frac{1}{2}$ member of the multiplet the intensity of the excitation of the first excited state (Fig. 1.9.2) obeys the intensity rule given above. Furthermore, the angular distribution for proton scattering by the level is quite similar to that for the first level of Cu^{63}.

The $\frac{5}{2}$ and $\frac{7}{2}$ members of the multiplet are probably the second and third excited states of Cu^{65}, but the $\frac{3}{2}$ member could be either the fourth or the fifth excited state. As shown in Fig. 1.9.2, both angular distributions are similar to that for proton scattering by the 2^+ state of Ni^{64}. If it is assumed that the fourth excited state of Cu^{65} is the $\frac{3}{2}$ member of the multiplet, the "center of gravity" is 1329 kev; if it is assumed that the fifth excited state is the $\frac{3}{2}$ member, the "center of gravity" is 1349 kev. Neither choice can be eliminated, since the excitation energy of the first 2^+ state of Ni^{64} is 1.34 $\pm$ 0.01 Mev (ref 5). Finally, using either the fourth or the fifth state as the $\frac{3}{2}$ member, the cross sections add to within a few percent of the Ni^{64} excited state cross section.

The configuration mixing which splits the degenerate multiplet has been considered quantitatively for the Cu isotopes by Bouten and Van Leuven.[6] Their calculation indicates that the $\frac{7}{2}$ levels are almost pure configurations of $p_{3/2}$ protons coupled to the 2^+ cores, in agreement with the simple model presented above. On this basis, the present data substantiate the choice of $\frac{7}{2}^{(-)}$ for the third excited state of both Cu isotopes, since for this choice the intensity rule given above is obeyed for proton scattering over most of the angular range. The three remaining members of the multiplet are more complex than the simple model predicts. Thus, the $\frac{3}{2}$ excited-state wave function contains some of the core ground-state wave function; this admixture reduces the excitation of the $\frac{3}{2}^{(-)}$ excited states. The effect of configuration mixing upon the $\frac{1}{2}^{(-)}$ members of the multiplets, although smaller, is evident in Figs. 1.9.1 and 1.9.2.

[4]R. Jambunathan, M. R. Gunye, and B. Saraf, *Phys. Rev.* **120**, 1839 (1960).

[5]*Nuclear Data Sheets*, compiled by K. Way *et al.*, Printing and Publishing Office, National Academy of Sciences National Research Council, Washington, 1960; J. Benvensite, A. C. Mitchell, and C. B. Fulmer, *Phys. Rev.* **130**, 309 (1963); see also Sec. 1.13.

[6]M. Bouten and P. Van Leuven, *Nuclear Phys.* **32**, 499 (1962).

1.10. DEUTERON OPTICAL MODEL ANALYSIS IN THE RANGE OF 11 TO 27 Mev[1]

C. M. Perey[2] and F. G. Perey

Deuteron elastic-scattering angular distributions have been analyzed by means of a simple optical model without spin-orbit potentials. Two of the discrete valleys in the parameter space of the model were used to analyze 52 angular distributions measured for target nuclei with $Z \geq 12$ and deuteron energies in the range 11 to 27 Mev, with particular emphasis given to data at energies of 11.8, 15, and 21.6 Mev. In order to determine the trends of the optical model parameters as a function of mass number and energy, four different sets of geometrical parameters were used and only the well depths, real and imaginary, were varied to provide a best fit to the experimental data.

[1]Abstract of paper submitted for publication in the *Physical Review*.

[2]Consultant.

The real well depths showed a smooth linear increase as a function of the Coulomb parameter $Z/A^{1/3}$ and a smooth linear decrease as a function of energy. The imaginary well depths showed fairly large fluctuations from element to element but no systematic trend as a function of mass number. For all four sets of parameters the imaginary well depth decreased rapidly for bombarding energies from 11 to 14 Mev and then increased slowly for energies from 15 to 27 Mev.

1.11. OPTICAL MODEL ANALYSIS OF 15-Mev DEUTERON ELASTIC-SCATTERING ANGULAR DISTRIBUTIONS

C. M. Perey[1] and F. G. Perey

Soon after the authors had completed a systematic analysis of deuteron elastic scattering in the range 11 to 27 Mev (see Sec. 1.10), Jolly *et al.*[2] reported angular distribution measurements for the elastic scattering of 15-Mev deuterons from 23 different elements. It was decided, therefore, to analyze the new data in the same manner.

Angular distributions for 9 of the 23 elements had been measured previously by Cindro and Wall,[3] and their data were included in our analysis. Both sets of data for these nine elements and the analysis of each set are shown in Fig. 1.11.1. With the exception of Au, the measured angular distributions from the two sets of data all differ quite markedly. Over the angular range used by Jolly *et al.*, Cindro and Wall quote errors of 5% for their data. Jolly *et al.* do not give an estimated error but indicate that all data points were measured independently several times and that the scatter of the points should represent the accuracy of the measurements. Even if an error of 10% is assumed for the new data – runs were taken to have a 1% statistical error in the counts in the elastic peak – the two sets of data are very different.

For the analysis, both sets of data were fitted for the smallest χ^2 by using the geometrical parameters identified as set C in ref 2 and allowing the two well depths V_s and W_D to be adjusted by the search code. The two fits are in good agreement for angles up to 50°, but in most cases they differ markedly for larger angles. This reflects the fact that for angles smaller than 50° the optical model differential cross sections for this energy and for this range of elements are not very sensitive to the parameters of the model.

The two sets of data for Fe and Cu can be made to agree with each other and with the optical model calculations up to 50° if the data of Cindro and Wall for angles greater than 30° are multiplied by 1.6 and 1.5, respectively. Although there is no indication in the paper of Cindro and Wall as to how such corrections could be justified, we have used these corrections in our analysis. For Rh and Pd, the data of Jolly *et al.* for angles up to 50° disagree both with the data of Cindro and Wall and with the optical model fits. If the data of Jolly *et al.* are multiplied by 0.7 and 0.82 for Rh and Pd, respectively, then the agreement is better. Since absolute cross sections for the data of Jolly *et al.* were obtained in a separate experiment, it was decided to correct these data by the factor indicated above for the rest of the analysis.

For Sn, the two sets of data are not too different except in the range of 25 to 75°. Since the optical model fits do not favor one or the other set of data and since they agree with each other remarkably well, no attempt was made to renormalize any of the data.

[1]Consultant.

[2]R. K. Jolly, E. K. Lin, and B. L. Cohen, *Phys. Rev.* **130**, 2391 (1963).

[3]N. Cindro and N. S. Wall, *Phys. Rev.* **119**, 1340 (1960).

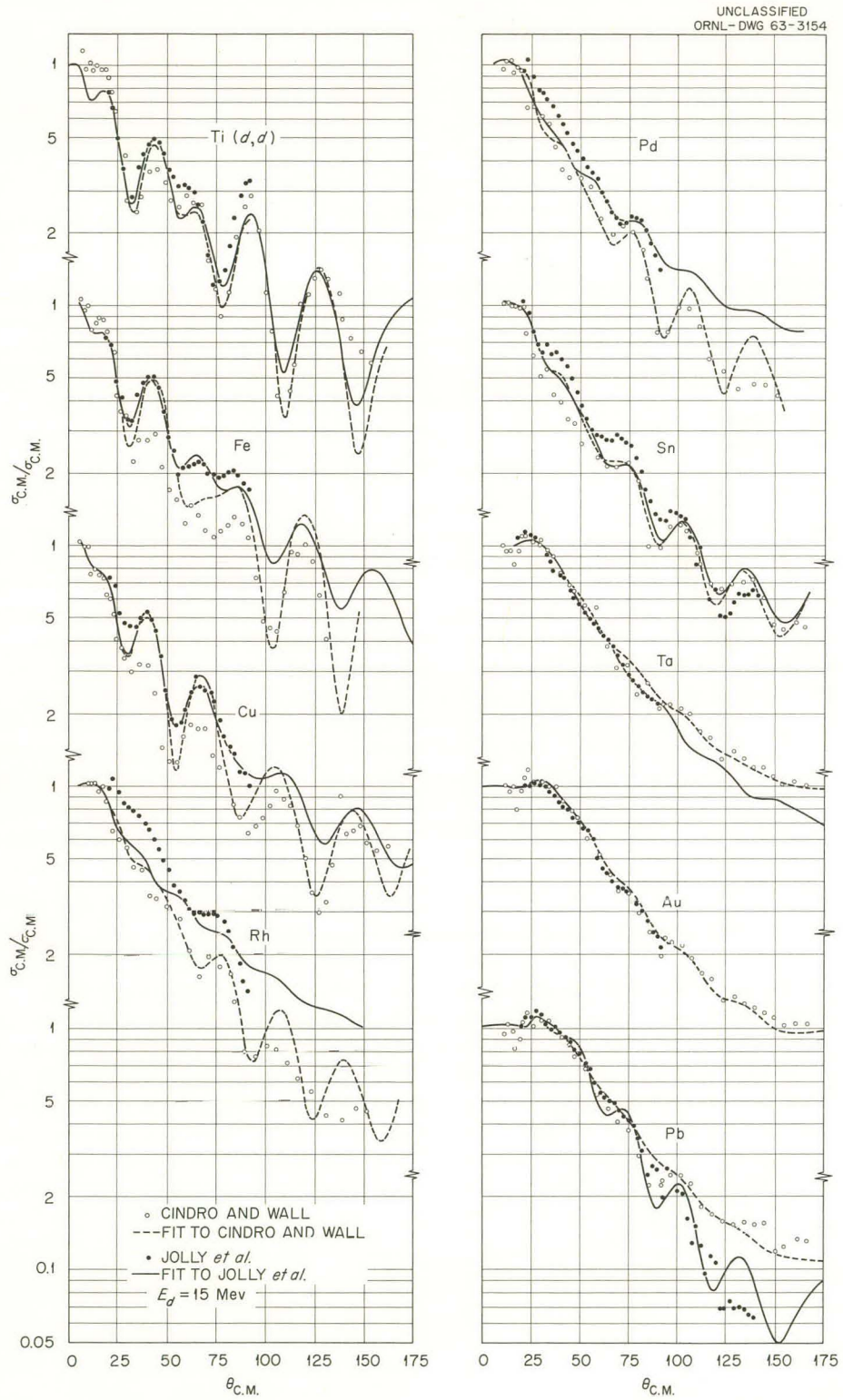

Fig. 1.11.1. Comparison of the Data of Jolly *et al.* and Cindro and Wall for Elastic Scattering of 15-Mev Deuterons.

For elements heavier than Sn the diffraction patterns are very much damped, and small differences in the data have much more pronounced effects on the optical model parameters. For Ta, the disagreement of the data is not very pronounced but the oscillations in the data are almost exactly out of phase, resulting in very different optical model parameters. In view of the systematic analysis, the well depths obtained from the data of Cindro and Wall are more satisfactory than those obtained from the data of Jolly *et al.* Although the data for Pb are not in good agreement for angles up to 90°, they oscillate in phase and the result is that they give similar real well depths for the two sets of data. For angles greater than 100°, the Pb data differ by a factor of about 2, resulting in imaginary well depths which differ by a factor of 2. As mentioned above, the two sets of data for Au are in excellent agreement.

The remaining data of Jolly *et al.* were used as given, and the results of the analysis are given in Fig. 1.11.2, where the well depths, both real and imaginary, are plotted as a function of the Coulomb parameter $Z/A^{1/3}$. The lines showing the trends of V_s on Fig. 1.11.2 are those obtained in the previous analysis (Sec. 1.10). For Er and Yb, the data of Jolly *et al.* for V_s are much lower than the line, and an attempt was made to find a deeper well which would fit the data. The results are shown as points in corresponding positions above the line, but they do not belong to the same family of potentials.

To conclude, in view of the great differences between the two sets of data, it seems dubious whether a more extensive analysis of the new

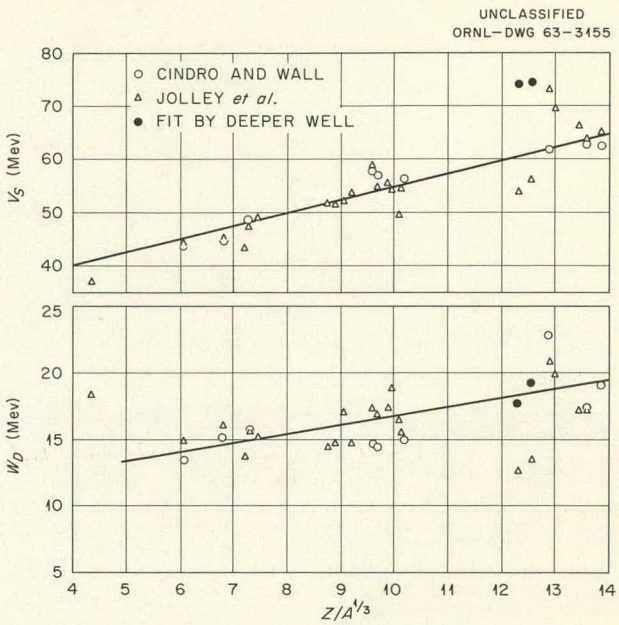

Fig. 1.11.2. The Real Well Depths (V_s) and Imaginary Well Depths (W_D) as Functions of $Z/A^{1/3}$ for 15-Mev Deuteron Optical Model Analysis. The lines indicate the trends of the parameters.

data would be meaningful or whether any significance can be attached to the departure from the linear trends of some of the well depths. We would like to stress the importance of measuring accurate cross sections, particularly for heavy nuclei, and for extending the measurements to large angles since the diffraction patterns are more pronounced at backward angles and therefore play a great role in determining the parameters of the optical model.

1.12. ELASTIC AND INELASTIC SCATTERING OF 5- TO 13.5-Mev DEUTERONS FROM Ni^{60}

J. K. Dickens, F. G. Perey, and R. J. Silva[1]

The recent optical model analysis by Perey and Perey of the elastic scattering of 11- to 27-Mev deuterons by medium-weight nuclei (see Sec. 1.10) showed that excellent fits of the experimental data can be obtained. However, for 11 Mev $\leqq E_d \leqq$ 14 Mev, the analysis showed that,

[1]Chemistry Division.

contrary to expectation, the surface imaginary part of the potential, W_D, decreases as a function of energy. Furthermore, the value of W_D obtained from an analysis of the data for 4.07-Mev deuteron elastic scattering by nickel cannot be obtained by extrapolating this parameter from values at higher energies. Thus, accurate experimental data at small energy intervals between 4 and 11 Mev are needed to determine the trends of W_D, as well as other optical model parameters, at these low energies.

Measurements of elastic scattering of deuterons by Ni^{60} have been obtained for the energy region 4.86 Mev $\leqq E_d \leqq$ 13.56 Mev. The Ni^{60} target was a self-supporting metal foil, ~2 mg/cm^2 thick, enriched to 99.8%. The deuteron beam was obtained from the ORNL tandem Van de Graaff. Pulse-height spectra of the scattered charged particles were obtained at 5° intervals between laboratory angles of 30 and 160°. The major contribution to the overall energy resolution (f.w.h.m.) was the thickness of the target to the low-energy deuterons.

The methods of reducing these data are discussed in Sec. 1.7. The measured absolute elastic differential cross sections are shown in Fig. 1.12.1. The onset of diffraction-like scattering with increasing energy is clearly evident. These data have been compared with those previously reported at 11.15 Mev (ref 2), 11.8 Mev (ref 3), and 13.5 Mev (ref 4). In all comparisons the relative cross sections agree very well. The absolute values of the present data are somewhat

[2]M. Takeda, *J. Phys. Soc. Japan* **15**, 557 (1960).

[3]R. Jahr, K. D. Muller, W. Oswald, and U. Schmidt-Rohr, *Z. Physik* **161**, 509 (1961); G. Igo, W. Lorenz, and U. Schmidt-Rohr, *Phys. Rev.* **124**, 832 (1961).

[4]N. Cindro and N. S. Wall, *Phys. Rev.* **119**, 1340 (1960).

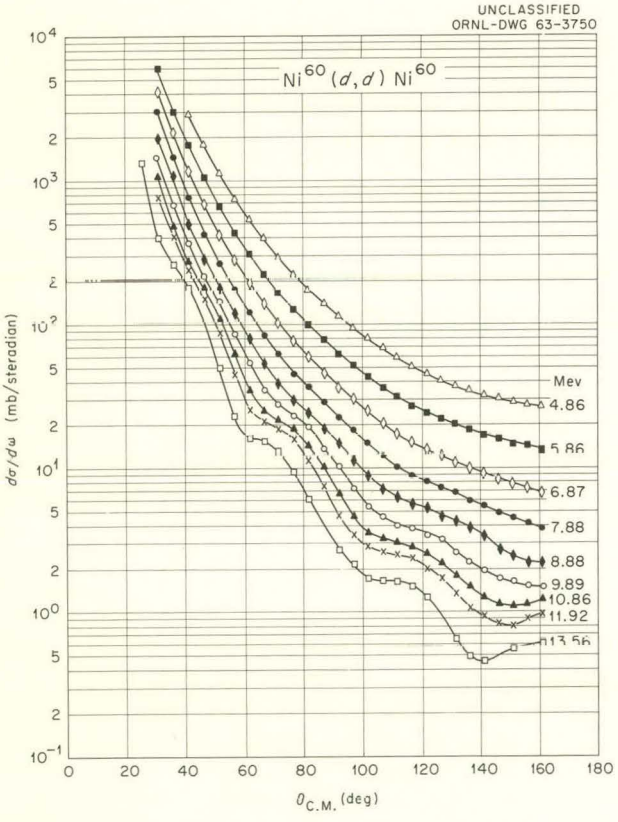

Fig. 1.12.1. Elastic Scattering of Deuterons from Ni^{60}. The lines are drawn to guide the eye and do not represent theoretical curves.

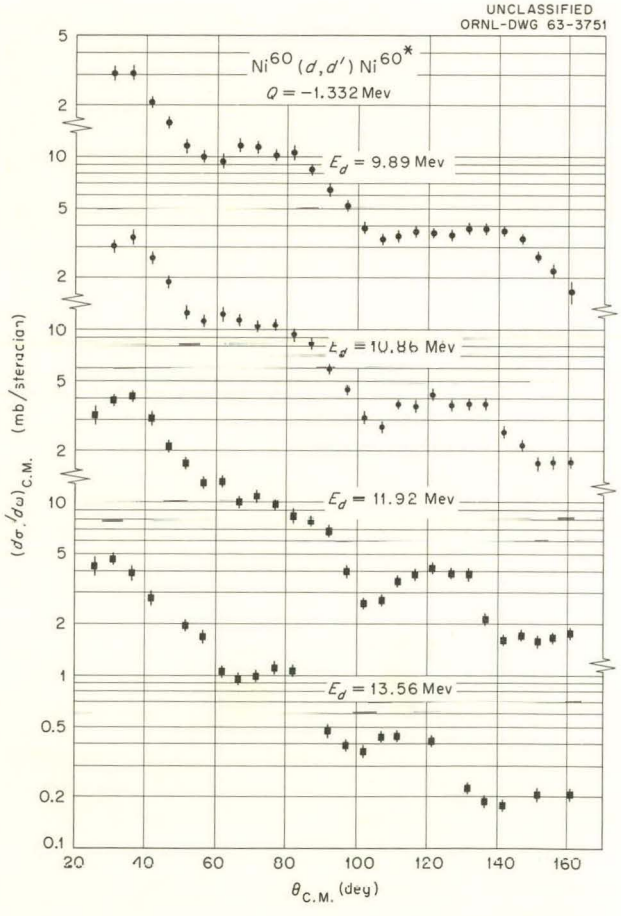

Fig. 1.12.2. Inelastic Scattering of Deuterons from the 2^+ First Excited State of Ni^{60} ($Q = -1.332$ Mev).

smaller in magnitude than the previously reported cross sections at 11.15 and 11.8 Mev, but agree well at 13.5 Mev.

In addition to the elastically scattered deuterons, the deuterons inelastically scattered by the first excited state of Ni^{60} ($Q = -1.33$ Mev) were obtained for the highest bombarding energies. These cross sections are shown in Fig. 1.12.2. They are similar to those obtained for proton scattering.

1.13. ENERGY LEVELS OF Ni^{64}[1]

J. K. Dickens, F. G. Perey, and R. J. Silva[2]

The published paper[1] will present the results of an investigation of the excited states of Ni^{64} through the study of the inelastic scattering of 11-Mev protons from an isotopically enriched target of Ni^{64}. Also included will be the excitation energies of 30 levels between 1.34 and 5.49 Mev that were obtained. For the level at 3.55 Mev a spin and parity assignment of 3^- is suggested.

[1]Submitted for publication in the *Physical Review* under the title "Level Structure of Ni^{64}."

[2]Chemistry Division.

1.14. PROTON EXCITATION OF THE TWO-PHONON STATES IN Ni^{62} AND Ni^{64}[1]

J. K. Dickens, F. G. Perey, R. J. Silva,[2] and T. Tamura[3]

The paper to be published[1] gives measurements that were made of differential cross sections for inelastic scattering of 11-Mev protons by the second, third, and fourth excited states of Ni^{62} and Ni^{64}. The data were analyzed within the framework of a vibrational model, assuming the states to be 0^+, 2^+, and 4^+ members of the two-phonon triplet. The analyses indicate spin assignments of 0^+, 2^+, and 4^+ to the 2.05-, 2.30-, and 2.34-Mev levels of Ni^{62}, respectively, and 0^+, 4^+, and 2^+ to the 2.28-, 2.62-, and 2.88-Mev levels of Ni^{64}, respectively.

[1]Abstract of paper submitted for publication in *Physics Letters*.

[2]Chemistry Division.

[3]Physics Division.

1.15. A FORTRAN PROGRAM FOR THE CALCULATION OF SCATTERING OF NUCLEONS FROM A NONLOCAL OPTICAL POTENTIAL[1]

F. G. Perey

The published report[1] gives a listing of a FORTRAN program for calculating the scattering of nucleons from a nonlocal optical potential. The report also gives the mathematical formulation of the problem and the numerical methods used in the code. The input to the program is explained, and each subroutine of the code is given a brief functional description.

[1]Published as ORNL-3429 (June 26, 1963).

1.16. IONIZATION OF LITHIUM BY ELECTRONS AND PROTONS

R. G. Alsmiller, Jr.

Gryzinski[1] recently introduced a formalism for calculating the ionization and excitation of atomic systems by charged-particle impact. This formalism has been used to calculate the ionization of lithium by electrons and protons. The calculations were carried out using two different approximation wave functions for the 2*s* electron in lithium.[2,3] The results are shown in Figs. 1.16.1 and 1.16.2. Also shown in the figures are the Born approximation results of McDowell and Peach.[4]

[1]M. Gryzinski, *Phys. Rev.* **115**, 374 (1959).

[2]T. Y. Wu and F. C. Yu, *Chinese J. Phys.* **5**, 162 (1944).

[3]E. Holoien, *Proc. Phys. Soc.* **68**, 297 (1955).

[4]M. R. McDowell and G. Peach, *Phys. Rev.* **121**, 1383 (1961); the wave function given in ref 2 was used in the calculations of McDowell and Peach.

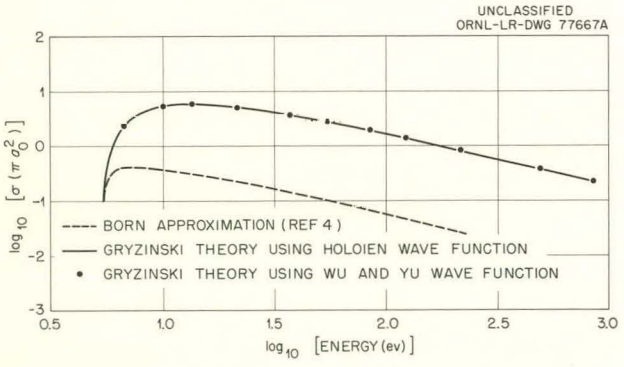

Fig. 1.16.1. Ionization of Lithium by Electrons.

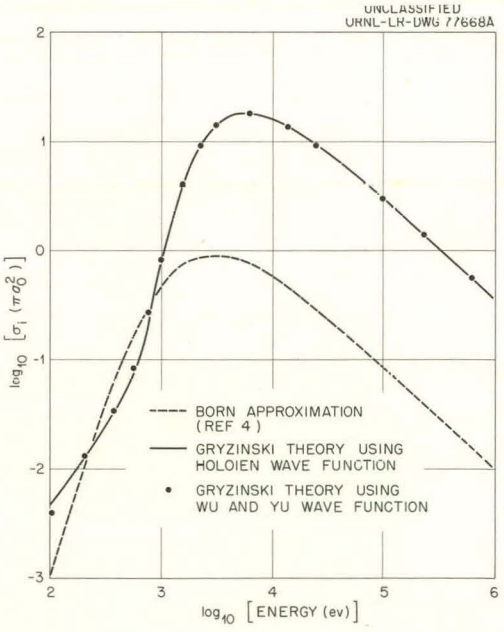

Fig. 1.16.2. Ionization of Lithium by Protons.

The calculated cross sections are very insensitive to the choice of wave function but are much larger than the Born approximation cross sections. Since the Born approximation usually overestimates the cross section, it seems reasonable to conclude that the values obtained here are unrealistically large, and thus we have an apparent failure of the Gryzinski theory.

It is difficult to state categorically why the theory is unreliable in this case while in other cases it has given very good results.[1,5] However, the answer seems to lie in the fact that the lithium electron is very loosely bound. Because of the use of a pure Coulomb force, the theory overestimates the importance of very low-energy transfers and will treat adequately only those processes in which these low-energy transfers are not allowed.

[5]R. G. Alsmiller, Jr., *Dissociation and Ionization of H_2^+ by Electrons and Protons*, ORNL-3232 (1962).

1.17. STATUS OF PULSED-NEUTRON MEASUREMENTS OF NEUTRON DIFFUSION PARAMETERS FOR ICE

E. G. Silver

The experiment[1] to measure the temperature dependence of the diffusion parameters for thermal neutrons in light-water ice was continued, but at a pace slowed by experimental difficulties associated with such components as the accelerator, the time analyzer, and the refrigerator. Also, the experiment was interrupted so that it could be moved to a new building (Bldg. 3114), where a larger experimental area with lower backscattering was available.

Apparatus

The setup of the experiment in its new location is shown in Fig. 1.17.1. The large distance of ~19 ft from the accelerator ground plane to the target necessitated the insertion of an electrostatic quadrupole lens to counteract beam spreading. After some experimentation the position shown was the one chosen to give the maximum target beam current. Attempts were made to energize the lens with a battery system, but they were only partially satisfactory. After a pair of regulated 3-kv power supplies, variable in 50-v steps, was installed, beam focusing of the target was satisfactory.

One of the chief problems in measuring decays in small assemblies is how to reduce the constant neutron background which degrades the decay data and limits the practical observation time after each neutron burst. In this system the chief source of background during the nominal "off" part of the cycle was due to a small beam current of deuterons scattered off the lens components or the deflection plates in the ion source. In order to reduce this source of background, a supplementary deflection system, consisting of a pair of 15-in.-long plates spaced 1 in. apart, was mounted in a section of the beam tubing located as shown in Fig. 1.17.1. A circuit[2] was constructed which places up to 1.2 kv on the deflection plates in synchronism with the deflection

[1]E. G. Silver, *Neutron Phys. Div. Ann. Progr. Rept. Sept. 1, 1962*, ORNL-3360, pp 63–67.

[2]Designed by R. J. Scroggs, Instrumentation and Controls Division.

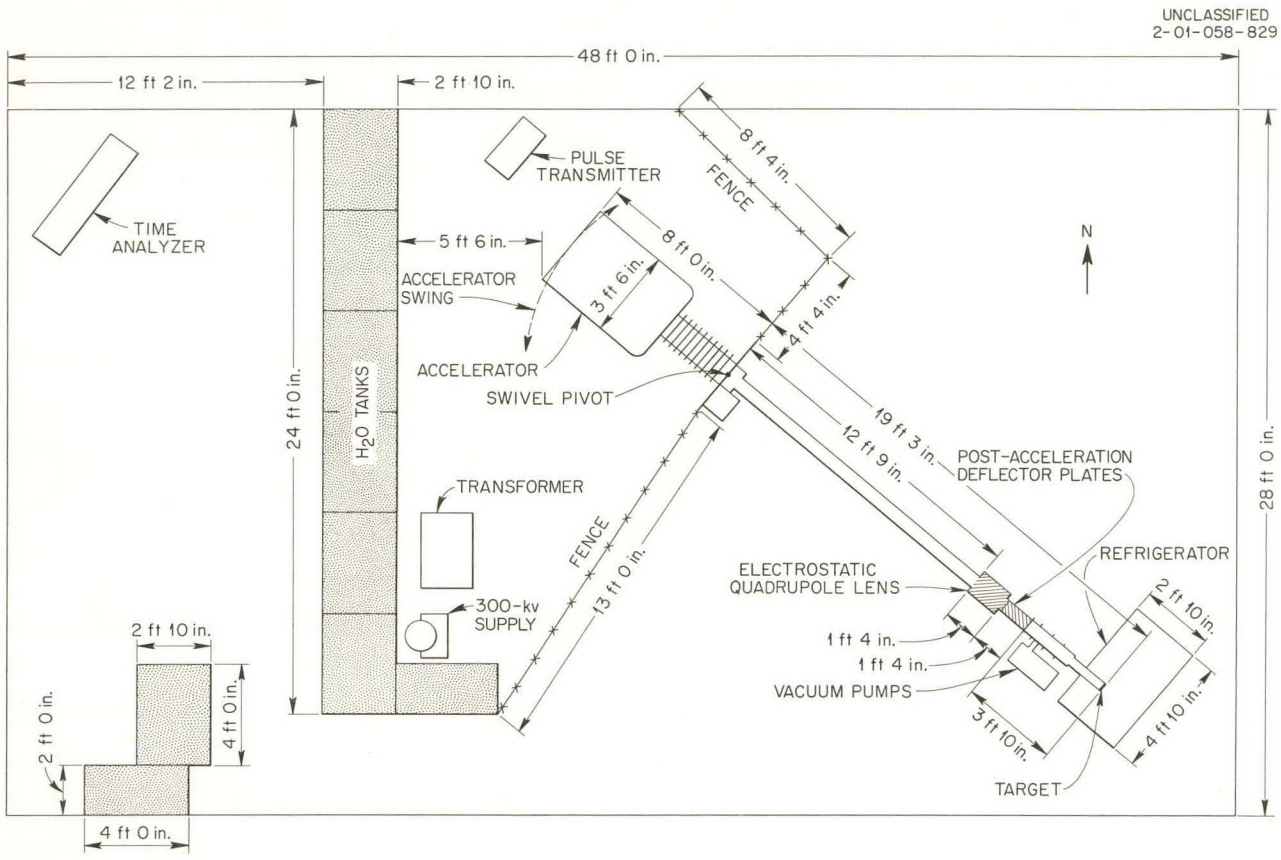

Fig. 1.17.1. Diagram Showing Relative Locations of Accelerator (Oriented for Ice Experiment), Quadrupole Lens, and Postaccelerator Deflectors.

voltage on the primary deflection system in the ion source. The rise time of the voltage on the deflection plates is of the order of 2 μsec. The background is reduced by a factor of 10 to 20 by the use of this system, which is now routinely employed in all measurements. A non-deflectable portion of the beam does exist and appears as a slight blue glow on a quartz viewer inserted in the beam, but this component gives rise to no neutrons. It is attributed to heavy ion contamination in the beam which stems from oil vapor and residual air in the vacuum system.

The length of the evacuated flight path from the primary pump to the target made it desirable to install an auxiliary vacuum station near the target end, as shown in Fig. 1.17.1. This helped to maintain low pressure at the target end of the system.

The entire accelerator is mounted on a fixed swivel pin at the ground-plane end of the machine, with transverse wheels at the rear end to allow the accelerator to swing through an arc of about 60°, so that the accelerator can be pointed in other directions for different experiments[3] and then easily be relocated to its original position.

Calibrations[4]

When the accelerator was ready to operate in the new location, calibrations were performed to obtain the absolute efficiency of a long counter in a fixed location relative to a neutron source; the counter was then used to determine the target yields as a function of beam energy. Also, an Am-Be neutron source was calibrated against a standard source, and the effects of distance and angle on the long counter response were measured.

[3]The design and installation of this swivel system, as well as the installation and maintenance of the accelerator and its associated equipment in Building 3114, were done by J. D. Kington.

[4]Summarized from: E. G. Silver, *Source-Strength and Long-Counter Response Calibrations at the BSF 300-kev Accelerator*, ORNL-TM-550 (Apr. 8, 1963).

The standard was an Am-Be source (No. 9955) calibrated by the National Bureau of Standards as having a yield of $(4.16 \pm 0.11) \times 10^6$ neutrons/sec. It was placed in a low-mass holder directly against the target end of the accelerator. The long counter response to this source was compared with the long counter response to neutrons produced by the accelerator. Suitable corrections for the energy response function of a Hansen-McKibben type of long counter were made on the assumption that the energy spectrum of an Am-Be source is identical to that of a Po-Be source.[5] The neutron yield per microampere of beam current was then measured as a function of accelerator voltage for both the $d(D,He^3)n$ and the $d(T,\alpha)n$ reaction. The result is shown in Fig. 1.17.2.

Then, with a second long counter in a fixed position as a monitor, the response of the first counter, both as a function of distance and as a function of angle of orientation, was measured for D-T (14-Mev) neutrons. The results are shown in Figs. 1.17.3 and 1.17.4.

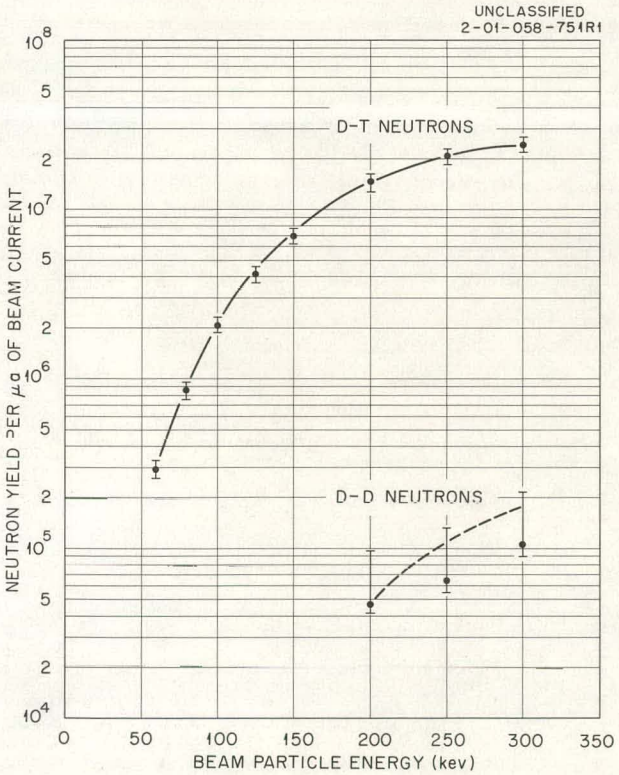

Fig. 1.17.2. Measured Total Neutron Production per Microampere of Beam Current as Function of Beam Energy.

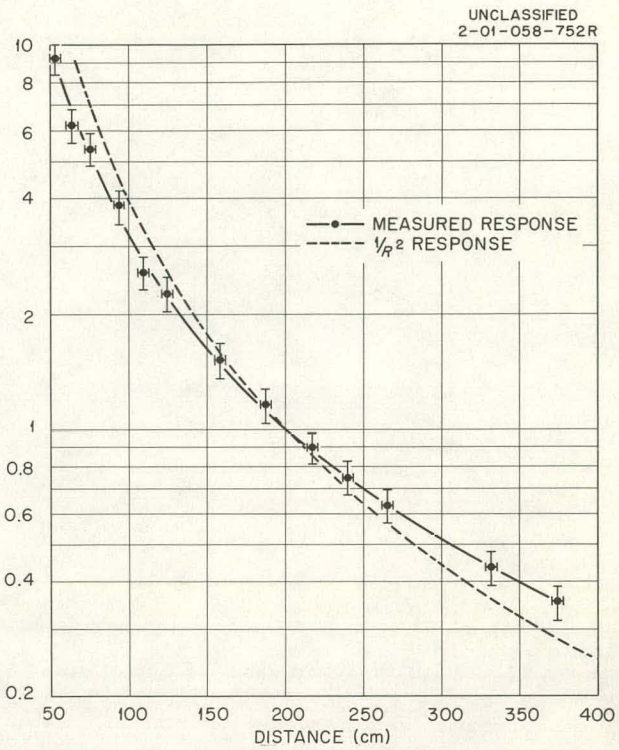

Fig. 1.17.3. Relative Response of Long Counter, at a Right Angle to Deuteron Beam, as a Function of Distance Between Front Face of Counter and D-T Neutron Source. The $1/R^2$ curve is shown for comparison. Both curves are normalized to unity at 200-cm separation.

A second Am-Be neutron source (No. 21) was calibrated by comparison with No. 9955 and found to have a yield of $(7.33 \pm 0.196) \times 10^6$ neutrons/sec.

Preparation of Small Ice Cylinders

A technique for growing small cylinders of air-free ice required for some of the measurements was developed. The apparatus is shown in Fig. 1.17.5. A thin-walled aluminum cylinder of the desired inside diameter and 4 to 5 in. longer than the final test body is set onto a glass plate and sealed to the plate with Apiezon Q sealing compound. A cover with a vacuum hose connection

[5] K. W. Geiger, Division of Applied Physics, National Research Council, Ottawa, Canada, private communication. See also K. W. Geiger and C. J. D. Jarvis, *Can. J. Phys.* **40**, 33–48 (1962).

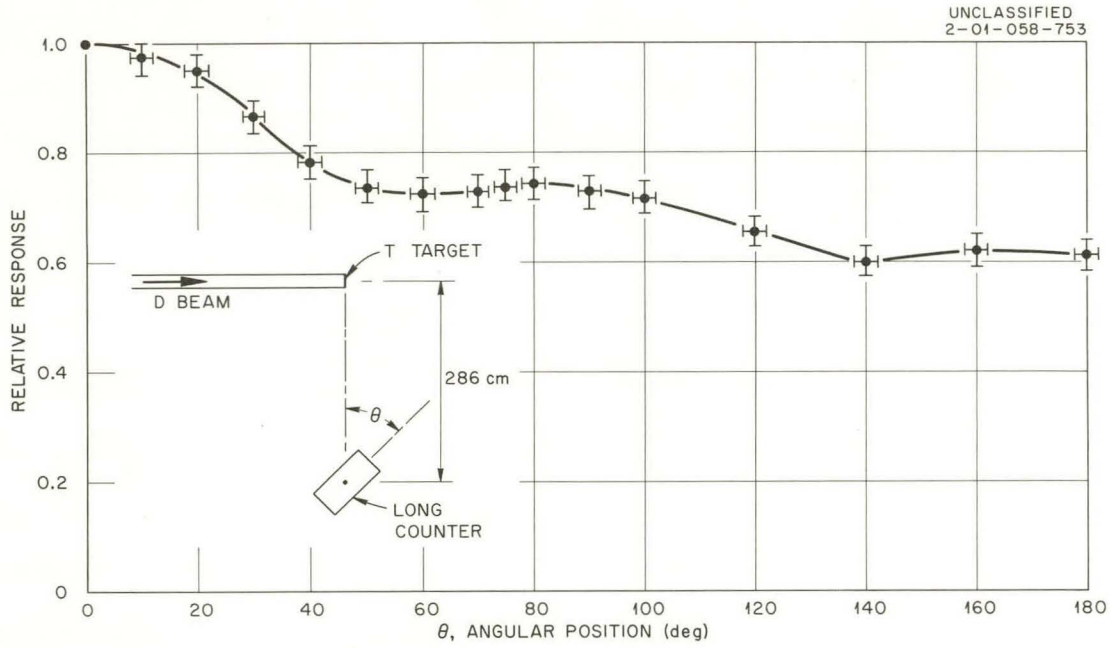

Fig. 1.17.4. Relative Response of Long Counter as a Function of Its Angular Position. At $\theta = 0°$, the front of the long counter was 265 cm from the target center.

and a rubber seal is placed on the cylinder, and the assembly is attached to the vacuum system. The vacuum system also is connected to a vessel containing water and to one containing mineral oil. The entire system, including the cylinder and the two containers, is then pumped for about 24 hr to remove the dissolved and trapped gases. Water is then added to the cylinder, by gravity under vacuum, to a level about 1 in. higher than the desired height, the remainder of the cylinder being filled with mineral oil, also by gravity flow. After the cylinder is disconnected from the vacuum system and solidly frozen at about –5°C, the temperature is gradually lowered to –75°C, which embrittles the sealing compound so that both it and the bottom glass plate can be easily removed from the cylinder. While the cylinder is maintained at –75°C, it is sawed off and placed in a lathe, where the sawed-off surface is machined parallel to the bottom surface at the correct length. In this way, a right-cylindrical ice body is attained. The cylindrical aluminum shell remains around the ice, and aluminum foil is used to seal the end surfaces to prevent sublimative evaporation of the material. When cadmium has been fitted over all surfaces, the cylinder is ready for pulse measurements.

Data Analysis

The decay data on the large ice bodies have all been analyzed by the Cornell method[6] for various waiting times after the neutron burst. In virtually all decays a small but very consistent trend of increasing absolute value of the decay constant with waiting time was observed. Figure 1.17.6 shows some typical curves of the calculated decay constant as a function of waiting time.

In all these analyses the data were fitted to a single exponential plus a flat background. It is easy to show that any combination of a background and positive-amplitude exponential decay components must give a composite curve of ln $N(t)$ vs time which is concave upwards, and therefore the observed steepening decay must be due to the inclusion of a negative-amplitude higher mode. The possibility that the apparent change of slope was due to an inherent error in the Cornell method was eliminated by using an iterative nonlinear least-squares-fit code calculation with the same model function to analyze some of the same decay

[6] R. G. Cornell, *A New Estimation Procedure for Linear Combinations of Exponentials*, ORNL-2120 (June 21, 1956).

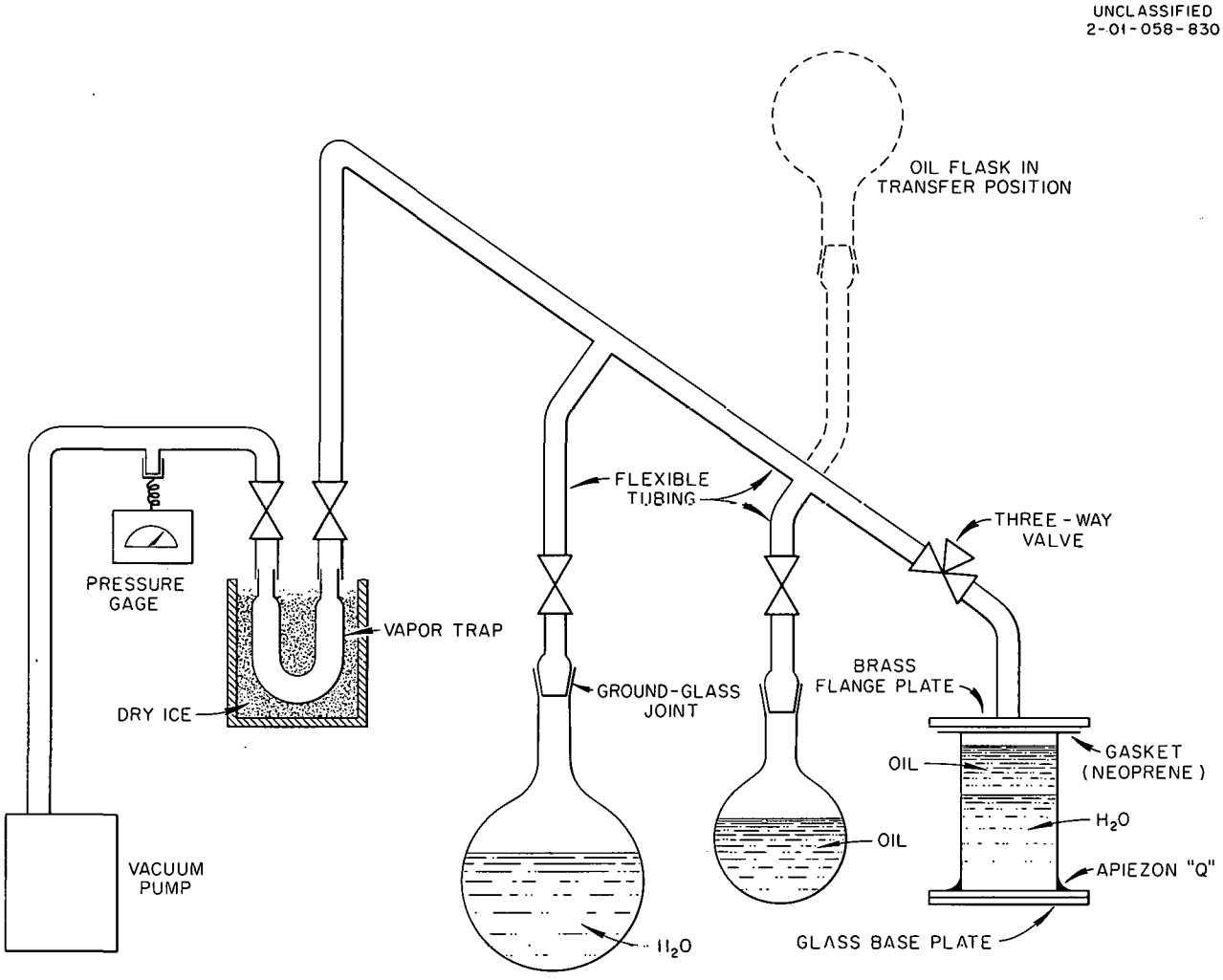

Fig. 1.17.5. Diagram of Vacuum System Used for Producing Air-Free Ice Cylinders. Both the water and oil containers may be raised for gravity transfer into aluminum cylinder.

curves. The comparison is shown in Fig. 1.17.7. Except for the variances, the results are very much alike, and the trend to steepening decay is still apparent. The larger standard errors in the Cornell-method results are due to this method ignoring statistical weights, so that any deviations from the fit due to statistics are interpreted as errors in the fit. The least-squares calculations were based on weights given by the count statistics for each channel.

If it is assumed that, in addition to the fundamental mode of decay constant λ, a higher mode of decay constant $c\lambda$ is present, then for the neutron population N at time t

$$N(t) = e^{-\lambda t} - ae^{-c\lambda t}, \qquad (1)$$

where a is the relative amplitude of the higher mode component at $t = 0$ and $N(0) = 1 - a$. It follows that the slope of the logarithm of the function $N(t)$ is given by

$$S(t) = \frac{d}{dt}\left[\ln N(t)\right]$$

$$= -\lambda\left[1 + (1-c)\sum_{n=1}^{\infty} a^n e^{n(1-c)\lambda t}\right]. \qquad (2)$$

From this, it follows that

$$S(0) = -\lambda(1 - ac)/(1 - a) . \quad (3)$$

Assuming that $a \ll 1$, that is, that the higher mode amplitude is small relative to the fundamental mode amplitude (in experiments thus far a has ranged from 0.005 to 0.05), the terms in higher powers of a may be neglected, and it follows that

$$S(t) \approx -\lambda[1 + (1 - c)ae^{(1-c)\lambda t}] . \quad (4)$$

The range of waiting time over which λ may be observed in this experiment is of the order of 1 reciprocal period, $(1/\lambda)$ sec. Therefore, a useful measure of the rate of change of the slope is the relative change over 1 reciprocal period, R:

$$R = \frac{S(1/\lambda)}{S(0)} = \frac{(1 - a)}{(1 - ac)}[1 + (1 - c)ae^{(1-c)}] . \quad (5)$$

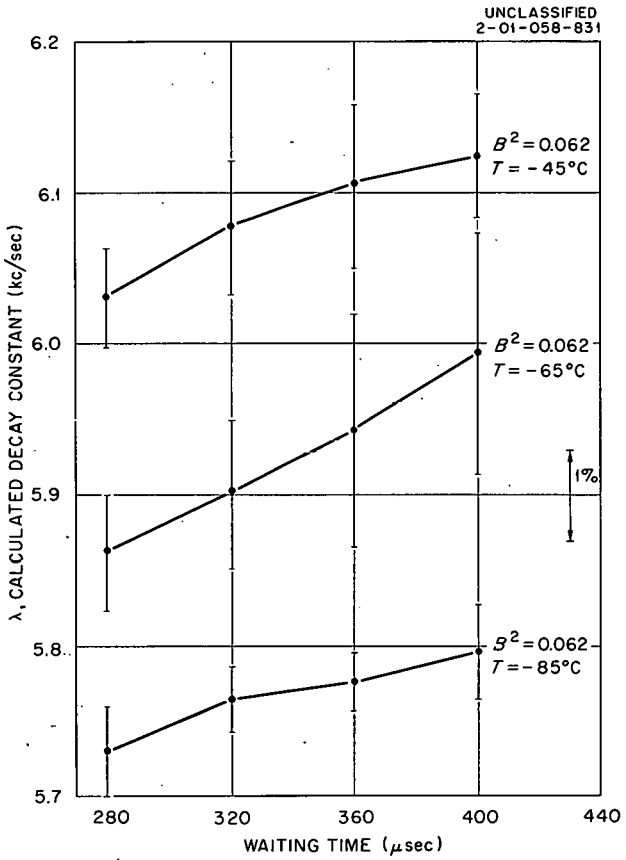

Fig. 1.17.6. Effect of Waiting Time from End of Neutron Irradiation to Beginning of Data Analysis on Decay Constant Computed by Cornell Method. Only one exponential is assumed to be present. Each point represents an analysis over 15 channels (600 μsec).

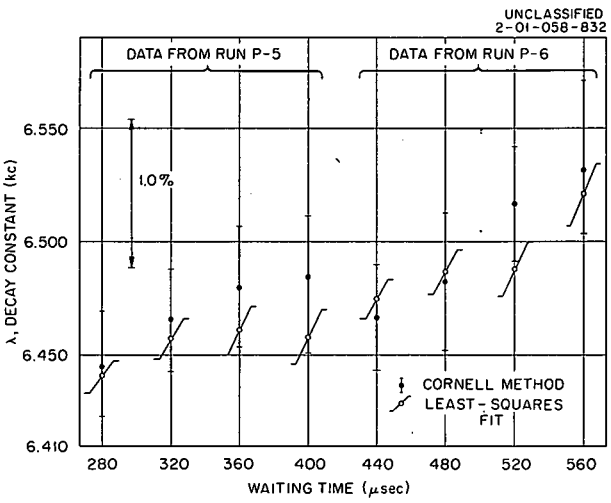

Fig. 1.17.7. Comparison of Cornell Method and Least-Squares-Fit Method of Calculating the Decay Constant, Based on the Model $N(t) = a_0 + a_1 e^{-\lambda t}$. Two sets obtained on the same ice body with different waiting times are shown.

Figure 1.17.8 is a plot of $(R - 1)$ as a function of a for several values of c. Figure 1.17.9 shows an artificial curve of λ vs waiting time resulting from a Cornell method of analysis of theoretical data obtained from Eq. (1), with $a = 0.03$ and $c = 2.0$. It seems clear that the model given by Eq. (1) is able to account for the observed changes in λ with waiting time; therefore all future decay data will be analyzed by this method, using a least-squares fit to the equation

$$C_k = A_0(\Delta t) + A_1(\Delta t)e^{-\lambda k(\Delta t)} + A_2(\Delta t)e^{-\lambda ck(\Delta t)} , \quad (6)$$

where A_0, the background counts per second, A_1, the counts per second due to the fundamental mode

at $t = 0$, A_2, the counts per second due to the higher mode at $t = 0$, and λ, the decay constant of the fundamental mode, are varied. The parameter c is assumed to be known from the dimensions of the ice body in question. The term C_k is the number of counts collected in the kth channel; all channels have a width of Δt sec. Partial results at the time of this report indicate that this model of analysis does eliminate the apparent progressive increase in $|\lambda|$ with waiting time that is observed when the simple one-decay model is used.

Future Work

At present the collection of decay data is continuing, and it is anticipated that this aspect of the experiment will be concluded within the coming year. In the future, all the decay data will be systematically analyzed by the model discussed above, and the resulting data will be used to determine the diffusion parameters of ice as a function of temperature.

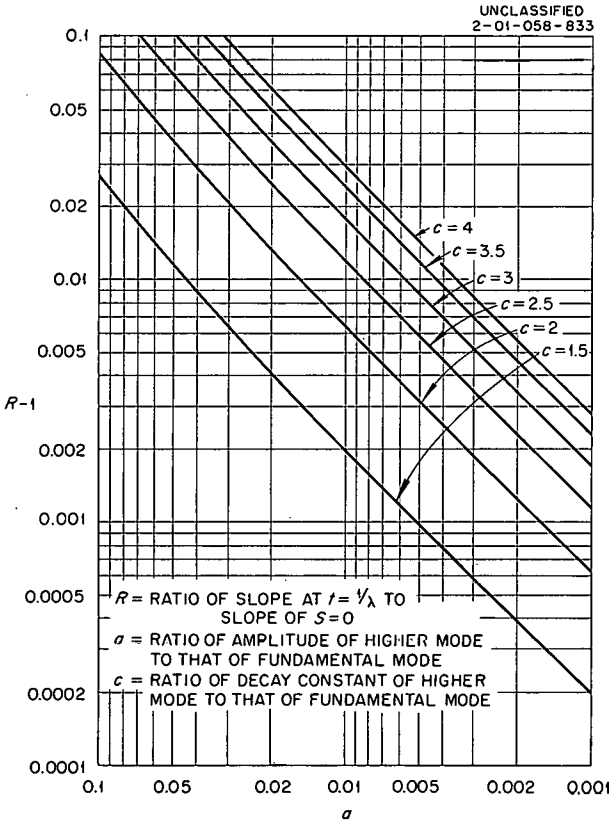

Fig. 1.17.8. Values of $(R - 1)$ vs a for Various Values of the Parameter c. (See text for definition of nomenclature.)

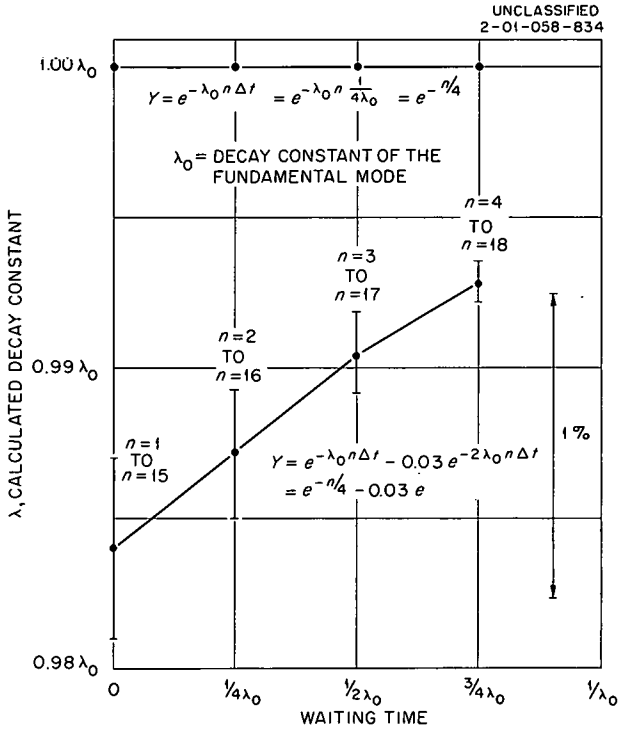

Fig. 1.17.9. Result of Cornell-Method Analysis on an Artificial Set of Decay Data, Without Statistical Variance, Constructed from the Equation $N(t) = e^{-\lambda_0 t} - 0.03\ e^{-2\lambda_0 t}$. The "channel widths" are $1/(4\lambda_0)$ sec wide, and each analysis extends over 15 channels. The decay constant of the pure fundamental mode is shown for comparison.

1.18. NOTE ON THE MEASUREMENT OF DEUTERON POLARIZATION

M. S. Bokhari[1]

In order to obtain the scattering matrix for deuterons scattered from a spin-zero target, triple-scattering measurements are generally required.[2] Such measurements are difficult to make, since a high initial beam intensity is required. It is the purpose of this note to show that by taking advantage of polarization properties inherent in pickup and stripping reactions the required information can be obtained from double-scattering experiments.

The unit spin of the deuteron makes the description of its scattering and polarization more complicated than that for particles of spin $\frac{1}{2}$, where only three components of a single vector are required. The theoretical treatment of this subject has been discussed by various authors.[2-10] In general, however, polarization of a deuteron beam will involve nine tensor components, T_{JM}, to a maximum rank of 2.

The zero-rank tensor is a scalar, normalized to unity. The first-rank tensors, T_{1M}, are the three axial components of a pseudovector representing the total spin, with the average values of the spins in the three directions given in terms of their expectation values, denoted by the broken brackets $\langle\ \rangle$. The terms $\langle T_{1M} \rangle$ will be referred to as "vector polarization." In scattering, and especially in (d,p) reactions, only those $\langle T_{1M} \rangle$ which represent components of the spin perpendicular to the scattering plane are involved.[11-13] The tensors of second rank, T_{2M}, introduce five more expectation values which relate the populations of the different spin states but in such a way that they have no influence on the average spin in any direction.

It has been shown[3] that the cross section at the second of the double deuteron elastic scatterings from a spin-zero target is given by

$$I = I_0 \left[1 + \langle T_{20} \rangle_1 \langle T_{20} \rangle_2 + 2\left(i\langle T_{11}\rangle_1 i\langle T_{11}\rangle_2 - \langle T_{21}\rangle_1 \langle T_{21}\rangle_2\right)\cos\phi + 2\langle T_{22}\rangle_1 \langle T_{22}\rangle_2 \cos 2\phi\right], \quad (1)$$

where I_0 is the cross section for unpolarized deuterons and ϕ is the angle between the first- and second-scattering planes. Subscript 1 refers to the polarization state of the beam after the first scattering, and subscript 2 to the polarization effect of the second scattering. The axis of quantization is taken along the direction of the beam between the first and second scatterings, with the y axis normal to the plane of the first scattering. For a spin-zero target,[2]

$$\langle T_{JM} \rangle_1 = (-1)^{J+M} \langle T_{J-M} \rangle_1$$

and

$$\langle T_{10} \rangle_1 = 0 \text{ (ref 2)}.$$

If the values of either $\langle T_{JM} \rangle_1$ or $\langle T_{JM} \rangle_2$ are known, seven of the eight components can be

---

[1] On loan from Pakistan Atomic Energy Commission.

[2] R. J. N. Phillips, *Deuteron Triple-Scattering Experiments*, AERE-R-3306 (March 1960).

[3] W. Lakin, *Phys. Rev.* **98**, 139 (1955).

[4] R. H. Dalitz, *Proc. Phys. Soc. (London)* **A65**, 175 (1952).

[5] A. Simon and T. A. Welton, *Phys. Rev.* **90**, 1036 (1953).

[6] A. Simon, *Phys. Rev.* **92**, 1050 (1953) and **93**, 1435 (1956).

[7] L. J. B. Goldfarb, *Nucl. Phys.* **7**, 622 (1958).

[8] H. Stapp, *Phys. Rev.* **107**, 607 (1957).

[9] H. B. Willard, *Helv. Phys. Acta, Suppl.* **6**, 175 (1960) and references cited therein.

[10] J. Hamilton, *Theory of Elementary Particles*, p 391, Oxford University Press, 1959.

[11] G. R. Satchler, R. Huby, and M. Y. Refai, *Nucl. Phys.* **9**, 94 (1958).

[12] G. R. Satchler, *Nucl. Phys.* **6**, 543 (1958).

[13] G. R. Satchler, *The Scattering and Polarization of Spin-One Particles*, ORNL-2861 (Jan. 6, 1960).

determined by single- and double-scattering measments. At present, however, no polarizer or analyzer exists for which the values of either $\langle T_{JM} \rangle$ are known, and therefore their determination is a complicated affair.

It has been theoretically predicted that deuterons resulting from the pickup reaction, in which a proton enters a nucleus, picks up a neutron, and emerges as a deuteron, are polarized. Since the process involves direct interaction of the two nucleons that form the deuteron, the resulting deuterons are mainly vector-polarized. Tensor terms[14-16] resulting from the spin effects of the two-body potential through which the pickup process occurs and from the spin effects of the nuclear potential in which the picked-up neutron is initially bound are considerably smaller than the vector polarization terms.

Once the deuteron beam with vector polarization has been obtained, the remaining problem becomes much simpler, with only the terms $\langle T_{1M} \rangle_1$ associated with the deuteron beam to be analyzed. It is well known that the protons from stripping reactions with polarized deuterons display a left-right asymmetry of distribution. On the main stripping peak of the proton angular distribution, this asymmetry is related to the incoming deuteron polarization, given by $P_d = \frac{2}{3} i \langle T_{11} \rangle_1$, as follows:[12]

$$\frac{L - R}{L + R} = 3 P_p P_d , \qquad (2)$$

where L is the number of protons scattered toward the left and R the number scattered to the right. The quantity P_p is the polarization of the stripped protons resulting from reactions using *unpolarized* deuterons. The quantity $\langle T_{11} \rangle_1$ can be directly obtained from the above relations.

The next step in the measurement of the various tensor components of deuteron polarization is a determination of the vector polarization produced when deuterons are elastically scattered from spin-zero targets. This may be done by observing the left-right asymmetry produced when polarized deuterons from the pickup reaction are elastically scattered from a spin-zero target, a method which also gives the angular distribution of $\langle T_{11} \rangle_2$.

Simultaneous measurement at $\phi = 0$, $\pi/2$, π, and $3\pi/2$ of deuterons that are elastically scattered twice[17] will allow the determination of the ratios B/A and C/A, where

$$A = 1 + \langle T_{20} \rangle_1 \langle T_{20} \rangle_2 ,$$

$$B = 2 \left(i \langle T_{11} \rangle_1 \, i \langle T_{11} \rangle_2 - \langle T_{21} \rangle_1 \langle T_{21} \rangle_2 \right),$$

$$C = 2 \langle T_{22} \rangle_1 \langle T_{22} \rangle_2 .$$

The quantities to the right of the equality signs will be recognized as the coefficients of the cos ϕ and cos 2ϕ of Eq. (1).

Finally, $\langle T_{10} \rangle$ can be measured by imposing a magnetic field upon the experiment to make the polarization axes precess relative to the deuteron motion.[2,3,13] This will afford measurements of all components separately. In terms of a spin operator S the components are related as follows:

$$T_{00} = 1 ,$$

$$T_{10} = (\sqrt{3}/2) S_z ,$$

$$T_1 \pm 1 = \mp (1/2\sqrt{3})(S_x \pm i S_y) ,$$

$$T_{20} = (1/\sqrt{2})(3 S_z^2 - 2) ,$$

$$T_2 \pm 1 = \mp (1/2\sqrt{3})(S_x \pm i S_y, S_z) ,$$

$$T_2 \pm 2 = (1/2\sqrt{3})(S_x \pm i S_y)^2 .$$

---

[14] K. R. Greider, *Nucl. Phys.* **14**, 498 (1960).

[15] K. R. Greider, *Phys. Rev.* **114**, 786 (1959).

[16] S. Watanabe, *Nucl. Phys.* **8**, 486 (1958).

[17] M. A. Al-Jeboori *et al.*, *Proc. Phys. Soc. (London)* **75**, 875 (1960).

1.19. THE SPECTRA OF GAMMA RAYS RESULTING FROM THERMAL-NEUTRON CAPTURE IN ISOTOPES OF ZIRCONIUM

G. T. Chapman, J. A. Harvey,[1] G. G. Slaughter,[1] and J. R. Bird[2]

Introduction

A program to measure the gamma-ray spectra resulting from the capture of neutrons in various isotopes was initiated during the past year as a cooperative effort by the Neutron Physics and Physics Divisions. This paper discusses the measurements for the isotopes of zirconium (Zr^{90}, Zr^{91}, Zr^{92}, Zr^{94}, and Zr^{96}), earlier work with other isotopes having been reported elsewhere.[3] Zirconium, which lies in the mass-number region of maximum *p*-wave strength function and minimum *s*-wave strength function, is of particular interest to the nuclear physicist. In addition, this element has become increasingly important in reactor technology, and a knowledge of the gamma rays resulting from neutron capture in zirconium isotopes is required by reactor engineers and shield designers who must consider these gamma rays as sources of heat and radiation damage.

Experimental Arrangement

The spectrometer for these measurements was the 9-in.-diam, 12-in.-long NaI(Tl) scintillator and shield previously used with the Model IV gamma-ray spectrometer.[4] The crystal was positioned along the flight path of the ORNL Fast Chopper,[5] approximately 5 m from its rotor. The axis of the crystal was placed to one side of the flight path to avoid a direct exposure of the crystal to neutrons. The enriched isotopic samples were placed in the neutron beam in such a position that some of the gamma rays resulting from the neutron captures in the samples would reach the crystal through a 4-in.-diam collimator. Shielding, in the form of lithium hydride and borated paraffin, prevented the direct passage of thermal neutrons through the collimator.

Both thermal-neutron and resonance-neutron capture-gamma-ray spectra were measured with the rotor stopped. For the thermal-neutron spectra a cadmium filter was oscillated in and out of the beam, and the difference between the filter-out and filter-in data gave the desired results. For the resonance-neutron measurements the cadmium filter remained in place and an enriched B^{10} filter was oscillated. All the data were recorded with a time-gated, two-section pulse-height analyzer having 128 channels per section.

---

[1] Physics Division.

[2] Visiting scientist from the U.K. Atomic Energy Research Establishment, Harwell, England.

[3] G. G. Slaughter *et al.*, *Phys. Div. Ann. Progr. Rept. Jan. 31, 1963*, ORNL-3425, p 60.

[4] G. T. Chapman *et al.*, *Neutron Phys. Div. Ann. Progr. Rept. Sept. 1, 1962*, ORNL-3360, p 5.

[5] R. C. Block, G. G. Slaughter, and J. A. Harvey, *Nucl. Sci. Eng.* 8, 112 (1960).

Table 1.19.1. Isotopic Composition of Zirconium Samples

Isotopic Constituent	Isotopic Abundance (at. %)				
	Zr^{90} Sample	Zr^{91} Sample	Zr^{92} Sample	Zr^{94} Sample	Zr^{96} Sample
Zr^{90}	97.80	5.00	2.29	1.91	9.19
Zr^{91}	0.95	90.88	0.92	0.51	2.02
Zr^{92}	0.65	3.29	95.7	0.85	27.20
Zr^{94}	0.49	0.84	1.0	96.49	4.22
Zr^{96}	<0.1	<0.2	0.09	0.26	57.36

The samples used for the measurements were in the form of ZrO_2, secured from the AEC Neutron Cross Section Sample Pool. Table 1.19.1 lists the isotopic composition of each sample and Table 1.19.2 gives the relative contribution of each isotope to the thermal-neutron cross section of the samples. Although traces of elements other than zirconium were present in each sample (less than 0.05 at. % in most cases), their presence contributed no measurable effects to the data.

Results

The gamma-ray spectra resulting from thermal-neutron capture by the nuclei of each isotope are shown in Figs. 1.19.1 through 1.19.5. The data have been only partially analyzed, but certain pertinent features are immediately evident. For example, the shape of the $Zr^{91} + n$ pulse-height distribution shown in Fig. 1.19.2 indicates that the distribution cataloged by Groshev *et al.*[6] as zirconium was, as implied in their atlas, primarily due to Zr^{91}. Since Zr^{91} contributes about 60% to the cross section of natural zirconium, this result is not unexpected. It is believed that the Zr^{91} spectrum may be taken to be a close approximation to the spectrum of natural zirconium.

In Figs. 1.19.1 and 1.19.3 through 1.19.5 a peak is evident at channel 84. This peak is due to captures in the aluminum of the flight-path tube and in other structural material surrounding the sources. The same peak probably exists in the $Zr^{91} + n$ data (Fig. 1.19.2) but is not so obvious because of the comparatively high intensity of the Zr^{92} gamma rays. A known distribution of the aluminum-capture gamma rays is available, so that this peak can be subtracted out during the completion of the analysis.

Particular attention should be called to the data for $Zr^{92} + n$ shown in Fig. 1.19.3. Two prominent peaks are found at about channels 42.5 and 58, indicating gamma rays with energies of about 4.2 and 5.2 Mev. The literature[7] gives only a partial decay scheme for Zr^{93}, showing only the lower energy levels and the level excited by neutron capture in Zr^{92}. These data indicate that two modes exist for decay from the neutron-excited level, as shown in Fig. 1.19.6. One of the modes is accomplished by the emission of a 4.26-Mev gamma ray to the 2.44-Mev level and the subsequent decay to the ground state of Zr^{93}. The other mode involves a decay to the 1.42-Mev level by the emission of a 5.27-Mev gamma ray, with subsequent decay to the ground state by the emission of other gamma rays. In addition, the data indicate that the intensities of the 4.26- and 5.27-Mev gamma rays are very nearly equal, although this cannot be stated with certainty without further analysis. Unfortunately, it was not practical during this experiment to observe the gamma rays from lower energy levels because of extremely high backgrounds at such energies. Further work employing coincidence measurements should complete the study.

[6] L. V. Groshev *et al.*, *Atlas of Gamma-Ray Spectra from Radiative Capture of Thermal Neutrons*, p 109, Pergamon, New York, 1959.

[7] K. Way *et al.*, *Nuclear Data Sheets*, vol 5 (set 1), National Academy of Sciences and National Research Council, 1962.

Table 1.19.2. Relative Contribution to Cross Section of Zirconium Isotopes in Zirconium Samples

Isotopic Constituent	Relative Contribution (%)				
	Zr^{90} Sample	Zr^{91} Sample	Zr^{92} Sample	Zr^{94} Sample	Zr^{96} Sample
Zr^{90}	85.6	0.36	0.89	1.9	5.4
Zr^{91}	12.6	98.9	5.6	7.9	18.2
Zr^{92}	1.4	0.59	93.1	2.1	40.2
Zr^{94}	0.35	0.06	0.35	87.8	2.3
Zr^{96}	0.09	0.01	0.04	0.30	33.9

Since the neutron time-of-flight resolution at the 5-m location is only 0.5 μsec/m (about 15% energy resolution at 100 ev),[8] the study of gamma rays resulting from the capture of neutrons in the resonance region above a few hundred volts is somewhat impeded. However, Fig. 1.19.7 shows a distribution of gamma rays resulting from resonance neutron captures obtained by inserting a B^{10} filter in the neutron beam as described above. The predominant gamma-ray energy seems to be about 5.3 Mev, with other possible gamma rays as shown by the smaller peaks.

[8]For future work in this program the crystal and sources will be moved to a point 25 m from the rotor. At this point the time-of-flight resolution is approximately 0.1 μsec/m, or five times better than at the 5-m location.

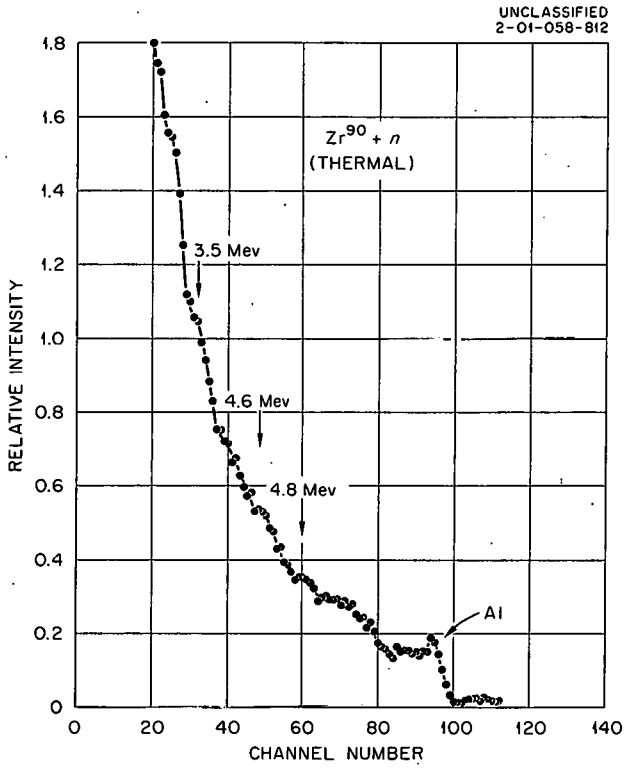

Fig. 1.19.1. Pulse-Height Distribution of Gamma-Ray Energies Resulting from Thermal-Neutron Capture in Zr^{90}.

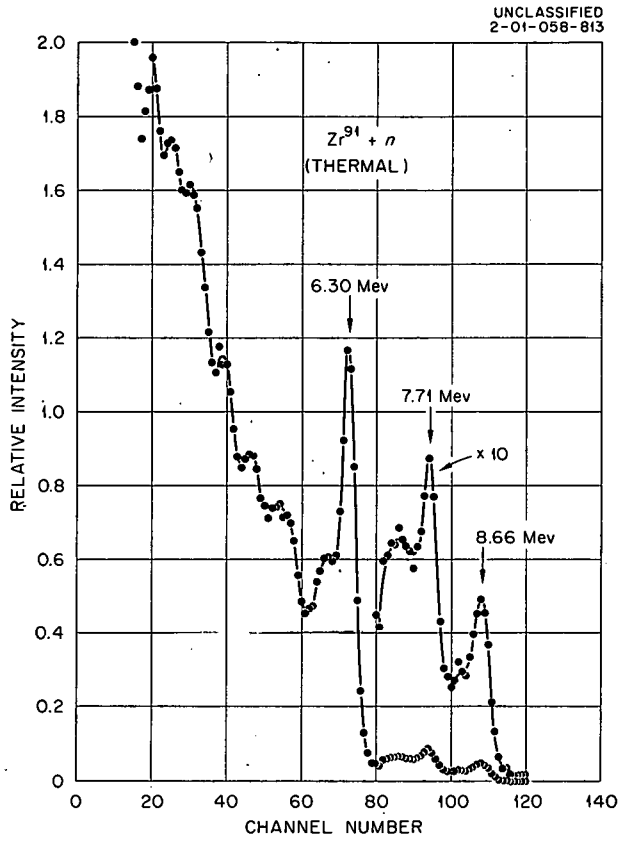

Fig. 1.19.2. Pulse-Height Distribution of Gamma-Ray Energies Resulting from Thermal-Neutron Capture in Zr^{91}.

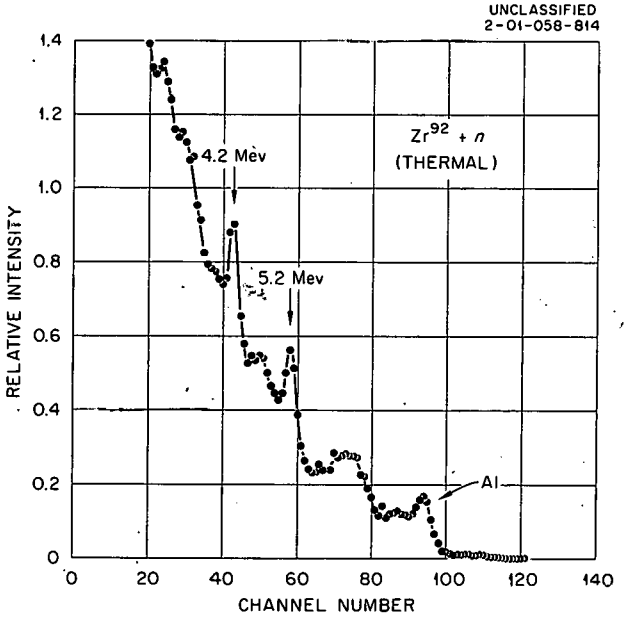

Fig. 1.19.3. Pulse-Height Distribution of Gamma-Ray Energies Resulting from Thermal-Neutron Capture in Zr^{92}.

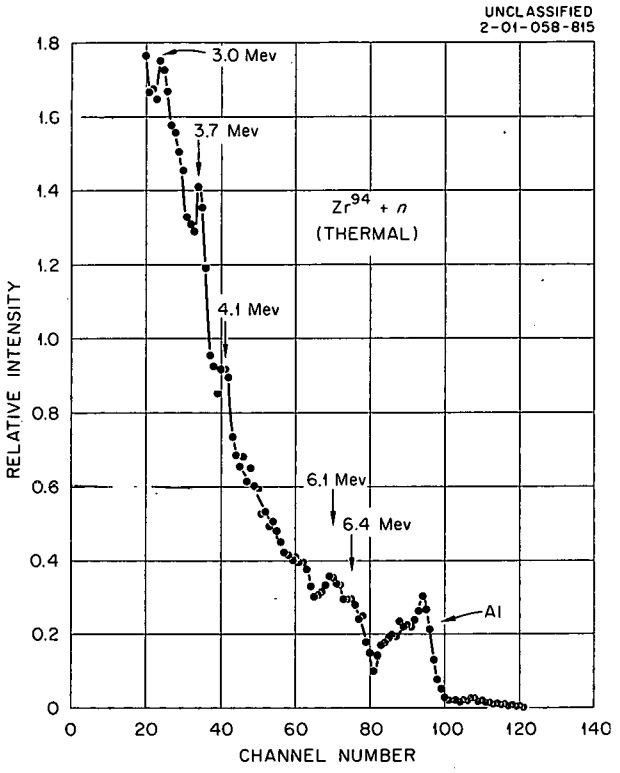

Fig. 1.19.4. Pulse-Height Distribution of Gamma-Ray Energies Resulting from Thermal-Neutron Capture in Zr^{94}.

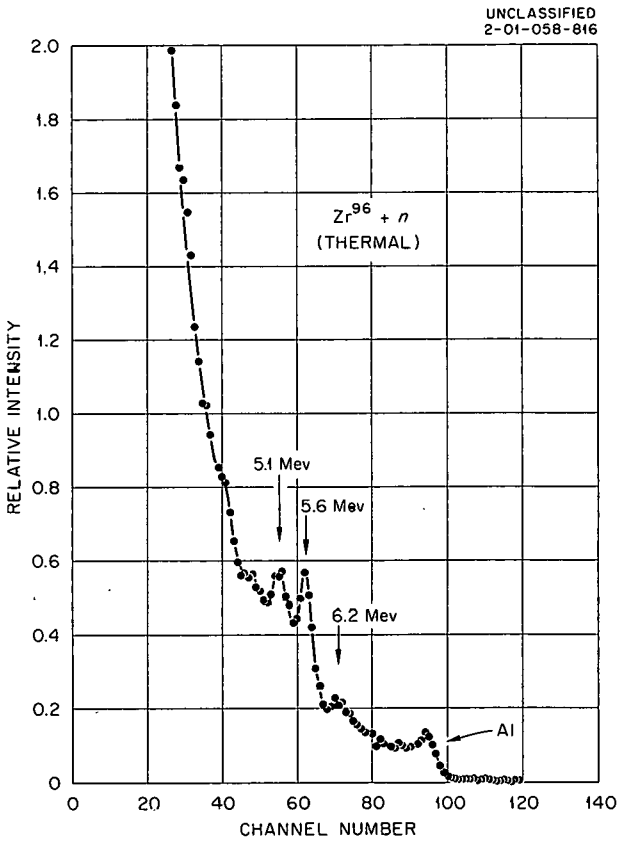

Fig. 1.19.5. Pulse-Height Distribution of Gamma-Ray Energies Resulting from Thermal-Neutron Capture in Zr^{96}.

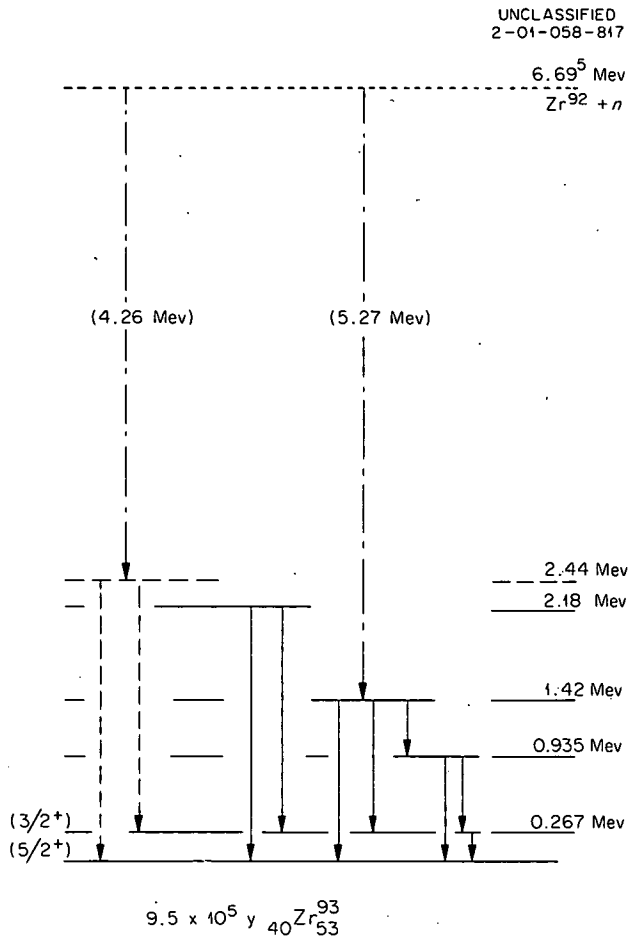

Fig. 1.19.6. Level Scheme for Zr^{93} (from ref 7) Showing the Proposed Scheme of Decay from the Neutron-Excited Level.

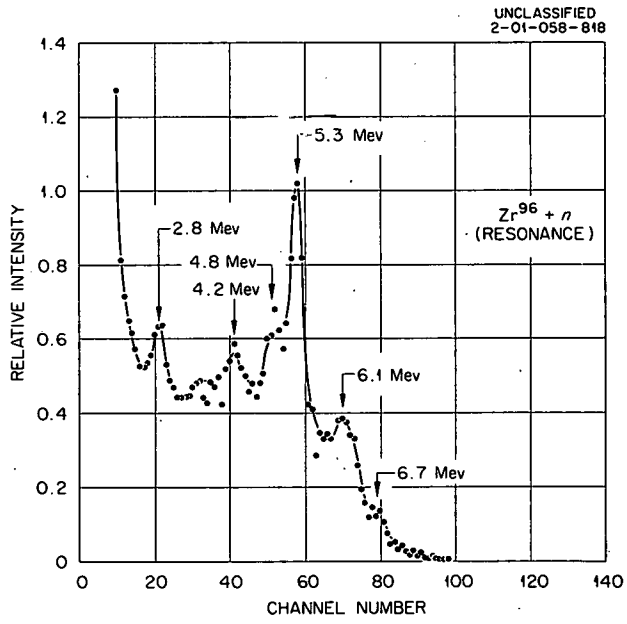

Fig. 1.19.7. Pulse-Height Distribution of Gamma-Ray Energies Resulting from Resonance-Neutron Capture in Zr^{96}.

2. Critical Experiments

THIS PAGE

WAS INTENTIONALLY

LEFT BLANK

2.1. PROMPT-NEUTRON DECAY CONSTANT VS BUCKLING FOR HYDROGEN-MODERATED 3% U^{235}-ENRICHED URANIUM

J. T. Mihalczo

Prompt-neutron decay constants for unreflected parallelepipeds of a homogeneous mixture of UF_4 and paraffin were determined as a function of buckling by the pulsed-neutron technique. The fuel mixture had a density of 4.5 g/cc and contained 92 wt % UF_4 in which the U^{235} enrichment of the uranium was 3.00%. The $H:U^{235}$ atomic ratio was 133.[1]

The buckling was varied in two ways: Cubes of various sizes were built, the largest being that required for criticality, and the size of the cubic critical assembly was reduced in one dimension only. The prompt-neutron decay constant was determined for each assembly, and the flux distribution in the critical assembly was measured. From the latter, the extrapolation distance for the critical cube was obtained.

The variation of the extrapolation distance, which is needed to compute the buckling, with the dimensions of the smaller assemblies was obtained from a DSN transport-theory calculation[2] using the 16-group cross-section values of Hansen and Roach.[3] In the calculation the slab equivalent of the cubic critical assembly was obtained by adding absorption to the slab until it was calculated to be critical with the same thickness as the experimental cube. The dependence of this absorption on energy was the same as the calculated energy dependence of the leakage from the equivalent sphere, which was obtained from the measured buckling and extrapolation distance. Stepwise reductions in the slab thickness were then made, and the extrapolation distance corresponding to each thickness was obtained from a least-squares analysis of the scalar fluxes in each group of the calculation. A leakage-weighted extrapolation distance was then calculated for each thickness.

The calculated change in extrapolation distance, together with the extrapolation distance inferred from the measured flux distribution in the critical cube, was used to obtain the dependence of the extrapolation distance on the variable dimension (side length) of the experimental assemblies. The results are shown in Fig. 2.1.1. With the extrapolation distance obtained in this way, the buckling was calculated and a plot of the prompt-neutron decay constant vs buckling is shown in Fig. 2.1.2.

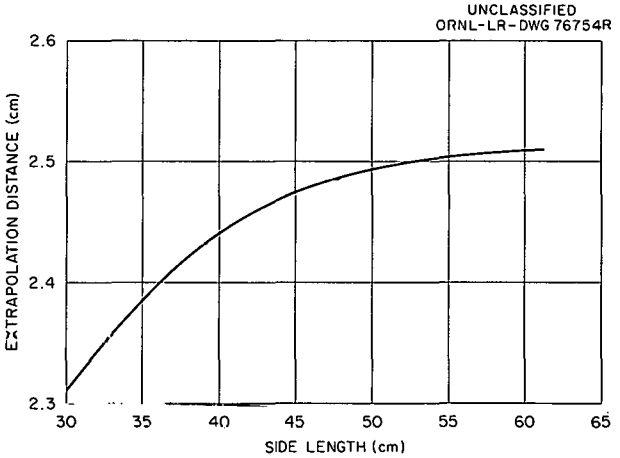

Fig. 2.1.1. Extrapolation Distance vs Side Length for a 3% U^{235}-Enriched Homogeneous Mixture of UF_4 and Paraffin.

[1] This work is a continuation of that reported previously: J. T. Mihalczo, *Neutron Phys. Div. Ann. Progr. Rept. Sept. 1, 1962*, ORNL-3360, p 37.

[2] B. G. Carlson and G. I. Bell, *Proc. Intern. Conf. Peaceful Uses Atomic Energy, 2nd, Geneva, 1958* 16, 535–49 (1959); B. G. Carlson, C. F. Lee, and J. Worlton, *The DSN and TDC Neutron Transport Codes*, LAMS-2346 (1960).

[3] G. E. Hansen and W. H. Roach, *Six and Sixteen Group Cross Sections for Fast and Intermediate Critical Assemblies*, LAMS-2543 (1961).

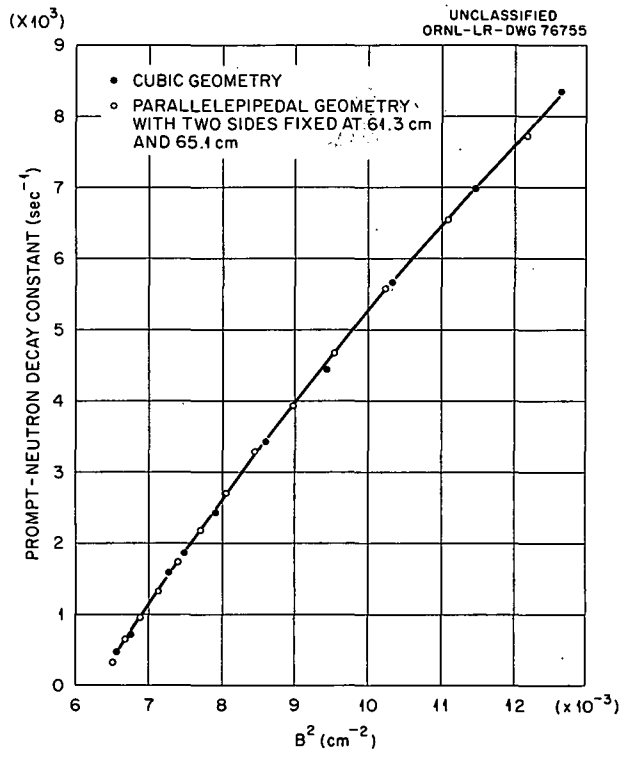

Fig. 2.1.2. Prompt-Neutron Decay Constant vs Buckling for 3% U^{235}-Enriched Homogeneous Mixture of UF_4 and Paraffin.

2.2. EFFECTS OF BOROSILICATE GLASS RASCHIG RINGS ON THE CRITICALITY OF AQUEOUS URANYL NITRATE SOLUTIONS

J. T. Thomas, J. K. Fox,[1] and E. B. Johnson

In order to better establish bases for the increasingly extensive use of borosilicate glass Raschig rings as fixed neutron absorbers in various processes involving uranium-bearing solutions, a series of experiments have been completed which extend the previous investigations of the effectiveness of this form of nuclear poison. The first ORNL work[2] of this type was primarily concerned with ordered arrays of Pyrex pipe in a single vessel, with only an exploratory measurement made with randomly oriented glass Raschig rings. In the present experiments glass rings, varying both in dimensions and in boron content, were immersed in cylinders of different diameters containing enriched uranyl nitrate solutions of different concentrations.

The largest cylinder employed was made of 48-in.-diam stainless steel. Two other vessels used in the experiments were a 30-in.-diam aluminum cylinder and a 20-in.-diam stainless steel cylinder. All vessels were 60 in. high and their tops were covered with a $\frac{1}{16}$-in.-thick sheet of stainless steel to minimize evaporation. An effectively infinite water reflector could be provided on the bottom and lateral surfaces of each cylinder, and in some experiments a 32-mil-thick cadmium sheet covered the sides of the vessel.

[1] Now with Phillips Petroleum, Idaho Falls.

[2] J. K. Fox and L. W. Gilley, *Neutron Phys. Div. Ann. Progr. Rept. Sept. 1, 1959*, ORNL-2842, p 78.

The fissile material was aqueous uranyl nitrate solution enriched to 92.6% in U^{235}. The solution concentration was varied between 415 and 63.3 g of uranium per liter.

The borosilicate glass Raschig rings were commercial items of different sizes and boron content. These variations in size are reflected in Table 2.2.1 as different glass volumes in the glass-solution mixtures. The boron content of the glass ranged between 0.5 and 5.7 wt %.

It was apparent from early source neutron multiplication tests that many of the glass-solution mixtures would be subcritical even though the tests were made in volumes as large as 48 in. in both diameter and height and the chemical concentration was near that required for minimum critical volume, at least in unpoisoned systems. Indeed there was strong evidence that an infinite quantity of some of the mixtures could not be made critical. A critical system could be established, however, by raising the level of the solution a few inches above the level of the glass bed, thereby providing the conditions necessary for exponential experiments. The critical slab above the glass-solution bed was operated at a power sufficient to provide a source of neutrons for the adjacent exponential column. This unique coupling of the two systems provided a radially symmetric neutron source with almost matched spectra.

Table 2.2.1 shows the conditions necessary to sustain criticality in the superimposed solution layer. Random irregularities in the top surface of the ring bed introduced an uncertainty of ± 0.3 in. in the glass-solution mixture height and must be considered in any attempt to assign a thickness to the critical slab of solution when the slab is reflected on one surface by solution-ring mixture.

Flux distributions in the subcritical ring beds were measured with a traversing BF_3 proportional counter, $\frac{1}{4}$ in. in diameter by 1 in. long, installed in a reentrant tube along the vertical axis of each cylinder. Figure 2.2.1 shows typical distributions, these particular ones having been measured in the reflected and unreflected 48-in.-diam cylinder and arbitrarily normalized to unity at a point 28 in. above the bottom of the column. The deviations of the points from linearity are probably due to the random orientation of the glass rings in the vicinity of the reentrant tube, i.e., the formation of "pockets" of solution. A portion of each flux distribution, selected to avoid boundary perturbations, was fitted by least squares to the relation $\phi = \phi_0 e^{-\gamma z}$, where γ is the reciprocal of the neutron relaxation length. The resulting values of γ are included in Table 2.2.1.

If in the equation for the material buckling of a cylindrical system the radial extrapolation distance, λ, is set equal to zero, maximum values of B_m^2 result, thus introducing conservatism upon the application of the results to safety problems. Imposing this condition on the data obtained in the 20-in.-diam cylinder for both unreflected and water-reflected mixtures in which the solution concentration was 415 g of uranium per liter and the glass had an approximate boron content of 4 wt % yields the upper two curves of Fig. 2.2.2, where the material buckling is plotted against the volume per cent of the mixture occupied by the glass. Two points obtained in the same manner for a 30-in.-diam cylinder in which the glass occupied 20.9 vol % lie well off the curves for the 20-in.-diam cylinder.

The two upper curves in Fig. 2.2.2 can be superposed, as indeed they should be since the buckling is a property of the material and not of the reflector, by assuming that the radial extrapolation distances of the reflected and unreflected cylinders are 5.0 and 2.9 in., respectively. The results of the superposition are shown as the lower curve on Fig. 2.2.2. Application of these same extrapolation distances to the data from the 30-in.-diam cylinder gives buckling values consistent with those from the smaller cylinder.

These same values of the extrapolation distance were assumed to be correct for all mixtures studied which contained ~24 vol % of glass in solution of the same concentration (415 g of uranium per liter), even though the boron content of the glass varied. The results are shown in Fig. 2.2.3, where the material buckling is plotted as a function of boron content. The pair of points at 5.7 wt % boron which lie on the curve are for the 48-in.-diam cylinder; all others are for the 20-in.-diam cylinder, those at 0.5 wt % boron representing critical systems. Extrapolation of the curve to zero boron content indicates a buckling of about 8×10^{-2} in.$^{-2}$. The point plotted on the ordinate at 19.9×10^{-2} in.$^{-2}$ represents the critical buckling of a 20-in.-diam cylinder containing no glass and is based on an estimated critical height of 6.3 ± 0.1 in. It would seem that the effective dilution of the solution by the presence

Table 2.2.1. Results from Experiments with Mixtures of Uranyl Nitrate Solution and Borosilicate Glass

(U^{235} Enrichment = 92.6 wt %)

Diameter of Cylinder (in.)	Reflector[a]	Type of Glass	Boron Content of Glass (wt %)	Glass Content of Mixture (vol %)	Glass Height (in.)	Solution Height (in.)	γ (Relaxation Length)$^{-1}$ ($in.^{-1}$)	Error in γ (95% Confidence Level)
Solution Concentration: 415 g of U per liter ($H:U^{235}$ = 59)								
48	Air	EN-1	5.7	24.1	46.5	44.68[b]		
	H_2O	EN-1	5.7	24.1	46.5	44.68[b]		
	Air	EN-1	5.7	24.1	30.0	34.31	0.189	± 0.022
	H_2O	EN-1	5.7	24.1	30.0	34.25	0.179	± 0.027
30	H_2O	Pyrex	4.0	20.9	50.0	50.0[b]		
	H_2O	Pyrex	4.0	20.9	35.9	39.49	0.092	± 0.016
	Air	Pyrex	4.0	20.9	35.9	39.75	0.118	± 0.015
20	H_2O	EN-1	5.7	24.1	34.6	40.64	0.257	± 0.017
	Air	EN-1	5.7	24.1	34.6	41.03		
	Air	KG-33	4.1	24.1	35.6	41.32	0.219	± 0.007
	H_2O	KG-33	4.1	24.1	35.6	40.84	0.198	± 0.018
	H_2O	Pyrex	4.0	20.9	33.8	38.53	0.145	± 0.011
	Air	Pyrex	4.0	21.0	33.6	38.67	0.171	± 0.016
	H_2O	Pyrex	4.0	21.0	33.6	38.29	0.142	± 0.017
	H_2O	KG-33	3.9	30.0	27.2	32.37	0.307	± 0.013
	Air	KG-33	3.9	30.0	27.2	32.69	0.322	± 0.012
	Air	R-6	0.5	24.0	21.4	10.86	Note that this mixture was critical	
	H_2O	R-6	0.5	24.0	21.4	8.34		
Solution Concentration: 279 g of U per liter ($H:U^{235}$ = 92)								
20	Air	KG-33	4.1	24.1	35.6	41.48	0.257	± 0.016
	H_2O	KG-33	4.1	24.1	35.6	41.12	0.239	± 0.029
Solution Concentration: 141 g of U per liter ($H:U^{235}$ = 191)								
20	Air	KG-33	4.1	24.1	35.6	41.47	0.312	± 0.022
	H_2O	KG-33	4.1	24.1	35.6	41.05	0.321	± 0.026
	Air	R-6	0.5	24.0	21.0	25.68	0.112	± 0.007
	H_2O	R-6	0.5	24.0	21.0	24.95	0.074	± 0.013
20[c]	Air	R-6	0.5	24.0	21.0	25.63	0.108	± 0.006
	H_2O	R-6	0.5	24.0	21.0	25.29	0.088	± 0.005
Solution Concentration: 94.4 g of U per liter ($H:U^{235}$ = 290)								
20[c]	Air	R-6	0.5	24.0	21.0	26.86	0.185	± 0.011
	H_2O	R-6	0.5	24.0	21.0	26.51	0.176	± 0.011
Solution Concentration: 63.3 g of U per liter ($H:U^{235}$ = 436)								
20[c]	Air	R-6	0.5	24.0	21.0	28.23	0.264	± 0.016
	H_2O	R-6	0.5	24.0	21.0	27.78	0.265	± 0.014

[a]The water reflector was effectively infinite and surrounded the bottom and lateral surfaces to approximately the height of the solution.

[b]This assembly was subcritical.

[c]32-mil-thick cadmium sheet around cylinder.

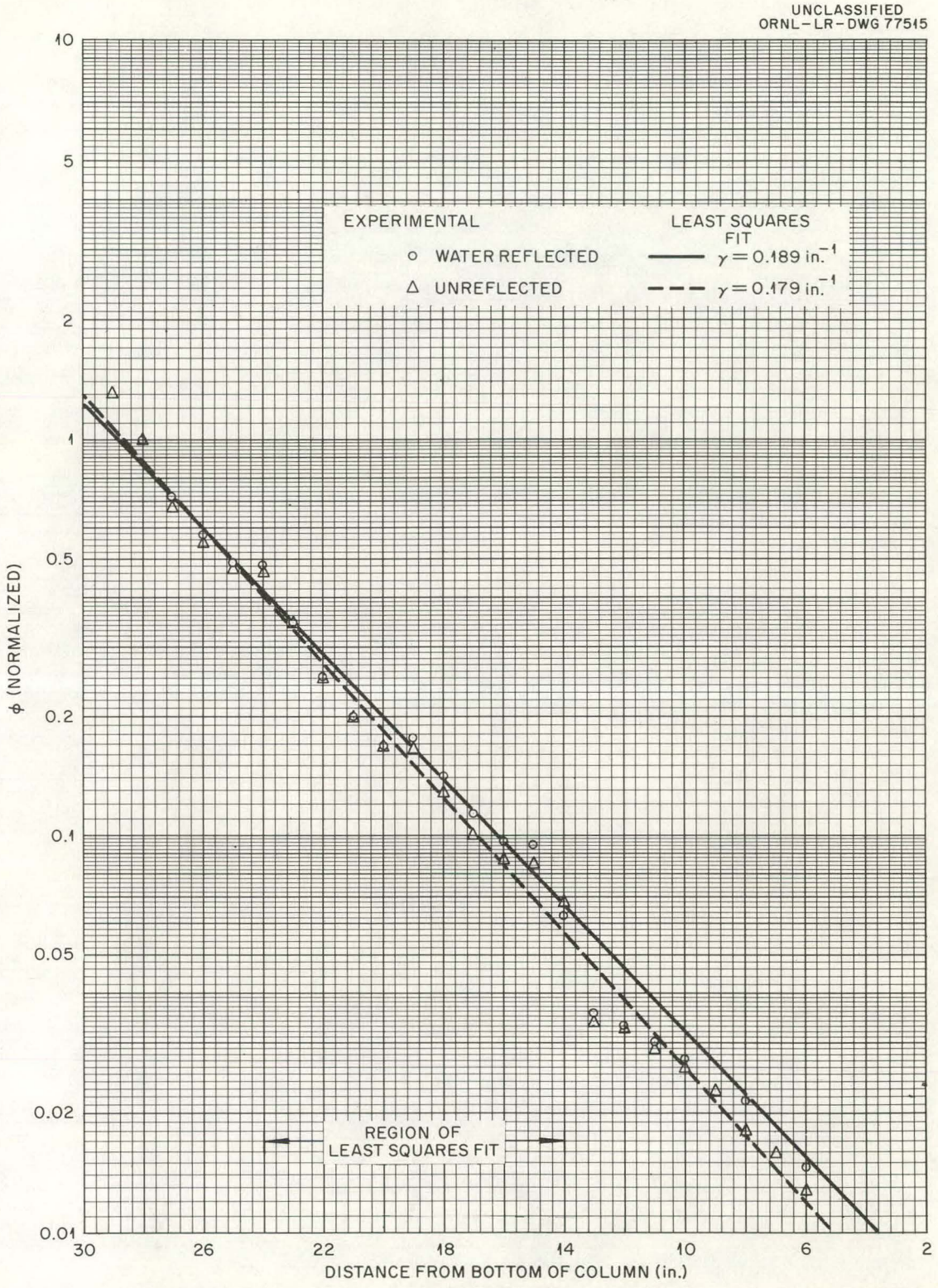

Fig. 2.2.1. Neutron Flux Distribution Along Axis of 48-in.-diam Cylinder.

of the glass is responsible for the material buckling being reduced by a factor of about 2. It can also be seen from this curve that, since $B_m^2 = 0$ for an infinite critical system ($k_\infty = 1$), $k_\infty \leq 1$ for every volume of aqueous $U(93)O_2(NO_3)_2$ at a concentration of 415 g of uranium per liter provided the glass occupies at least 24.1% of the volume, contains a minimum of 3.3 wt % boron, and is uniformly distributed.

It should be emphasized that the mere presence of borosilicate glass in a vessel which contains uranium-bearing solution will not necessarily

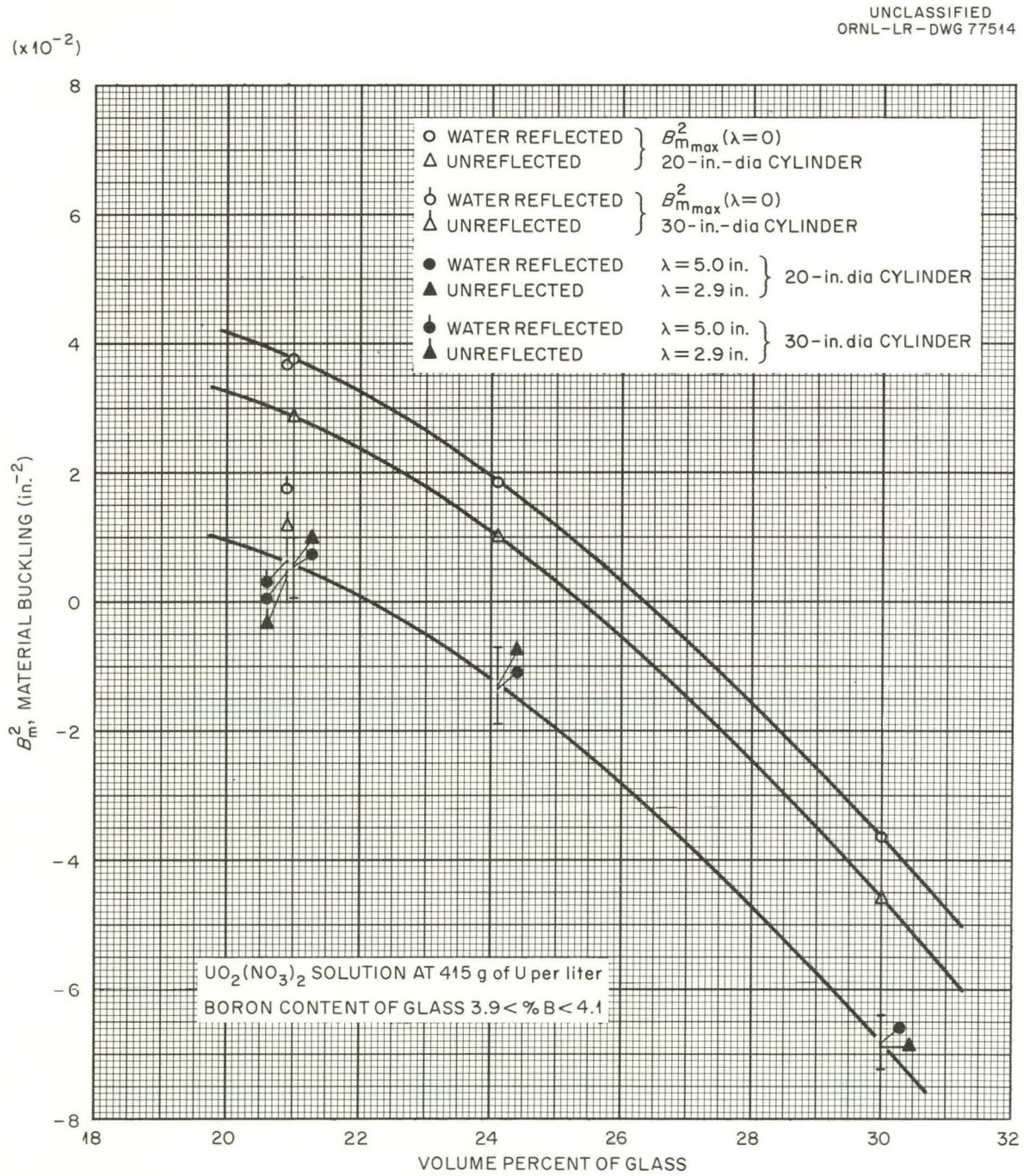

Fig. 2.2.2. Material Buckling of Mixtures of $U(93)O_2(NO_3)_2$ Solution and Borosilicate Glass Raschig Rings Containing 4 wt % Boron as a Function of Percent Volume of Glass in the Mixture.

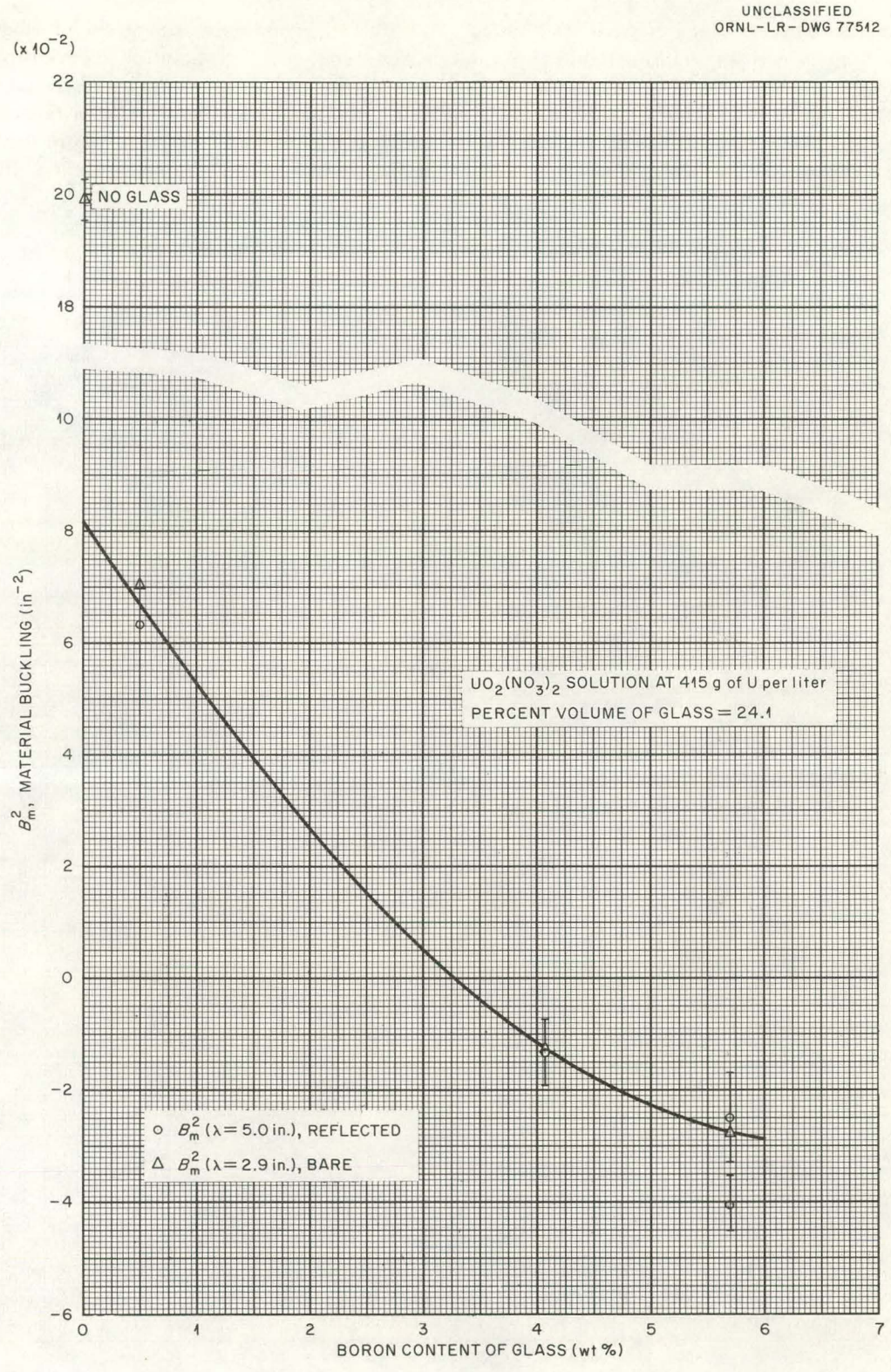

Fig. 2.2.3. Material Buckling of Mixtures of $U(93)O_2(NO_3)_2$ Solution and Borosilicate Glass Raschig Rings for a Constant Volume Percent of Glass in the Mixture as a Function of Weight Percent Boron in the Glass.

prevent the criticality of that system – as shown, for example, in the last entry in the table under a solution concentration of 415 g of uranium per liter. In this case, the rings contained 0.5 wt % boron and the system was critical with the solution height well below the top of the ring bed. In order to further investigate the effect of rings of this boron content, the solution concentration was decreased until the maximum material buckling was less than zero. The results of these measurements are shown in Fig. 2.2.4, where the maximum buckling ($\lambda = 0$) is plotted against solution con-

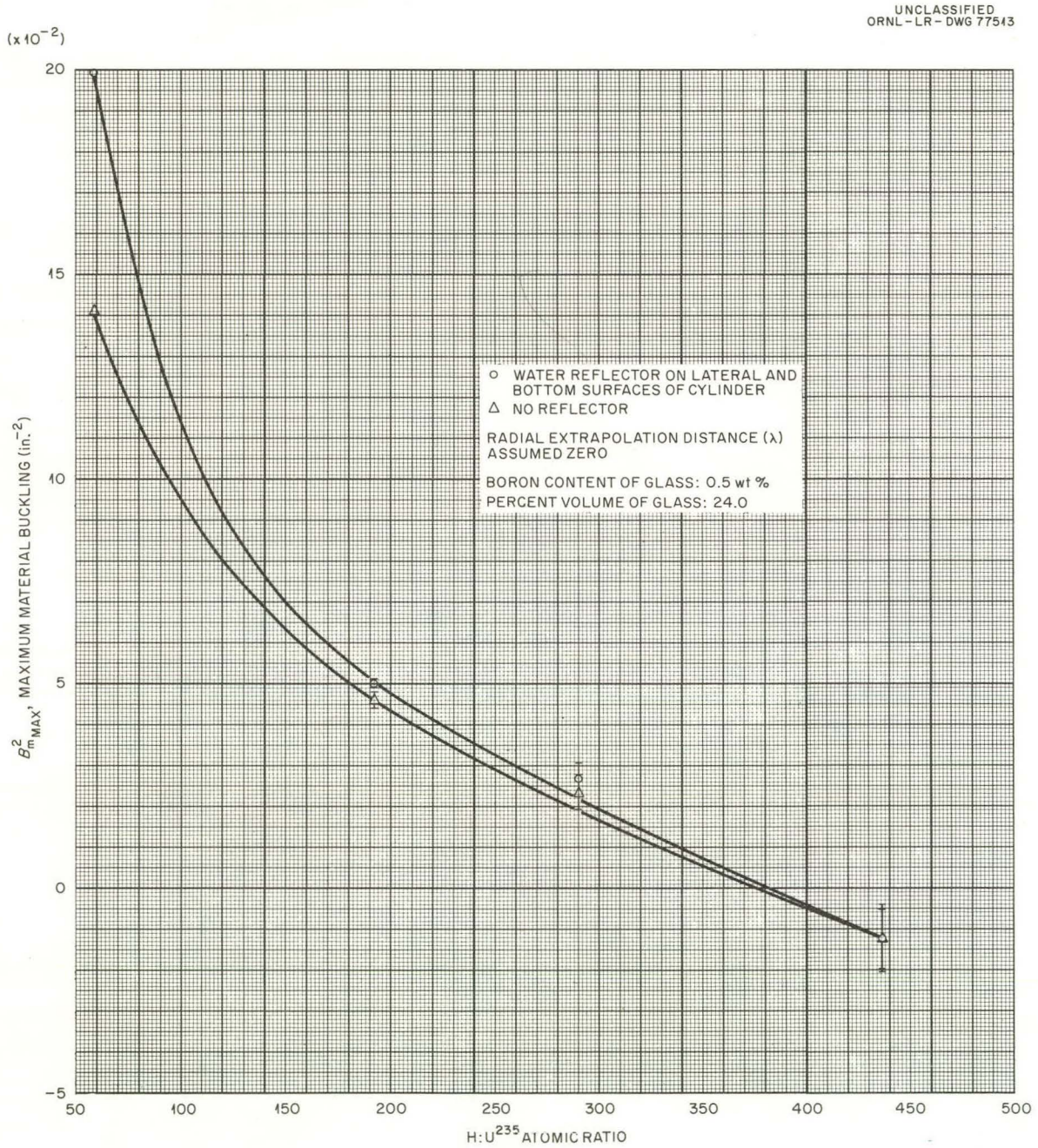

Fig. 2.2.4. Maximum Material Buckling ($\lambda = 0$) of Mixtures of $U(93)O_2(NO_3)_2$ Solution and Borosilicate Glass Raschig Rings in a 20-in.-diam Stainless Steel Cylinder.

centration. These curves indicate that any system containing Raschig rings of 0.5 wt % boron which occupy at least 24% of the volume of the mixture will have a value of $k_{\infty} < 1$ (since the extrapolation distance is greater than zero) if the solution concentration is $\leq$ 72 g of uranium per liter ($H:U^{235} \geq 380$).

These data have been published in greater detail as ORNL TM-499.[3]

[3] J. T. Thomas, J. K. Fox, and E. B. Johnson, *Critical Mass Studies, Part XIII*, ORNL TM-499 (Feb. 6, 1963).

2.3. NEUTRON MULTIPLICATION BY EXPERIMENTAL GAS-COOLED REACTOR FUEL ASSEMBLIES

E. B. Johnson

Experiments were conducted to determine the source neutron multiplication of fuel assemblies for the Experimental Gas-Cooled Reactor (EGCR) under conditions which might exist in transportation and storage. Twenty-eight fuel assemblies were arranged to yield maximum nuclear reactivity under conditions which might be expected for out-of-reactor environments. It was found that these 28 assemblies cannot be made critical when water-moderated and -reflected.

These experiments are reported in detail elsewhere.[1]

[1] E. B. Johnson and R. K. Reedy, Jr., *Neutron Multiplication by Experimental Gas-Cooled Reactor Fuel Assemblies*, ORNL TM-433 (Nov. 27, 1962); see also p 7 in *Nuclear Safety Program Semiann. Progr. Rept. June 30, 1963*, ORNL-3483.

2.4. MEASUREMENT AND CALCULATION OF THE PROMPT-NEUTRON DECAY CONSTANT AND EFFECTIVE BUCKLING AS A FUNCTION OF SIZE FOR HOMOGENEOUS URANIUM SOLUTIONS

D. W. Magnuson

It has been suggested that pulsed-neutron measurements of the prompt-neutron decay constant, α, could be useful in characterizing subcritical assemblies of fissile materials. Within the limits of diffusion theory, the buckling, B^2, is a quantity that is defined by the dimensions and the extrapolation distance. Therefore, it was desired to measure α as a function of B^2 for a wide range of uranium concentrations in aqueous solutions and to compare the results with calculated values.

The measurements made thus far have been for a uranyl nitrate solution having a concentration of $\sim$65 g of uranium per liter and a U^{235} enrichment of 93.2%. They have included measurements of flux distributions and prompt-neutron decay constants for both critical and subcritical conditions in both spherical and cylindrical geometries.

The calculations, which have been performed for spherical geometry only, were made with the 16-group cross-section values of Hansen and

Roach[1] in Carlson's[2] S_n transport code in the S_4 approximation. There is evidence from the calculated flux distributions that the asymptotic flux exists over only a small central volume of these systems. The calculations also show that the assumption of an energy-independent buckling or extrapolation length is not valid for critical systems at this uranium concentration.

The calculations for a sphere whose critical radius was 18.47 cm gave prompt-neutron lifetime values of 20.4, 26.7, and 33.6 μsec as determined from $\sum_n \phi_n \overline{(1/v)}_n$, β/α, and β_{eff}/α, respectively. The calculated value of α for the same sphere was 239.6 sec^{-1}, which is to be compared with a measured value of 234.6 sec^{-1}.

A comparison of the calculated fluxes in a subcritical sphere having a radius of 11.15 cm with those in the 18.47-cm critical sphere shows that the neutron fluxes in the epithermal groups in the subcritical sphere are approximately two-thirds as large as those in the critical sphere. The fractions of the neutrons produced in each group were 0.9090 and 0.8591 for the thermal groups in the 11.15- and 18.47-cm spheres, respectively. The 5% increase in the fissions from thermal neutrons in the 11.15-cm sphere is due to the larger escape probability of fast neutrons in a system made subcritical by reducing its physical size and is similar to the diffusion cooling of a Maxwell-Boltzmann distribution in pulsed moderator systems. When measured flux distributions were used to find an effective extrapolation distance, the values were found to decrease for subcritical systems, in agreement with the calculated spectral change.

A detailed report summarizing these measurements has been written and will be issued.

[1] G. E. Hansen and W. H. Roach, *Six and Sixteen Group Cross Sections for Fast and Intermediate Critical Assemblies*, LAMS-2543 (1961).

[2] B. G. Carlson and G. I. Bell, *Proc. Intern. Conf. Peaceful Uses Atomic Energy, 2nd, Geneva, 1958* **16**, 535–49 (1959); B. Carlson, C. F. Lee, and J. Worlton, *The DSN and TDC Neutron Transport Codes*, LAMS-2346 (1960).

2.5 CRITICAL ARRAYS OF U(93.2) METAL CYLINDERS

J. T. Thomas

In order to further establish bases for regulations governing the transport and storage of individually subcritical units of fissile materials, a series of critical experiments has been performed with three-dimensional arrays of U(93.2) metal cylinders.[1] The elementary pieces used to form the units consist of 11.519-cm-diam metal cylinders containing ~5.2 kg and ~10.5 kg of U(93.2) as shown in Fig. 2.5.1. The density of the uranium is 18.76 g/cc. In one series of arrays two of the larger cylinders were combined to form cylindrical units containing ~21 kg of U(93.2) and in another series one of the smaller cylinders was added to form units containing ~26 kg of U(93.2).

The cylinders were supported on stainless steel rods passing through two 0.508-cm-diam holes parallel to the axis of each cylinder and located 8.547 cm apart on a diameter. The rods were positioned vertically and the units were separated by spacers of appropriate length cut from close-fitting stainless steel tubing. The rods and spacers are pictured in Fig. 2.5.1, and the details of a 27-unit array are shown in Fig. 2.5.2.

[1] Earlier experiments with subcritical units of fissile materials have been reported by L. W. Gilley and J. T. Thomas, *Trans. Am. Nucl. Soc.* **4**, 54 (1961); J. T. Mihalczo and J. J. Lynn, *Trans. Am. Nucl. Soc.* **2**, 80 (1959); and J. T. Thomas and J. K. Fox, *Neutron Phys. Div. Ann. Progr. Rept. Sept. 1, 1962*, ORNL-3360, p 37.

The critical conditions for the units containing ~21 kg of U(93.2) are summarized in Table 2.5.1, which gives the surface-to-surface spacing required for criticality for 8- and 27-unit arrays. Many of the arrays were reflected and in some arrays neutron-moderating materials surrounded the individual units. The critical conditions for unmoderated arrays of units containing ~26 kg of U(93.2) are presented in Table 2.5.2.

Within the range of these experiments, the effect of placing a 15.24-cm-thick paraffin reflector around an array of a particular density was to reduce the number of units required for criticality by a factor of about 12. The critical number was further reduced by a factor of approximately 2 by the addition of 1.270-cm-thick Plexiglas between adjacent units.

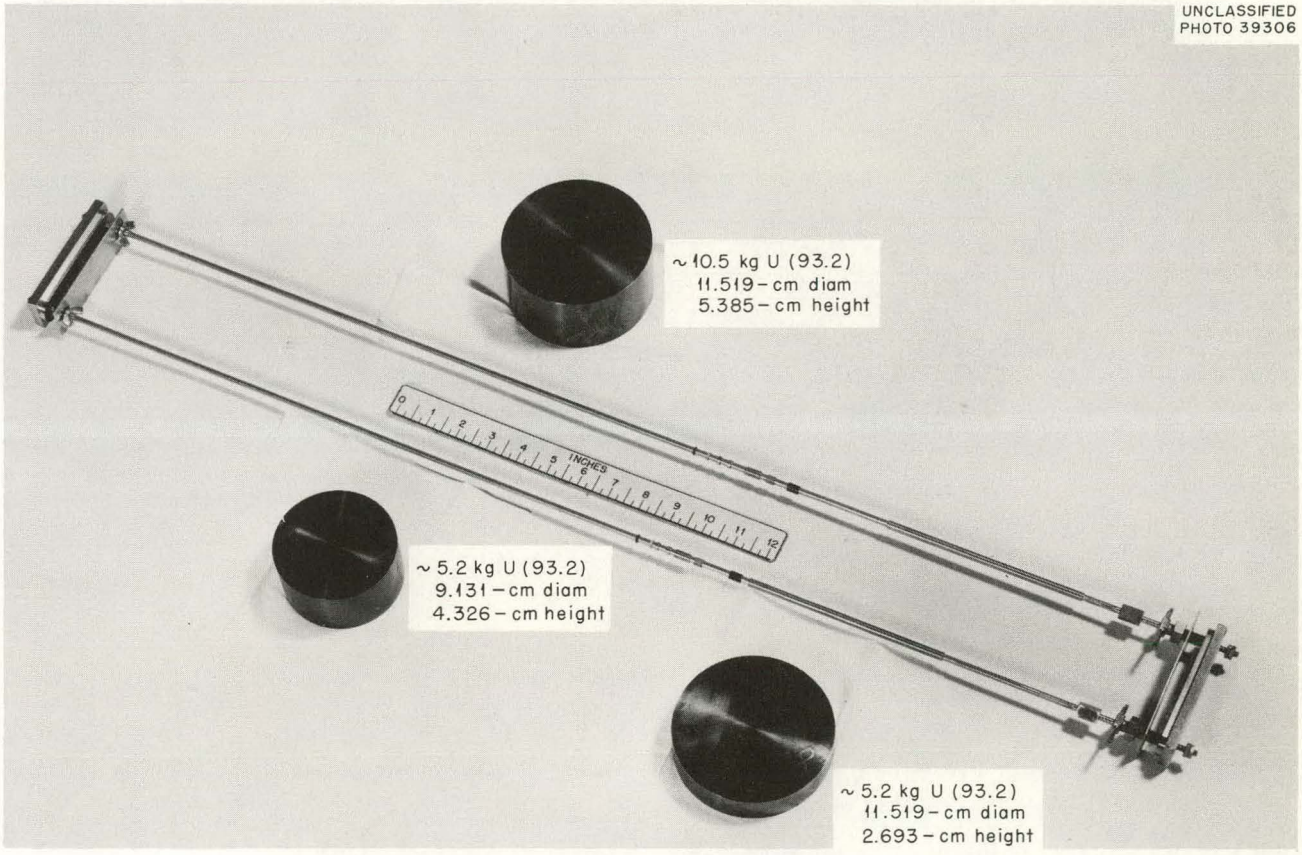

Fig. 2.5.1. U(93.2) Metal Pieces Used to Form Subcritical Units and Supporting Stainless Steel Rods and Spacers.

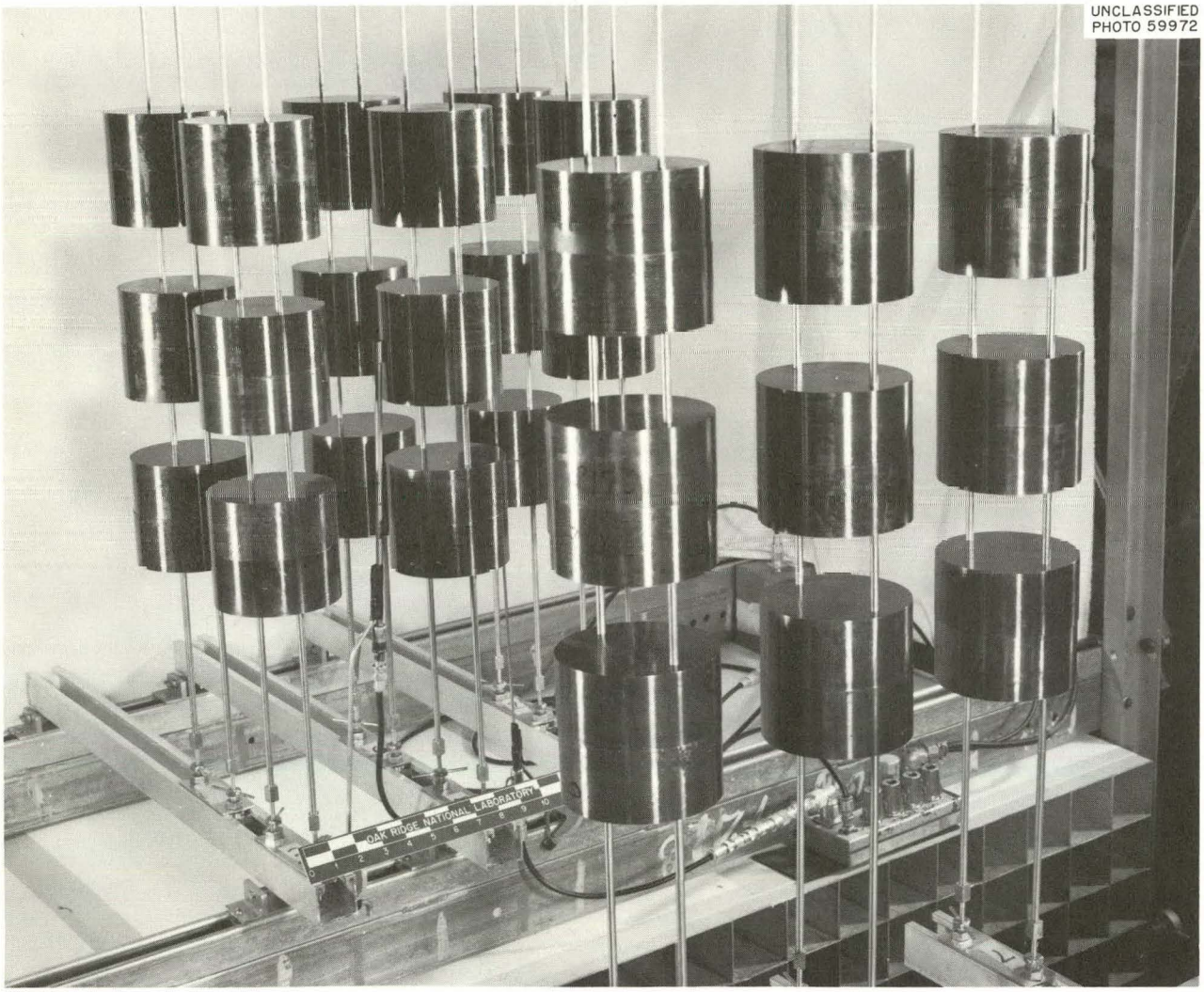

Fig. 2.5.2. Unreflected and Unmoderated 27-Unit Array of U(93.2) Metal Cylinders. Average weight of U^{235} per unit is 19.457 kg; spacing between surfaces of adjacent units is 6.363 ± 0.013 cm at criticality.

Table 2.5.1. Critical Conditions for Uniform Arrays of ~21-kg U(93.2) Metal Cylinders

Units: 11.519-cm diameter, 10.770-cm height; uranium metal density, 18.76 g/cc

Number of Units in Array	Average Mass of Unit (kg of U)	Paraffin Reflector Thickness (cm)	Surface-to-Surface Separation (cm)	Average Uranium Density in Array (g/cc)
		No material between units		
8	20.805	0	2.217 ± 0.013	8.600
8	20.960	0	2.248 ± 0.013	8.530
		1.27	3.678 ± 0.026	6.309
		2.54	5.710 ± 0.026	4.301
		3.81	8.207 ± 0.026	2.849
		7.62	11.509 ± 0.026	1.780
		15.24	11.986 ± 0.026	1.673
27	20.877	0	6.363 ± 0.013	3.840
		1.27	8.547 ± 0.026	2.704
		3.81	14.764 ± 0.026	1.192
		7.62	18.720 ± 0.026	0.780
		15.24	19.147 ± 0.026	0.747
		Each unit centered in 15.57 × 15.57 × 14.38 cm Plexiglas box[a] with 0.635-cm-thick walls		
8	20.960	0	4.239 ± 0.013	5.646
		1.27	5.875 ± 0.026	4.178
		7.62	12.573 ± 0.026	1.552
		15.24	12.929 ± 0.026	1.485
		Each unit centered in 17.86 × 17.86 × 17.15 cm Plexiglas box[a] with 1.270-cm-thick walls		
8	20.960	0	6.619 ± 0.013	3.678
		1.27	8.611 ± 0.026	2.678
		15.24	14.503 ± 0.026	1.229
		Units centered in 5-in. Schedule 40 pipe; 13.18-cm outside height, 14.13-cm outside diameter, and 0.66-cm wall thickness		
8	20.960	0	3.239 ± 0.013	6.898
		Units centered in the above 5-in. Schedule 40 pipe surrounded by 0.635-cm-thick Plexiglas boxes		
8	20.960	0	5.169 ± 0.013	4.740

[a]Outside dimensions.

Table 2.5.2. Critical Conditions for Uniform Arrays of ~26-kg U(93.2) Metal Cylinders

Units: 11.519-cm diameter, 13.462-cm height; uranium metal density, 18.76 g/cc

Number of Units in Array	Average Mass of Unit (kg of U)	Paraffin Reflector Thickness (cm)	Surface-to-Surface Separation (cm)	Average Uranium Density in Array (g/cc)
8	26.218	0	3.543 ± 0.013	6.844
		1.27	5.423 ± 0.026	4.870
		3.81	11.532 ± 0.026	1.984
		7.62	15.697 ± 0.026	1.222
		15.24	16.378 ± 0.026	1.136
27	26.113	0	8.494 ± 0.013	3.001
		1.27	11.323 ± 0.026	2.041
		3.81	19.606 ± 0.026	0.823

2.6. CRITICAL EXPERIMENTS AND CALCULATIONS WITH ANNULAR CYLINDERS OF U(93.2) METAL

J. T. Mihalczo

A series of critical experiments with annular cylinders of uranium metal was performed to verify the adequacy of the S_n method of solving the transport equation for this geometry. The uranium has a density of 18.76 g/cc and is enriched to 93.2% in the U^{235} isotope. Unreflected annuli with outside diameters as large as 15 in. and inside diameters as small as 7 in. were assembled to delayed critical, and the prompt-neutron decay constant was measured by the Rossi-α technique.[1] In the Rossi-α measurements two detectors were used with a Technical Measurement Corporation 256-channel analyzer having a time-of-flight logic unit. A signal from a plastic scintillator sensitive to neutrons and gamma rays triggered the time analyzer, and the time distribution of neutrons detected by a small U^{235} spiral fission counter was measured. The resulting values of the decay constant, together with the measured reactivities of the various assemblies, are shown in Table 2.6.1.

Multiplication constants of the experimental configurations were calculated by multigroup transport theory using the S_n method[2] in the S_8 approximation, the TDC computer code,[3] and the six-group cross-section values of Hansen and Roach[4] for the U^{235} and U^{238} isotopes. Fission of U^{234} and of U^{236} was included, and the absorption and scattering properties of these isotopes were assumed to be the same as those of U^{238}. The calculated values of the multiplication constant, which are included in Table 2.6.1, are in agreement with the measured reactivities.

The prompt-neutron decay constants obtained from the Rossi-α measurements with the annular cylinders at delayed critical are somewhat smaller than those obtained for solid uranium metal

[1] J. Orndoff, *Nucl. Sci. Eng.* 2, 450 (1957).

[2] B. G. Carlson and G. I. Bell, *Proc. Intern. Conf. Peaceful Uses Atomic Energy, 2nd, Geneva, 1958* 16, 535–49 (1959).

[3] B. Carlson, C. F. Lee, and J. Worlton, *The DSN and TDC Neutron Transport Codes*, LAMS-2346 (1960).

[4] G. E. Hansen and W. H. Roach, *Six and Sixteen Group Cross Sections for Fast and Intermediate Critical Assemblies*, LAMS-2543 (1961).

assemblies since the flight time of the neutrons across the center void constitutes a large fraction of the prompt-neutron lifetime.[5] At delayed critical the prompt-neutron decay constant is inversely proportional to the prompt-neutron lifetime, and the proportionality constant, the effective delayed-neutron fraction, is taken to be 0.0067. The prompt-neutron lifetime for the 11-in.-OD by 7-in.-ID assembly is 9.8×10^{-9} sec, which is to be compared with 6.2×10^{-9} sec for solid uranium metal assemblies.

The effect of inserting graphite (National Carbon type ATL; ρ = 1.7 g/cc) and beryllium (ρ = 1.83 g/cc) into the center cavity was also determined, and comparisons of the experimental results with calculated values are included in Table 2.6.1. The calculations of these experiments by the TDC code used the 16-group cross-section values of Hansen and Roach,[3] with U^{234} and U^{238} treated as above.

In general, the agreement between calculation and experiment is good and demonstrates the adequacy of the S_n method in the S_8 approximation for assemblies with large central voids.

[5] J. T. Mihalczo, *Trans. Am. Nucl. Soc.* **6**, 60 (1963).

Table 2.6.1. Experimental and Calculated Results for Cylindrical Annuli of U(93.2) Metal

Dimensions		Average Height[a] (in.)	Mass (kg of U)	Content of Center Cavity	Reactivity[b] (cents)	Calculated k_{eff}	Prompt-Neutron Decay Constant[c] (sec^{-1})
Outside Diameter (in.)	Inside Diameter (in.)						
11	7[d]	7.31	157.9	Air	−16.5	0.9900	$(0.686 \pm 0.008) \times 10^6$
13	7	5.74	165.6	Air	− 4.2	1.0014	$(0.883 \pm 0.009) \times 10^6$
13	7	5.26	151.9	C	+15.6	1.0013	
13	9[e]	6.08	128.7	C	− 5.3	1.0033	
15	7	4.23	179.0	Air	−13.5	0.9981	$(0.950 \pm 0.010) \times 10^6$
15	7	4.10	173.6	C	−24.6	0.9963	
15	7	3.98	168.6	Be	− 6.3	1.0035	
15	9	5.93	205.6	Air	−26.7	1.0027	$(0.840 \pm 0.008) \times 10^6$
15	9	5.35	185.3	C	−11.5	0.9980	

[a] Irregular top; fuel height increment, 0.062 in.; fuel radial increment, 1.0 in. The uncertainty in the average height is less than 0.03 in.

[b] Upon complete reassembly the change in the reactivity was less than ±5 cents. Reactivities of the assemblies have been corrected for support structure.

[c] Error from least-squares analysis of the counter data.

[d] A 7-in.-diam, 1.38-in.-thick disk was located at the bottom of the cavity, and a 7-in.-diam, 1.25-in.-thick disk was located with its top surface 0.13 in. below the top of the annulus.

[e] 1-in. carbon reflector.

2.7. PROMPT-NEUTRON DECAY PROPERTIES AND CRITICAL DIMENSIONS OF UNMODERATED CYLINDRICAL U(93.2) METAL ASSEMBLIES WITH LARGE GAPS

J. T. Mihalczo

The series of critical experiments which began with parallelepipedal U(93.2) metal assemblies having large gaps at their midplanes[1,2] has been extended to include cylindrical assemblies in which the flat surfaces of 7-, 11-, and 15-in.-diam disks are separated by as much as 9 in. The critical separation distances of two disks vs the thickness of one disk (one-half the total metal thickness of the assembly) is shown in Fig. 2.7.1 for assemblies of all three diameters.

Corresponding prompt-neutron decay constants were obtained by the Rossi-α technique, in which the time distribution of prompt neutrons associated with a common ancestor is measured. A typical set of data collected in a Rossi-α measurement using a Technical Measurement Corporation 256-channel analyzer with a neutron time-of-flight logic unit is shown in Fig. 2.7.2. For this measurement a proton-recoil detector was used to trigger the time analyzer, and the signal, after a delay of 6.1 μsec, was from two spiral fission counters. The data prior to the peak represent the buildup of the neutron population before the decay. The decay constants measured by this technique for the three sets of disks are given in Fig. 2.7.3.

Values of the effective delayed-neutron fraction, β_{eff}, which are required to obtain the prompt-neutron lifetimes from the measured decay constants, have been computed for the 11-in.-diam assemblies from transport-theory calculations using the S_n method of solution of the transport equation and the cross sections referred to in Sec. 2.6. The adequacy of the S_n method in the S_8 approximation and of the six-group cross-section sets used for the calculations of these assemblies was demonstrated, since the calculated multiplication factors for 11 different experimental configurations are between 0.99 and 1.002.

The values of β_{eff} were obtained from the difference in the multiplication factor calculated first with the unmodified fission-neutron spectrum and then with the spectrum modified by subtracting the delayed neutrons in four energy groups (3 through 6) out of the calculation. This modification, for which the delayed-neutron energy distribution of Batchelor and McK. Hyder[3] and the yields of Keepin *et al.*[4] were used, included subtracting the delayed neutrons from the fast fission of U^{238}. The fraction of fissions arising in the U^{235} and U^{238} isotopes obtained from the S_8 calculations was used to determine the magnitude of the modification of the fission spectrum.

[1] J. T. Mihalczo, *Neutron Phys. Div. Ann. Progr. Rept. Sept. 1, 1962*, ORNL-3360, p 39.

[2] J. T. Michalczo, *Trans. Am. Nucl. Soc.* **6**, 60 (1963).

[3] R. Batchelor and H. R. McK. Hyder, *J. Nucl. Energy* **3**, 7 (1956).

[4] G. R. Keepin *et al.*, *Phys. Rev.* **107**, 1044 (1957).

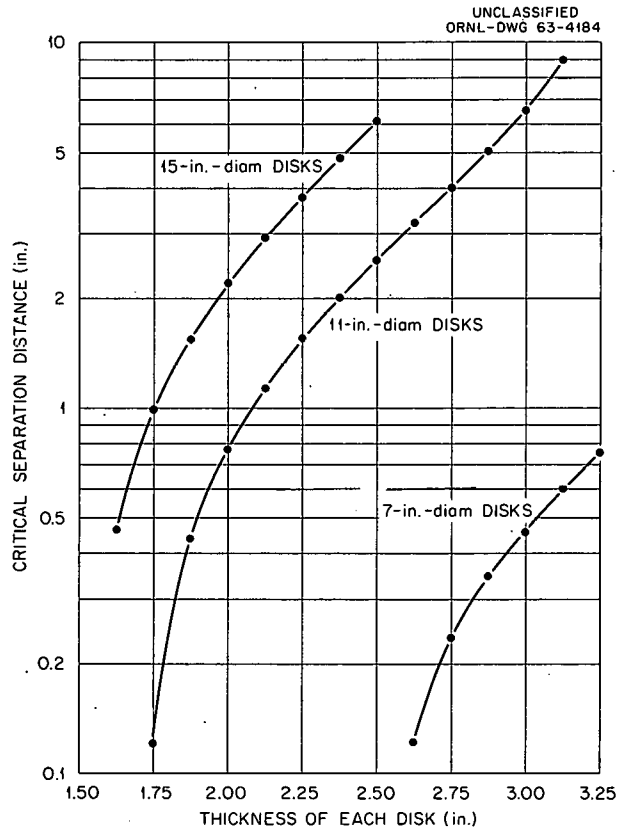

Fig. 2.7.1. Critical Separation Distances of Two Interacting U(93.2) Metal Disks as a Function of the Thickness of One Disk.

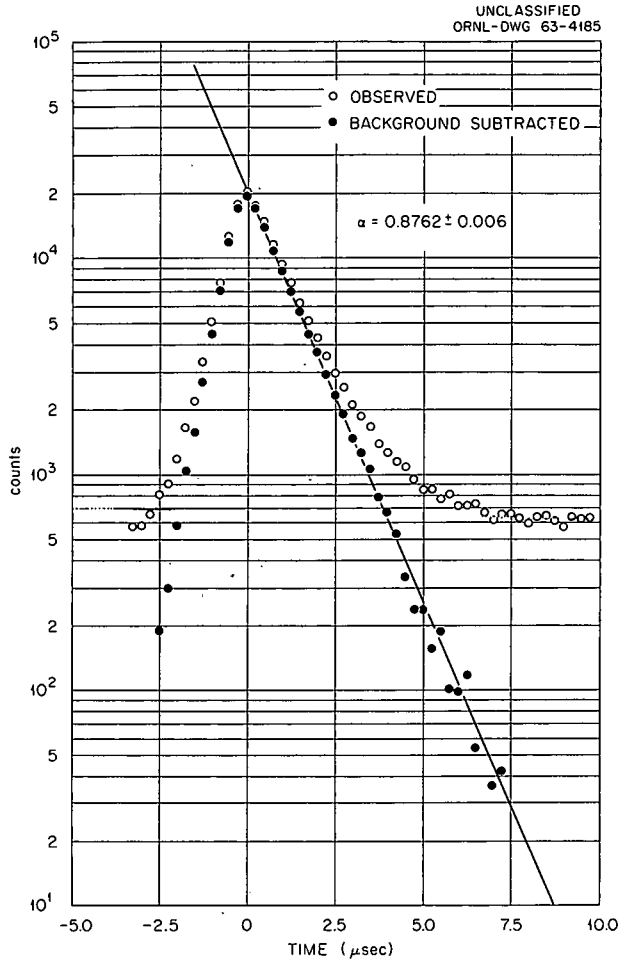

Fig. 2.7.2. Typical Detector Response vs Time in Rossi-α Measurement.

For the purpose of this calculation, half the fissions in U^{234} and U^{236} were assumed to be U^{235} fissions and the other half to be U^{238} fissions. The calculated percent fission occurring in U^{235} was independent of separation, and the computed value of β_{eff} was 0.00671, with a variation of 10^{-5} over the separation distances used in the experiments. The prompt-neutron lifetimes obtained from the calculated values of β_{eff} for the 11-in.-OD disks are plotted in Fig. 2.7.4.

It has been shown[2] that the expression describing the dependence of the prompt-neutron lifetime on the gap width is

$$l = l_s + t(x)\frac{P(x)}{1 - R(x)}, \qquad (1)$$

where

l = prompt-neutron lifetime,

l_s = prompt-neutron lifetime if the neutron flight time across the gap were zero,

$P(x)$ = probability that a neutron born in one disk leaks into the other,

$R(x)$ = probability that a neutron incident on one disk will be reflected into the other disk,

$t(x)$ = average neutron flight time from one disk to the other.

Since the agreement between the experimental and calculated multiplication factors discussed above is good, the fluxes obtained in the S_n calculation can be used to compute the functions[5] used in the right-hand side of Eq. (1). The following paragraphs describe how these functions are computed.

The neutron lifetime in any assembly is equal to the change in the multiplication constant resulting from the addition throughout the assembly of an absorber with cross sections numerically equal to the reciprocal of the velocity, or

$$l = \frac{[\phi_s^{+}, (1/v)\phi_d]}{[\phi_s^{+}, \nu\Sigma_f \chi(E)\phi_d]}, \qquad (2)$$

where

ϕ_s^{+} = static adjoint flux,

ϕ_d = forward dynamic flux,

Σ_f = fission cross section,

$\chi(E)$ = energy spectrum of neutrons from fission,

ν = number of neutrons per fission.

The inner product notation signifies integration over angle, volume, and energy. An integration over the volume occupied by uranium yields l_s.

The function P is obtained from the output fluxes of the static-forward k calculations. The fluxes are used in a code which computes the leakage in intervals in both the r and z directions. The angular distribution of neutrons on the surfaces of the assembly (see Fig. 2.7.5) is calculated by using a spatial interval of less than 10^{-5} cm surrounding the volume occupied by uranium. This information is then used to obtain P, which

[5]Programs to compute these functions on the IBM-7090 were written by G. E. Whitesides of ORGDP.

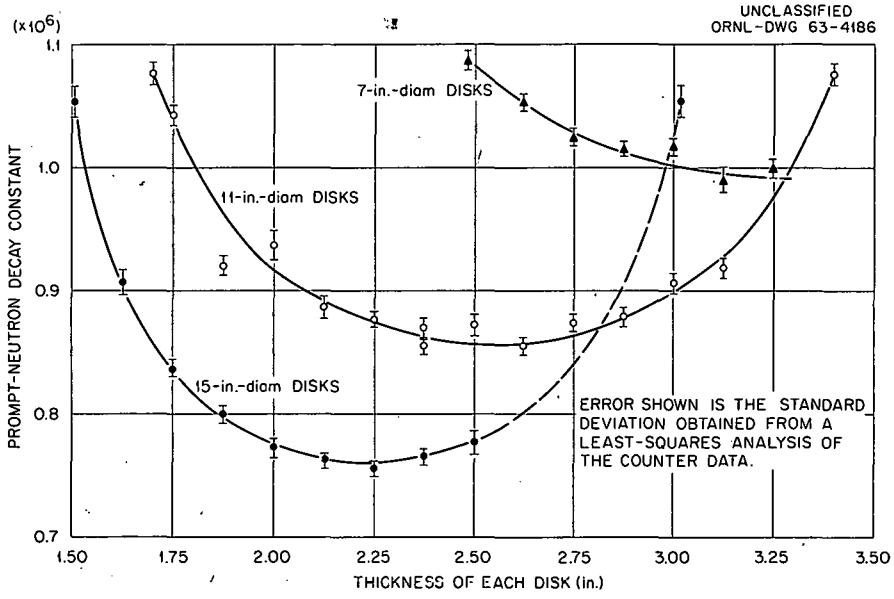

Fig. 2.7.3. Prompt-Neutron Decay Constant of Two Interacting U(93.2) Metal Disks as a Function of the Thickness of One Disk.

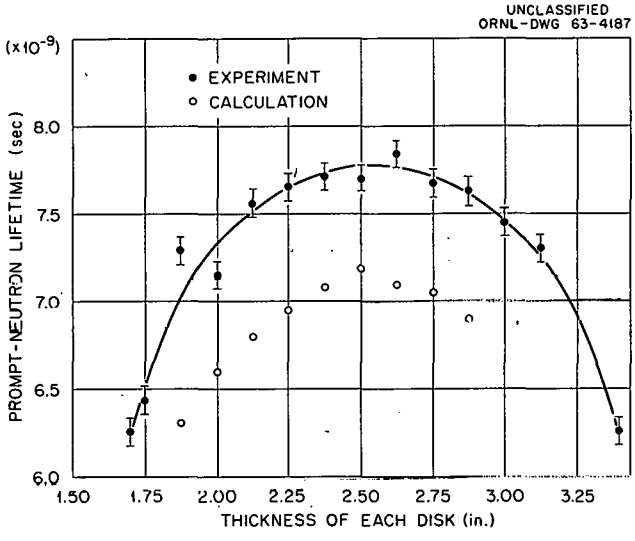

Fig. 2.7.4. Prompt-Neutron Lifetime of Two Interacting 11-in.-diam U(93.2) Metal Disks as a Function of the Thickness of One Disk.

is calculated by dividing the leakage into surface 2 by the number of neutrons born in disk A, which is equal to one-half of k_{eff} since the disks are identical.

The static-forward fluxes are also used to calculate R, the probability that a neutron incident on one disk will be reflected into the other disk. A TDC source calculation is performed in which the upward directed flux obtained from the static-forward k calculation is fixed on surface 2, and the fission cross section is removed from disk A. The TDC source calculation is then made to obtain the new flux in disk A. Since the surface 2 source is held constant, it is as though disk B were there with its original flux distribution. It cannot reflect neutrons and hence allows one to look at only singly reflected neutrons. The output from this calculation can then be used to calculate the leakage, which in turn is used to calculate R as

$$R = \frac{\text{leakage into surface 2}}{\text{leakage into surface 1}}.$$

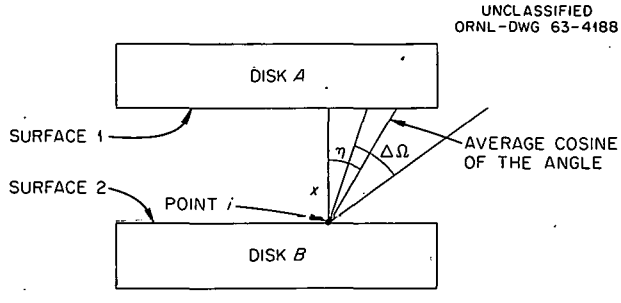

Fig. 2.7.5. Geometry for Calculations.

Evaluations of $P(x)$ and $R(x)$ have been made for the 11-in.-diam disks and are given in Fig. 2.7.6.

The calculation of the average neutron flight time, t, is made by assuming that neutrons are moving from the bottom disk and entering the top disk. A grid is placed over the bottom disk for the purpose of determining the origin of the flux in a given solid angle. The size of the grid is specified as an input number. For a given radial point in the top disk, one is able to determine the average distance, $\overline{D}$, traveled by a neutron entering through each angle:

$$\overline{D}(r,\Omega) = \frac{\sum_{\text{area}} D(\text{of each area})\Delta A}{\sum_{\text{area}} \Delta A} .$$

The integration on the top disk, over the angles and over all energy, is performed as follows:

$$t = \frac{\sum_{g=1}^{G}\sum_{i=1}^{R}\sum_{j=1}^{\Omega} \phi(g,i,\Omega)\,\overline{\eta}(i,\Omega)\,\frac{x}{\overline{\eta}(i,\Omega)}\,\frac{1}{v_g}\,\Delta A'(i)}{\sum_{g=1}^{G}\sum_{i=1}^{R}\sum_{j=1}^{\Omega} \phi(g,i,\Omega)\,\overline{\eta}(i,\Omega)\,\Delta A'(i)} ,$$

where

x = distance between disks,

Ω = angle,

i = radial point,

g = energy group,

v = velocity,

ϕ = flux,

$\overline{\eta}(i,\Omega) = x/\overline{D}(i,\Omega)$,

$\Delta A'$ = incremental area on the top disk.

The calculations of t have not yet been performed. The prompt-neutron lifetime calculated by use of Eq. (2) for the 11-in.-diam disks is included in Fig. 2.7.4. Although the values show qualitatively the same dependence on disk thickness as do the experimentally determined ones, they are as much as 10% lower in magnitude. This disagreement is about the same as that obtained in the comparison of the Godiva I experiments and calculations.[6]

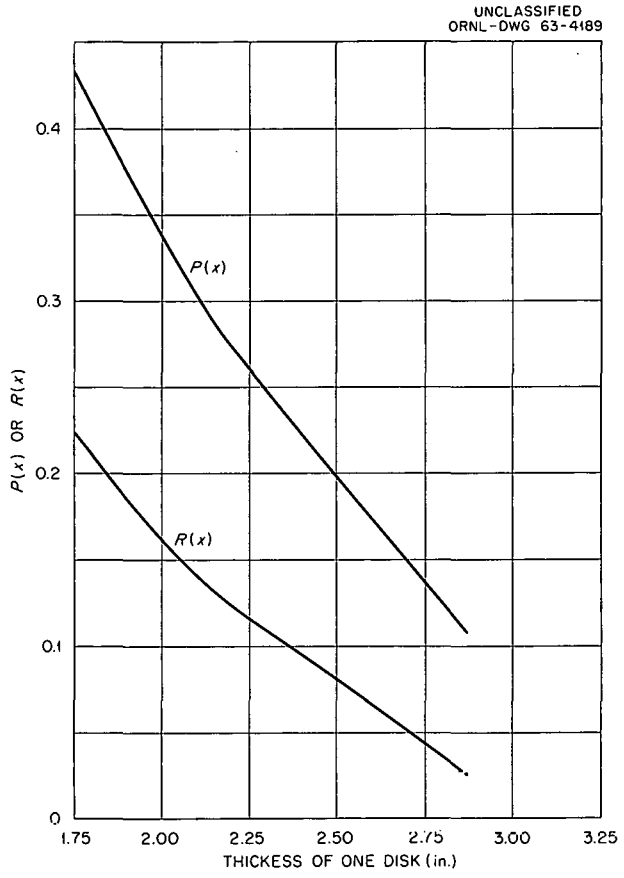

Fig. 2.7.6. $P(x)$ and $R(x)$ vs Disk Thickness for 11-in.-diam Disks.

[6] G. E. Hansen, pp 445–455 in *Physics of Fast and Intermediate Reactors, Proceedings of a Seminar on the Physics of Fast and Intermediate Reactors*, vol. 1, International Atomic Energy Agency, Austria, 1962.

2.8. DSN TRANSPORT CALCULATIONS OF CRITICAL SPHERES OF URANIUM SOLUTIONS

D. W. Magnuson

Calculations have been made of the multiplication factors of several water-reflected and unreflected critical spheres of uranyl nitrate or uranyl fluoride aqueous solutions. Carlson's[1] S_n transport code, DSN, was used in the S_4 approximation with the 16-group cross-section values of Hansen and Roach.[2] The critical conditions and the calculated multiplication constants are given in Table 2.8.1. It is concluded that this code and cross-section set can be used with confidence for these solutions over the complete range of concentrations. It is believed that the difference between the calculated and experimental multiplication factors is due primarily to errors in the experimental determination of atomic densities and to errors in the cross sections.

[1] B. G. Carlson and G. I. Bell, *Proc. Intern. Conf. Peaceful Uses Atomic Energy, 2nd, Geneva, 1958* 16, 535–49 (1959); B. Carlson, C. F. Lee, and J. Worlton, *The DSN and TDC Neutron Transport Codes*, LAMS-2346 (1960).

[2] G. E. Hansen and W. H. Roach, *Six and Sixteen Group Cross Sections for Fast and Intermediate Critical Assemblies*, LAMS-2543 (1961).

Table 2.8.1. Critical Conditions and Calculated Multiplication Factors for Bare and Reflected Spheres

Critical Conditions														
Sphere Radius[a] (cm)		Reflector Condition	Atomic Density[b] × 10^{-24} (atoms/cm^3)										Reference	Calculated Effective Multiplication Factor
Inner	Outer		U^{233}	U^{234}	U^{235}	U^{236}	U^{238}	H	O	F	N	B		
11.52	11.68	Reflected		8.70–06	8.326–04	4.30–06	4.73–05	6.336–02	3.35–02	1.786–03			c	0.9961
11.80	11.96	Reflected		5.40–06	5.095–04	2.70–06	2.89–05	6.445–02	3.33–02	1.093–03			c	0.9904
13.20	13.33	Reflected	1.577–04				1.60–06	6.597–02	3.33–02	3.186–04			d	1.0046
13.20	13.33	Reflected		2.87–06	2.429–04	1.31–06	1.36–05	6.553–02	3.30–02	5.214–04			d	0.9955
16.00	16.13	Reflected	1.001–04				1.00–06	6.638–02	3.34–02	2.022–04			d	1.0166
16.00	16.13	Reflected		1.52–06	1.287–04	6.90–07	7.18–06	6.629–02	3.34–02	2.756–04			d	1.0117
16.00	16.13	Bare	1.742–04				1.70–06	6.637–02	3.35–02	3.518–04			d	0.9988
16.00	16.13	Bare		3.80–06	3.209–04	1.70–06	1.79–05	6.530–02	3.33–02	6.886–04			d	0.9870
18.35	18.50	Bare		1.65–06	1.538–04	9.20–07	9.90–06	6.538–02	3.40–02		3.32–04		e	0.9941
27.90	28.10	Reflected		5.70–07	5.265–05	2.80–07	3.00–06	6.687–02	3.35–02	1.130–04			c	1.0123
27.90	28.10	Bare		7.36–07	6.004–05		3.60–06	6.676–02	3.35–02	1.288–04			c	1.0122
34.60	34.92	Bare			4.807–05		3.48–06	6.623–02	3.38–02		1.87–04		f	1.0082
34.60	34.92	Bare			6.796–05		4.93–06	6.603–02	3.39–02		2.55–04	1.28–05	f	1.0058
34.60	34.92	Bare	4.330–05				9.97–07	6.636–02	3.36–02		1.18–04		f	1.0047
34.60	34.92	Bare	5.009–05				1.15–06	6.630–02	3.37–02		1.36–04	5.08–06	f	1.0041
61.01	61.78	Bare			3.619–05		2.61–06	6.639–02	3.36–02		1.12–04		f	1.0107
61.01	61.78	Bare	3.347–05				7.81–07	6.647–02	3.35–02		7.53–05		f	1.0011

[a] All spheres constructed of aluminum (6.016×10^{22} atoms/cm^3).
[b] Atomic densities given as a number and an exponent; e.g., 1.0–01 means 1.0×10^{-1}.
[c] J. K. Fox *et al.*, *Neutron Phys. Div. Ann. Progr. Rept. Sept. 1, 1958*, ORNL-2609, p 42.
[d] J. T. Thomas, J. K. Fox, and D. Callihan, *Nucl. Sci. Eng.* 1, 20 (1956).
[e] D. W. Magnuson, Sec. 2.4, this report.
[f] R. Gwin and D. W. Magnuson, *Nucl. Sci. Eng.* 12, 364 (1962).

2.9. SMALL GRAPHITE- OR BERYLLIUM-REFLECTED UO_2 CRITICAL ASSEMBLIES

J. T. Mihalczo

Three small critical assemblies of U^{235}-enriched UO_2, reflected in two cases by graphite and in the third by beryllium, have provided data to verify calculational methods for these types of assemblies. This work is described in previous publications.[1]

[1] J. T. Mihalczo, *A Small Graphite-Reflected UO_2 Critical Assembly*, ORNL TM-450 (1962) (Classified); *Part II*, ORNL TM-561 (1963) (Classified); *A Small Beryllium-Reflected UO_2 Critical Assembly*, ORNL-TM-655 (1963) (Classified).

2.10. HIGH FLUX ISOTOPE REACTOR CRITICAL EXPERIMENT NO. 2

D. W. Magnuson

The High Flux Isotope Reactor Critical Experiment No. 2 has been completed, and plans are being formulated for a third series of experiments. Detailed reactivity calibration data and power distribution measurements with two additional sets of control plates were obtained for the reactor designers and have been reported.[1,2] As a result, the third series of critical experiments, which will closely resemble the present reactor concept, will include redesigned control plates and a core-fuel distribution different from that of the preceding experiment.

[1] D. W. Magnuson, *High Flux Isotope Reactor Critical Experiment No. 2, Part VII. Reactivity and Power Distribution Measurements with Two-Section Control Plates*, ORNL CF-62-9-75 (Sept. 13, 1962).

[2] D. W. Magnuson, *High Flux Isotope Reactor Critical Experiment No. 2, Part VIII. Reactivity and Power Distribution Measurements with 4-3/4-in.-long Middle Section in the Control Plates*, ORNL CF-62-10-105 (Oct. 31, 1962).

2.11. PRELIMINARY CALCULATIONS AND PREPARATIONS FOR A ONE-DIMENSIONAL CRITICAL-ASSEMBLY EXPERIMENT

E. G. Silver and E. B. Johnson

Introduction

The initial phases of an experimental and calculational program designed to investigate the effects of small motions of fuel plates on the reactivity of pool-type reactors and to determine the adequacy of available machine codes for calculating the magnitude of such effects were described previously.[1] The primary purpose of the program is to determine whether fuel-plate motions such as might be caused by a pressure transient

[1] E. G. Silver *et al.*, *Neutron Phys. Div. Ann. Progr. Rept. Sept. 1, 1962*, ORNL-3360, pp 12–16.

during a nuclear excursion would act as a significant mechanism to effect reactivity compensation or augmentation and whether they must, therefore, be taken into account in achieving a detailed quantitative understanding of the reactivity compensation process.[2,3]

In the initial experiments[1] the reactivity effects of several fuel-location perturbations in the Bulk Shielding Reactor I (BSR-I) were measured. The perturbations were achieved by removing one or more fuel plates from a three-element central region of the reactor and adding plates containing half the normal amount of fuel in such a way as to leave the total amount of fuel in the core and the biaxial symmetry of the reactor unchanged. In general, two-dimensional diffusion-theory calculations of the expected reactivity changes made with the PDQ-2 code were in poor agreement with the measurements. Furthermore, in calculations corresponding to a series of measurements in which the fuel had been effectively moved toward a fuel-free region having the dimensions of a control-rod well, the sign of the reactivity effect was incorrect. A one-dimensional check calculation with the DSN transport-theory code revealed that the relative flux rise in a water space and the flux depression in the compensating region of increased fuel density had been underestimated by a factor of more than 3 in the diffusion-theory calculation, if it is assumed that the thermal flux shape calculated by the transport-theory method is correct. It was tentatively concluded that the poor agreement was due to the basic inadequacy (not unexpected) of diffusion theory to handle correctly the type of small-volume, large cross-section perturbation produced by the conditions of this experiment.

Since no adequate transport-theory reactor code was available to check this preliminary proposition by further calculations, it was decided to perform a critical experiment whose configuration would be simple enough to be described successfully by available codes and yet would allow the type of perturbations encountered in the first phase of the project. The design requirements for this experiment were the following:

1. The geometry should be essentially "one-dimensional" so that the DSN code could be directly applied; a slab of large transverse dimensions with no reflection at the slab edges would be desirable so as to minimize problems of computing the transverse leakage.
2. The core should be of the plate type and consist of highly enriched uranium in a U-Al alloy so as to simulate as closely as possible a pool-type reactor. The metal-to-water ratio, water gap, and fuel-plate dimensions also should be as much like the values in the BSR-I as possible, so that results from this experiment could be compared with the initial BSR-I measurements.
3. The critical core (i.e., the number of plates) should be sufficiently thick for the projected perturbations not to be too large.
4. Other factors being equal, the expected differences between diffusion theory and transport theory should be maximized so as to establish clearly the relative accuracies of the two methods.

Parameter Calculations

Fuel for the experiment was found to be available in the form of plates of unclad U-Al alloy, each 2.95 in. wide, 72 in. long, and 0.058 in. thick. The plates contain 10.5 wt % uranium, which amounts to 58.6 g of U^{235} per plate or 0.043 g of U^{235} per square centimeter of fuel plate. The BSR-I fuel plates contain 0.018 g of U^{235} per square centimeter, but there is additional aluminum in the frame of the fuel plates and in the side plates.

Figure 2.11.1 shows the uranium volume concentration and the metal-to-water ratio as a function of plate spacing for the proposed core, with the values at the BSR-I plate spacing given for comparison. It is to be noted that, owing to the side plates and other structure, the BSR-I has a higher metal-to-water ratio at the same plate spacing and the center-to-center spacing in the proposed core would have to be 135 mils to equal the metal-to-water ratio of the BSR-I; however, with the lower fuel loading in the BSR-I plates, the plate spacing required to give the same *uranium concentration* in the proposed core would be about 390 mils. Obviously, some compromise between these limits was required.

[2]E. G. Silver *et al.*, *Nuclear Safety Program Semiann. Progr. Rept. June 30, 1962*, ORNL-3319, pp 5–10.

[3]E. G. Silver, *Nuclear Safety Program Semiann. Progr. Rept. June 30, 1963*, ORNL-3483, p 3.

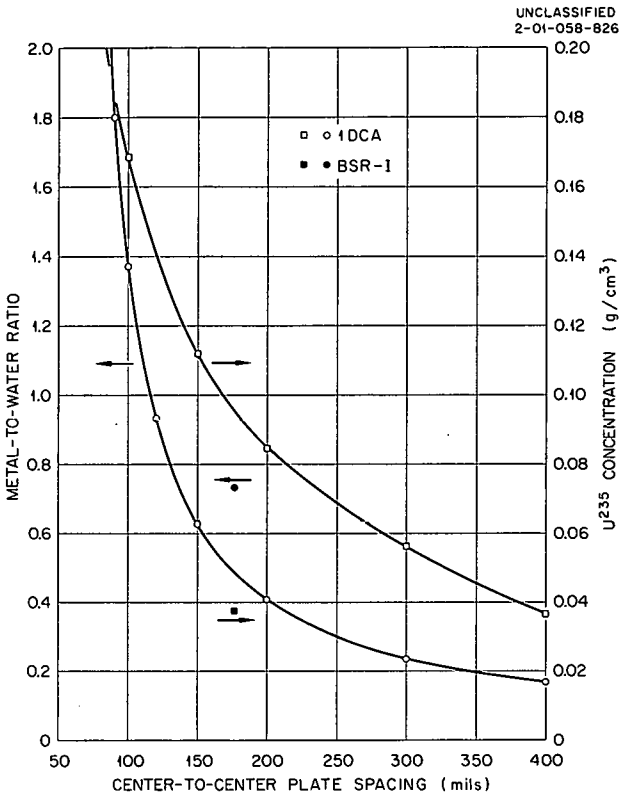

Fig. 2.11.1. Effect of U-Al Plate Spacing on Metal-to-Water Ratio and on Volume Concentration of U^{235}. Corresponding values for BSR-I shown for comparison.

Initially it was intended to use the plates in their full length (72 in.) and to combine them into "elements," each element consisting of 10 edge-joined plates which would give transverse core dimensions of 72 by 29.5 in. However, diffusion-theory (MODRIC code) calculations on a homogenized model of such a core indicated that the resulting critical slab would be extremely thin, ranging from 4.05 in. (20.3 elements thick) at a 200-mil spacing to 5.54 in. (13.8 elements thick) at a 400-mil spacing and that perturbations planned for the experiment would result in very large reactivity changes since one element would represent 5 to 7.5% of the total fuel inventory. In addition, the 72-in.-long plates would be difficult to support rigidly enough to maintain uniform spacing, and the great excess of length over width of the core would be uneconomical in terms of total fuel inventory. Therefore, it was decided to cut a number of fuel plates into 2-ft lengths.

Figure 2.11.2 shows the critical core thickness as a function of spacing of the 2-ft-long plates for various core widths, ranging from 10 plates per element (29.5 in. wide) to 4 plates per element (11.8 in. wide). On the same figure the number of elements making up each core is also shown. In all cases an increase in plate spacing increases the slab thickness but decreases the number of fuel plates in the slab. Increasing the spacing would also decrease the expected difference between diffusion and transport theory calculations. A spacing of 200 mils was therefore chosen to maximize the number of fuel plates.

It would appear that for a given spacing the core thickness, and thus the number of fuel elements in the core, could be materially increased by narrowing the fuel element to about 1 ft instead of 2 ft (four plates instead of eight). However, a serious calculational difficulty, described below, arises with such a small unreflected transverse dimension.

All the calculations discussed above were for homogenized core models. When elements were described explicitly as separate regions in later calculations, it developed that, because of the change in the calculated transverse leakage due to the metal plates, the critical thickness was strongly dependent on the number of elements explicitly specified and on the method of calculating transverse leakage. Two ways of doing the latter were available with the MODRIC code. One was to let the code calculate the diffusion length for each region and each energy and then to hand calculate the extrapolation distance from these diffusion lengths for each energy group and region. (Each fuel plate and each water gap, as well as the homogeneous portion of the core, would be a region). The other method was to let the code calculate a flux-weighted energy-and-region-averaged diffusion constant and to use this to obtain a single fixed extrapolation distance which would apply to all energy groups and regions.

Both methods were used to obtain the results presented in Fig. 2.11.3, which shows the effect on the calculated critical slab thickness of varying the number of explicitly described fuel plates for transverse dimensions of 2 by 2 ft and of 2 by 1 ft. (Note that the two sets of curves have the same ordinate scale but different suppressed zeros.) The code allows only 20 regions, which limits the calculations to 17 plates ($8\frac{1}{2}$ for each core half); however, a parameter-search calculation was performed to find a fictitious homogeneous

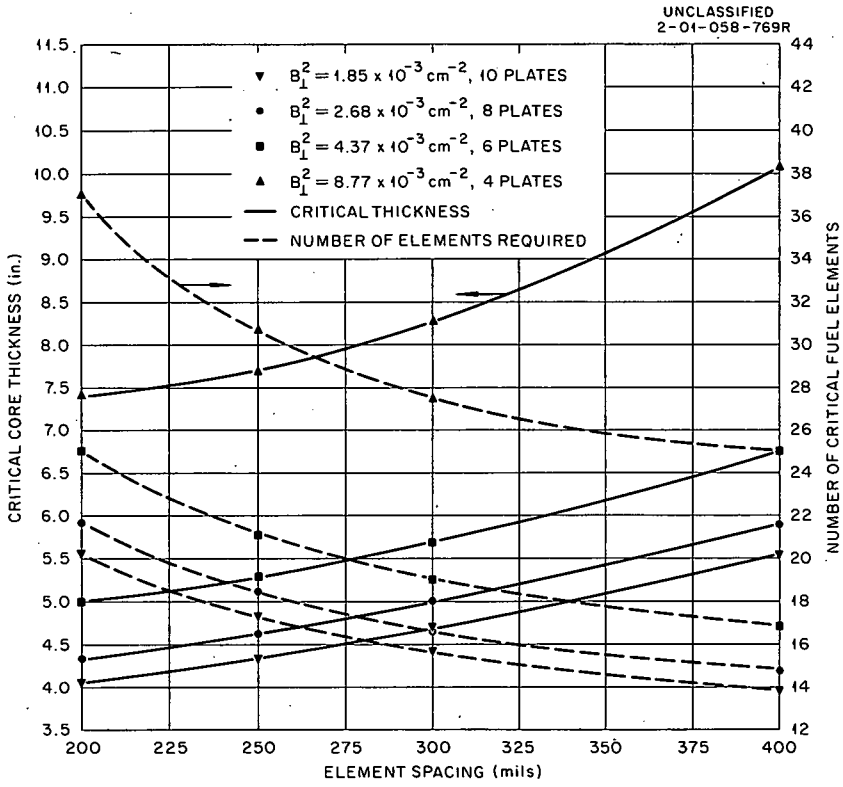

Fig. 2.11.2. Effect of Element Spacing on Critical Core Thickness and on Critical Number of Fuel Elements for Various Transverse Core Dimensions.

core composition which would have the same reactivity effect as a region of the same thickness made up of explicitly specified plates and water spaces. In this way the explicit-plate calculation could be extended to the entire slab thickness. It will be observed from Fig. 2.11.3 that when transverse dimensions of 2 by 1 ft are used the critical thickness increases sharply as the number of explicitly specified plates is increased (and the homogeneous region correspondingly decreased), and also that there is a greater difference between the two calculational methods. These variations are reduced drastically when the 2 by 2 ft dimensions are used; therefore the dimensions selected for the proposed core are 24 by 23.6 in.

A number of calculations were then performed for the final design parameters, with explicitly described plates assumed to be in different regions of the core and the rest of the core composed of homogenized material adjusted in fuel content so as to give the same reactivity effect as explicitly specified plates (when used in the region occupied by the inner 17 fuel plates). Figure 2.11.4 shows the results of these calculations. (Note: There is only a 4.5% variation in the critical thickness due to the different core models shown.) Table 2.11.1 gives the parameters for the one-dimensional critical assembly (1DCA) core as finally designed.

Figure 2.11.5 shows the calculated thermal flux in the 1DCA core with 17 explicitly described central plates. It is to be noted that there is a large flux peak in the reflector due to the reflector-moderated nature of the assembly (the core is strongly undermoderated).

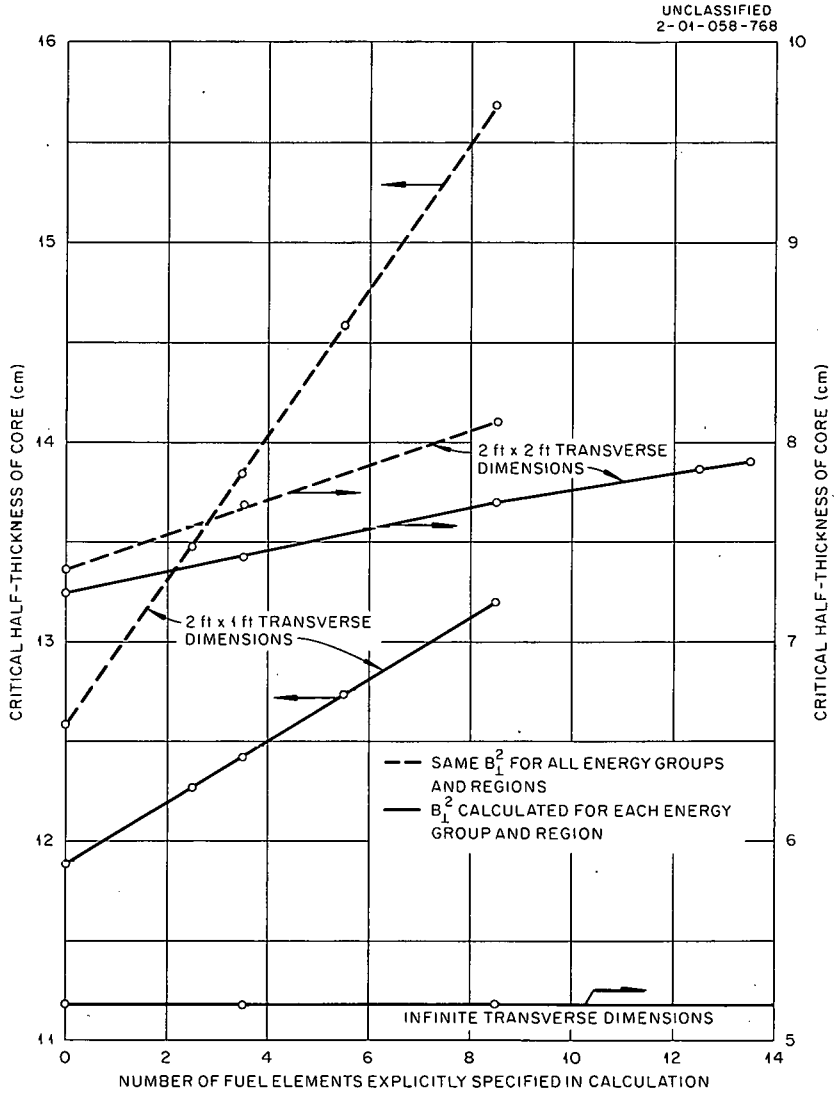

Fig. 2.11.3. Effect of the Number of Plates Explicitly Specified in the Calculation on the Core Thickness for Two Different Sets of Transverse Dimensions and Two Models of Transverse Leakage. (Note that the ordinate scale is the same for all curves but that the suppressed zero values differ.)

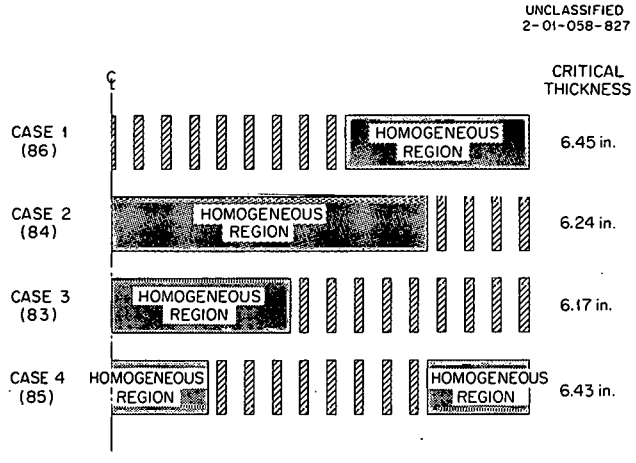

Fig. 2.11.4. Schematic Diagram Showing the Dependence of the Location of Explicitly Specified Plates in Diffusion-Theory Calculations on the Critical-Core Thickness of 1DCA. (The homogeneous regions in all these calculations have been modified so as to yield the same multiplication as a plate region of the same thickness at the core center.)

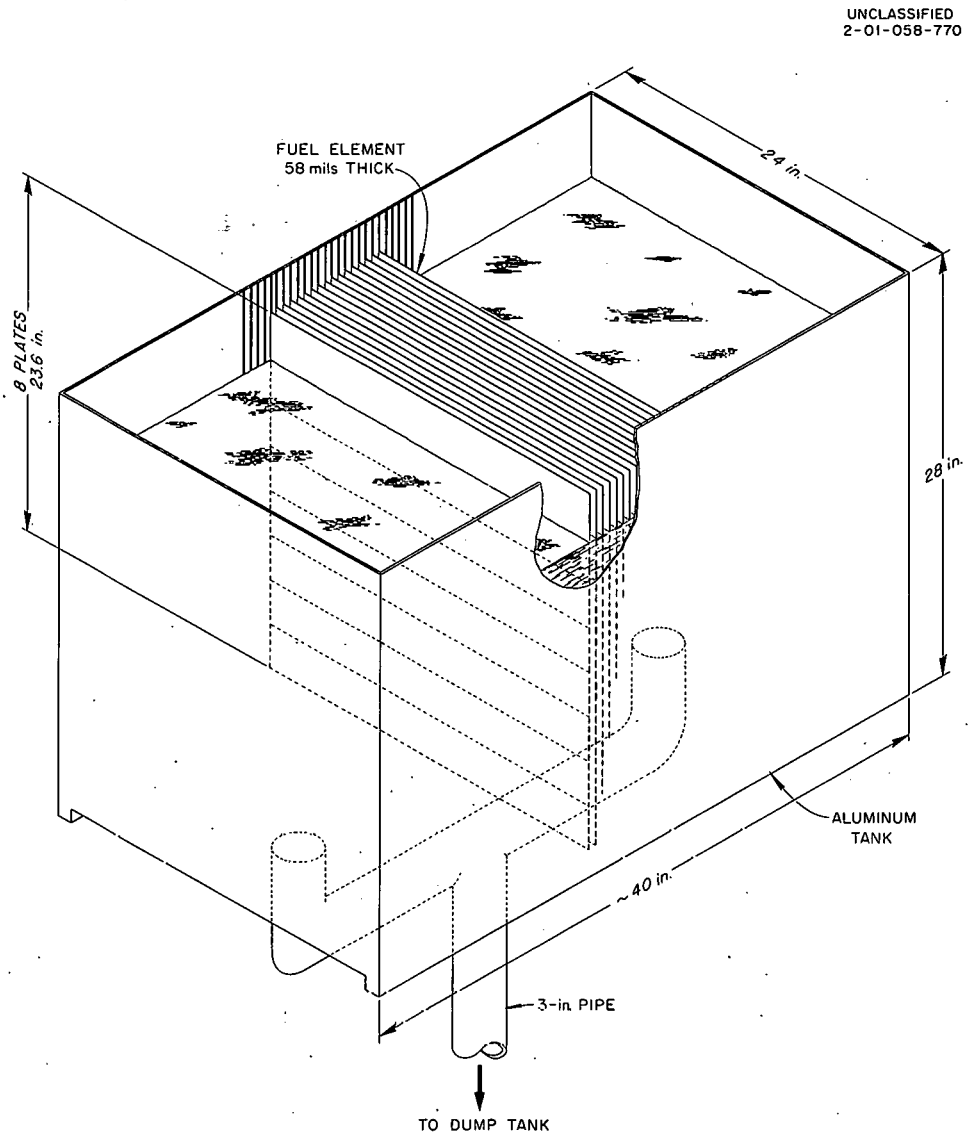

Fig. 2.11.5. Diagram of the Experimental Arrangement of 1DCA. The interplate spacing-control strips of aluminum are not shown.

Table 2.11.1. Description of 1DCA Critical Experiment

Composition	
Fuel	U-Al alloy (93% U^{235}); 10.5 wt % U
Cladding	None
Moderator	H_2O, room temperature
Reflector	H_2O, room temperature
Dimensions	
Fuel plates	2.95 by 24 by 0.058 in.
Fuel element	23.6 by 24 by 0.058 in. (8 plates)
Element spacing	0.200 in. center to center (0.142-in. H_2O space)
Slab thickness	~6.3 in., based on MODRIC calculations
Reflector thickness	>6 in. on 24 by 23.6 in. surfaces
Nuclear Data	
U^{235} concentration	2.16×10^{20} atoms/cm^3
Hydrogen concentration	4.75×10^{22} atoms/cm^3
Aluminum concentration	1.72×10^{22} atoms/cm^3
Metal-to-water ratio	0.41

Experimental Setup

The experimental work with the 1DCA core will be performed at the Critical Experiments Facility in the core tank constructed as shown in Fig. 2.11.6. The slots in the central core region are spaced at 100-mil intervals so that fuel can be added between normally spaced fuel plates. An equal water level is maintained between the fuel plates by means of a small flow channel along the bottom of each long side of the core tank.

Two aluminum strips, about 0.5 in. wide and of the thickness of the water gap, will be inserted into each water space between the fuel elements. The strips will be spaced so as to divide the free span of the fuel plates into three equal segments, thus diminishing the possibility of errors in fuel-plate locations to an acceptable level.

The first experiment with the 1DCA core will be to establish the critical thickness of an unperturbed fuel slab with all elements spaced 200 mils center-to-center and with the water height essentially level with the top of the fuel elements. If necessary, aluminum plates will be used in the outermost elements. The reactivity effect of small changes in the water height will be determined.

Once the critical thickness of the unperturbed core is known, perturbed configurations will be loaded, including cores with fuel moved toward and away from the core center.

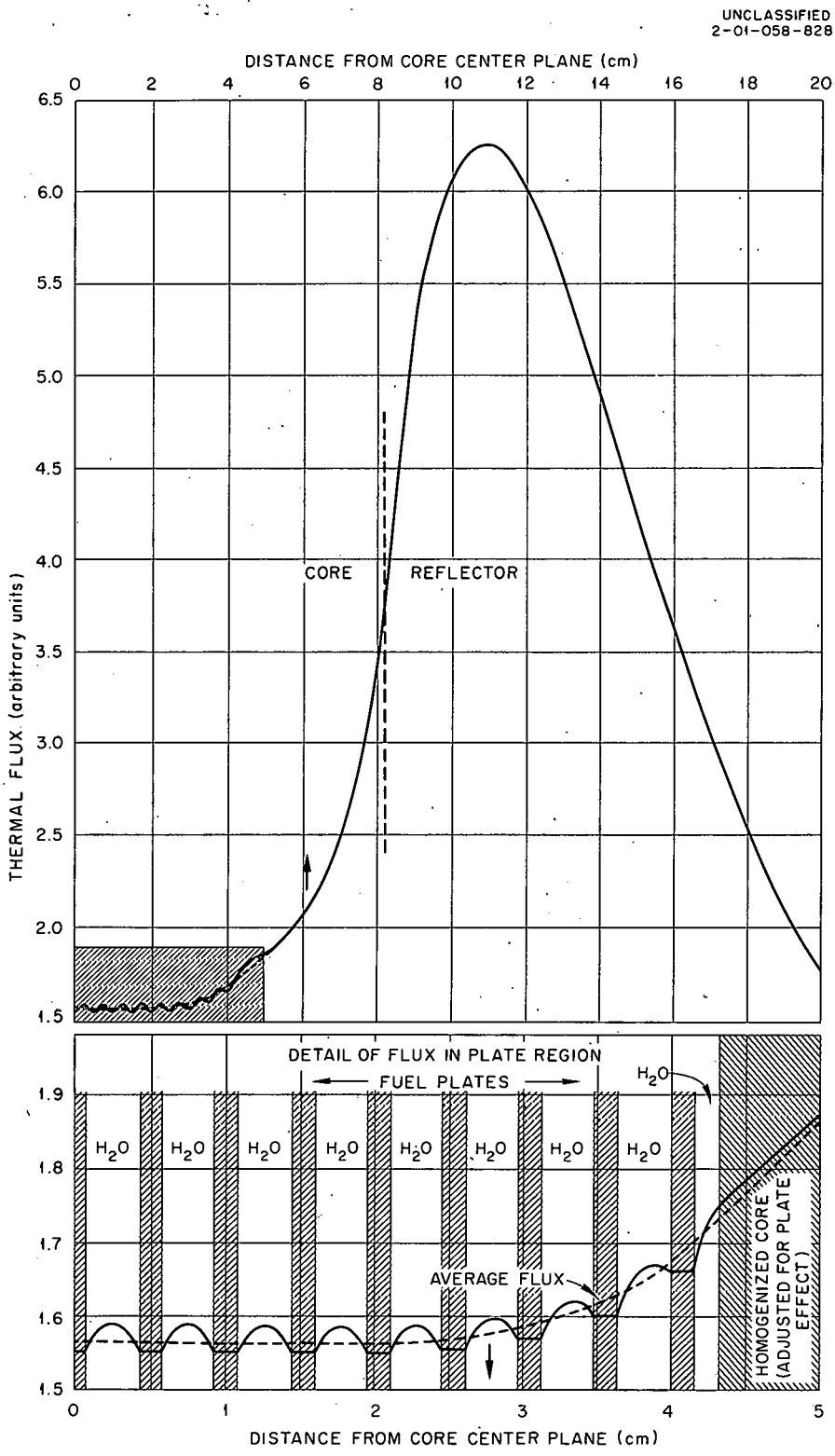

Fig. 2.11.6. Calculated Thermal-Neutron Flux (Diffusion Theory) for Unperturbed 1DCA Core with 17 Explicitly Specified Fuel Plates in Core Center and a Homogenized Region Modified to Same Reactivity Worth as Plate Region.

2.12. APPLICATION OF MONTE CARLO CALCULATIONAL TECHNIQUES TO THE STUDY OF FAST CRITICAL ASSEMBLIES

W. E. Kinney, J. T. Mihalczo, and I. Happer

The Monte Carlo calculational method has been widely applied to many neutron physics problems,[1] but, because of high computing costs and the lack of adequate cross-section data, seldom to criticality studies. Still, it represents the only means for calculating complex assemblies such as those described in Sec. 2.5, and, with more detailed microscopic data becoming available and with the cost per computing operation decreasing, it seems reasonable that the method should be developed as a routine calculational tool to predict the properties of critical assemblies. As a first step in this direction, Monte Carlo calculations have been performed for several simple unmoderated, unreflected uranium metal assemblies which had been made critical experimentally.

The computer code used for the calculations was the 05R code,[2] a general-purpose Monte Carlo

[1] R. Kraft and C. J. Wensrich, *Monte Carlo Methods. A Bibliography Covering the Period 1949 to June 1961*, UCRL-6581 (Sept. 11, 1961).

[2] R. R. Coveyou, J. G. Sullivan, and H. P. Carter, *The 05R Code: A General Purpose Monte Carlo Reactor Code for the IBM-704 Computer*, a paper presented at the Symposium on Codes for Reactor Computations, Vienna, 1961; see also *Neutron Phys. Div. Ann. Progr. Rept. Sept. 1, 1958*, ORNL-2609, p 87.

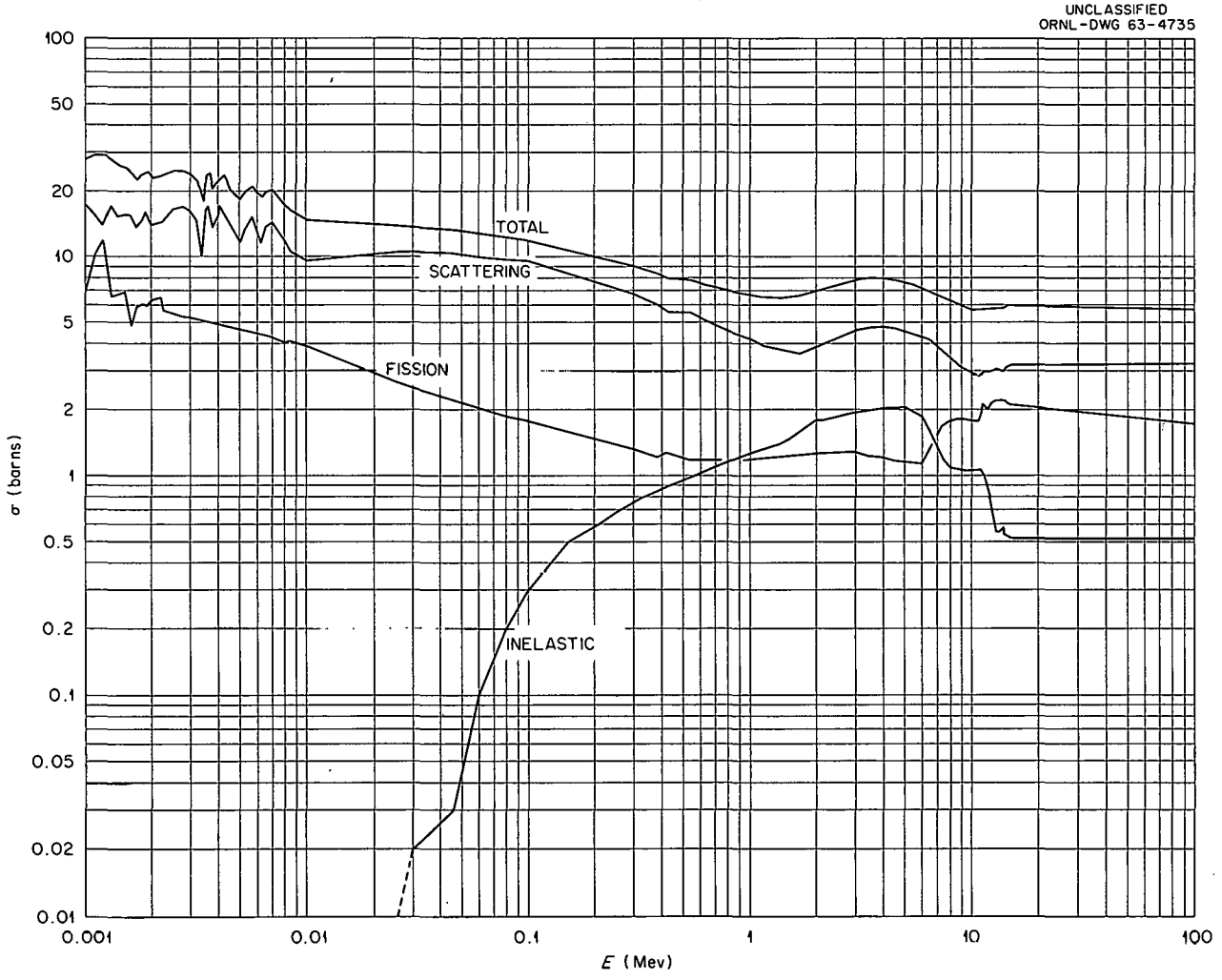

Fig. 2.12.1. U^{235} Total, Scattering, Fission, and Nonelastic Cross Sections.

neutron transport code. Only highly U^{235}-enriched uranium systems were considered, and they were assumed to contain U^{235} and U^{238} only. Cross-section values from BNL-325[3] were used where possible, with Howerton's compilation[4] serving as a basis for separating the scattering and inelastic cross sections. The resulting cross sections are shown in Figs. 2.12.1 and 2.12.2. The angular distributions from BNL-400[5] were used to obtain the Legendre expansion coefficients f_1 through f_8 shown in Table 2.12.1. The angular distributions for U^{238} and U^{235} were taken to be identical. Inelastic scattering was treated with evaporation theory,[6] and the variation of ν with energy was taken to be $\nu(E) = 2.43 + 0.115E$ (Mev).

The systems considered were a 17.42-cm-diam sphere corresponding to the Godiva I Reactor,[7] a 12.7 by 12.7 by 23.15 cm parallelepiped, and 17.77-, 27.93-, and 38.08-cm-OD cylinders whose heights were approximately 12.6, 8.7, and 7.6 cm,

[3]D. J. Hughes and R. B. Schwartz, *Neutron Cross Sections*, 2d ed., BNL-325 (July 1, 1958).

[4]R. J. Howerton, *Semi-Empirical Neutron Cross Sections*, part II, vol. I, UCRL-5351 (Nov. 1958).

[5]M. D. Goldberg, V. M. May, and J. R. Stehn, *Angular Distributions in Neutron Induced Reactions*, BNL-400, vol. II, 2d ed. (October 1962).

[6]A. M. Weinberg and E. P. Wigner, *The Physical Theory of Neutron Chain Reactors*, p 103, University of Chicago Press, 1958.

[7]R. E. Peterson and G. A. Newby, *Nucl. Sci. Eng.* 1, 112–125 (1956).

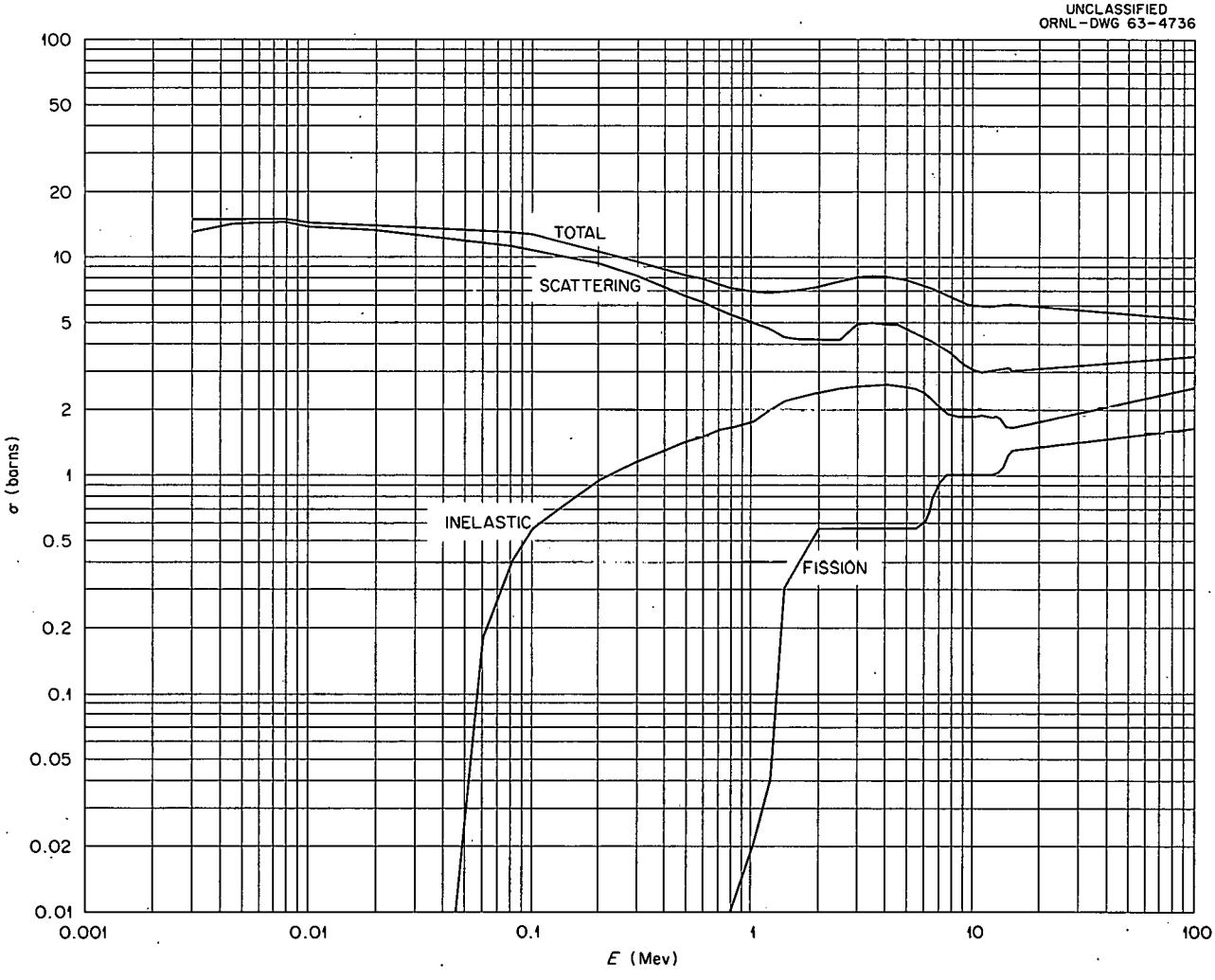

Fig. 2.12.2. U^{238} Total, Scattering, and Fission Cross Sections.

Table 2.12.1. Legendre Expansion Coefficients

Energy (ev)	f_1	f_2	f_3	f_4	f_5	f_6	f_7	f_8
1.00×10^8	8.73×10^{-1}	7.52×10^{-1}	6.37×10^{-1}	5.36×10^{-1}	4.54×10^{-1}	3.83×10^{-1}	3.22×10^{-1}	2.68×10^{-1}
1.50×10^7	8.73×10^{-1}	7.52×10^{-1}	6.37×10^{-1}	5.36×10^{-1}	4.54×10^{-1}	3.83×10^{-1}	3.22×10^{-1}	2.68×10^{-1}
7.00×10^6	7.85×10^{-1}	6.51×10^{-1}	5.55×10^{-1}	4.55×10^{-1}	3.47×10^{-1}	2.34×10^{-1}	1.52×10^{-1}	9.58×10^{-2}
2.80×10^6	7.60×10^{-1}	6.15×10^{-1}	4.86×10^{-1}	3.90×10^{-1}	2.60×10^{-1}	1.48×10^{-1}	8.14×10^{-2}	4.32×10^{-2}
2.50×10^6	6.53×10^{-1}	4.94×10^{-1}	3.50×10^{-1}	2.61×10^{-1}	1.36×10^{-1}	4.28×10^{-2}	1.96×10^{-3}	-6.35×10^{-3}
2.00×10^6	5.37×10^{-1}	3.58×10^{-1}	2.99×10^{-1}	2.01×10^{-1}	7.55×10^{-2}	2.52×10^{-2}	4.90×10^{-3}	-4.20×10^{-3}
1.25×10^6	5.37×10^{-1}	3.90×10^{-1}	2.59×10^{-1}	1.33×10^{-1}	6.83×10^{-2}	3.52×10^{-2}	1.47×10^{-2}	4.31×10^{-3}
1.17×10^6	5.13×10^{-1}	3.24×10^{-1}	1.51×10^{-1}	5.03×10^{-2}	1.69×10^{-2}	6.89×10^{-3}	2.89×10^{-3}	2.51×10^{-3}
1.10×10^6	4.85×10^{-1}	3.30×10^{-1}	2.03×10^{-1}	8.72×10^{-2}	3.07×10^{-2}	1.34×10^{-2}	5.48×10^{-3}	-1.08×10^{-3}
1.00×10^6	4.12×10^{-1}	2.16×10^{-1}	1.79×10^{-1}	6.25×10^{-2}	8.84×10^{-3}	2.92×10^{-3}	4.26×10^{-3}	3.35×10^{-4}
9.50×10^5	4.34×10^{-1}	2.60×10^{-1}	1.12×10^{-1}	3.63×10^{-2}	3.39×10^{-3}	-2.63×10^{-3}	-3.11×10^{-4}	8.22×10^{-4}
7.70×10^5	4.19×10^{-1}	2.16×10^{-1}	8.10×10^{-2}	2.10×10^{-2}	4.96×10^{-3}	2.07×10^{-3}	-2.69×10^{-4}	-1.93×10^{-3}
7.20×10^5	3.79×10^{-1}	1.88×10^{-1}	6.65×10^{-2}	1.22×10^{-2}	-3.42×10^{-3}	-2.08×10^{-3}	5.28×10^{-4}	7.24×10^{-4}
6.50×10^5	3.94×10^{-1}	1.88×10^{-1}	6.29×10^{-2}	1.26×10^{-2}	3.59×10^{-3}	1.94×10^{-3}	-8.64×10^{-4}	-1.87×10^{-3}
6.00×10^5	3.44×10^{-1}	1.75×10^{-1}	3.69×10^{-2}	5.44×10^{-3}	-5.00×10^{-3}	-3.17×10^{-3}	-6.72×10^{-4}	1.16×10^{-3}
5.50×10^5	3.38×10^{-1}	1.41×10^{-1}	4.79×10^{-2}	1.43×10^{-2}	1.95×10^{-3}	-4.00×10^{-4}	-5.06×10^{-4}	-2.99×10^{-5}
5.00×10^5	3.48×10^{-1}	1.34×10^{-1}	5.13×10^{-2}	1.88×10^{-2}	5.05×10^{-3}	-2.21×10^{-3}	-3.12×10^{-3}	-7.60×10^{-4}
4.15×10^5	2.60×10^{-1}	8.06×10^{-2}	1.76×10^{-2}	2.07×10^{-3}	-1.68×10^{-3}	-1.28×10^{-3}	-1.76×10^{-4}	4.38×10^{-4}
3.50×10^5	2.36×10^{-1}	7.10×10^{-2}	1.78×10^{-2}	4.14×10^{-3}	-1.11×10^{-3}	-2.28×10^{-3}	-1.63×10^{-3}	6.74×10^{-4}
2.00×10^5	1.50×10^{-1}							
1.00×10^5	7.20×10^{-2}							
6.00×10^4	3.30×10^{-2}							
1.00×10^4	2.80×10^{-3}							
1.00×10^{-4}	2.80×10^{-3}							

respectively (see Table 2.12.2). In each case the isotopic composition of the system was assumed to be 4.508×10^{22} U^{235} nuclei per cubic centimeter and 2.942×10^{21} U^{238} nuclei per cubic centimeter.

The results of the calculations are given in Table 2.12.3, where "order of expansion" means the highest order Legendre expansion coefficient which was used to describe the angular distribution of elastically scattered neutrons. As was hoped, there is agreement among the values of multiplication constants for the various assemblies, and, as was anticipated, the constants are not equal to unity. The effect of the anisotropic elastic scattering angular distribution can be seen by comparing the multiplication constants obtained from calculations using an eight-order and a first-order expansion and, for the sphere, amounts to 9%.

A computed Godiva leakage spectrum is compared with an experimental spectrum[8] in Fig. 2.12.3 and is seen to be in good agreement above 1 Mev but to be low for energies below 1 Mev.

[8] L. Stewart, *Nucl. Sci. Eng.* **8**, 595–597 (1960).

The calculations are continuing, with the microscopic cross sections being varied within their experimental errors to determine the effect on the multiplication constant.

Table 2.12.2. Cylindrical Systems Considered in Monte Carlo Calculations of Multiplication Constants

Cylinder Diameter (cm)	Regions Used in Calculation	
	Radial Segments (cm)	Height (cm)
17.77		12.626
27.93	0–8.89	8.577
	8.89–11.43	8.743
	11.43–13.96	8.748
38.08	0–8.89	7.636
	8.89–11.43	7.790
	11.43–13.97	7.795
	13.97–16.51	7.641
	16.51–19.04	7.630

Table 2.12.3. Calculated Multiplication Constants for Various Uranium Metal Systems

Assembly	Order of Expansion	Number of Iterations	Multiplication Constant
Sphere (Godiva I)	8	15	1.037 ± 0.010
		15	1.027 ± 0.011
		15	1.038 ± 0.009
		50	1.038 ± 0.005
			Average 1.036 ± 0.005
	1	25	1.128 ± 0.007
Parallelepiped	8	10	1.030 ± 0.017
		15	1.056 ± 0.012
		15	1.026 ± 0.011
			Average 1.038 ± 0.008
	1	10	1.118 ± 0.010
Cylinder No. 1	8	10	1.057 ± 0.011
		50	1.041 ± 0.005
			Average 1.046 ± 0.006
	1	10	1.113 ± 0.011
Cylinder No. 2	8	10	1.042 ± 0.009
	1	10	1.110 ± 0.008
Cylinder No. 3	8	10	1.048 ± 0.016
	1	10	1.114 ± 0.010

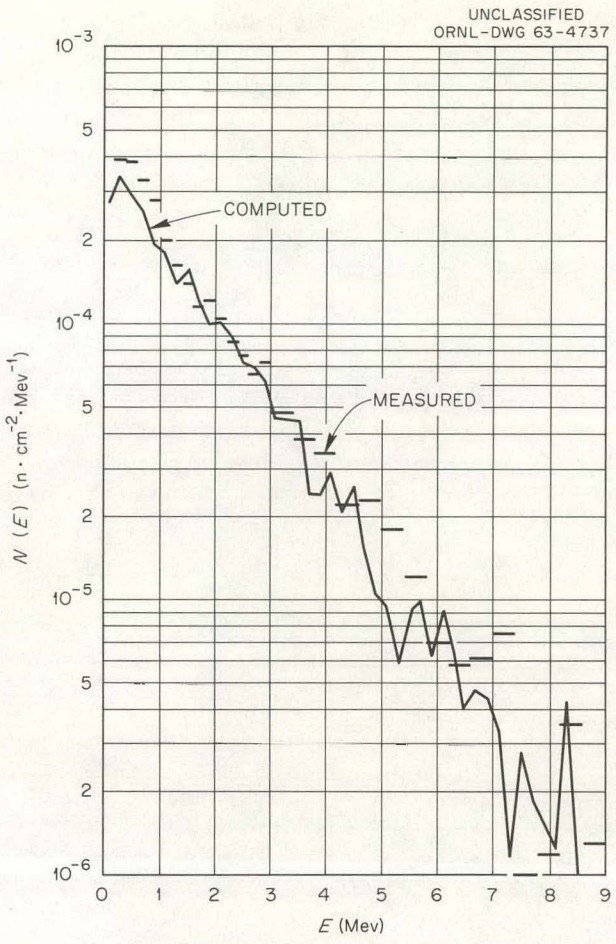

Fig. 2.12.3. Comparison of Calculated and Measured Godiva Leakage Spectra.

2.13. REACTIVITY EFFECTS OF VARIOUS REFLECTORS NEAR THE HEALTH PHYSICS RESEARCH REACTOR

L. W. Gilley

The reactivity effects of several Plexiglas reflectors on the Health Physics Research Reactor (HPRR),[1] an unreflected and unmoderated right cylindrical core of 90 wt % U(93.2)–10 wt % Mo, have been measured in order to obtain a basis for predicting the effects of proposed experiments at the Dosimetry Applications Research (DOSAR) Facility. Since the reactor core will usually be operated inside an aluminum safety cage and at times with a stainless steel crash plate suspended below the core, determinations of the worths of

[1]Critical experiments with the HPRR, both at zero power and under superprompt-critical conditions, have been reported previously: J. T. Mihalczo, *Neutron Phys. Div. Ann. Progr. Rept. Sept. 1, 1962*, ORNL-3360, p 41; J. T. Mihalczo, *Reactivity Calibrations and Fission-Rate Distributions in an Unmoderated, Unreflected Uranium-Molybdenum Alloy Research Reactor*, ORNL TM-189 (May 1962); W. E. Kinney and J. T. Mihalczo, *Oak Ridge National Laboratory Fast Burst Reactor Critical Experiments and Calculations*, ORNL CF-61-8-71 (August 1962); and J. T. Mihalczo, *Super-Prompt-Critical Behavior of an Unmoderated, Unreflected Uranium-Molybdenum Alloy Assembly*, ORNL TM-230 (May 10, 1962).

the safety cage and crash plate were included. The effects of the reactor building floor and of a reactor storage pit as a function of the core position were also measured.

Effect of Safety Cage and Crash Plate

The safety cage is designed to surround the HPRR core so that experimental apparatus will be prevented from approaching the core any closer than about $\frac{3}{4}$ in. The cage is fabricated from perforated aluminum (62% voids) and surrounds the reactor core as shown in Fig. 2.13.1. The crash plate, which will protect the core in the event it is dropped, is a 2.5-cm-thick stainless steel plate supported 32 cm below the bottom edge of the core by three supporting legs as shown in Fig. 2.13.2. The reactivity worth of the safety cage, measured with calibrated control rods with the reactor 3 m above the floor, was found to be 26 cents, while that of the crash plate plus its three support legs is 20 cents.

Reactivity Effect of Floor

The reactivity contribution of the floor of the reactor building to the HPRR core was measured as a function of the distance of the core above the floor, again with the 3-m height used as a reference point. In these measurements the steel

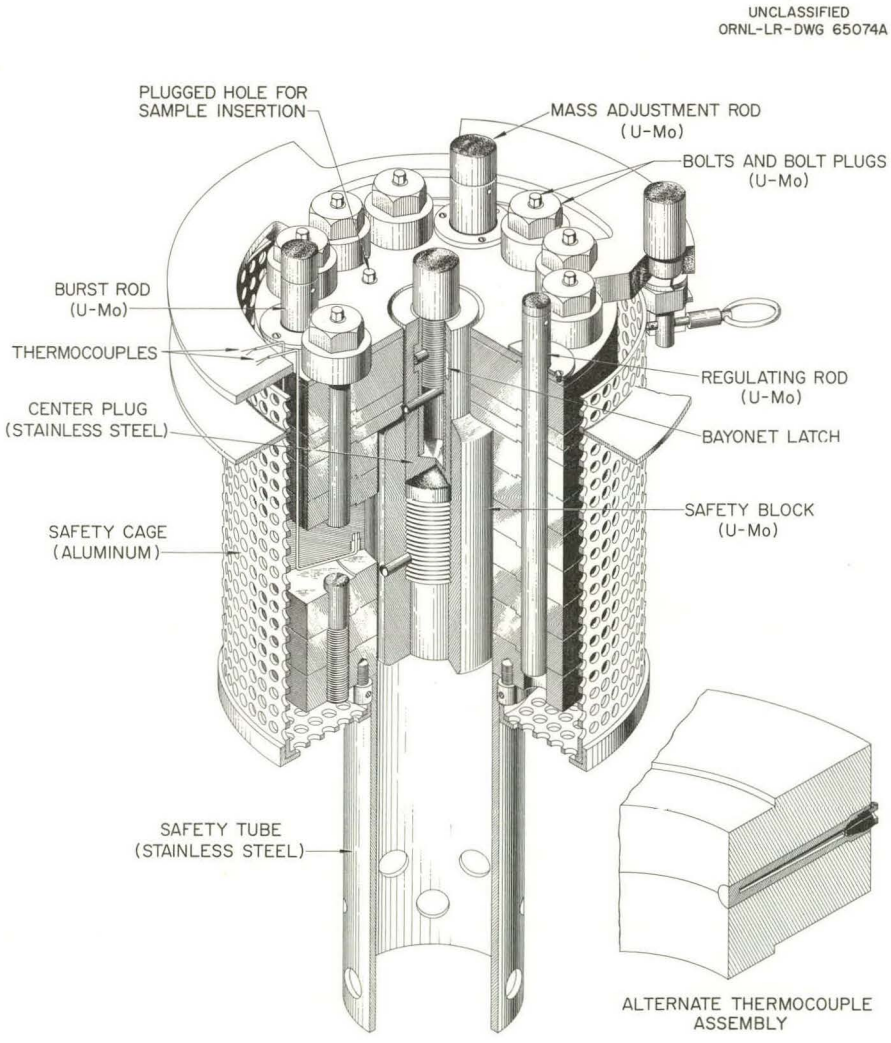

Fig. 2.13.1. Health Physics Research Reactor Core.

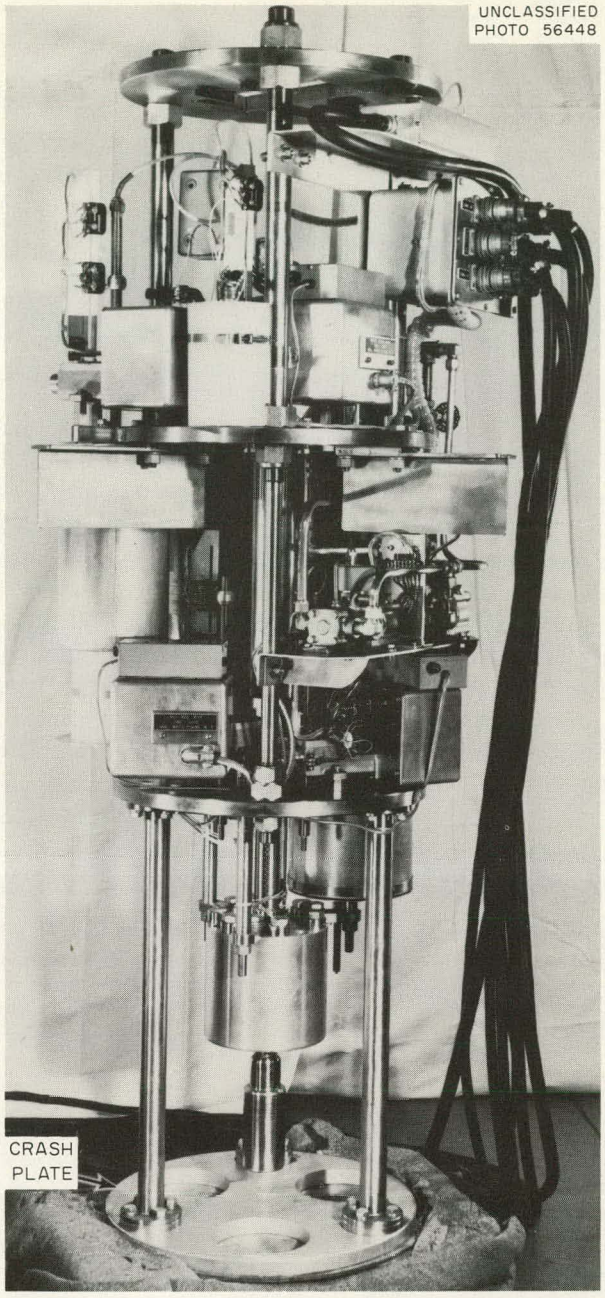

Fig. 2.13.2. HPRR Support Structure Shown with Dummy Core Crash Plate Below Core.

crash plate was absent, and the aluminum safety cage and stainless steel safety tube (see Fig. 2.13.1) were present. The results of these measurements are shown in Fig. 2.13.3. These data were obtained with the reactor positioned directly over one of the two storage pits and with the pit door closed. Each pit door is fabricated from steel plate, 7 ft 1 in. by 6 ft 4 in. by 7 in. thick. Since the remainder of the floor is a 6-in.-thick concrete slab, the reactivity effect when concrete is the principal reflector was compared with the effect when steel is the principal reflector for a reactor height of 36 cm. The difference in reactivity was too small to measure.

Reactivity Effect of Storage Pit

The two storage pits in the HPRR building are concrete-lined and have approximate dimensions of 5 by 5 by 7 ft deep. The reactivity effect of lowering the reactor to its normal storage position in a pit, with the safety cage, safety tube, and crash plate attached and the pit door open, was measured. The results are given in Fig. 2.13.4. The lowest position that the reactor can reach in the pit is −176 cm, at which position the worth of the pit, obtained by extrapolation of the experimental data, is 183 cents. The lowest measured position was at −174 cm, at which point the worth of the pit is 181 cents. Again the reference reactor position was a 3-m height above the floor.

Reactivity Effects of Plexiglas Reflectors

In the first group of measurements to determine the reactivity effects of various Plexiglas reflectors, 20 pieces of Plexiglas, each 25.4 cm high by 29.2 cm wide by 2.54 cm thick, were arranged in two rows, one immediately above the

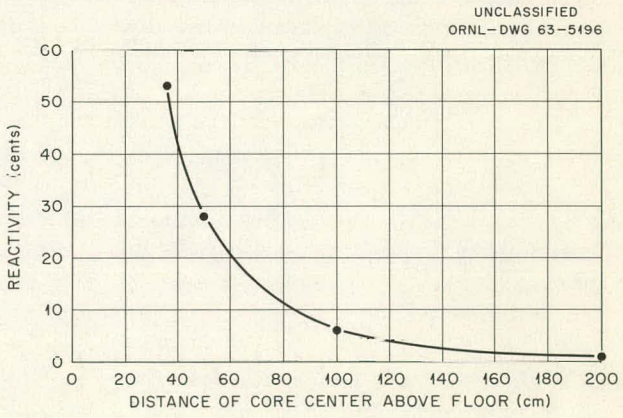

Fig. 2.13.3. Reactivity of HPRR Core as a Function of Distance Above Floor.

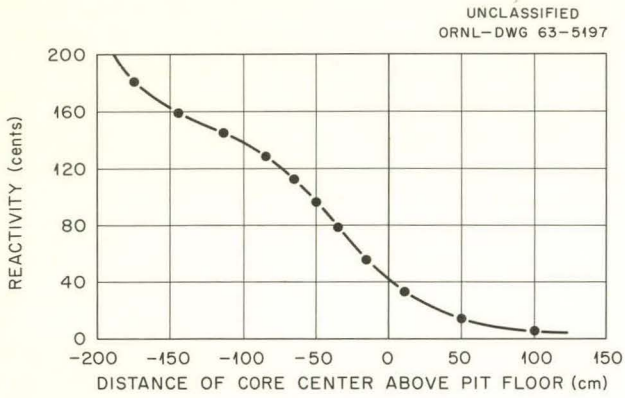

Fig. 2.13.4. Reactivity of HPRR Core as a Function of Position in Storage Pit.

other, on an arc of 1-m radius from the center of the core. Thus, there was essentially one row of ten reflectors 50.8 cm high, each reflector being spaced about 5 cm from its neighbor. The reactor core and reflectors were positioned vertically so that the center of the core and the center of each 50.8-cm-high reflector were at the same level (1.86 m above the floor). The reflectors were oriented so as to be perpendicular to a radius vector from the center of the core to the center of the reflector, giving a near-surface area of 14,834 cm^2 at essentially 1 m. The worth of these 20 reflectors was measured to be 3.7 cents.

The worth of 30 of the Plexiglas pieces positioned on a 205-cm radius arc was also measured. Eighteen of the reflectors were positioned vertically so that their centers were at the same level as the center of the core (2 m above the floor) and each was spaced about 5 cm from its neighbor. The remaining 12 reflectors were positioned on top of the center 12 of the original 18. The worth of this array is about 1 cent.

A further investigation of the effects of reflectors on the HPRR core was made by measuring the worth of several Plexiglas reflectors as a function of distance from the center of the core. The most extensive data were obtained with a reflector having a near-surface area of 2970 cm^2 and a thickness of 5.1 cm. This reflector was composed of eight of the Plexiglas pieces described above supported on an aluminum framework so that the center of the reflector was at the same level as the center of the core (2.06 m above the floor) and the surface was perpendicular to a radius vector from the center of the core. The results of these experiments are given as curve ρ_1 in Fig. 2.13.5. The reactivities of other Plexiglas reflectors having the same area and orientation as described above but having thicknesses of 2.54 and 7.6 cm are plotted in Fig. 2.13.5 as curves ρ_3 and ρ_4, respectively. A similar reflector having an area of 4450 cm^2 and a thickness of 5.1 cm was evaluated at three positions as follows:

150.5 cm	~0
100.0 cm	1.0 cent
39.7 cm	28.0 cents

Because of physical and reactivity limitations, these reflectors could not be moved closer than about 16 cm from the core; therefore estimates of the reactivity worth at positions nearer the core were obtained by comparison of these data to reactivities obtained with a smaller reflector which had previously been evaluated as a function of distance during the original critical experiments for the HPRR core.[1] This latter reflector was a 20.3 by 20.3 by 2.5 cm thick piece of Plexiglas curved to the same radius as the core. The data

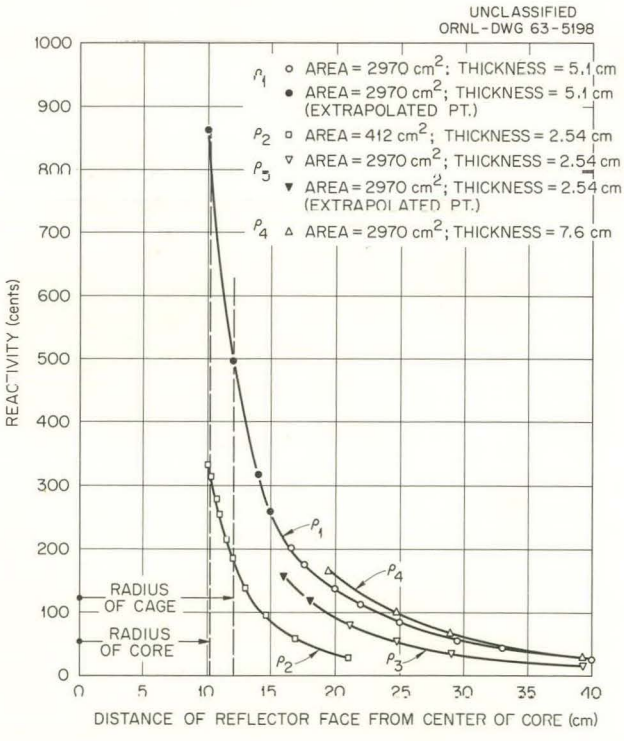

Fig. 2.13.5. Reactivity of HPRR Core as a Function of Plexiglas Reflector Distance from Core.

for this reflector are shown in Fig. 2.13.5 as curve ρ_2.

The procedure used to extrapolate the experimental data of ρ_1 was as follows. The ratio ρ_1/ρ_2 was plotted as a function of distance over the range for which experimental data existed for each curve, as shown in Fig. 2.13.6, and then this curve was extrapolated to 10.15 cm, which is the edge of the core. Estimated values of ρ_1 near the core were obtained from the relation

$$\rho_1(x) = \frac{\rho_1(x)}{\rho_2(x)}\,\rho_2(x)\,,$$

where the value of $\rho_1(x)/\rho_2(x)$ is taken from Fig. 2.13.6 and the value of $\rho_2(x)$ is taken from the experimental curve in Fig. 2.13.5. Extrapolated values of ρ_3 were obtained in a similar manner from the ρ_3/ρ_1 curve included in Fig. 2.13.6. The extrapolated values for both curves are included in Fig. 2.13.5.

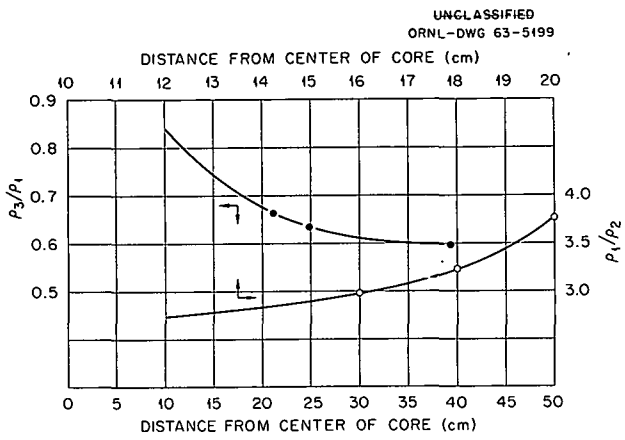

Fig. 2.13.6. ρ_3/ρ_1 and ρ_1/ρ_2 as a Function of Distance from the HPRR Core Center.

2.14. REACTIVITY CHANGES ASSOCIATED WITH RAPID LOCALIZED TEMPERATURE CHANGES IN THE HEALTH PHYSICS RESEARCH REACTOR CORE

D. R. Ward

As part of a continuing program to further define the characteristics of the Health Physics Research Reactor (HPRR) (see Sec. 2.13), a series of experiments was performed to determine whether reactivity changes resulting from a temperature change in a portion of the core could occur before the temperature change is indicated by any of the core thermocouples. The knowledge of such changes is especially important for outside burst operations[1] of the HPRR, since the size of the burst (total number of fissions produced) depends on the total reactivity in the core when the burst rod is inserted, a reactivity increase of 1 cent being worth approximately a 25% increase in the burst size for a burst 1×10^{17} fissions. Since the reactor has a temperature coefficient of reactivity of -0.17 cent/°F, it is conceivable that a sudden flash of sunlight or a cool wind could change the amount of available reactivity. While the effect of heating the core (as by sunlight) would be to decrease the reactivity of the core and thus to decrease the amount of the burst, the effect of cooling the core (as by a cool wind) would be to increase the size of the burst, possibly to the extent that the core would be destroyed. Thus it is necessary that any changes in the core temperature be known from the time that the core reactivity is measured until the burst rod is fired.

Monitoring of the core temperature is effected by five stainless-steel-jacketed iron-constantan thermocouples at various positions in and on

[1]One of the prime uses of the HPRR is to produce short-term (~60-μsec) high-intensity (~50,000-Mw) bursts of fission radiation by the rapid insertion of a fixed amount of fuel (burst rod) into the nonmultiplying core which has a preset amount of reactivity.

the core (see Fig. 2.13.1 in Sec. 2.13). In order to study the adequacy of the thermocouples for detecting localized temperature changes, three experiments were performed. In the first a single heat lamp was used to heat the reactor core, and the responses of the thermocouples were compared with the control-rod adjustments that were required to maintain the reactor at a constant power while the core was heating and also, by turning off the lamp, while the core was cooling. This procedure was repeated in a second experiment, in which three heat lamps were used and the lamp-core separation distance was greater. In the final experiment an equilibrium core temperature was first achieved with heat lamps and the change in temperature was produced by blowing air at ambient temperature over the core.

Two of the HPRR thermocouples (Nos. 1 and 2) are silver-soldered into brass plugs that screw into fuel disks at locations near the center of the core where the fission density is 7 and 15%, respectivity, below the peak fission density; they have a recorder range of 800°F. Two other thermocouples (Nos. 3 and 4) are located in slots under washers and are pressed against the top surface of the core by U-Mo bolts. The recorder span for thermocouple No. 3 is 0 to 800°F and for thermocouple No. 4 is 0 to 200°F. Thermocouple No. 5, which is held against the lower surface of the core by a heavy ($\sim\frac{1}{4}$ in.) stainless steel guide tube, has a recorder readout of 0 to 200°F.

Experiment 1

In the first experiment a single heat lamp (GE 115 v, 375 w) was placed $\frac{1}{4}$ in. from the surface of the core on the side farthest from the five thermocouples. (The safety cage was removed for these experiments.) The reactor was brought to a level power of about 0.2 w and the heat lamp was then switched on. Repeated adjustments were made to the mass adjustment rod to restore the reactor to level power as the core became warmer, and these rod readings were recorded with relationship to time, as were the readings of the five thermocouples. The heat lamp was switched off after 30 min, but the mass adjustment rod readings and thermocouple readings vs time were recorded for an additional 30 min.

Changes in the mass adjustment rod readings were converted into changes in reactivity by means of the official HPRR plot of control-rod worth vs distance of travel, and temperature changes of each of the five thermocouples were converted into reactivity changes by means of the 0.17 cent/°F relationship. The results are plotted in Fig. 2.14.1. The change in reactivity during core heatup, which is actually negative, is plotted as positive for convenience. Under these severe test conditions, it was observed that the average reactivity as measured with the mass adjustment rod was as much as 2.4 cents greater than that indicated by the most responsive thermocouple. Stated another way, the average core temperature differed from that indicated by the most responsive thermocouple by the equivalent of 2.4 cents of reactivity.

In this extreme test, the heat was applied to the location most unfavorable to the thermocouples. If, by contrast, the heat is applied to a favorable location, the thermocouple response will be very rapid, as shown by the steep curve near the left of Fig. 2.14.1. This curve was obtained by aiming the heat lamp at the bottom of the core where thermocouple 5 is located. The heat lamp again was $\frac{1}{4}$ in. from the core and the thermocouple was in its normal position, locked between the safety tube and the bottom of the core.

Experiment 2

In the second experiment, heat was applied to the core more uniformly by using three lamps spaced at 120° intervals around the core at a distance of 1 ft from the core. Again, care was taken to avoid aiming the lamps directly at the thermocouples. Results for this run are shown in Fig. 2.14.2. It may be seen that under these less severe heating conditions, the maximum difference in response of the most sensitive thermocouple and the mass adjustment rod is only 0.4 cent. It should be noted that the slope of the thermocouple curves rather closely duplicates the slope of the mass adjustment rod curve, thus confirming the accuracy of the previously established core temperature relationship of 1°F = 0.17 cent. It may be further noted that the thermocouple curves also follow the mass adjustment rod cooling curve.

The fact that thermocouple No. 5 is located at the bottom of the core makes it especially responsive to temperature changes outside the core. This is demonstrated by the steeper-than-average

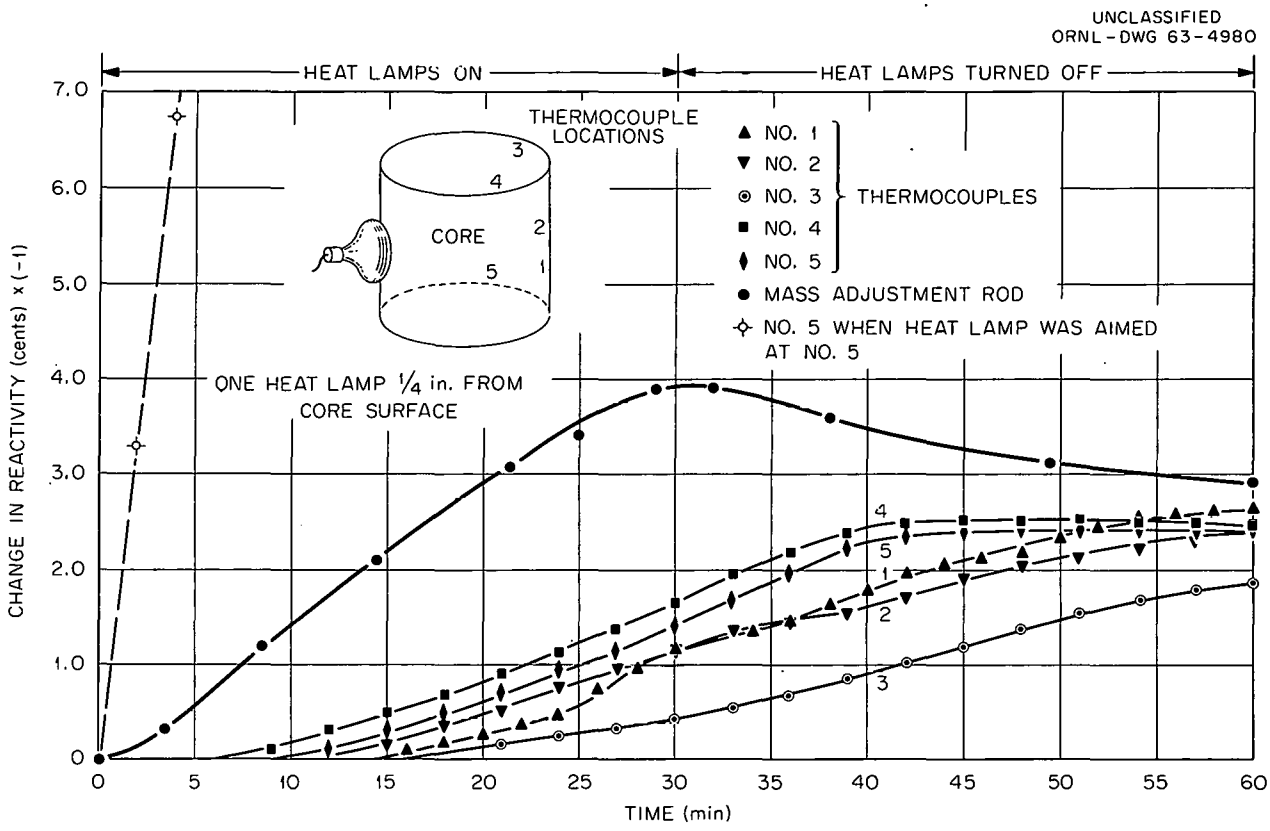

Fig. 2.14.1. Mass Adjustment Rod Response Compared with Thermocouple Response While Core Is Heated Locally.

slope on the cooling portion of its curve in Fig. 2.14.2 and by its very rapid response shown at the left side of Fig. 2.14.1. Thermocouples 4 and 5 are of greatest importance during the preparation for a burst, because their readouts are approximately four times as sensitive as those of the other three thermocouples.

It should be recognized that even though the heating conditions used in the second experiment were less severe than those used for the first experiment, they were still relatively severe. A simple test showed, for example, that the temperature of a mercury thermometer held 1 ft from a heat lamp rose roughly three times as fast as it did when the thermometer was moved from the shade out into the bright sunshine. Thus, the three heat lamps of the second experiment produced roughly nine times the heat that might be expected if the reactor were suddenly exposed to bright sunlight.

Experiment 3

In the third experiment an attempt was made to simulate more realistic conditions, such as those which might be encountered if the reactor core were subjected to unexpected cooling from a breeze during outdoor burst preparation. A 16-in. office fan was calibrated with an air velocity meter and was found to produce a wind of about 8 mph at a distance of 3 ft. Supplying air sufficiently cooler than ambient would have been difficult, so it was decided that comparable results could be achieved by heating the core and blowing air at ambient temperature across it.

Three heat lamps were used to raise the temperature of the core from an ambient of 70°F to 90°F. The lamps were then rearranged to maintain a core equilibrium temperature of 90°F, and the reactor was brought to a power of about 0.2 w.

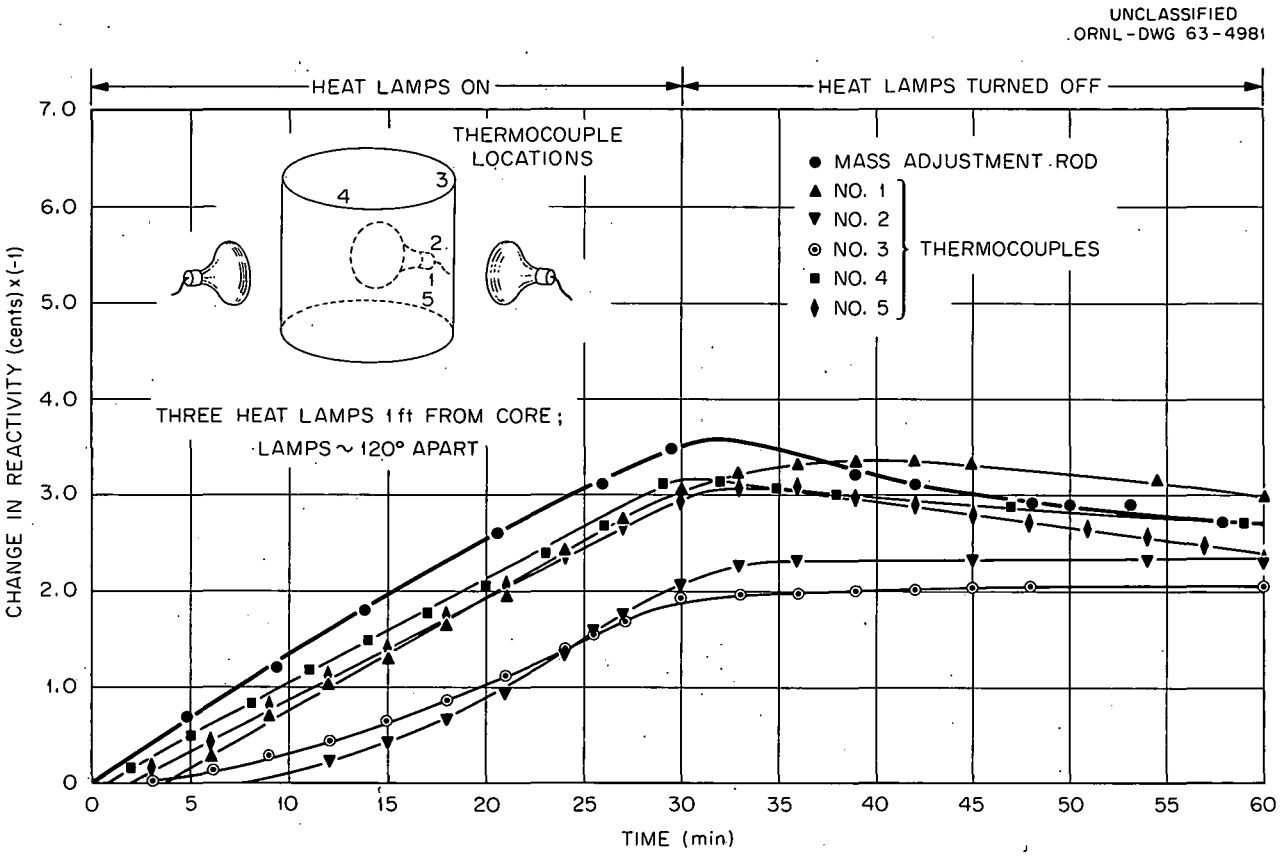

Fig. 2.14.2. Mass Adjustment Rod Response Compared with Thermocouple Response While Core Is Heated from Three Directions.

When temperature equilibrium conditions were assured and the reactor was operating at exactly level power, the fan was switched on remotely and temperature changes were noted, along with the changes in mass adjustment rod settings needed to maintain the reactor at level power.

These results are plotted in Fig. 2.14.3. In this more realistic experiment the thermocouple curves follow the mass adjustment rod curve rather closely except for thermocouples 3 and 5, which responded more quickly to the breeze since they were on the side of the core nearest the fan. The 8-mph breeze created by the fan might well be exceeded during reactor operation outdoors on a gusty day; however, the 20°F temperature difference is considerably more severe than would be expected during a period in which preparations are being made for an outdoor burst.

Conclusions

It can be concluded from the results of these three tests that the thermocouples, as they now exist, are adequate for monitoring the core temperature during outdoor burst preparation since bursts will be attempted only during favorable weather conditions.

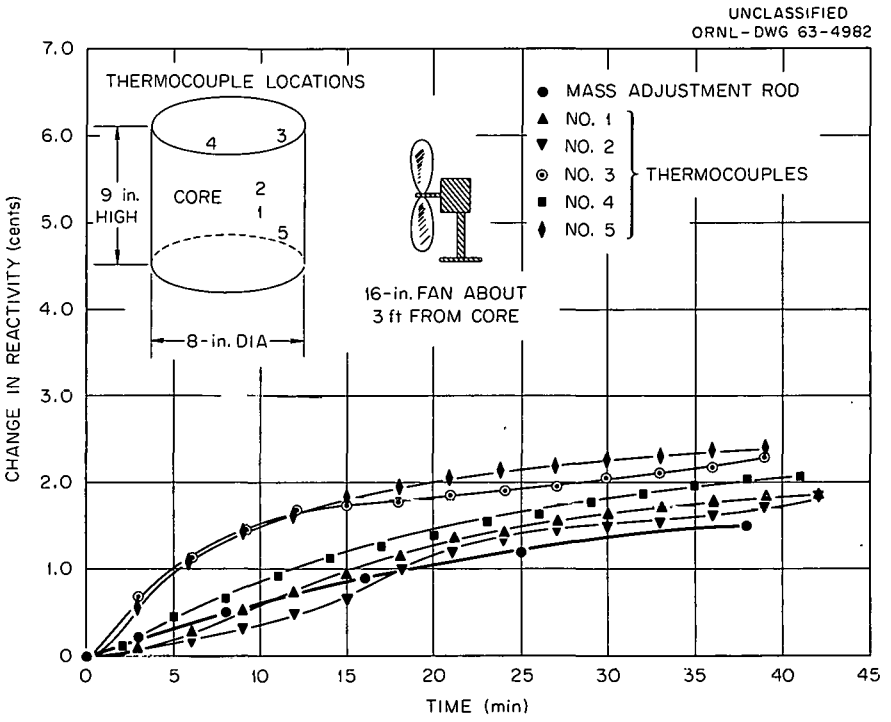

Fig. 2.14.3. Mass Adjustment Rod Response Compared with Thermocouple Response While Core Is Cooled by 8-mph Breeze.

THIS PAGE

WAS INTENTIONALLY

LEFT BLANK

3. Reactor Shielding

THIS PAGE

WAS INTENTIONALLY

LEFT BLANK

3.1. MEASURED GAMMA-RAY SPECTRA FROM A STAINLESS STEEL REACTOR: STATUS REPORT

G. T. Chapman, K. M. Henry, J. D. Jarrard, and R. L. Cowperthwaite

A measurement of the pulse-height spectrum of gamma rays emitted from the surface of a stainless steel water-moderated and -reflected reactor core was reported previously.[1] A further study of the data during preparations for reducing the measured pulse-height distribution to a gamma-ray spectrum has resulted in the identification of the sources that contribute much of the structure in the data.

Figure 3.1.1 shows the pulse-height spectrum at various distances from the reactor for gamma rays emitted normal to the reactor surface. The data have been corrected for the energy-dependent collimator geometry (see Sec. 6.2) and normalized to a nominal 1-w reactor power. In addition, the data have been analytically adjusted (Sec. 6.3) to correct for the slight gain shift mentioned in the previous report[1] and for crystal intrinsic efficiency.

It will be noticed in Fig. 3.1.1 that the spectrum above 5 Mev is predominantly due to gamma rays resulting from the capture of thermal neutrons in the reactor structural material. A few of these gamma-ray energies and the isotopes responsible are indicated on the figure for reference. The peak at about 6 Mev arises from two Fe^{57} capture gamma rays of almost equal intensity and with energies[2] of 5.914 and 6.015 Mev, respectively. These energies and many others in the measured spectrum[3] are too close together to be resolved (see below) by the large NaI(Tl) crystal[1] used. Another Fe^{57} capture gamma ray is found at 7.639 Mev, and it appears as the most distinct peak in the high-energy capture spectrum. The distribution between 8.5 and 9.0 Mev is composed of gamma rays for strongly excited levels in Cr^{54} at 8.881 Mev and in Ni^{59} at 8.532 and 8.997 Mev, and from a weak contribution from Fe^{57} at 8.872 Mev. Above 9 Mev, the major contribution comes from Cr^{54} at 9.716 Mev and from Fe^{58} at 10.16 Mev.

Below 5 Mev the spectrum shown in Fig. 3.1.1 is apparently composed of gamma rays which constitute the expected continua of prompt-fission and fission-product gamma rays plus the very strong contribution from the 2.21-Mev level excited by thermal-neutron capture in the hydrogen of the water. The data show an intensity maximum for this particular gamma ray at about 5 cm from the reactor surface. This is expected, since the number of thermal neutrons available for capture in the water is greatest at about 4 cm from the reactor surface.

A peak in the data at about 6.9 Mev seems to disappear as the spectrometer is moved away from the reactor surface. The origin of this contamination is not yet understood, but appears to be a capture gamma ray associated with some material in the spectrometer shield or cone.

Figures 3.1.2 and 3.1.3 show the effect on the spectrum as the spectrometer is rotated about points in the water at 10 and 25 cm from the surface of the reactor. (Note: "PCA" in these figures refers to the Pool Critical Assembly in which the stainless steel core was assembled.) At increased angles, the hydrogen-capture gamma ray (2.21 Mev) becomes very predominant and shows little attenuation relative to the higher-energy portion of the spectrum. This again implies that the origin of these water-capture gamma rays

---

[1] G. T. Chapman *et al.*, *Neutron Phys. Div. Ann. Progr. Rept. Sept. 1, 1962*, ORNL-3360, p 3.

[2] L. V. Groshev *et al.*, *Atlas of Gamma-Ray Spectra from Radiative Capture of Thermal Neutrons* (translated by J. B. Sykes), Pergamon, New York, 1959.

[3] At least 80 levels below 5 Mev in the major components of stainless steel are reported by Groshev *et al.*[2]

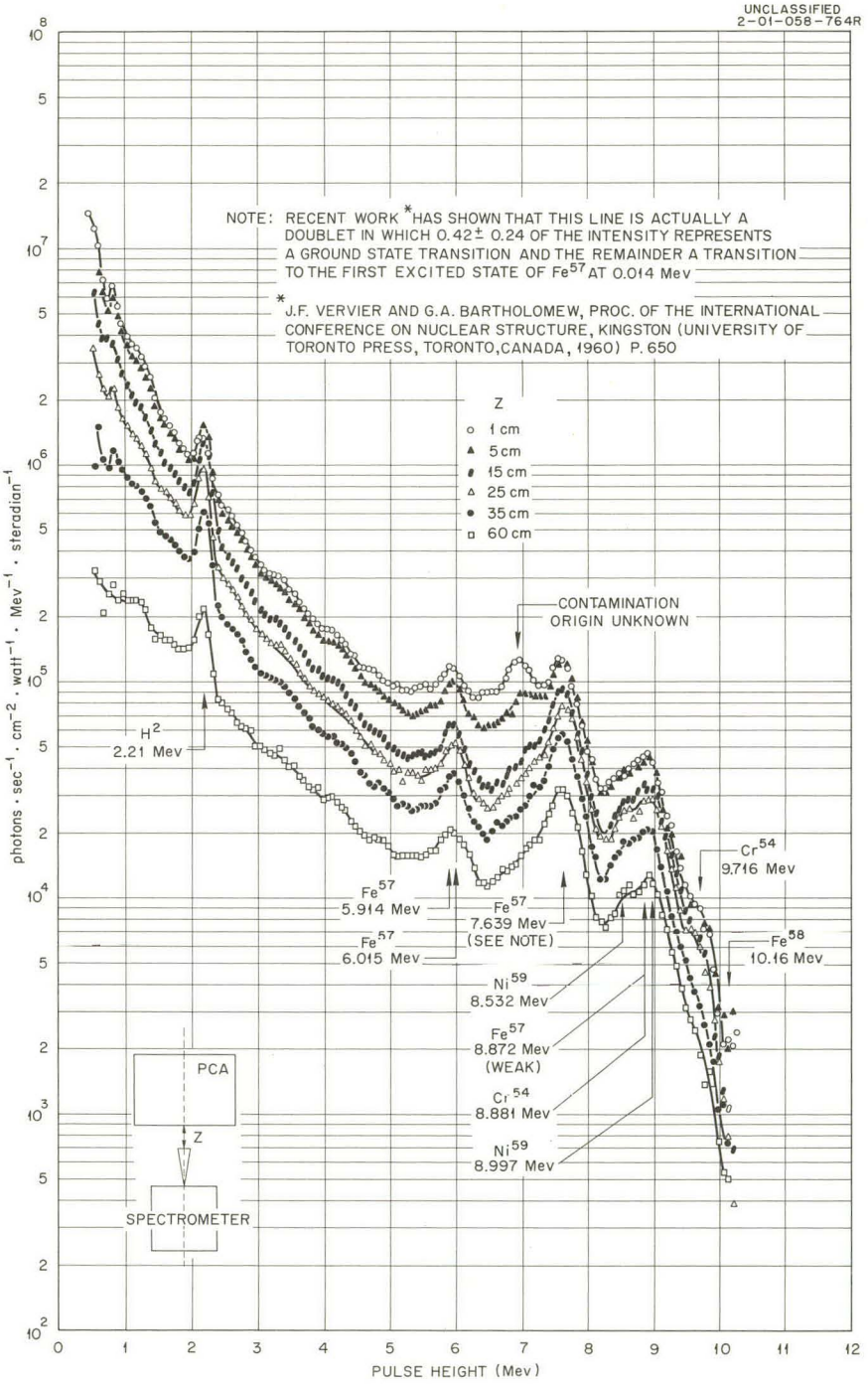

Fig. 3.1.1. Pulse-Height Distribution of Gamma Rays Emitted Normal to the Surface of a Stainless Steel Reactor as a Function of the Distance in Water from the Reactor Surface. The lines are drawn only to indicate the individual sets of data.

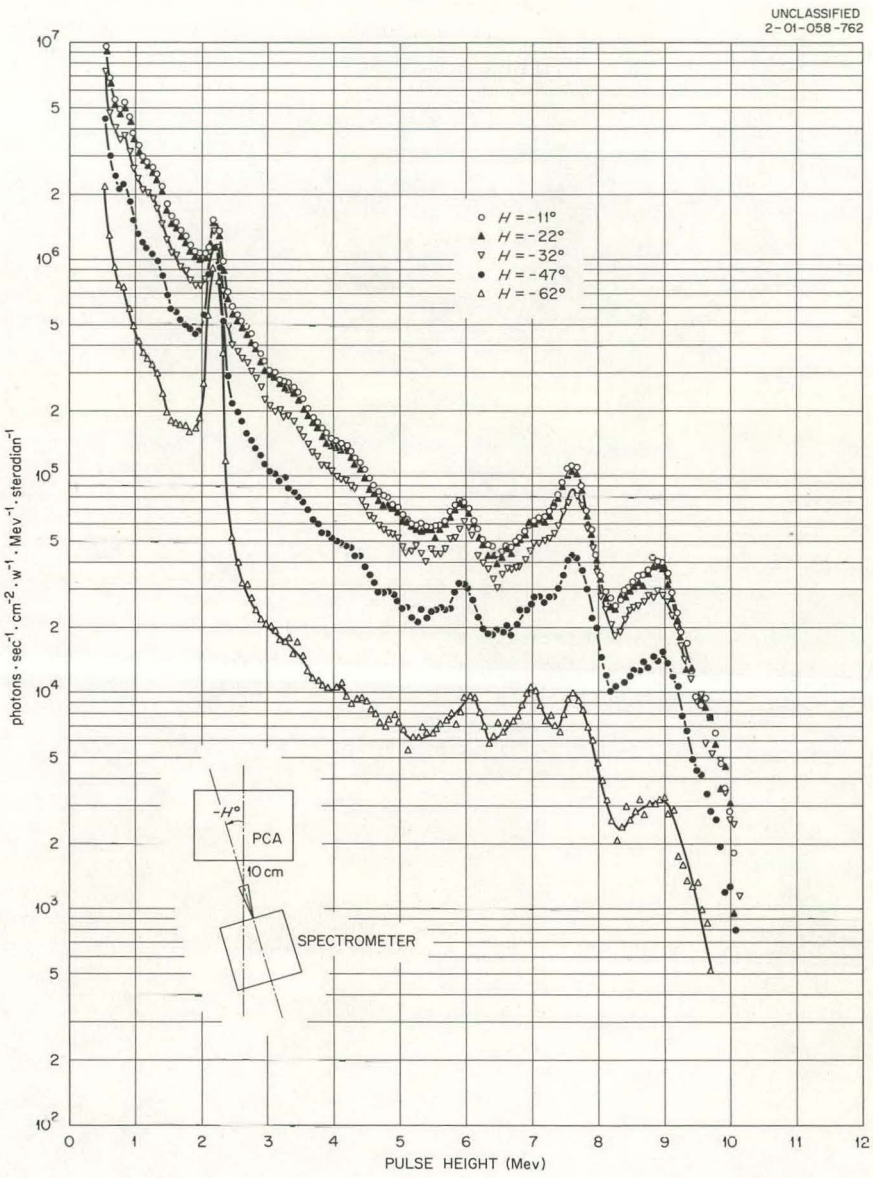

Fig. 3.1.2. Pulse-Height Distribution of Gamma Rays as a Function of Angle About a Point in Water 10 cm from the Reactor Surface. The lines are drawn only to indicate the individual sets of data.

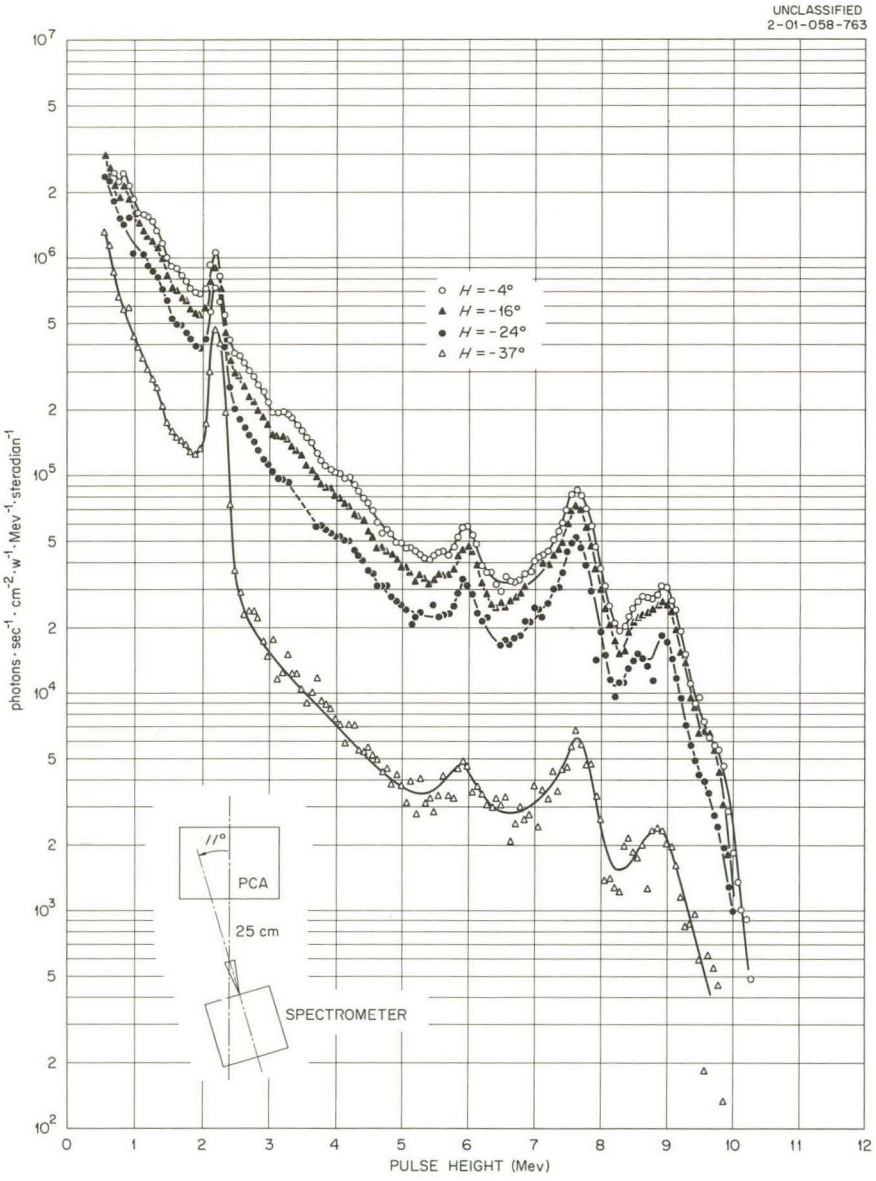

Fig. 3.1.3. Pulse-Height Distribution of Gamma Rays as a Function of Angle About a Point in Water 25 cm from the Reactor Surface. The lines are drawn only to indicate the individual sets of data.

is primarily in the shield-reflector region rather than in the core of the reactor. Other than this relative change in the intensity of the hydrogen-capture gamma ray, the general shape of the spectrum remains constant with changes in angle.

Other gamma rays resulting from thermal-neutron capture by the elements contained in stainless steel exist, with energies ranging down to very low levels. However, these emitting levels are closely spaced and very numerous below 5 Mev.[2,3] In addition, the intensities (photons per capture) of gamma rays from these levels are small compared with those of the gamma-ray sources described above which also contribute to the spectrum below 5 Mev. Consequently, because of the close spacing of the levels and limited ability of the crystal to resolve gamma rays having only small separations in energy (as shown by the measured resolution curve of Fig. 3.1.4), these lower-energy gamma rays are not expected to appear in these data as distinct peaks. Furthermore, this smearing effect, inherent in the crystal response, tends to overemphasize the magnitude of the distributions at lower energies, thus making the spectrum appear somewhat softer than it actually is. A partial "unscrambling" of the data, which is under way, should correct for these effects to some extent and give a more accurate approximation of the true photon-energy distribution.

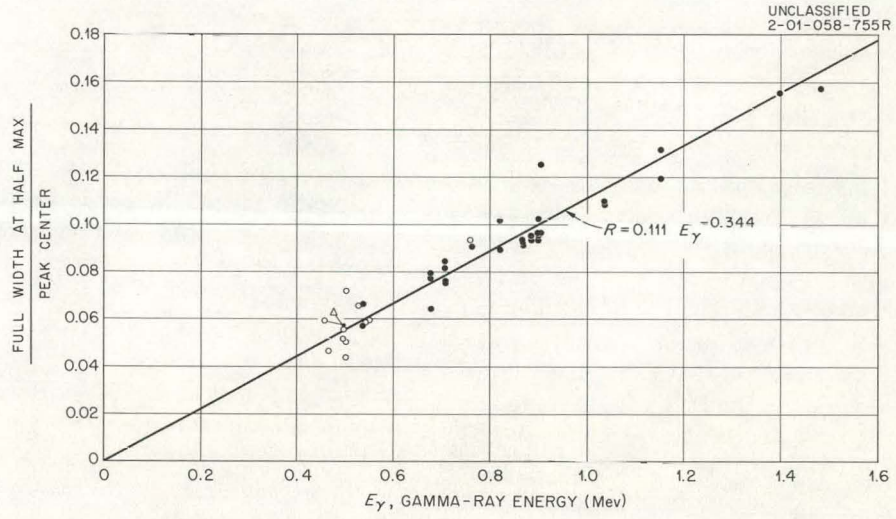

Fig. 3.1.4. The Measured Resolution of the Model IV Gamma-Ray Spectrometer as a Function of Gamma-Ray Energy.

3.2. MEASUREMENTS OF FAST-NEUTRON SPECTRA WITHIN AND AT VARIOUS DISTANCES FROM THE BULK SHIELDING REACTOR I

M. S. Bokhari,[1] V. V. Verbinski, and J. D. Kington

Introduction

The shielded-diode spectrometer described in Sec. 6.1 was used to measure the spectra of fast neutrons within the core of the Bulk Shielding Reactor I (BSR-I), at the core-shield interface, and at various positions within the shield. A knowledge of such spectra is of value to several disciplines. These include reactor design, the analysis of fast-neutron activation and damage experiments, the experimental verification of neutron transport calculations in shields, and the calibration of threshold foil spectrometers and dosimeters. Various methods exist for evaluating fast-neutron transport in shields, including dosimeter measurements, threshold foil spectrometry, nuclear emulsion techniques, and time-of-flight measurements in conjunction with an electron linear accelerator; but for measurements with a reactor as the neutron source the shielded-diode spectrometer is eminently suitable in regard to satisfactory counting rates, energy resolution, capability of operation behind thick shields, and the ability to perform satisfactorily in radiation fields having a high gamma-ray to neutron-flux ratio. Because of the necessity of shielding the diodes against the intense gamma radiation from the reactor, the spectrometer can measure only the spectrum of the directed flux, $\phi(\mu,r,E)$; however, within the reactor the spectrum of $\phi(\mu,r,E)$ should be nearly identical to that of the scalar flux, $\phi(r,E)$, where the neutron flux gradient is quite small. At points exterior to the reactor, measurements of $\phi(\mu,r,E)$ for particular values of μ can serve as checks for the predictions of various calculational methods. If these predictions are verified, it is reasonable to utilize such methods to obtain a complete knowledge of $\phi(\mu,r,E)$ and of its integral over μ, that is, the scalar flux $\phi(r,E)$.

Experimental Configuration

The arrangement of the reactor and the spectrometer in the Bulk Shielding Facility pool is shown in Fig. 3.2.1. BSR-I loadings 96A and 98, differing only in that loading 98 had an element removed to permit measurements within the core, were used for these experiments. The shielded-diode spectrometer was positioned in the horizontal midplane of the reactor, and data were obtained as functions of θ, the horizontal angle between the prolonged reactor center line and the center line of the spectrometer, and of r, the distance from the reactor face to the end of an $\sim 17\frac{1}{2}$-in.-long air-filled aluminum tube extending from the end of the spectrometer collimator. Sulfur pellets positioned 20 and 40 cm from the reactor face were used to monitor the relative power of the reactor. The relative power, as determined from the activity induced in the sulfur, is estimated to be known to within 2%. A 0.5-cm-thick Li^6 thermal-neutron shield was placed in the throat of the spectrometer collimator during all measurements.

Spectrometer Response Variation with Reactor Power

The response of the shielded-diode spectrometer to monoenergetic neutrons has been shown elsewhere (Sec. 6.1) to be a Gaussian peak whose width at half-height, a measure of the resolution, is a function of the energy. However, subjecting the instrument to intense gamma radiation results in both an increase in the width of the peak for monoenergetic neutrons and a channel shift that is a constant for all pulse heights (therefore a baseline shift). Both the width increase and the channel shift can be measured by sending pulses from a pulse generator through the spectrometer preamplifiers in the actual operating environment.

In order to minimize these effects as much as possible, the following procedure was devised for selecting a suitable reactor power for each angle and distance. The reactor was initially brought to a low power level and the position of the epithermal peak and its width at half-maximum were recorded. It was ensured that this width was the same as that recorded for $r = 0$ cm and $\theta = 0°$ – approximately $7\frac{1}{2}$ channels with the amplifier gain settings used in the present experiments. Then the reactor power was raised in steps, and

[1]United States Agency for International Development Fellow, on loan from the Pakistan Atomic Energy Commission.

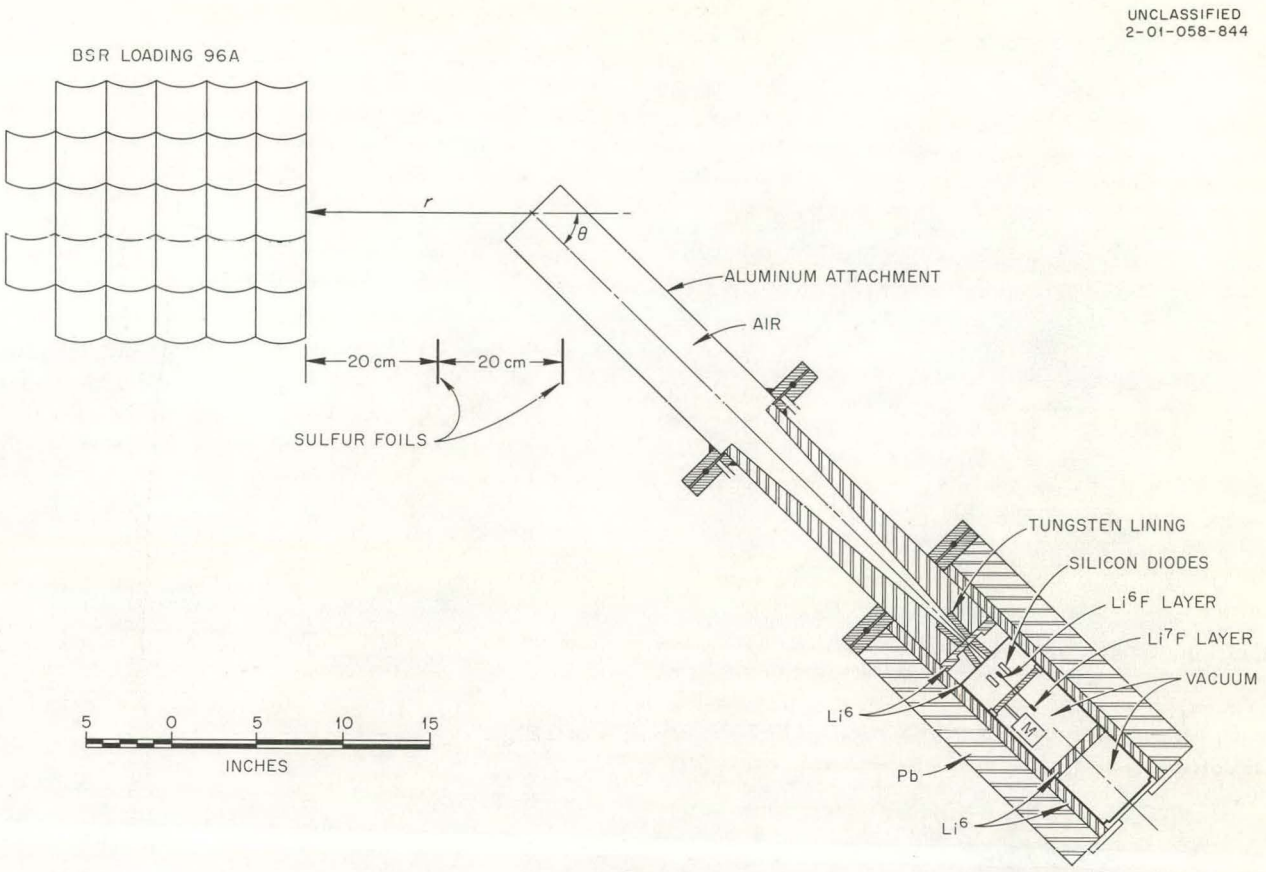

Fig. 3.2.1. Experimental Arrangement of BSR-I and Shielded-Diode Spectrometer in the BSF Pool.

the position of the epithermal peak and its width at half-maximum, Δ, were recorded for each step. Typical plots of the position of the peak and Δ as functions of reactor power are shown in Figs. 3.2.2*a* and 3.2.2*b*, respectively. Both the peak position and Δ remained constant until a reactor power of ~6.5 kw was reached, after which they began to increase rapidly. From these plots the maximum safe power level for this particular configuration (r = 10 cm and θ = 0°) was set at 5 kw.

For measurements at θ = 40.5 and 51° the increase in half-width was found to be negligible. For measurements at r = 60 cm and θ = 0°, however, the gamma-ray pileup completely obscured the epithermal peak at a reactor power of 100 kw. At this depth and angle the ratio of gamma rays to neutrons is at its highest, increasing from 2×10^0 to $\sim 2 \times 10^3$ as r increases from 0 to 60 cm (ref 2). For this case, then, the reactor was first run at a low power, ~30 kw, and the fast-neutron spectrum was measured. The count rate due to neutrons having energies > 1 Mev was determined and was used as a guide for increasing the reactor power to the point that statistically reasonable counting rates could be achieved without excessive gamma-ray pileup. The feasible reactor power was found to be ~70 kw, although at this level the channel shift mentioned above was observed. Since the observed shift in the spectral details agreed with the results of pulser tests, a correction for the effect was easily applied.

[2] *Selected Reference Material, U.S. Atomic Energy Program; Research Reactors,* TID-5275 (1955), chap. 2.

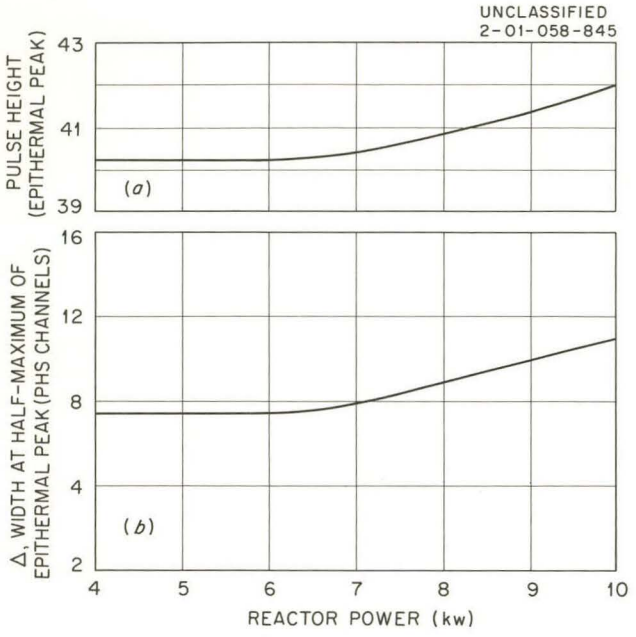

Fig. 3.2.2. Response of Shielded-Diode Spectrometer for $r = 10$ cm and $\theta = 0°$. (a) Position of the epithermal neutron peak vs reactor power; (b) width at half-maximum of the epithermal neutron peak vs reactor power.

Data Treatment

The determination of the spectrometer efficiency is described in Sec. 6.1. Some assumptions regarding the differential reaction cross section for the $Li^6(n,\alpha)T$ reaction were required because of the lack of data in the neutron energy range from 2.15 to 14 Mev. In particular, it was assumed that the differential cross section, averaged about 90° in the center-of-mass system, could be reasonably represented by the total reaction cross section reduced by a factor of 13.3. Thus, when more complete data for the differential cross section, $\sigma(\theta)$, become available, the spectral shapes presented here should be corrected by the ratio $[\overline{\sigma}(90°)/\sigma_{total}] \times 13.3$. For more precise results, $\sigma(\theta)$ would have to be weighted by the net solid angle of acceptance of the spectrometer for each value of θ.

The method of background subtraction has also been covered in Sec. 6.1. Before these subtractions were made, the effectiveness of the collimator and spectrometer shield in eliminating background from scattered neutrons in the water surrounding the spectrometer was proved by plugging its wedge-shaped aperture with water.

Transmission corrections for the presence of the 0.5-cm-thick Li^6 shield, the stainless steel encapsulation of the Li^6, and the aluminum windows of the spectrometer were not applied to the data, since the effect of these corrections is to raise the spectrum at 5 Mev only about 5% relative to the 1- and 10-Mev points.

Results and Discussion

A typical pulse-height distribution for the spectrum at the face of the reactor is shown in Fig. 3.2.3. The epithermal peak extends out to about 1 Mev. Efforts have been made to subtract this

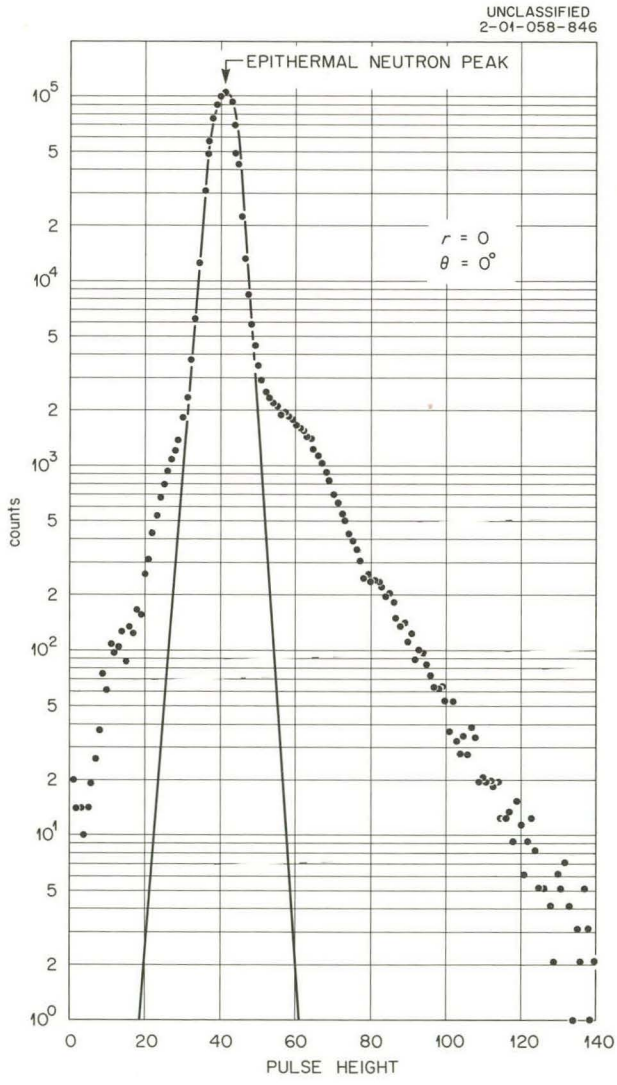

Fig. 3.2.3. Pulse-Height Distribution of Neutrons from the BSR-I at $r = 0$ and $\theta = 0°$.

peak, additionally broadened by the effect of the gamma-ray field, from each spectrum; however, the uncertainty in the data becomes very large below 1 Mev, so that the most satisfactory solution is to repeat the measurements below 1 Mev with a substantially thinner layer of Li^6F, a thinner supporting membrane for the Li^6F, and a thinner layer of gold on the diodes. At the energies concerned the count rate is high; therefore the use of a thin foil would be acceptable. The lower energy limit should then approach 0.2 Mev.

Seven curves are shown in Fig. 3.2.4, representing the spectra of the forward-directed reactor flux, $\phi(\mu = 1,r,E)$, for r = 0, 10, 20, 30, 40, 50, and 60 cm over the neutron energy range 1 to 12 Mev. These data show a general hardening of the neutron spectrum with increasing water thickness and the existence of dips in the spectrum which correspond to the most prominent peaks of the total cross section of oxygen.[3] The dips become more pronounced with increased penetration distance. Elsewhere in this report (Sec. 3.4) are described measurements of fast-neutron transport through water, made with a much more localized source that was well separated from the nearest face of a water slab. The spectra of the forward-directed flux obtained in these experiments show an even greater variation with oxygen cross section, because of better energy resolution and the different geometry.

Figure 3.2.5 compares the spectrum obtained at $r = 0$ and $\theta = 0°$ with the spectrum measured at the same position with a proton-recoil telescope by Cochran and Henry.[4] The agreement in shape is excellent. The shielded-diode data show a higher intensity of fast neutrons – for instance, 1.4×10^6 neutrons $\cdot$ cm^{-2} $\cdot$ sec^{-1} $\cdot$ w ^{1} $\cdot$ Mev^{-1} at 2 Mev compared with 1.22×10^6 neutrons $\cdot$ cm^{-2} $\cdot$ sec^{-1} $\cdot$ w^{-1} $\cdot$ Mev^{-1} for the recoil-proton spectrometer data – but the difference is well within the uncertainty in the absolute reactor power in the present work. A more accurate determination of the absolute power is planned.

In Figs. 3.2.6 and 3.2.7 are shown the spectra at $\mu = 0.76$ ($\theta = 40.5°$) and $\mu = 0.63$ ($\theta = 51°$), respectively. Note that the reactor is in direct view of the spectrometer for r = 10 cm, $\theta = 51°$, and for r = 20 cm, $\theta = 40.5°$. These spectra are only slightly harder above 4 Mev than those for larger values of r, where the spectrometer cannot see the reactor.

The effects of the oxygen resonances are essentially lost both in the measurements for $\mu < 1$ and in those for water thicknesses that do not allow the spectrometer to view the reactor directly. (This was also noticed for $\mu < 1$ in the measurements described in Sec. 3.4.) At $\theta = 51°$, r = 20 cm, only the very edge of the reactor is in view, and the spectrum is nearly identical to those taken when the reactor is not seen. This indicates that most of the neutrons take the shorter route from near the center of the reactor face and subsequently scatter. It is interesting to note in Fig. 3.2.7 the almost identical shapes of the spectra for r = 30 and 40 cm at $\theta = 51°$, where the reactor is not seen.

Figure 3.2.8 shows spectra at r = 40 cm for three values of θ – 0, 40.5, and 51°. A trend toward spectral hardening with decreasing angle is evident.

In Fig. 3.2.9 three neutron spectra are shown. The solid curve is the U^{235} fission spectrum measured by Cranberg *et al.*[5] The dashed curve is the spectrum measured with the shielded-diode spectrometer at r = 0 cm, while the points are the spectrum at r = –7.5 cm (inside the reactor). All three spectra are normalized at 3 Mev. The spectrum at r = 0 cm is the upper limit in hardness of the spectrum existing at the center of the core (at r = –15 cm) where the volume of the central fuel element would be the principal contributor. Above 4.3 Mev the fission spectrum represents a lower limit of hardness, which would never be reached within a pool-type thermal reactor. From this figure it appears that the spectrum at r = –7.5 cm is probably very nearly the same as that which exists at the core center.

A further conclusion may be reached by recourse to measurements of the shape of the thermal-neutron flux made earlier within the BSR-II,[6] a stainless-steel-clad core. The flux gradient for thermal neutrons was found to be slowly varying along the core center line in the horizontal midplane. Since

[3]D. J. Hughes and R. B. Schwartz, *Neutron Cross Sections, Second Edition*, BNL-325 (1958).

[4]R. G. Cochran and K. M. Henry, *Fast-Neutron Spectra of the BSF Reactor*, ORNL CF-53-5-105 (May 29, 1953).

[5]L. Cranberg *et al.*, *Phys. Rev.* **103**, 662 (1956).

[6]E. G. Silver and K. M. Henry, *Neutron Phys. Div. Ann. Progr. Rept. Sept. 1, 1960*, ORNL-3016, p 35 and Fig. 2.1.5.

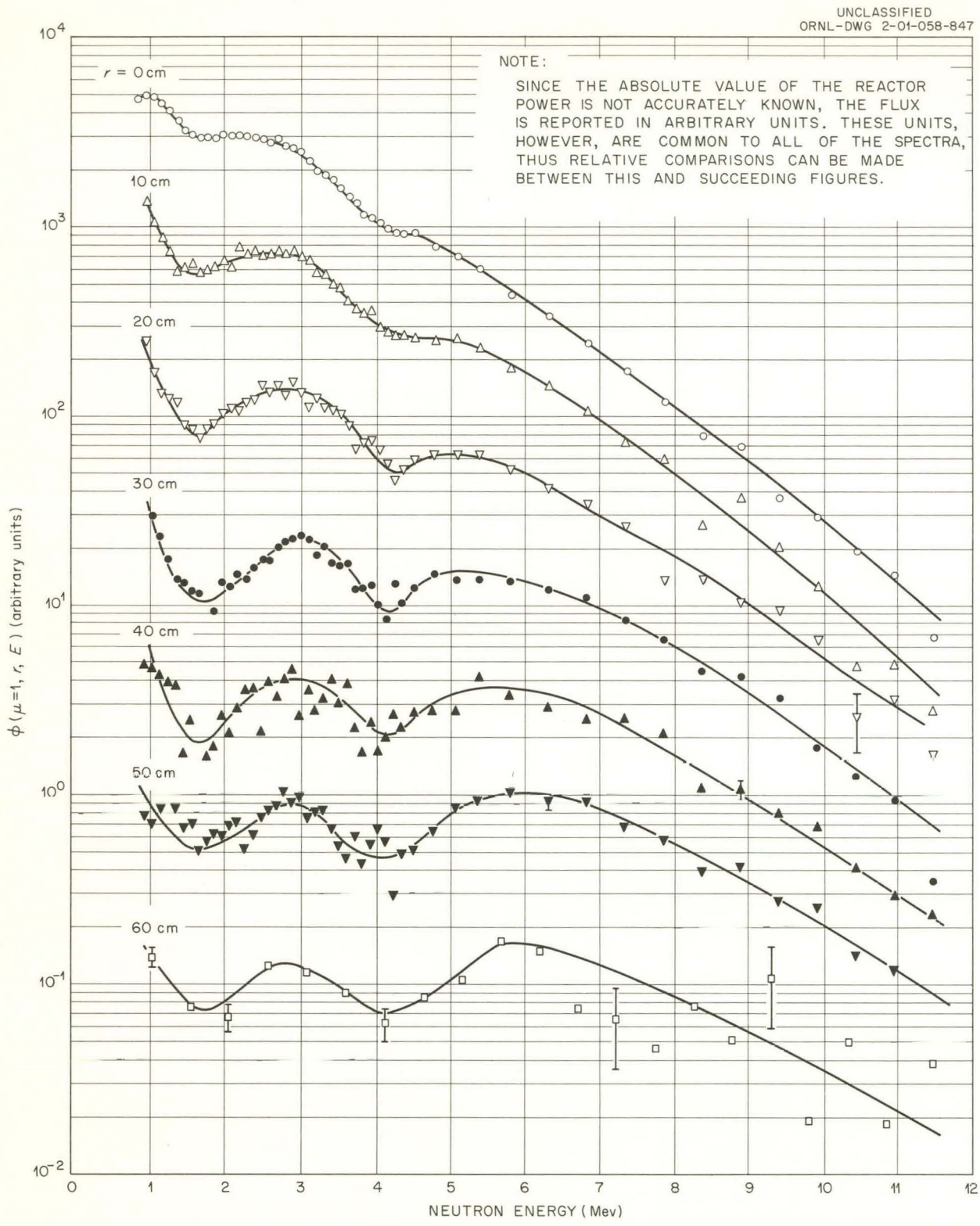

Fig. 3.2.4. BSR-I Fast-Neutron Spectra at $\theta = 0°$ and $r = 0$, 10, 20, 30, 40, 50, and 60 cm.

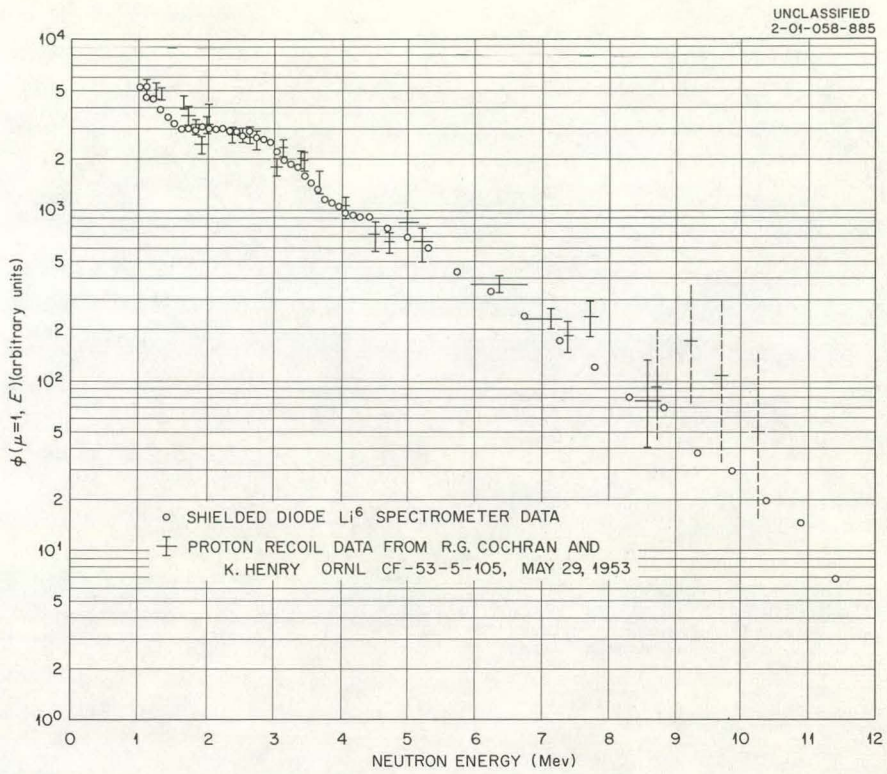

Fig. 3.2.5. Comparison of BSR-I Fast-Neutron Spectra Measured with the Shielded-Diode Spectrometer and with a Recoil-Proton Telescope.

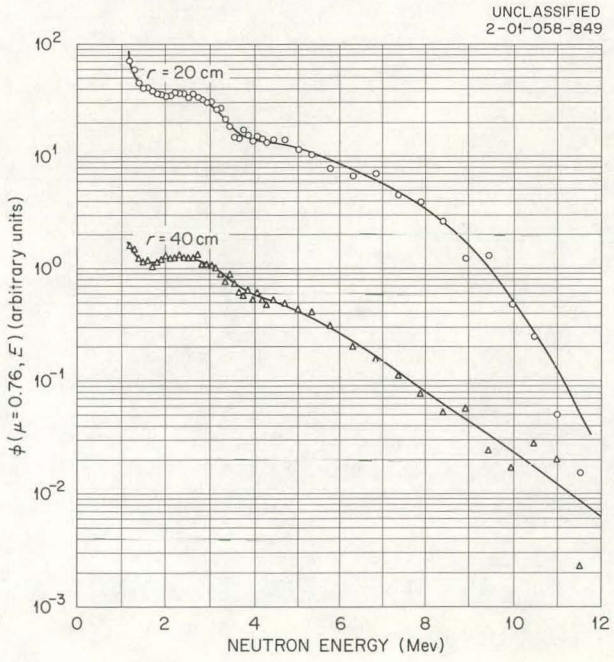

Fig. 3.2.6. BSR-I Fast-Neutron Spectra at $\theta = 40.5°$ and $r = 20$ and 40 cm.

the fission rate is proportional to the thermal-neutron density, the fast-neutron distribution should resemble that for thermal neutrons. If it is accepted that the differences between the aluminum cladding of the BSR-I and the steel cladding of the BSR-II do not appreciably affect the flux distribution, then the flux gradient at $r = -7.5$ cm in the BSR-I can be expected to be small and slowly varying, and the directed flux at this point should very nearly represent the scalar flux within the reactor.

Conclusions

The shielded-diode spectrometer has been demonstrated to be capable of measuring neutron spectra within a pool-type reactor, at its surface, and at points in water as far as 60 cm from the reactor. Although for the measurements at 60 cm and $\theta = 0°$ the reactor power level was restricted to 7% of its 1-Mw capability because of the gamma-ray background, for the measurements at 40 cm

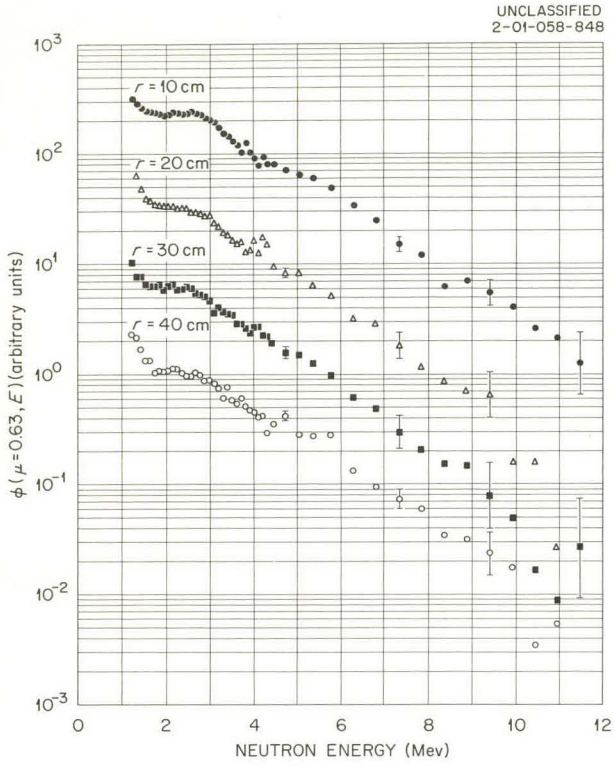

Fig. 3.2.7. BSR-I Fast-Neutron Spectra at $\theta = 51°$ and $r = 10$, 20, 30, and 40 cm.

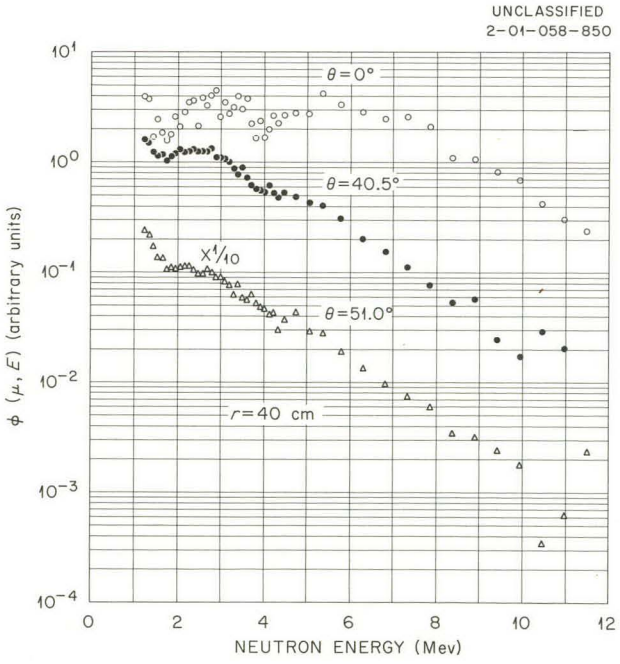

Fig. 3.2.8. BSR-I Fast-Neutron Spectra at 40 cm for $\theta = 0$, 40.5, and 51°.

and $\theta = 51°$ the full reactor power could be used. This means that improving the shielding by moving the diodes slightly farther apart (into the umbra of the collimator) and moving the 0.5-cm-thick Li^6 disk in the collimator farther from the diodes should make it possible to measure the spectra in water out to a distance of about 80 cm. Extension of the data to 100 cm may be possible by increasing the diode area.

The data are suitable for direct comparisons with shielding calculations.

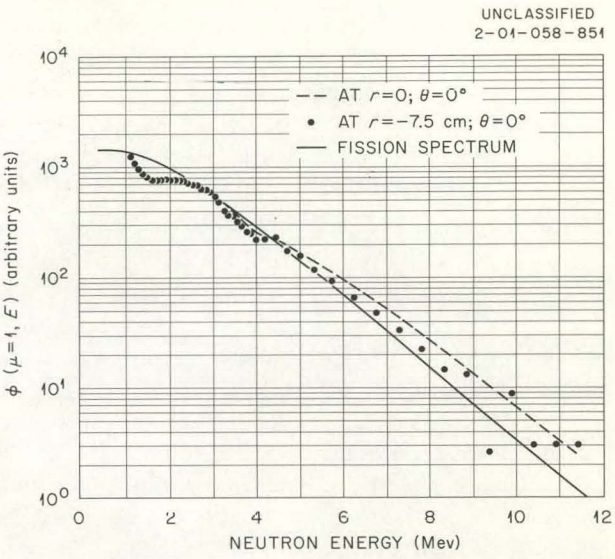

Fig. 3.2.9. Comparison of U^{235} Fission Spectrum with BSR-I Spectrum at $r = 0$ and -7.5 cm.

3.3. MEASUREMENT OF THE FAST-NEUTRON BEAM SPECTRUM FROM THE TOWER SHIELDING REACTOR II

M. S. Bokhari,[1] V. V. Verbinski, and H. A. Todd[2]

Introduction

Experiments to measure the intensities and spectra of the neutrons scattered from several elements located in a collimated beam of fast neutrons from the Tower Shielding Reactor II (TSR-II)[3] are discussed in Sec. 3.12. As part of this program, the fast-neutron spectrum of the direct beam was measured with the shielded-diode spectrometer described in Sec. 6.1. Knowledge of the beam spectrum, as well as its intensity, is required as input data for the Monte Carlo calculations which correspond to the experiment and are reported in Sec. 3.13.

The reasons for using the shielded-diode spectrometer for the present measurements were as follows: (1) this instrument is known to work satisfactorily in high gamma-ray backgrounds (see Sec. 6.1) and its response is linear with neutron energy; (2) the shape of the pulse-height distribution given by this spectrometer for monoenergetic neutrons is Gaussian; therefore the neutron spectrum is obtained directly by simply dividing the raw spectrum by the detection efficiency for the various neutron energies (that is, stripping techniques for unfolding the data are not required); (3) it was intended to compare the results with spectra obtained with nuclear plates and with

[1]United States Agency for International Development Fellow, on loan from the Pakistan Atomic Energy Commission.

[2]Instrumentation and Controls Division.

[3]L. B. Holland and C. E. Clifford, *Description of the Tower Shielding Reactor II and Proposed Preliminary Experiments*, ORNL-2747 (1959).

hydrogenous scintillators[4] which employ pulse-shape discrimination to reject gamma-ray pulses and unfolding techniques to get the true beam spectrum from the observed pulse-height distribution. Only the comparison with nuclear-plate data is presented here; the liquid-scintillator data are still being processed.

Spectrometer Efficiency and Acceptance Angle

In order to determine the absolute intensity of the neutron beam at any arbitrary distance, x, from the reactor, it is essential to know both the efficiency of the neutron detector and the solid angle of the source subtended at the neutron detector (the "cone of acceptance") at any distance x. Figure 3.3.1 gives a plot of the counter efficiency vs neutron energy. These data were calculated on the basis of the experimentally measured value of the efficiency for thermal-neutron detection (see Sec. 6.1). In order to promote confidence in the use of the calculated values for the fast-neutron-detection efficiency, the response of the spectrometer to neutrons from a thin U^{235} fission plate was observed. A 30-mil-thick U^{235} fission plate was exposed to thermal neutrons from the Oak Ridge Graphite Reactor thermal column. The spectrometer was covered on all sides with 30-mil-thick cadmium to eliminate thermal-neutron pulses which would tend to obscure the fission-neutron pulses. The fission-neutron spectrum as measured with the shielded-diode spectrometer is shown on Fig. 3.3.2. A comparison with the measurements made by Cranberg *et al.*,[5] also plotted, shows good agreement within the statistical limits of the experiment. This observation gives sufficient confidence in the accuracy of the results presented here.

The geometrical arrangement of the spectrometer and the TSR-II is illustrated in Fig. 3.3.3. The reactor was placed inside a spherical lead-water shield from which a neutron beam emerged through a 6-in.-diam air-filled collimator. The spectrometer was placed at a distance of $18\frac{3}{8}$ in. away from the outer end of the collimator. The cone of acceptance, ω, of the neutron beam has been estimated to be $\sim 5.93 \times 10^{-3}$ steradian with this arrangement.

[4]F. J. Muckenthaler, private communication.

[5]L. Cranberg *et al.*, *Phys. Rev.* **103**, 662 (1956).

Results and Discussion

Figure 3.3.4 shows the pulse-height distribution obtained with the shielded-diode spectrometer in the TSR-II neutron beam. It consists of an epithermal peak superimposed upon the neutron spectrum. The absolute intensity spectrum as a function of energy was obtained by subtracting the epithermal peak and the background, the results of which are shown in Fig. 3.3.5. The fission spectrum of Cranberg *et al.*, arbitrarily normalized at ~ 2.8 Mev, is also shown in Fig. 3.3.5. It is clear that above a neutron energy of 4 Mev the TSR-II spectrum is harder than the fission spectrum. The dips in the TSR-II spectrum between 1

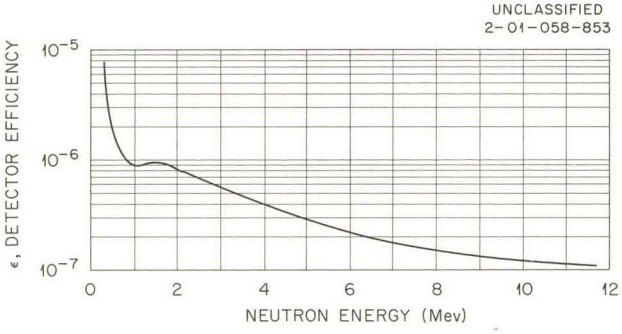

Fig. 3.3.1. Shielded-Diode Spectrometer Efficiency vs Neutron Energy.

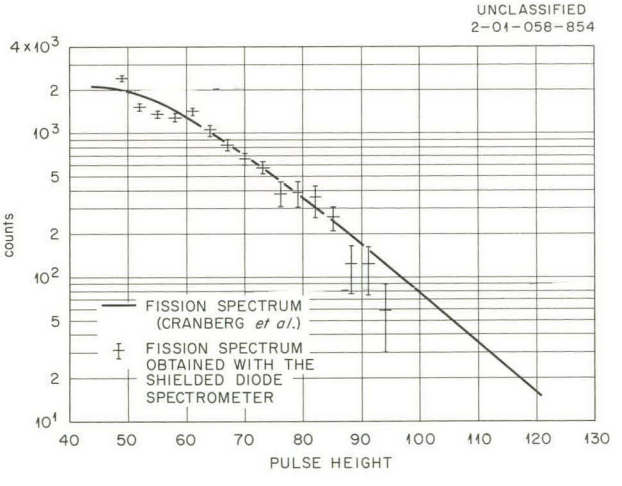

Fig. 3.3.2. Uranium-235 Fission Spectrum Obtained with Shielded Diode Spectrometer Compared with Spectrum Measured by Cranberg *et al.*

UNCLASSIFIED
2-01-058-852

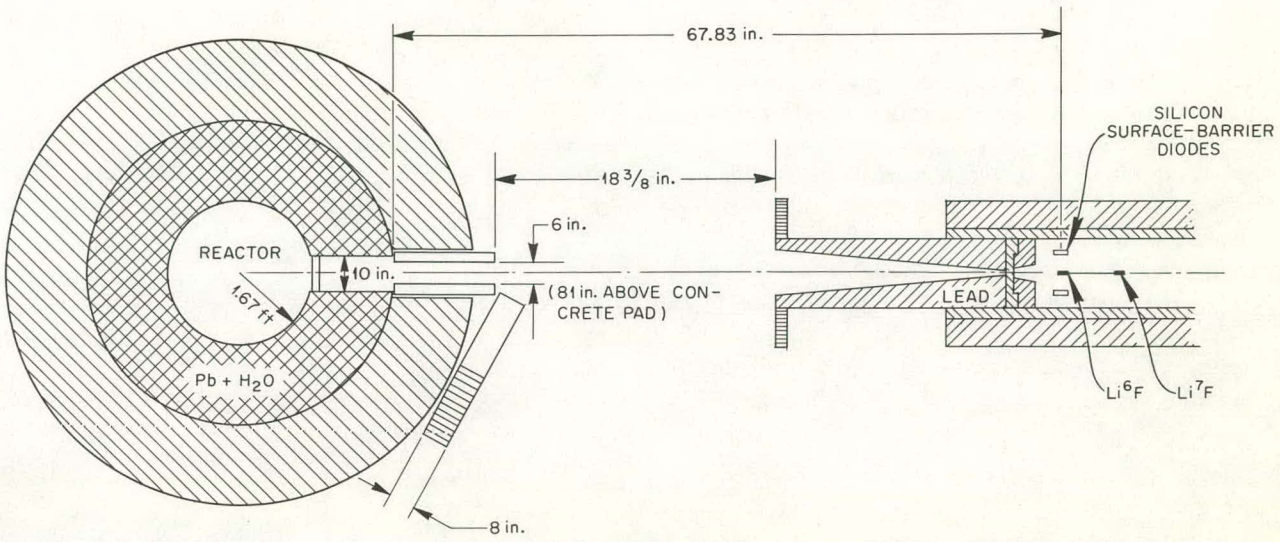

Fig. 3.3.3. Experimental Arrangement for Measurement of TSR-II Fast-Neutron Beam Spectrum.

UNCLASSIFIED
2-01-058-855

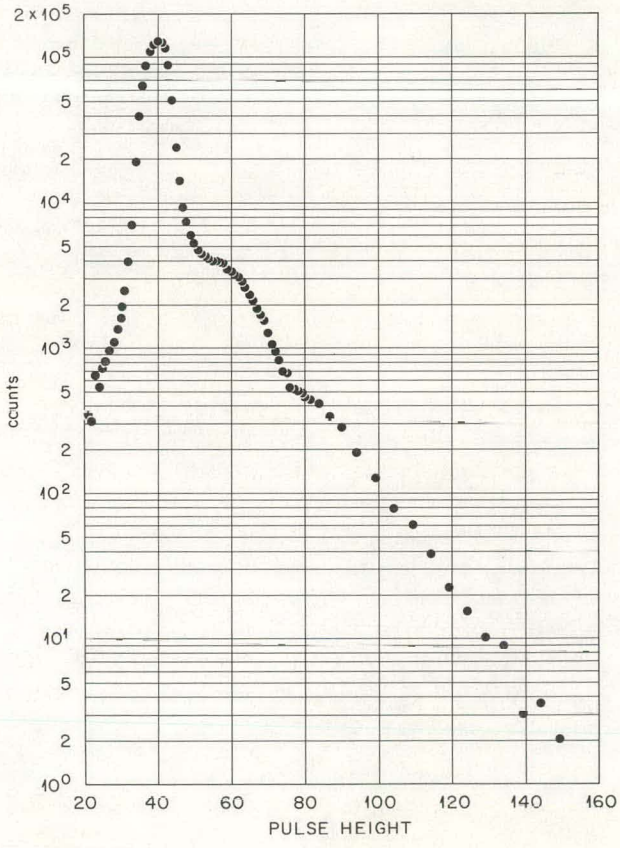

Fig. 3.3.4. Pulse-Height Spectrum of the TSR-II Neutron Beam.

UNCLASSIFIED
2-01-058-856

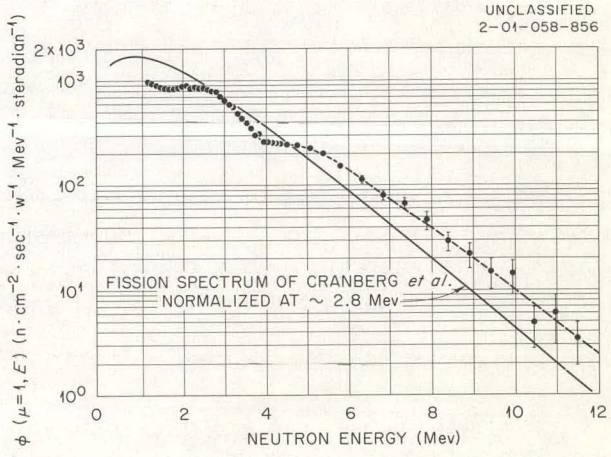

Fig. 3.3.5. Absolute Intensity of the TSR-II Neutron Beam.

and 2 Mev and between 3.7 and 4.3 Mev correspond to a high average value of the oxygen total cross section in these regions. These dips were also observed in the spectra from the face of the BSR-I (Sec. 3.2), but are more pronounced in the spectrum from the TSR-II beam, in which the neutrons passed through an additional 6 cm of water after leaving the reactor core.

Figure 3.3.6 gives a comparison of these results with nuclear-plate data taken at $7\frac{1}{2}$ ft from the

end of the 6-in. collimator. Within the poor statistics of the nuclear-plate data, there is a general similarity of spectral shape and good agreement of absolute intensity in the region from 1.2 to 4.2 Mev. Above 4.2 Mev the statistical error in the nuclear-plate data is too large to afford a good comparison.

The shielded-diode data were used as an input to Monte Carlo calculations of the scattered fast-neutron dose (see Sec. 3.13) for various scattering angles in the horizontal plane. The calculated dose rate based on the measured direct-beam spectrum is within 20% of that obtained with a dosimeter for the scattering angles of 45, 90, and 135°.

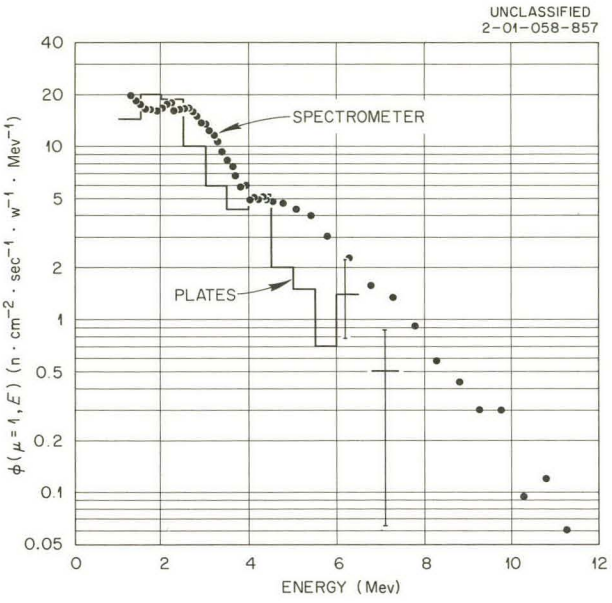

Fig. 3.3.6. Comparison of TSR-II Fast-Neutron Beam Spectral Measurements with the Shielded-Diode Spectrometer and with Nuclear Plates.

3.4. MEASUREMENTS OF FAST-NEUTRON TRANSPORT IN WATER BY TIME-OF-FLIGHT TECHNIQUES

V. V. Verbinski, J. Kirkbride,[1] P. Phelps,[1] and J. C. Courtney[2]

A joint effort by Oak Ridge National Laboratory and General Atomic to measure the details of fast-neutron transport in water has been initiated, the fundamental purpose being to furnish a source of accurate experimental data against which the predictions of various calculational methods can be tested. Water was chosen as the experimental material because the differential cross sections for hydrogen are very accurately known and oxygen cross sections are relatively well known. Also, since the effective threshold for inelastic scattering in oxygen is high (σ_{inel} approx. = 50 mb at 6.8 Mev),[3] current uncertainties in differential cross sections for inelastic scattering should be relatively unimportant. Further, the resonance structure of the oxygen induces pronounced fluctuations in the spectra transmitted through water, the reproduction of which should challenge the capabilities of the most sophisticated transport codes. The experimental results will also provide a sensitive check on the group averaging of differential scattering cross sections for the DSN[4]

[1]General Atomic, San Diego, Calif.

[2]Catholic University, Washington, Graduate Fellow, Oak Ridge Institute of Nuclear Studies.

[3]D. J. Hughes and R. B. Schwartz, *Neutron Cross Sections*, BNL-325, 2d ed. (1958).

[4]For the theory underlying DSN codes, see C. E. Lee, *The Discrete* S_n *Approximation to Transport Theory*, LA-2595 (1962).

and various Monte Carlo codes. In addition, measurements of the uncollided and small-angle-scattered components of the neutron flux were included in the present work, and these have possible importance in Monte Carlo deep-penetration biased-weighting techniques which were recently devised (see Sec. 3.5).

The experimental procedure employed time-of-flight techniques similar to those used in earlier measurements[5-7] of the spectral and spatial details of neutron fluxes in LiH. In addition, independent measurements of the attenuation of the source neutrons by the water slab were made with threshold foils.

Experimental Arrangements

Two slightly different experimental arrangements were used, one referred to as the small-source geometry and the other as the large-source geometry. The small-source geometry, shown in Fig. 3.4.1, was used for measurements of neutrons that penetrated a 30-cm-thick water slab by scattering through small angles (0, 2, and 4°). In this arrangement a 30-Mev electron beam from the accelerator emerged from the LINAC vacuum system through a 10-mil-thick titanium window and then hit a 5-cm-diam by $1\frac{3}{4}$-cm-thick lead target, producing a photoneutron spectrum which roughly approximates a fission neutron spectrum. The water slab, which could be removed for measurements of the source spectrum, was positioned so that its center was 65 cm from the center of the target. A 2-in.-diam by $2\frac{1}{2}$-in.-long cylindrical xylene scintillator, containing 5 g of *p*-terphenyl and 0.2 g of POPOP per liter, was located at the end of a flight tube approximately 53 m from the source.

Neutrons which penetrated the water slab and reached the detector were collimated at two positions along the tube, one about 2 m from the source and the other approximately 35 m from the source, so that the effects of any scattering materials in the collimated beam could be corrected for by the factor

$$e^{\Sigma_t(E)T},$$

where Σ_t is the macroscopic total cross section of the scattering element and T is its thickness (in cm). After leaving the first collimator, the neutrons passed through 14 m of vacuum, a 0.05-m-thick lead filter, 33 m of argon, a total of about 4 m of air, and a total aluminum window thickness of about 0.0005 m.

The first collimator was a 7.6-cm-diam hole in the concrete wall of the experimental cave narrowed to a $1\frac{3}{4}$-cm-wide vertical slot in a 14-cm-thick lead wall as shown in Fig. 3.4.1. A $\frac{1}{8}$-in.-thick layer of powdered B_4C (natural) at the collimator opening absorbed slow neutrons (which could simultaneously arrive at the detector from several earlier LINAC bursts) and thus effectively eliminated the production of capture gamma rays which would have increased the background when pulse-shape discrimination was not employed. The second collimator consisted of a 20-cm-square opening through 30 cm of paraffin and 10 cm of lead.

In order to obtain scattering angles of approximately 2 and 4°, the lead target was displaced from the axis of the flight tube by 2.3 and 4.6 cm, respectively.

The second experimental arrangement, referred to as the large-source geometry and shown in Fig. 3.4.2, was used to measure the neutron leakage spectra as a function of slab thickness for scattering angles of 0 and 30°. It is similar to the arrangement described above except that a larger scintillator was required to compensate for the reduced neutron flux at 30°. The detector used was a 5-in.-diam by 5-in.-long encapsulated cylinder of NE-213.[8] This scintillator has excellent pulse-shape discrimination properties which were utilized for the rejection of gamma-ray-induced counts; however, since the pulse-shape discriminator becomes immobilized when this slower scintillator is exposed to large gamma-ray bursts, it was necessary to surround the lead target with additional lead to reduce the number of source gamma rays. [The scintillator, though very fast, is doped to provide a slow component (approximately one-fifth the integrated fast component) used for pulse-shape discrimination]. This was accomplished by placing the target at the center of a lead cube having an edge dimension of 20 cm. The target was positioned in a central through-hole in the

[5] V. V. Verbinski *et al.*, *Neutron Phys. Div. Ann. Progr. Rept. Sept. 1, 1962*, ORNL-3360, pp 105 and 111.

[6] V. V. Verbinski, *Trans. Am. Nucl. Soc.* **5**, 213 (1962).

[7] V. V. Verbinski, *Trans. Am. Nucl. Soc.* **6**, 190 (1963).

[8] Nuclear Enterprises, Ltd., Canada.

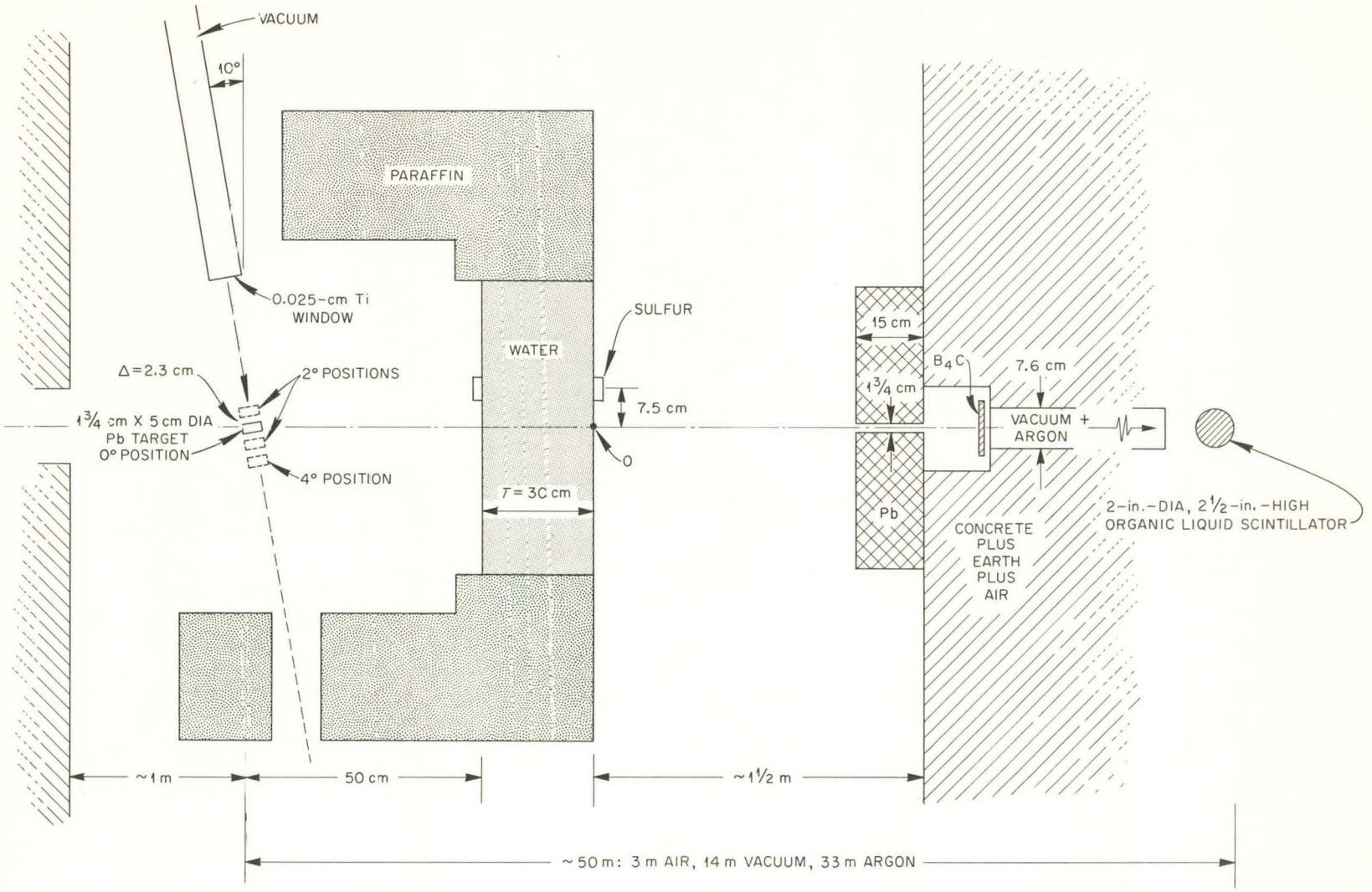

Fig. 3.4.1. Arrangement for the Small-Source Experiments.

cube, which also provided an entry for the electron beam.

The target and slab could be rotated about the point marked "0" in Fig. 3.4.2 to permit the 30° measurements, a 40-cm distance from the center of the target to the center of the near face of the slab being maintained constant. This necessitated slightly different target positions for the different slab thicknesses.

The narrow lead collimator was not used with the large-source geometry.

Time-of-Flight Electronics

For the small-source measurements, the detector photomultiplier was gated "on" between the arrival of the target bremsstrahlung at the scintillator and the arrival of the fast neutrons. Time reference signals were obtained from the LINAC injector pulse. An absolute time reference was obtained from the time of arrival of the bremsstrahlung pulse at the scintillator, since the bremsstrahlung time of flight is precisely known. The bremsstrahlung and neutron pulses were timed with a 31.25-nsec/channel time-of-flight module of a 1024-channel Technical Measurement Corporation (TMC) analyzer.

For the large-source measurements the detector photomultiplier was gated "on" by the pulses from a small plastic scintillator positioned near the lead target. These pulses gave a relative time reference, while the absolute time reference was based upon the time of arrival of the target bremsstrahlung at the fast-neutron detector. The signal from the small plastic scintillator started an Eldorado Electronics Co. time-interval meter (clock) which counted in 10-nsec intervals until a neutron pulse was detected. For a neutron pulse to be accepted, a triple coincidence was required between signals from a linear amplifier, a pulse-shape discrimination amplifier, and a fast tunnel-diode discriminator circuit, all obtained from the dynodes and anode of the single scintillator photomultiplier tube. The tunnel-diode discriminator pulse provided the accurate time reference for stopping the Eldorado clock. The highest, or controlling, bias was determined by the linear amplifier, which was also used for gain calibration.

The time-interval meter output was converted to binary-coded decimal output and fed to an arithmetic (dividing or "scale-expanding") unit, whose digital output was fed directly into the memory of a 400-channel TMC analyzer. The arithmetic unit was set to divide by two, resulting in a 20-nsec time window, because of the limited LINAC running

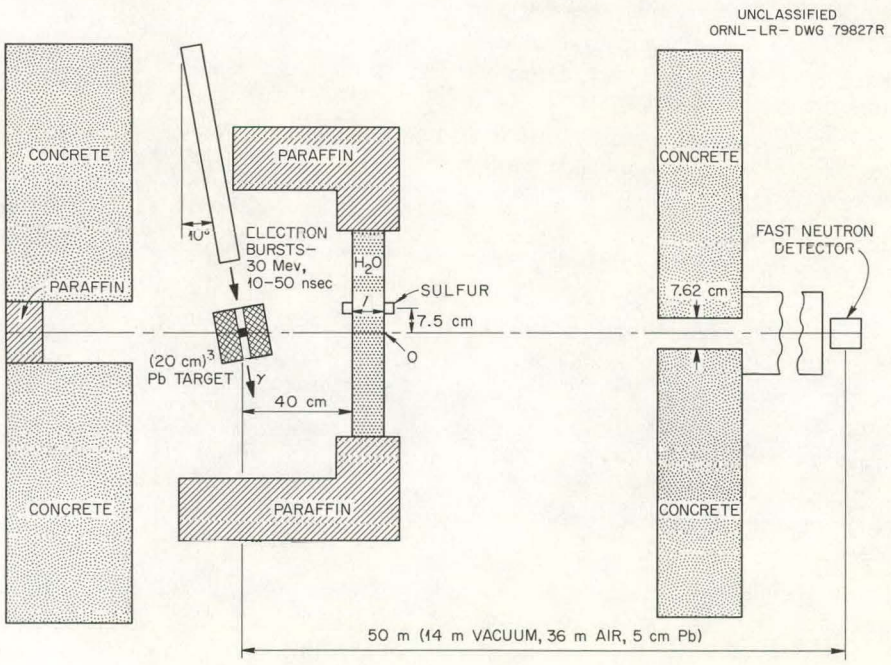

Fig. 3.4.2. Arrangement for the Large-Source Experiments.

time available for these experiments, the limited number of channels in the analyzer, and the ±10-nsec resolving time of the clock. Thus the minimum-width LINAC pulse used was 20 nsec.

The use of the NE-213 scintillator in the large-source experiments made it necessary to consider the effects of afterglow in the scintillator. These effects were minimized by gating on the photomultiplier as late as possible without losing fast neutrons. In addition, the very short input time constant (<1 nsec) of the tunnel-diode discriminator resulted in negligible time-integration of the afterglow pulse.

Except for the use of a digital clock instead of a time-to-pulse height converter and for the addition of the fast tunnel-diode discriminator for precise timing, the circuitry for the present work was basically the same as that used in the LiH experiments.[5]

Results

All results are shown as time-of-flight spectra weighted by the detector sensitivity, since the calibration of the two detectors used in these experiments is still in progress. Nevertheless, the qualitative features and many of the quantitative features of the data are apparent even in the time-of-flight spectra. Conversion of the time-of-flight data to energy spectra will be made before final publication of these results.

The small-source data have been normalized to a beam current of 1 amp, a 20-nsec pulse width, a 25-min run time, and a pulse frequency of 360 pulses/sec. The large-source data have been normalized to a beam current of 1 amp, a 20-nsec pulse width, a 60-min run time, and a pulse frequency of 360 pulses/sec, although for the 30° measurements with 20- and 30-cm-thick slabs the pulse width was increased to 50 nsec in order to improve counting statistics.

No corrections have been made for attenuation in the 5-cm-thick lead filter, the argon gas, the air thicknesses, or the B_4C filter.

Small-Source Experiments. – The results of the experiments utilizing the small source and the narrow collimator are shown in Fig. 3.4.3. The highest curve is the measured source spectrum. Just below this curve is shown the spectrum obtained through 30 cm of water at 0° (that is, with the source on the axis of the flight tube). Bracketing this curve are nine points computed by multiplying the unattenuated source spectrum data (from the curve above) by

$$e^{-\Sigma_t(E)T}.$$

The proximity of these points to the measured spectrum indicates that the experiment is very nearly a "good geometry" experiment and that the transmitted flux observed at 0° is the uncollided flux.

The remaining two curves of Fig. 3.4.3 show the leakage spectra with the source displaced laterally 2.3 and 4.6 cm from the axis of the tube. These

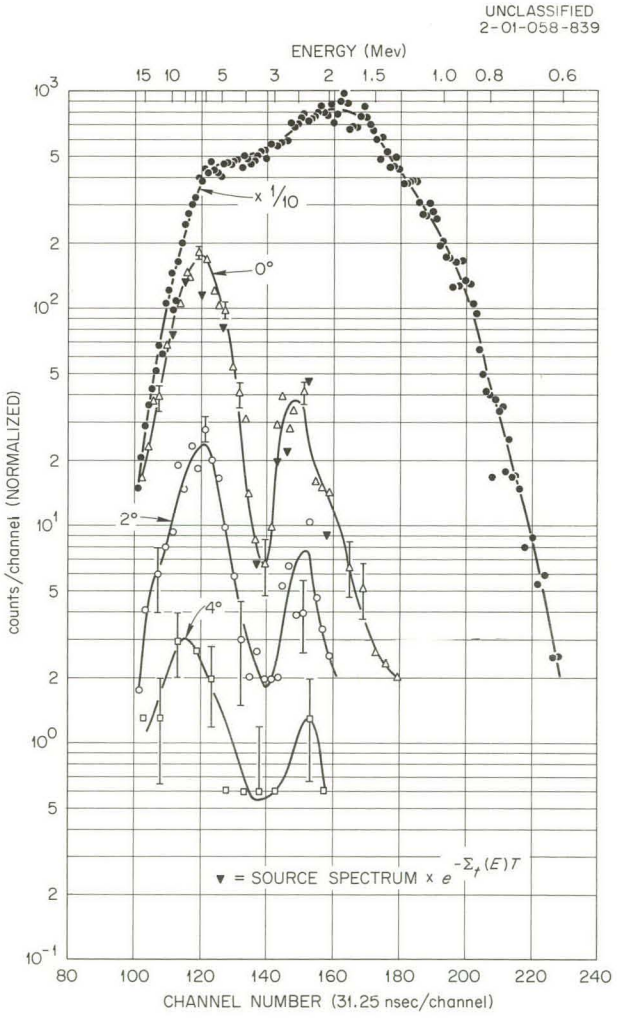

Fig. 3.4.3. Comparison of Leakage Spectra Through 30 cm of Water at 0, 2, and 4° from Slab Normal with Unattenuated Source Spectrum.

displacements correspond to single-scattering angles of 2 and 4°, respectively, at the center of the water slab. The 2° spectrum has about 15% of the magnitude of the 0° curve immediately above. Since from 30 to 40% of the 2° spectrum is due to uncollided neutron leakage through the 15-cm-thick lead collimator, an upper limit of about 10% of the 0° flux can be assigned to the 2°-scattered spectrum. Since at 4° neutrons penetrating the lead collimator encounter the thick concrete wall, the unscattered lead-transmission correction does not apply, and the upper limit to the 4°-scattered spectrum is seen to be about 2% of the 0° spectrum.

Large-Source Experiments. – Since the narrow lead collimator was not used for the large-source experiments, the precollimator-detector complex viewed a 7.6-cm-diam region at the center of the lead target cube during measurements of the unattenuated source spectrum at 0°. Thus not all of the neutrons escaping from the 20-cm cube were sampled by the detector, and the measured source spectrum is not exactly suitable as input for calculations. For the most precise results it will be necessary to measure the source over several regions and thus determine a distribution to be used as input. Alternatively, the spectrum measured from the small source can be used to calculate the energies and spatial distributions of neutrons escaping from the lead cube.

Figure 3.4.4 shows the measured 0° spectrum of the large source for water-slab thicknesses of 0, 20, and 40 cm. The source spectrum is relatively smooth, while the spectra transmitted through water reflect the resonance structure of the oxygen total cross section.[3] Thus the broad peak in the oxygen cross section from 3.2 to 3.8 Mev and the strong resonance at 1 Mev produce deep dips in the spectrum, while the windows at 2.3, 6.3, and 6.5 Mev result in peaks. The oxygen window at 8 Mev begins to show an effect on the data for the 40-cm-thick slab.

The neutron attenuation from 20 to 40 cm of water is approximately

$$e^{-\Sigma_t(E)T}$$

in the regions of the cross-section windows, while it is much less than

$$e^{-\Sigma_t(E)T}$$

in the regions of the peaks. It is clear that the windows transmit neutrons which thereafter act as source neutrons for lower energies.

If the attenuation shown in the high peaks of the 20- and 40-cm slab spectra (at 6 and 2.3 Mev) is extrapolated back to a zero water thickness, the result is in agreement with the measured source spectrum within about 25%. Within the limited validity of this extrapolation, this suggests that the 7.6-cm-diam region of the lead contributed four-fifths of the neutrons eventually reaching the detector, and the measured source spectrum may be, for the purpose of calculations, a sufficiently good representation of the true source spectrum.

The 30° spectra for the large source are shown in Fig. 3.4.5, the top curve being that for the source and the lower curves showing the effects of attenuation by 10, 20, and 30 cm of water. The

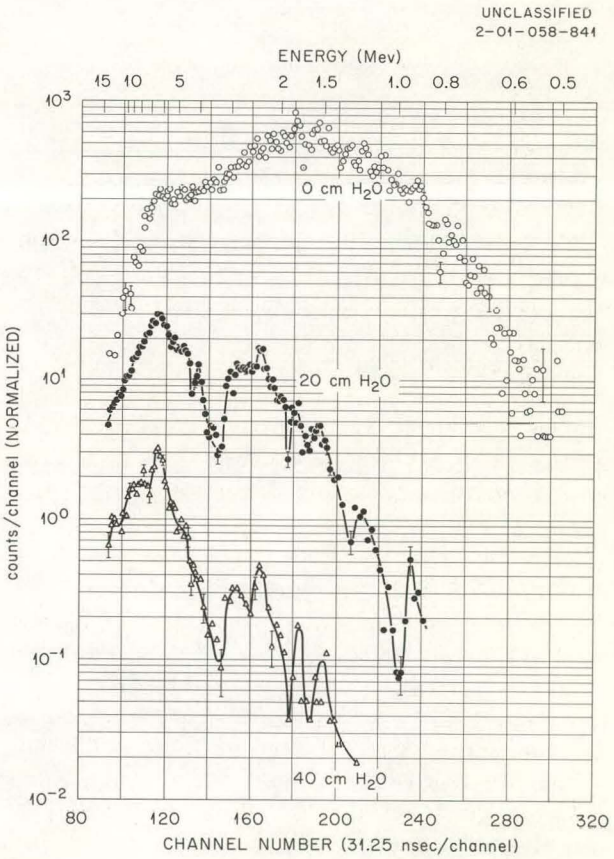

Fig. 3.4.4. Comparison of Leakage Spectra Through 20 and 40 cm of Water with Unattenuated Source Spectrum (0° from Slab Normal).

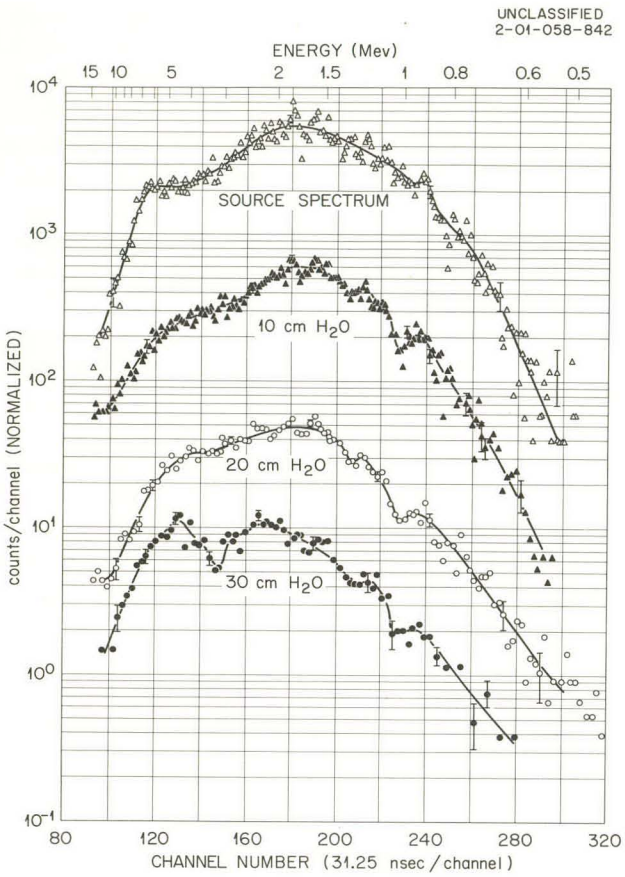

Fig. 3.4.5. Comparison of Leakage Spectra Through 10, 20, and 30 cm of Water with Unattenuated Source Spectrum (30° from Slab Normal).

spectra from the 10- and 20-cm-thick slabs resemble the source spectrum except at 1 Mev, where a strong oxygen resonance exists, and above 6 Mev. The spectrum from the 30-cm-thick slab, however, differs markedly above 2 Mev. A dip appears at about 3.5 Mev, which corresponds to the dip observed in the 0° spectra of the 20- and 40-cm slabs. The prominent peak observed at about 6.5 Mev in Fig. 3.4.4, however, appears to be shifted downward in energy to about 4.5 Mev in Fig. 3.4.5, a factor of $\cos^2(30°)$. This would indicate that scattering by hydrogen is the dominant effect. If the 30° spectrum for 30 cm of water is real, it shows that the 30° neutrons at deep penetrations result from scattering of the 0° neutrons (Fig. 3.4.4) near the face of the slab farthest from the source.

The attenuation by the 30-cm-thick slab appears to be abnormally small relative to the attenuations by the 10- and 20-cm-thick slabs, especially for energies >4 Mev, where the attenuation over the additional 10 cm of water appears to be less than

$$e^{-\Sigma_t(E)T}.$$

This may result from some of the LINAC electrons striking the lead cube rather than the target disk. The lead cube had to be moved relative to the accelerator beam tube each time the slab thickness was altered in the 30° measurements. The fraction of electrons striking the face of the cube (and thereby missing the target disk from which the electron current was monitored) should increase as the cube is moved farther from the window of the accelerator beam tube, because the electron beam diverges due to the scattering by the 0.025-cm-thick titanium exit window. Also, moving the source for each slab thickness can result in a source misalignment for any individual run. Judging from the attenuations produced by the 10- and 20-cm-thick slabs in the energy region below 3 Mev, where the shapes of the 10-, 20-, and 30-cm-thick slab spectra are about the same, a neutron excess of 30 to 40% appears to be produced at the face of the cube.

The sudden change of the 30° spectrum shape between 20 and 30 cm of penetration, whether real or erroneous, requires a more careful measurement of 30° leakage for thicknesses of 30 to 40 cm of water. These depths are within the present capabilities of the LINAC time-of-flight techniques.

Sulfur Activation Data. – In order to obtain a measure of water-slab attenuation independent of running time, beam current, or other factors, pairs of sulfur disks were simultaneously exposed on either side of the water slabs, positioned 7.5 cm off the source-shield axis. The positions are shown in Figs. 3.4.1 and 3.4.2. Five pairs of foils were used, a pair each for the 10-, 30-, and 40-cm-thick slabs, and two pairs for the 20-cm-thick slab. Data from the latter pairs agreed to within 9% and were averaged. The ratio of the activity of the sulfur disk farthest from the source to the activity of the disk nearest the source, corrected for the $1/R^2$ dependence, is a measure of

the attenuation by the slab. The data[9] are plotted in Fig. 3.4.6. The points representing the 20-, 30-, and 40-cm data fall on a straight line (semilog plot), which, however, does not extrapolate to unity. In other words, the attenuation is approximately an exponential function of slab thickness for thicknesses greater than about 15 cm of water. This is somewhat in contrast to similar data obtained in a previous experiment[7] with LiH of 0.75 g/cm^2 compactness, in which the attenuation became exponential before a 10-cm-thickness was traversed. The difference may be due to the resonance structure of oxygen, which causes a 0°-leakage spectrum from 20 cm of water to be much different from the source spectrum. It therefore requires a greater depth in water for the spectral shape to attain a state of quasi-equilibrium.

Summary and Conclusions

For a small source and with a high degree of angular resolution the transmitted flux through a water slab is reduced by the factor

$$e^{-\Sigma_t(E)T}.$$

At about 2° from slab normal, the angular flux is at most about 10% of the 0° flux, and at 4° it is reduced to 2% or less of the 0° flux.

With the large neutron source (poorer angular resolution) the 0° leakage spectra for 20- and 40-cm-thick slabs are attenuated by

$$e^{-\Sigma_t(E)T}$$

only at those energies where windows exist in the oxygen total cross section. The neutrons in these peaks become the source neutrons for deeper penetrations. Results with 40-cm-thick slabs show that 6- to 8-Mev neutrons dominate.

For 30° leakage the shape of the spectrum changes abruptly between slab thicknesses of 20 and 30 cm. The need for deep-penetration data is pointed out by this result, since earlier work with LiH for slab thicknesses up to 20 cm did not show this effect.[5]

From the results detailed above, it is clear that shielding against fission neutrons by water can be improved by adding dense aggregates or elements having large cross sections in the 6- to 8-Mev region, such as nickel, copper, iron, or zinc, provided that minimizing the weight of the shield is not important.

Attenuation measurements using sulfur activation show that the high-energy flux falls off nearly exponentially as a function of slab thickness for thicknesses greater than ~15 cm.

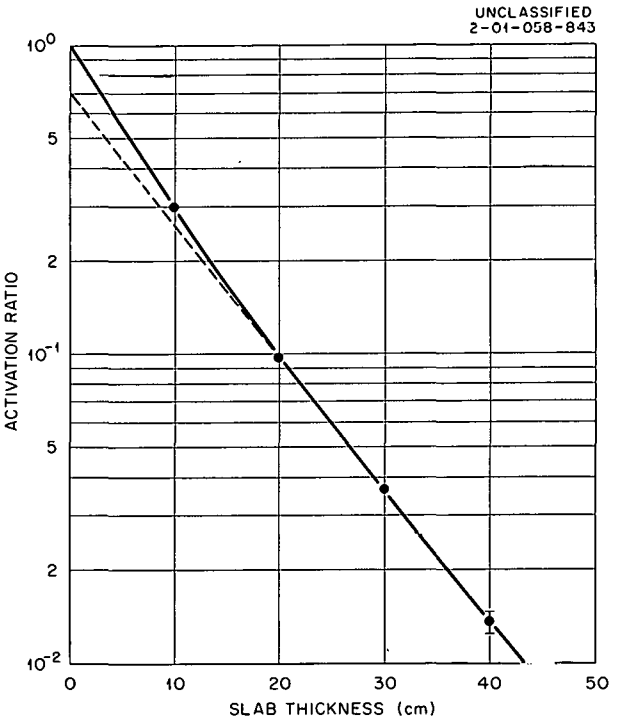

Fig. 3.4.6. Sulfur Activation Ratio as a Function of Thickness of a Water Slab.

[9] It should be observed that these data are for finitely thick slabs. The more common measurement is that of attenuation vs distance from source, where the detector is embedded in the medium and is subject to the effects of backscattering from portions of the medium following the detector.

3.5. MONTE CARLO CALCULATIONS OF FAST-NEUTRON PENETRATION IN LITHIUM HYDRIDE

F. H. S. Clark, F. B. K. Kam, and N. A. Betz[1]

A variety of Monte Carlo calculations of the penetration of lithium hydride by fission neutrons have been performed not only to determine some of the fundamental neutron shielding properties of lithium hydride but also to study the channels through which neutrons penetrate a configuration similar to, but not typical of, a SNAP (Space Nuclear Auxiliary Power) shield. The feasibility of certain SNAP shield experiments was also investigated. The major objections to performing reactor shielding experiments on systems intended for space use have been that air scattering might overwhelm any signal at the detector and that auxiliary shields provided to suppress the air-scattered radiation might themselves scatter in an intolerable background. In order to investigate these effects, a set of calculations was made for a 50.8-g/cm^2-thick lithium hydride shield protected by a shielding collar as shown in Fig. 3.5.1. The collar thicknesses were taken to be 38.8, 44.8, and 50.8 g/cm^2, and the source-detector separation distance was taken as 455 cm. The source was assumed to be an 11-cm-radius disk, and the detector was assumed to be enclosed by a perfect, conical collimator subtending the large end of the shield.

The calculations were performed with the program, or genus of programs, known as 05R (see Sec. 5.6). The lithium nonelastic cross sections tabulated in LA-2643[2] were used, and, apart from interpolations made within the tables, no approximation was made nor was any model imposed on the data. The contribution to output per neutron was recorded in a frequency distribution, and this enabled the statistical validity of the results to be assessed with rather more confidence than is common.

Considerable effort was spent in finding importance sampling and related techniques appropriate to the problem. Among those considered were importance sampling on source energy and angle, systematic sampling of the first-collision region, various weight standards for Russian roulette and for splitting, and biasing the choice of the angle of scatter and the length of flight between collision points.

The results of the calculation are shown in Table 3.5.1, where "Signal Dose" is the dose due to neutrons transported through the shield alone and "Background Dose" is that arriving at the detector after some interaction with the collar. The results indicate that meaningful experimental work can be performed.

Table 3.5.1. Signal and Background Neutron Doses Through Lithium Hydride Shield Surrounded by Lithium Hydride Collar

ρt, Collar Thickness (g/cm^2)	Dose[a]	
	Signal	Background
50.8	4.1×10^{-17}	6.2×10^{-18}
44.8	4.1×10^{-17}	8.1×10^{-18}
38.8	4.1×10^{-17}	3.0×10^{-17}

[a] rad/hr at detector per isotropically distributed neutron at source.

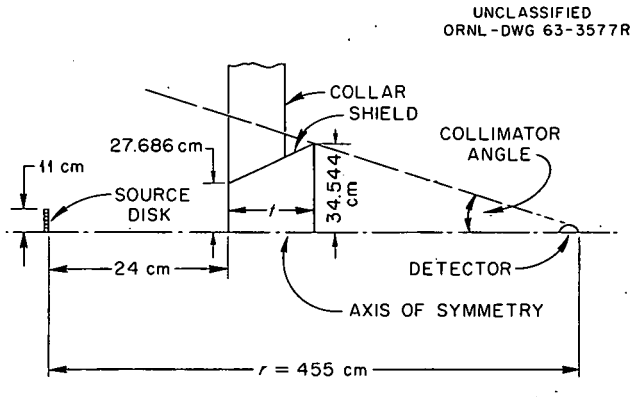

Fig. 3.5.1. Shield-Collar Geometry for Calculations of Neutron Penetration Through Lithium Hydride.

The calculations to determine some of the fundamental shielding properties of lithium hydride were performed both for an infinite-slab geometry, described by Fig. 3.5.1 when the collar and shield

[1] Mathematics Division.

[2] L. Rosen and L. Stewart, *Neutron-Induced Disintegration of Li^6 and Li^7 by 5- to 14-Mev Incident Neutrons*, LA-2643 (1961).

have the same thicknesses and the detector is uncollimated, and for the shield section alone (i.e., Fig. 3.5.1 with no collar present). Computations were made of the total dose on the axis of symmetry at the detector position for slab and shield thicknesses of 40, 44.8, and 50.8 g/cm^2. The results for the infinite-slab calculation are given in Table 3.5.2 and those for the shield section without the collar are presented in Table 3.5.3.

If it is assumed that the medium is describable by a kernel

$$G(S,\rho,l) = e^{-\rho/\lambda}K(S)/l^2 ,$$

where

l = source-detector separation distance (cm),

S = constant = length of minimum-attenuation straight-line trajectory in the system (source to detector) (g/cm^2),

$S + \rho_{max}$ = length of maximum-attenuation straight-line trajectory in the system (source to detector) (g/cm^2),

and $0 \leq \rho \leq \rho_{max}$, then the data are well fitted by setting $\lambda = 4.83 \pm 0.020$ g/cm^2. Earlier moments method calculations[3] for a point-source infinite-medium geometry produced – in this range of material thickness – a corresponding value for λ of 5.44 g/cm^2.[3,4] The difference in the two values is much too large to be attributed to geometric differences. It should be noted that lithium cross sections available to the earlier computations were very incomplete.

A value of $(2.12 \pm 0.13) \times 10^{-10}$ (rad/hr)/(neutron/sec) was obtained for the dose rate through the 50.8-g/cm^2-thick infinite slab. This is to be compared with a value of 1.16×10^{-9} (rad/hr)/(neutron/sec) obtained by interpolating NDA moments method calculations[4] for the same distance, in g/cm^2, and converting from reps to rads (assuming that 1 rep = 0.93 rad). Geometric considerations again make these numbers not strictly comparable, but the geometric effect is certainly small compared with this difference. Recent

Table 3.5.2. Calculated Neutron Doses Through Various Thicknesses of an Infinite Slab of Lithium Hydride

(Isotropic Disk Source)

ρt, Slab Thickness (g/cm^2)	$4\pi r^2 G(t)$ (rad/source neutron)[a]
40	$(5.55 \pm 0.44) \times 10^{-13}$
44.8	$(2.24 \pm 0.24) \times 10^{-13}$
50.8	$(5.88 \pm 0.36) \times 10^{-14}$

[a] $4\pi r^2 = 2.59 \times 10^6$ cm^2.

[3] R. Aronson and C. N. Klahr, p 85 in "Shielding," vol III, part. B, of *Reactor Handbook*, 2d ed., revised, Interscience, New York, 1962.

[4] H. Goldstein, NDA-42 (classified).

Table 3.5.3. Neutron Fluxes and Doses Through Lithium Hydride Shield

(No Collar; Isotropic Disk Source)

Shield Thickness (g/cm^2)	$4\pi r^2 \phi n$ (neutrons/source neutron)	$4\pi r^2 D_n$ (rad · cm^2/source neutron)	Ratio: Dose at Detector / Flux at Detector
40	8.49×10^{-5}	3.64×10^{-13}	4.29×10^{-9}
44.8	2.22×10^{-5}	1.07×10^{-13}	4.82×10^{-9}
50.8	6.43×10^{-6}	3.28×10^{-14}	5.11×10^{-9}

measurements at Atomics International[5] suggest that the NDA computations lead to doses that are too high and to relaxation lengths that are too long, and our calculations are in general agreement with this conclusion.

As can be seen from Table 3.5.3, the dose through the shield with no collar present is less by a factor of approximately 2 than that transmitted by the infinite slab. These data have not been analyzed in the above fashion to determine a value of λ, since the statistical deviation of these numbers was not determined in the calculation. It should be noted, however, that the statistical deviation of the numbers for the shield transmission must be larger than that for the infinite slab since both were derived from the same Monte Carlo calculation. As can be seen by the ratio of the dose to neutron flux at the detector, the flux arriving at the detector must consist of quite energetic neutrons. Since the ratio appears to be increasing as the shield becomes thicker, there is indication that the spectrum is still not in equilibrium.

[5]S. G. Wogulis, Atomics International; private communication.

3.6. THE $1/A$ SOLUTION TO THE BOLTZMANN EQUATION FOR A HEAVY MEDIUM AND COMPARISON WITH OTHER METHODS

R. E. Maerker

Considerable interest has developed in France recently in attempting to improve upon the results of age theory for obtaining the slowing-down density in a nonhydrogenous medium up to distances of the order of 100 cm. This paper presents a condensed version of a report issued at Fontenay-aux-Roses of work done by the author in collaboration with F. LeBerre during a year's study in France.[1]

It is conjectured that age theory fails at the larger penetration distances because of the assumption of near-isotropy of the flux. The theory presented here makes no such assumption, and involves an approximation to the scattering integral completely independent of the angular distribution of the flux.

For the case of a plane isotropic monoenergetic source of fast neutrons embedded in an infinite medium of mass number A, under the assumptions of isotropic elastic scattering and no inelastic scattering, the Boltzmann equation may be written as

$$\mu \frac{\partial \phi(x,u,\mu)}{\partial x} + \Sigma_t(u)\phi = \frac{(A+1)^2}{8\pi A} \int_{u-q}^{u} e^{-(u-u')}\, du' \iint_{\text{sphere}} d\Omega' \Sigma_s(u')\phi(x,u',\mu') \times \delta\left[\vec{\Omega}\cdot\vec{\Omega}' - \frac{A+1}{2} e^{-(u-u')/2} + \frac{A-1}{2} e^{(u-u')/2}\right] + \frac{\delta(u)\delta(x)}{4\pi}, \quad (1)$$

[1]F. LeBerre and R. Maerker, *Comparison of Several Mathematical Methods for Calculating the Slowing-Down Density in a Heavy Medium*, DEP/SEPP 263/63, Centre d'Etudes Nucléaires de Fontenay-aux-Roses.

where

$\phi(x,u,\mu)$ = flux/steradian-unit lethargy,

$\Sigma_T(u)$ = total cross section in cm^{-1},

$\Sigma_s(u)$ = scattering cross section in cm^{-1},

$q = 2\ln\left(\frac{A+1}{A-1}\right)$,

δ = Dirac delta function,

$\vec{\Omega}$ = direction of the neutron specified by μ, in the direction cosine along x, and ψ,

$\vec{\Omega}'$ = direction of the neutron before the collision that changed its direction to $\vec{\Omega}$,

$u = \ln\frac{E_0}{E}$, the lethargy.

Expanding

$$f(u' \rightarrow u, \vec{\Omega}' \rightarrow \vec{\Omega}) = \frac{(A+1)^2}{8\pi A} e^{-(u-u')} \delta\left[\vec{\Omega}\cdot\vec{\Omega}' - \frac{A+1}{2} e^{-(u-u')/2} + \frac{A-1}{2} e^{(u-u')/2}\right]$$

in Legendre polynomials of $\vec{\Omega}\cdot\vec{\Omega}' = \cos\Theta$,

$$f(u' \rightarrow u, \vec{\Omega}' \rightarrow \vec{\Omega}) = \sum_l \frac{2l+1}{2} f_l(u' \rightarrow u) P_l(\cos\Theta),$$

where

$$f_l(u' \rightarrow u) = \frac{(A+1)^2}{8\pi A} e^{-(u-u')} P_l\left[\frac{A+1}{2} e^{-(u-u')/2} - \frac{A-1}{2} e^{(u-u')/2}\right],$$

and, since

$$\cos\Theta = \mu\mu' + \sqrt{1-\mu^2}\sqrt{1-\mu'^2}\cos(\psi-\psi'),$$

by the addition theorem for Legendre polynomials

$$P_l(\cos\Theta) = P_l(\mu) P_l(\mu') + \text{terms in } \cos n(\psi-\psi').$$

Integrating the first term on the right of Eq. (1) over ψ' thus yields

$$\sum_l \frac{2l+1}{2} P_l(\mu) \int_{-1}^{1} P_l(\mu')\, d\mu' \int_{u-q}^{u} \frac{(A+1)^2}{4A} e^{-(u-u')} \times P_l\left[\frac{A+1}{2} e^{-(u-u')/2} - \frac{A-1}{2} e^{(u-u')/2}\right] \Sigma_s(u')\phi(x,u',\mu')\, du',$$

so that Eq. (1) may now be rewritten as

$$\mu\frac{\partial\phi}{\partial x} + \Sigma_T(u)\phi = \sum_l \frac{2l+1}{2} P_l(\mu)\, h_l(x,u,A) + \frac{\delta(u)\delta(x)}{4\pi}. \qquad (2)$$

Taking the Fourier transform of Eq. (2) with respect to x yields

$$[\mu i\alpha + \Sigma_T(u)]\Phi(\alpha,u,\mu) = \sum_l \frac{2l+1}{2} H_l(\alpha,u,A)\, P_l(\mu) + \frac{\delta(u)}{4\pi}, \tag{3}$$

where

$$\Phi(\alpha,u,\mu) = \int_{-\infty}^{\infty} e^{-i\alpha x}\, \phi(x,u,\mu)\, dx,$$

$$H_l(\alpha,u,A) = \int_{-\infty}^{\infty} e^{-i\alpha x}\, h_l(x,u,A)\, dx,$$

with the transform variable α being real.

Expanding $\phi(x,u,\mu)$ and $\Phi(\alpha,u,\mu)$ in Legendre polynomials, we have

$$\phi(x,u,\mu) = \sum_m \frac{2m+1}{2} P_m(\mu)\, \phi_m(x,u),$$

and

$$\Phi(\alpha,u,\mu) = \sum_m \frac{2m+1}{2} P_m(\mu)\, \Phi_m(\alpha,u),$$

so that Eq. (3) may be integrated over μ to give

$$\Phi_0(\alpha,u) = \sum_l \frac{2l+1}{2} a_l[\alpha, \Sigma_T(u)] H_l(\alpha,u,A) + \frac{\delta(u)}{2\pi\alpha} \arctan\frac{\alpha}{\Sigma_T(u)}, \tag{4}$$

where

$$a_l(\alpha,u) = \int_{-1}^{1} \frac{P_l(\mu)\, d\mu}{\mu i\alpha + \Sigma_T(u)},$$

and

$$H_l(\alpha,u,A) = \int_{u-q}^{u} e^{-(u-u')} \frac{(A+1)^2}{4A} P_l\left[\frac{A+1}{2} e^{-(u-u')/2} - \frac{A-1}{2} e^{(u-u')/2}\right] \Sigma_s(u')\Phi_l(\alpha,u')\, du'. \tag{5}$$

The a_l's satisfy the recurrence relation

$$a_l(\alpha,u) = \frac{2l-1}{l}\frac{2}{i\alpha}\delta_{0,l-1} - \frac{2l-1}{l}\frac{\Sigma_T(u)}{i\alpha} a_{l-1} - \frac{l-1}{l} a_{l-2},$$

where the δ here represents the Kronecker delta.

A first integral to be used in conjunction with Eq. (4) may be obtained by integrating Eq. (3) over μ:

$$i\alpha\Phi_1(\alpha,u) + \Sigma_T(u)\Phi_0(\alpha,u) = H_0(\alpha,u,A) + \frac{\delta(u)}{2\pi}. \tag{6}$$

Let us suppose that $\Sigma_s(u')\Phi(x,u',\mu)$, and consequently $\Sigma_s(u')\Phi_l(\alpha,u')$, may be adequately represented by the first two terms in the Taylor series expansion about u. Then

$$\Sigma_s(u')\Phi_l(\alpha,u') \cong \Sigma_s(u)\Phi_l(\alpha,u) + (u' - u)\frac{\partial}{\partial u}\left[\Sigma_s(u)\Phi_l(\alpha,u)\right],$$

and

$$H_l(\alpha,u,A) = \frac{(A+1)^2}{4A}\left\{I_l(A)\,\Sigma_s(u)\Phi_l(\alpha,u) - J_l(A)\frac{\partial}{\partial u}\left[\Sigma_s(u)\Phi_l(\alpha,u)\right]\right\},$$

where

$$I_l(A) = \int_{u-q}^{u} e^{-(u-u')} P_l\left[\frac{A+1}{2}e^{-(u-u')/2} - \frac{A-1}{2}e^{(u-u')/2}\right] du', \tag{7}$$

and

$$J_l(A) = \int_{u-q}^{u} e^{-(u-u')}(u-u') P_l\left[\frac{A+1}{2}e^{-(u-u')/2} - \frac{A-1}{2}e^{(u-u')/2}\right] du'. \tag{8}$$

If A is large compared with unity, $q \cong 4/A$. If, further, $u > q$, then Eqs. (7) and (8) become

$$I_l(A) = \int_0^q e^{-t} P_l\left(\frac{A+1}{2}e^{-t/2} - \frac{A-1}{2}e^{t/2}\right) dt,$$

and

$$J_l(A) = \int_0^q te^{-t} P_l\left(\frac{A+1}{2}e^{-t/2} - \frac{A-1}{2}e^{t/2}\right) dt.$$

Through terms of order $1/A$,

$$\frac{(A+1)^2}{4A} I_{2k+1} = \frac{2}{3A}\delta_{1,2k+1},$$

$$\frac{(A+1)^2}{4A} I_{2k} = \delta_{0,2k},$$

$$\frac{(A+1)^2}{4A} J_{2k+1} = -\frac{2}{3A}\delta_{1,2k+1},$$

$$\frac{(A+1)^2}{4A} J_{2k} = \frac{2}{A}\delta_{0,2k}.$$

Equation (4) becomes, through terms of order $1/A$,

$$\Phi_0(\alpha,u) = \frac{\delta(u)}{2\pi\alpha}\arctan\frac{\alpha}{\Sigma_T(u)} + \frac{2}{\alpha}\arctan\frac{\alpha}{\Sigma_T(u)}\left[\frac{\Sigma_s(u)\Phi_0}{2} - \frac{1}{A}\frac{\partial}{\partial u}(\Sigma_s\Phi_0)\right]$$

$$+ \frac{2i}{A\alpha}\left(\frac{\Sigma_T}{\alpha}\arctan\frac{\alpha}{\Sigma_T} - 1\right)\left[\Sigma_s\Phi_1 + \frac{\partial}{\partial u}(\Sigma_s\Phi_1)\right],$$

and Eq. (6) becomes

$$i\alpha\,\Phi_1(\alpha,u) + \Sigma_T(u)\Phi_0(\alpha,u) = \Sigma_s(u)\Phi_0 - \frac{2}{A}\frac{\partial}{\partial u}(\Sigma_s\Phi_0) + \frac{\delta(u)}{2\pi}.$$

Eliminating $\Phi_1(\alpha,u)$ from the two equations above gives a first-order differential equation for Φ_0 if the term $(\partial^2/\partial u^2)[\Sigma_s(u)\Phi_0(\alpha,u)]$ is neglected. The solution to this first-order differential equation may be written

$$\Sigma_s(u)\Phi_0(\alpha,u) = \int_0^u \frac{R(\alpha,t)}{P(\alpha,t)}\, e^{-\int_t^u [Q(\alpha,v)/P(\alpha,v)]\,dv}\, dt, \tag{9}$$

where

$$P(\alpha,u) = \frac{2\Sigma_T}{A\alpha}\arctan\frac{\alpha}{\Sigma_T} + \frac{2\Sigma_T}{A\alpha^2}\left(\frac{\Sigma_T}{\alpha}\arctan\frac{\alpha}{\Sigma_T} - 1\right)\left[\Sigma_a + \frac{2}{A}(\Sigma_s + \Sigma_s')\right],$$

$$Q(\alpha,u) = \frac{\Sigma_T}{\Sigma_s} - \frac{\Sigma_T}{\alpha}\arctan\frac{\alpha}{\Sigma_T} + \frac{2\Sigma_T}{A\alpha^2}\left(\frac{\Sigma_T}{\alpha}\arctan\frac{\alpha}{\Sigma_T} - 1\right)(\Sigma_a + \Sigma_a'),$$

$$R(\alpha,u) = \frac{\Sigma_T\delta(u)}{2\pi\alpha}\arctan\frac{\alpha}{\Sigma_T} + \frac{\Sigma_T}{\pi A\alpha^2}\left(\frac{\Sigma_T}{\alpha}\arctan\frac{\alpha}{\Sigma_T} - 1\right)\{\Sigma_s\delta(u) + [\Sigma_s\delta(u)]'\}.$$

In the above equations a prime denotes differentiation with respect to u, and $\Sigma_a(u)$ is the absorption cross section.

The total flux $\phi(x,u) = 2\pi\phi_0(x,u)$, and is obtained by taking the inverse Fourier transform of $\Phi_0(\alpha,u)$:

$$\phi(x,u) = 2\int_0^\infty \Phi_0(\alpha,u)\cos\alpha x\, d\alpha.$$

The moments $M_n(u)$ of the total flux $\phi(x,u)$ are readily calculated from the transform $\Phi_0(\alpha,u)$. Thus,

$$M_n(u) = \int_{-\infty}^{\infty} x^n\phi(x,u)\,dx = 2\pi \int_{-\infty}^{\infty} x^n\phi_0(x,u)\,dx \qquad n = 0, 1, 2, \ldots.$$

Since $\phi_0(x,u) = \phi_0(-x,u)$, the odd moments are zero. The even moments may be written

$$M_{2n}(u) = 2\pi\int_{-\infty}^{\infty} x^{2n}\,\phi_0(x,u)\,dx \qquad n = 0, 1, 2, \ldots.$$

Now,

$$\frac{\partial^{2n}}{\partial\alpha^{2n}}[\Phi_0(\alpha,u)] = (-1)^n \int_{-\infty}^{\infty} x^{2n}\, e^{-i\alpha x}\, \phi_0(x,u)\, dx\ ,$$

so that

$$M_{2n}(u) = 2\pi(-1)^n \left[\frac{\partial^{2n}}{\partial\alpha^{2n}}\Phi_0(\alpha,u)\right]_{\alpha=0}\ . \tag{10}$$

A numerical example was chosen to compare the results of the $1/A$ theory with those of the age theory and a Monte Carlo calculation.

For E_0 = 2.5 Mev and carbon (A = 12) as the medium, which is a relatively demanding value of A with which to test the theory, the absorption cross section $\Sigma_a(u)$ is negligible for all energies below 2.5 Mev, and Eq. (9) simplifies to, with $\Sigma_T(u) = \Sigma_s(u) = \Sigma(u)$,

$$\Phi_0(\alpha,u) = \frac{3}{\pi\Sigma(u)}\, e^{-\int_0^u [Q(\alpha,v)/P(\alpha,v)]\, dv}\ ,$$

where

$$\frac{Q(\alpha,v)}{P(\alpha,v)} = \frac{6}{\dfrac{[\Sigma(v)/\alpha]\ \arctan\,[\alpha/\Sigma(v)]}{1-[\Sigma(v)/\alpha]\ \arctan\,[\alpha/\Sigma(v)]} - \dfrac{\Sigma(v)}{6\alpha^2}\,[\Sigma(v)+\Sigma'(v)]}\ .$$

The expression for the total flux becomes

$$\phi(x,u) = \frac{6}{\pi\Sigma(u)} \int_0^{\infty} \cos\,\alpha x\, e^{-\int_0^u [Q(\alpha,v)/P(\alpha,v)]\, dv}\, d\alpha\ , \tag{11}$$

which can be compared with the age theory expression

$$\phi(x,u) = \frac{A}{4\Sigma(u)\sqrt{\pi}}\, \frac{e^{-x^2/4\tau(u)}}{\sqrt{\tau(u)}}\ , \tag{12}$$

where

$$\tau(u) = \frac{A}{6(1-\frac{2}{3}A)} \int_0^u \frac{du'}{\Sigma^2(u')}\ .$$

Table 3.6.1 illustrates a comparison of Eqs. (11) and (12), where $\Sigma(u)$ was taken from BNL-325 and the results are hand-calculated. It should be pointed out that $\Sigma'(u)/\Sigma(u)$ must be of order 1 or less for the $1/A$ theory to hold, and thus any resonance or antiresonance peaks which occur in the cross section must be smoothed in some averaging manner. Thus the slowing-down density derived from $1/A$ theory is more accurately an average value over a finite energy interval.

Table 3.6.1. Comparison of $\phi(x,u)$ Calculated by $1/A$ Theory and Age Theory

x (cm)	$u = 1.145$			$u = 2.55$			$u = 4.15$			$u = 15$		
	ϕ_{age}	$\phi_{1/A}$	$\phi_{1/A}/\phi_{age}$	ϕ_{age}	$\phi_{1/A}$	$\phi_{1/A}/\phi_{age}$	ϕ_{age}	$\phi_{1/A}$	$\phi_{1/A}/\phi_{age}$	ϕ_{age}	$\phi_{1/A}$	$\phi_{1/A}/\phi_{age}$
0	0.78	0.81	1.04	0.45	0.46	1.02	0.37	0.36	0.97	0.26	0.26	1.00
7.7	0.65	0.62	0.95	0.40	0.39	0.98	0.33	0.33	1.00	0.24	0.24	1.00
15.4	0.37	0.32	0.86	0.27	0.25	0.93	0.24	0.23	0.96	0.21	0.21	1.00
38.5	0.0075	0.016	2.15	0.017	0.016	0.94	0.025	0.025	1.00	0.071	0.067	0.94

With the aid of Eqs. (9) and (10), expressions may be derived for the moments $M_{2n}(u)$. The results are presented in Figs. 3.6.1–3.6.3, where comparisons with a Monte Carlo calculation[2] and age-theory expressions are also given.

From these numerical examples, it is difficult to compare the merits of $1/A$ theory with those of the age theory, and a more detailed analysis through large penetration distances with the aid of a digital computer is required to determine whether or not the $1/A$ theory is superior to the age theory, which is known to underestimate the flux at large distances. A possible indication that $1/A$ theory is better at the larger penetration distances is the last entry in Table 3.6.1 for $u = 1.145$ (~ 0.8 Mev), but the possibility of calculational errors reduces the significance of this result.

Both the age theory and the $1/A$ theory developed up until now suffer from the obvious defect that they should not represent the slowing-down density at energies near the source energy at all well because they neglect any consequence of the discontinuities of the flux at the first scattering limit, $u = q$. If an attempt is made to improve upon the $1/A$ theory by taking into consideration the discontinuity in the flux at $u = q$, a problem is immediately encountered in that I_l and J_l defined earlier are functions of u as well as A and contain terms of order $1/A$ for $l > 1$. However, a $P_1, 1/A$ theory may be developed which should still improve on the $1/A$ theory and age theory for small u. The starting point for such a theory would be Eqs. (7) and (8), which become for $0 < u < q$

$$I_l(A,u) = \int_0^u e^{-t} P_l\left(\frac{A+1}{2} e^{-t/2} - \frac{A-1}{2} e^{t/2}\right) dt ,$$

and

$$J_l(A,u) = \int_0^u te^{-t} P_l\left(\frac{A+1}{2} e^{-t/2} - \frac{A-1}{2} e^{t/2}\right) dt .$$

The decomposition of $\Sigma_s(u')\Phi_l(\alpha,u')$ in the region $0 < u < q$ must contain a term proportional to the uncollided flux transform:

$$\Sigma_s(u-t)\Phi_l(\alpha,u-t) = \Sigma_s(0)\Phi_l(\alpha,0)\delta(u-t) + \Sigma_s(u)\Phi_l(\alpha,u) - t\frac{\partial}{\partial u}[\Sigma_s(u)\Phi_l(\alpha,u)] , \qquad (13)$$

[2]Sivagnanam, unpublished work at the Centre d'Etudes Nucléaires de Fontenay-aux-Roses.

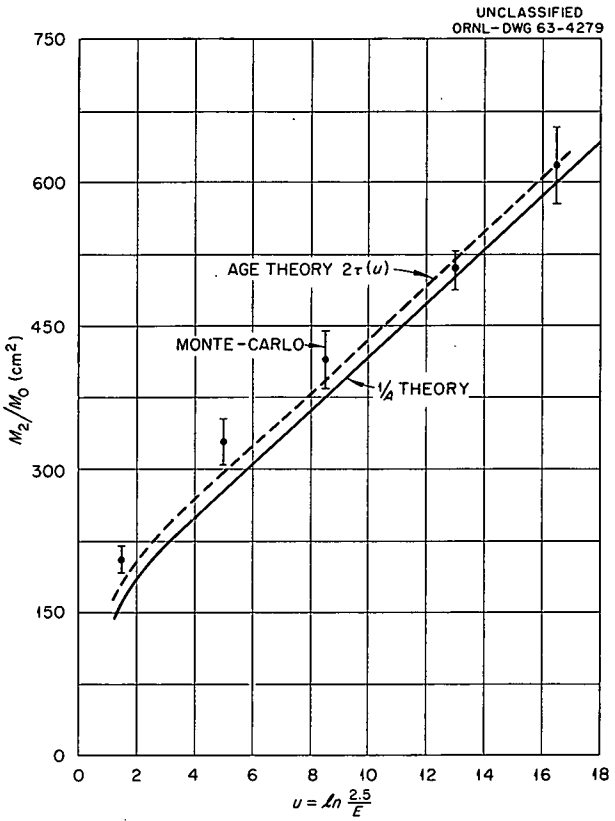

Fig. 3.6.1. Comparison of M_2/M_0 as Calculated by $1/A$ Theory, Age Theory, and Monte Carlo.

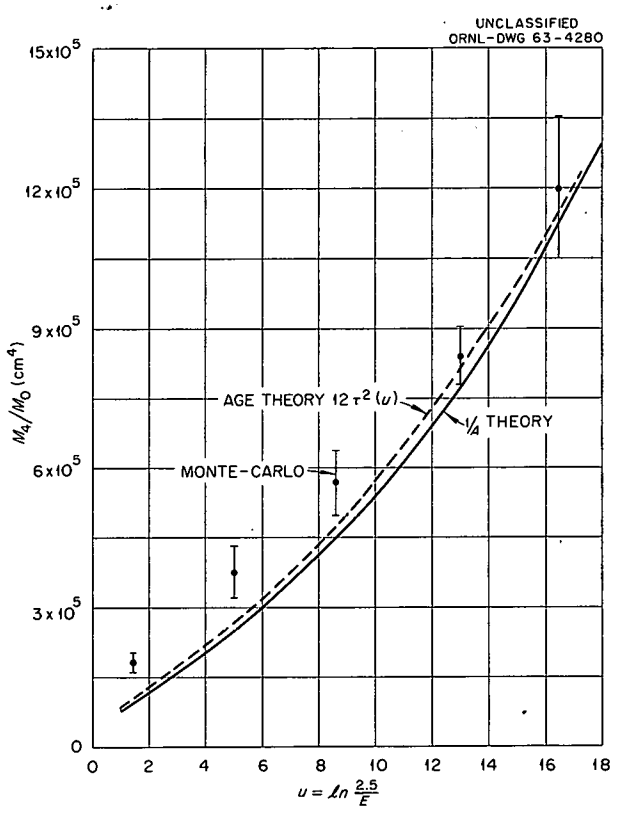

Fig. 3.6.2. Comparison of M_4/M_0 as Calculated by $1/A$ Theory, Age Theory, and Monte Carlo.

where $\Phi_l(\alpha,0) = a_l(\alpha,0)/4\pi$. Thus, from Eq. (5),

$$H_l(\alpha,u,A) = \frac{(A+1)^2}{4A}\left\{ I_l(u,A)\Sigma_s(u)\Phi_l(\alpha,u) - J_l(u,A)\frac{\partial}{\partial u}[\Sigma_s(u)\Phi_l(\alpha,u)] \right.$$
$$\left. + \Sigma_s(0)\frac{a_l(\alpha,0)}{4\pi}e^{-u}P_l\left(\frac{A+1}{2}e^{-u/2} - \frac{A-1}{2}e^{u/2}\right)\right\}. \quad (14)$$

From Eq. (4), a discontinuity in $\Phi_0(\alpha,q)$ and hence in $\phi(x,q)$ occurs because of the disappearance of the neutrons suffering a single collision, and is

$$\Sigma_s\Phi_0(\alpha,q-) - \Sigma_s\Phi_0(\alpha,q+) = \frac{(A+1)^2}{16\pi A}\Sigma_s(0)\Sigma_s(q)\,e^{-q}\sum_l \frac{2l+1}{2}a_l(\alpha,q)a_l(\alpha,0)P_l(-1)$$
$$= \frac{(A-1)^2}{16\pi A}\Sigma_s(0)\Sigma_s(q)\sum_l \frac{2l+1}{2}a_l(\alpha,q)a_l(\alpha,0)(-1)^l.$$

Expanding $I_l(u,A)$ into a series of terms through order $1/A$ and of $J_l(u,A)$ through order $1/A^2$ for $l = 0$ and 1, substituting into Eq. (14) and expanding H_l through terms of order $1/A$, then eliminating

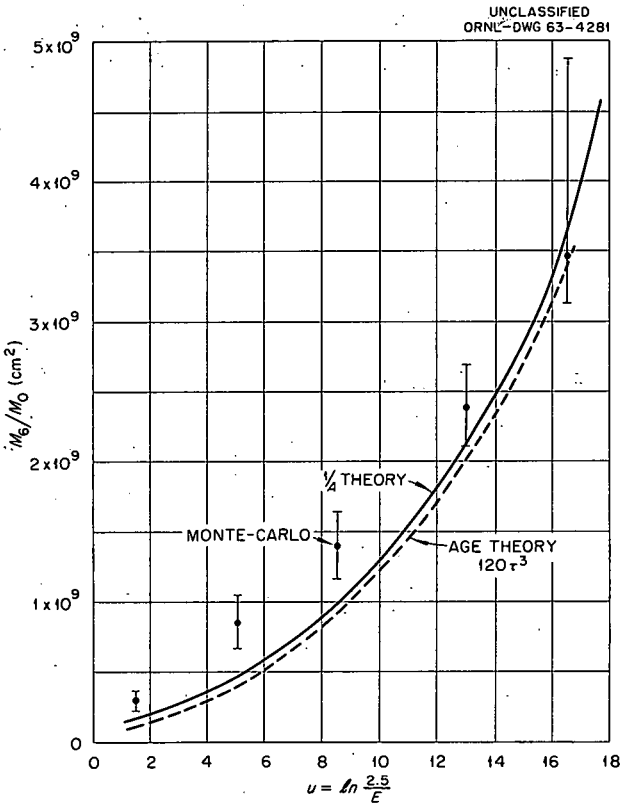

Fig. 3.6.3. Comparison of M_6/M_0 as Calculated by $1/A$ Theory, Age Theory, and Monte Carlo.

$\Phi_1(\alpha,u)$ as before leads to a first-order differential equation for $\Phi_0(\alpha,u)$ in the range $0 < u < q$. The scattered flux is discontinuous at $u = 0$ as well as at $u = q$. For $u = 0$, $H_l = 0$, and the scattered flux is zero, but for $u \rightarrow 0$ from positive values, through $l = 1$ terms,

$$\lim_{u\to 0} \Sigma_s \Phi_0(\alpha,u) = \frac{\Sigma_s^2(0)}{8\pi}\left(\frac{A}{4}+\frac{1}{2}\right)[a_0^2(\alpha,0) + 3a_1^2(\alpha,0)] .$$

The slowing-down density in the region $q < u < 2q$ may be calculated, once the slowing-down density in the region $0 < u < q$ is known, by decomposing $H_l(\alpha,u,A)$ into two integrals, one from $(u - q)$ to q, which involves the previously calculated fluxes in the region $0 < u < q$ and is the source function, and the other from 0 to $(u - q)$, for which the fluxes are to be calculated. The entire procedure may be carried on through all the ranges of u in steps of q but the mathematical complexity increases with each step; it should suffice to stop this calculation at $u = 2q$ and introduce $\Phi_0(\alpha,2q)$ as a boundary condition to Eq. (9) and proceed for higher u using $1/A$ theory.

For the case of carbon, $E_0 = 2.5$ Mev, and $\Sigma_T(u) = \Sigma_s(u) = \Sigma_s = 0.200\ \text{cm}^{-1}$, values of $2\pi\Sigma\Phi_0(\alpha,u)$ are given in Table 3.6.2 as calculated by P_1, $1/A$ *theory*. Following Eq. (13), $\Sigma\Phi_0(\alpha,u)$ is linear in u for $0 < u < q$ and $q < u \leq 2q$. Also presented are the values of $2\pi\Sigma\Phi_0(\alpha,2q)$ as calculated from Eq. (9) from the $1/A$ theory.

The difference in the last two columns of Table 3.6.2 in the Fourier transform of the slowing-down density is considerable for large α and affects the flux at the larger penetration distances, as can be seen from Table 3.6.3.

It is to be observed that for small x the three theories agree, surprisingly enough, but that as x increases, the $P_1, 1/A$ theory gives higher and probably more correct values for energies near that of the source.

Table 3.6.2. Values of $2\pi\Sigma\Phi_0(\alpha,u)$ Calculated from $P_1, 1/A$ Theory for $0 < u \leq 2q$ and Comparison with $1/A$ Theory at $u = 2q$

α	$2\pi\Sigma\Phi_0(\alpha,0+)$	$2\pi\Sigma\Phi_0(\alpha,q-)$	$2\pi\Sigma\Phi_0(\alpha,q+)$	$2\pi[\Sigma\Phi_0(\alpha,2q)]_{P_1,1/A}$	$2\pi[\Sigma\Phi_0(\alpha,2q)]_{1/A}$
0	3.5	7.5	5.5	5.9	6.0
0.1	2.8	5.8	4.0	3.9	4.3
0.3	0.96	2.3	1.1	0.90	0.14
0.5	0.33	1.1	0.38	0.29	0.12
0.8	0.088	0.57	0.12	0.10	1.7×10^{-3}
1.0	0.044	0.41	0.071	0.056	1.6×10^{-4}
2.0	0.00	0.13	0.010	0.007	3.3×10^{-10}

Table 3.6.3. Comparison of the Total Fluxes at $u = 2q$ Calculated by the Different Theories

x (cm)	Age Theory	$1/A$ Theory	$P_1, 1/A$ Theory
0	0.30	0.35	0.39
10	0.14	0.12	0.11
20	0.015	0.016	0.022
25	0.0027	0.0030	0.010

3.7. FAST-NEUTRON DOSE RATES BEHIND SLABS OF WATER AND OF CONCRETE: COMPARISON OF TSF EXPERIMENTAL RESULTS WITH CALCULATIONS

R. M. Freestone, Jr.

Introduction

Curves of neutron dose transmission factors as functions of material thickness and angle of neutron incidence have been published by Allen *et al.*[1] Their results were obtained from Monte Carlo calculations which employed a splitting technique to allow the calculation of deep penetrations. The published transmission factors have been utilized, together with an experimentally measured neutron spectrum of the Tower Shielding Reactor II (TSR-II), to compute dose rates behind various thicknesses of water and concrete for comparison with experimental measurements made with the TSR-II.

Method

The dose transmission factors of Allen *et al.* were calculated for monoenergetic neutrons incident at specified angles upon laterally infinite slabs of various materials. Data are generally given for six source energies, 0.5, 1, 2, 3, 5, and 14 Mev, and for as many as four incident angles, 0, 30, 45, and 70°. The first step in the present calculation was to cross plot the transmission factors vs neutron energy for various material thicknesses. From these plots, interpolations were made for energies at which data were not given.

The neutron energy spectrum to which the factors of ref 1 were applied is shown in Fig. 3.7.1. It was measured at a distance of 40 ft from the TSR-II, which was enclosed in the reactor shield identified as COOL-I. It was with this configuration that most of the experimental data available for comparison were obtained. Both the reactor[2] and the COOL-I reactor shield[3] are described elsewhere.

The calculation proceeded as follows: The experimental spectrum, over the range 0 to 10 Mev, was divided into 15 energy intervals, the widths of which were chosen so as to achieve the greatest detail in the region where the spectrum varied rapidly. Integration over each energy width and

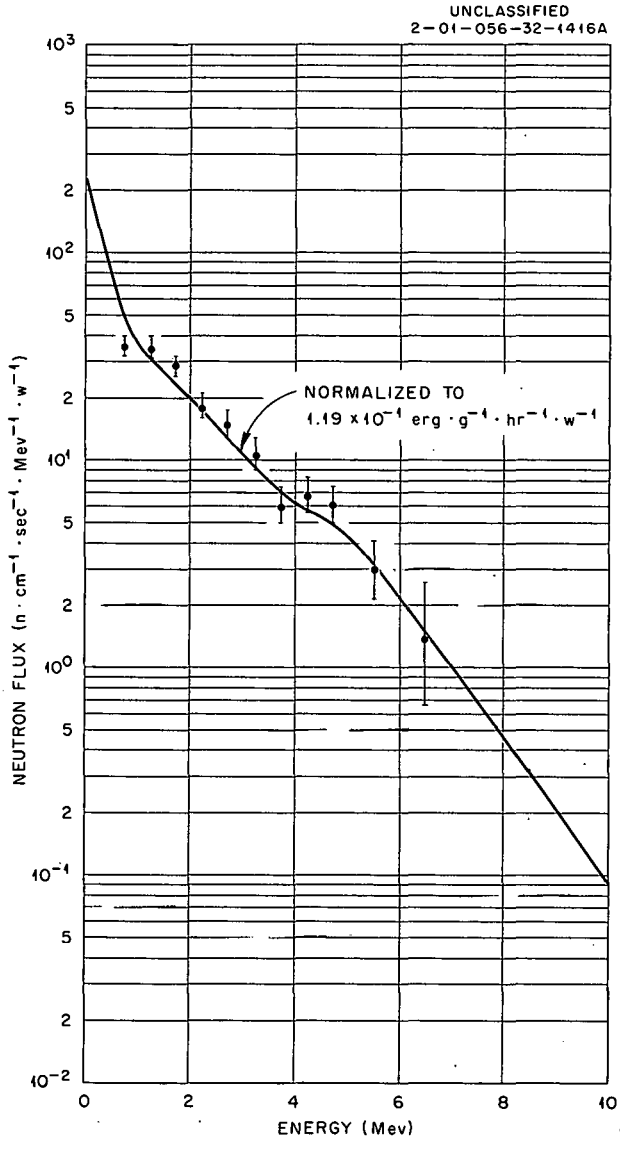

Fig. 3.7.1. Neutron Spectrum of the Tower Shielding Reactor II in the COOL-I Shield.

[1] F. J. Allen, A. T. Futterer, and W. P. Wright, *Neutron Transmission Versus Thickness for Some Common Materials*, BRL-1174 (September 1962).

[2] L. B. Holland *et al.*, *Neutron Phys. Div. Ann. Progr. Rept. Sept. 1, 1960*, ORNL-3016, p 42.

[3] L. B. Holland *et al.*, *Neutron Phys. Div. Ann. Progr. Rept. Sept. 1, 1962*, ORNL-3360, p 123.

multiplication by the first collision flux-to-dose conversion factors for standard tissue given in *NBS Handbook* 75[4] resulted in values of dose rate due to the neutrons within each of the 15 energy widths. The dose conversion factor corresponding to the mean energy of each width was used. This "dose-rate spectrum" was then used as the source term against which the transmission factors of Allen *et al.*[1] were applied. The transmission factors computed by Allen *et al.* used multicollision flux-to-dose conversion factors, whereas first-collision dose conversion factors were used in the present calculation. This difference will not seriously affect the present results, since the two curves can be arbitrarily normalized to within ±10% in shape, which is well within the error of the experimental measurements used for comparisons. All experimental data were obtained from dosimeters calibrated against a single-collision dose curve. With the unattenuated dose-rate spectrum computed, the remainder of the calculation involved simply multiplying the dose increment by the transmission factor appropriate to the mean energy of the interval and to the material and incident angle of interest. The sum over all energy intervals then gave the total transmitted dose rate for any required configuration of material.

Available Experimental Data[5]

The experimental data utilized in these comparisons was not taken especially for this purpose, and thus is not exactly suitable. The data on water penetration, for example, results from a measurement in which a collimated beam from the TSR-II in the beam shield was allowed to impinge upon a 5-ft cube of water contained within ¼-in.-thick steel walls. The beam emanated from a 10-in.-diam cylindrical hole in the shield. A 2-in.-thick lead disk was placed at the inner end of the hole. The distance from the center of the reactor to the center of the cube was 101 ft. The dose rates were normalized to the dose rate measured in air at the same distance.

The experimental data for concrete were compiled from a series of measurements made beneath 6-ft square concrete slabs covering a 4-ft-diam concrete-lined hole in the ground at the Tower Shielding Facility. The original measurements consisted of dose-rate traverses in air down the center line of the hole, and for the present purpose the dose value directly under the concrete was selected from each traverse. The TSR-II was stationed a constant 100-ft distance from the center of the top of the slab for these measurements.

Results

Experimental and calculated fast-neutron dose rates are compared in Fig. 3.7.2 for neutrons incident at 0 and 70° upon light water. An important difference between the calculation and the experiment must be noted. The calculation is

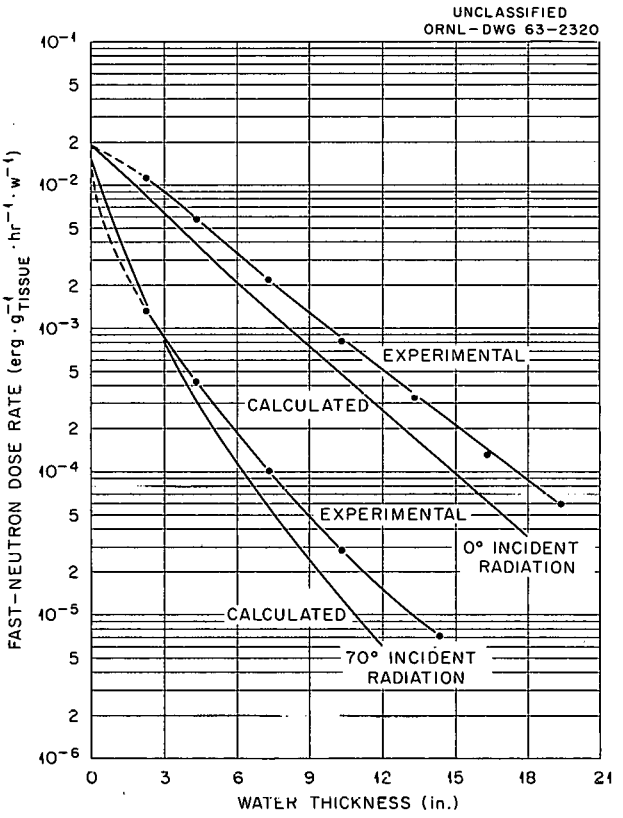

Fig. 3.7.2. Fast-Neutron Dose Rate as a Function of the Thickness of a Slab of Water. Radiation incident at 0 and 70° to slab normal.

[4] "Measurement of Absorbed Dose of Neutrons, and of Mixtures of Neutrons and Gamma Rays," *Natl. Bur. Std. (U.S.), Handbook,* vol 75 (1961).

[5] The water-slab data is unpublished; the concrete-slab data has been compiled in a report to be published: *Measurements of Radiation Intensities in Vertical Holes and an Adjoining Tunnel at the Tower Shielding Facility,* by L. B. Holland, ORNL-3513.

based upon the use of the measured uncollimated COOL-I spectrum. As is noted above, the experimental water data resulted from a measurement in which a collimated beam struck a 5-ft cube of water contained within ¼-in.-thick steel walls. The steel was accounted for in the calculation by first computing the doses transmitted at 0 and 70° through ¼ in. of iron, using the transmission factors of BRL-1174[1] and then using the resulting dose spectra as source terms to compute the attenuations through water. This simplified treatment obviously neglects any effects on angular and energy distribution of the neutrons due to interactions in the steel, which will result in some change in the transmission factors.

The curves were normalized at zero water thickness for the 0° case. The discrepancies between experiment and calculation are due, at least in part, to the fact that the calculated transmission factors are for the dose transmission through finite slabs, while in the experiment the detector was followed or backed by water. It may also be possible that the spectrum of COOL-I differs sufficiently from that of the collimated beam to affect the comparison.

Calculated fast-neutron dose rates behind various thicknesses of concrete are compared with experiment in Fig. 3.7.3 for a nearly plane-collimated source (the TSR-II in the COOL-I shield at 100-ft distance) at 0 and 45° incidence. Normalized at zero concrete thickness, the 0° case results in exact agreement, while the computed curve for 45° appears to have a slightly steeper slope than the exponentially fitted experimental data. At the 18-in. thickness, the difference amounts to about 50%.

Figure 3.7.4 displays the computed and experimentally measured dose rates from a nearly plane-

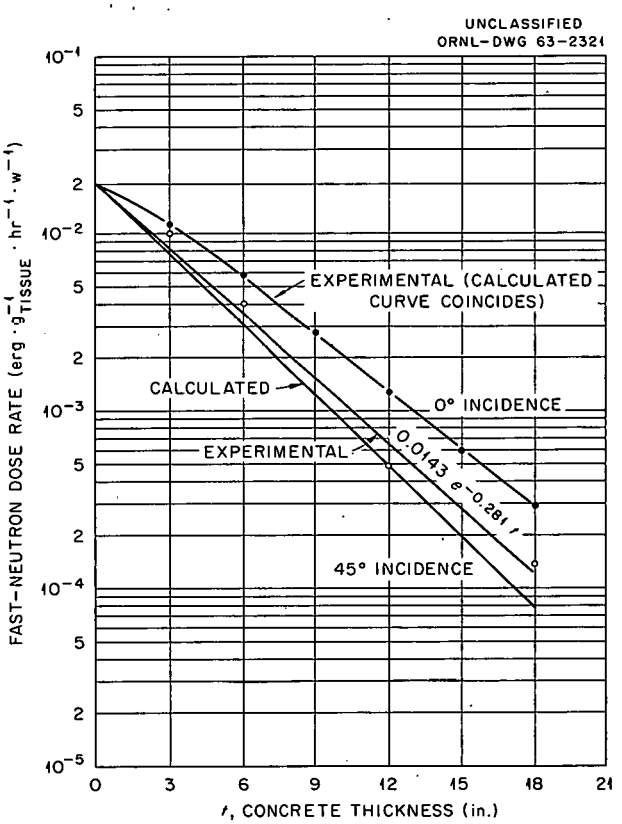

Fig. 3.7.3. Fast-Neutron Dose Rate as a Function of the Thickness of a Slab of Ordinary Concrete. Radiation incident at 0 and 45° to slab normal.

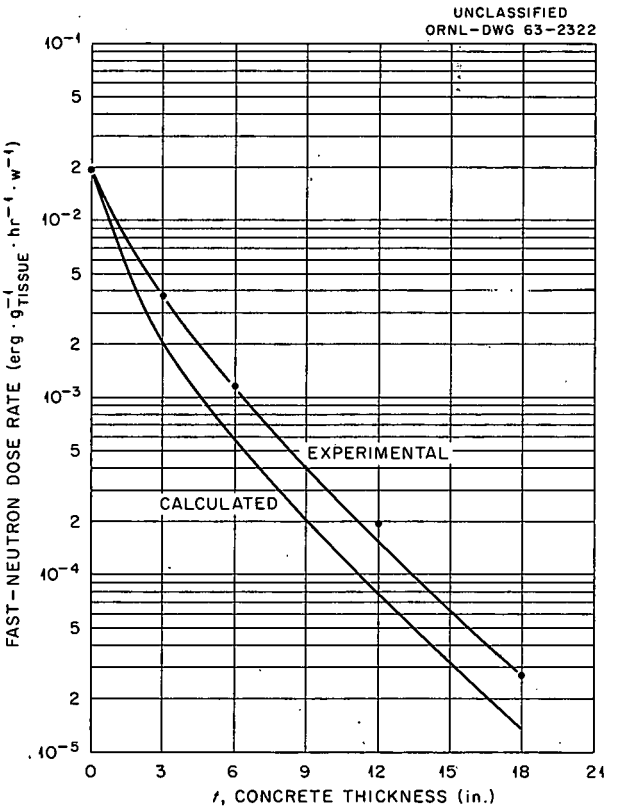

Fig. 3.7.4. Fast-Neutron Dose Rate as a Function of the Thickness of a Slab of Ordinary Concrete. Radiation incident at 75° to slab normal.

collimated source at 100 ft along a line incident at 75° to the normal on concrete. After the first 3 in. of concrete, through which the calculated dose rate drops much more rapidly than the experimental dose rate, the calculated curve effectively parallels the experimental dose rate, the single discrepancy being at the 12-in. thickness and amounting to about 27%. The error in the experimental data can be as large as 30%.

3.8. A STUDY OF THE RADIATION SHIELDING CHARACTERISTICS OF BASIC CONCRETE STRUCTURES AT THE TOWER SHIELDING FACILITY[1]

V. R. Cain

Introduction

A research program with the ultimate goal of producing simple calculational methods for estimating the protection against prompt weapons radiation afforded by various typical structures is being undertaken at ORNL. The first experiment in this program was carried out at the Tower Shielding Facility (TSF) in consultation and cooperation with the Office of Civil Defense, Department of Defense. It consisted of radiation-intensity measurements in two concrete-shielded bunkers and an interconnecting tunnel.

The immediate goals of the experiment were (1) to study the attenuation of radiation by various thicknesses of reinforced concrete slabs, (2) to investigate the buildup of radiation intensities within the structures by scattering in the walls, and (3) to study the transmission of radiation down a tunnel having two right-angle bends. This paper describes the experiment and presents a cross section of the results.

Equipment and Arrangement

Prompt weapons radiation were simulated by the use of the Tower Shielding Reactor II (TSR-II) enclosed in the COOL-I shield. Both the reactor and the shield are described elsewhere.[2,3] Although the presence of water and auxiliary lead shielding above the top of the core prevents the uniform emission of radiation in about half of the 2π solid angle in the upper hemisphere of the TSR-II, the remainder, plus the uniform radiation emitted by the lower hemisphere, simulates an isotropic source such as a weapon burst fairly well.

The general layout of the TSF area for three experiments is mapped in Fig. 3.8.1. The two concrete bunkers and the tunnel are shown in Fig. 3.8.2. The bunkers, as the figure shows, are constructed so that the shield thickness on the front face of one and on the top face of the other can be varied. The thickness of concrete and soil surrounding all other faces is sufficient to make them black to the incident radiation. The three-legged 3 by 8 ft tunnel connecting the bunkers can be seen in the figure. The center leg of the tunnel is 15 ft 2 in. long, and the two end legs are each 6 ft 4 in. long, as measured from the bunker to the center line of the middle leg.

Five concrete shields were available for the open face of each bunker, varying, in 4-in. steps, from 4 to 20 in. in thickness. For convenience in handling, they were made in two sections. The

[1] Summarized from ORNL-3464 (to be published).

[2] L. B. Holland and C. E. Clifford, *Description of the Tower Shielding Reactor II and Proposed Preliminary Experiments*, ORNL-2747 (1959); L. B. Holland *et al.*, *Neutron Phys. Div. Ann. Progr. Rept. Sept. 1, 1959*, ORNL-2842, p 39; L. B. Holland *et al.*, *Neutron Phys. Div. Ann. Progr. Rept. Sept. 1, 1960*, ORNL-3016, p 42.

[3] L. B. Holland *et al.*, *Neutron Phys. Div. Ann. Progr. Rept. Sept. 1, 1962*, ORNL-3360, p 122.

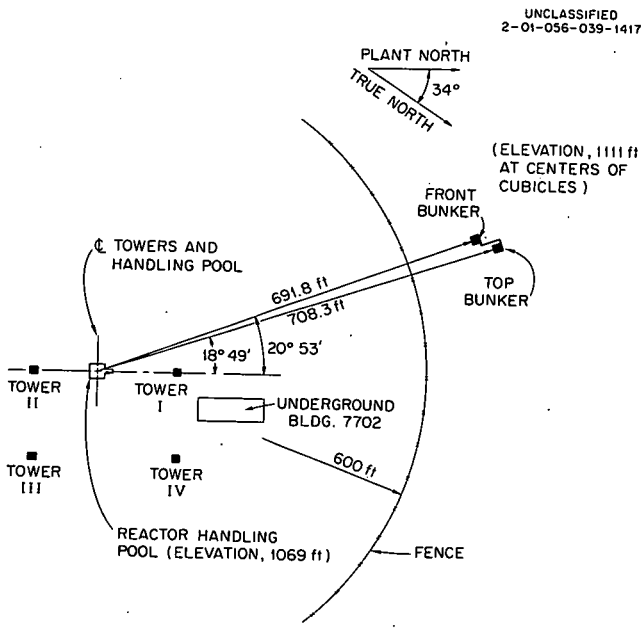

Fig. 3.8.1. Site Plan of the Tower Shielding Facility Showing Location of Bunkers.

ordinary concrete was reinforced by $\frac{1}{2}$-in.-diam steel bars on 4-in. centers running the long way and by $\frac{3}{8}$-in.-diam steel bars on 6-in. centers running the short way. An analysis of the concrete is given below:

Element	Abundance (wt %)
Aluminum	2.65
Calcium	22.12
Carbon	4.83
Hydrogen	0.36
Iron	1.32
Magnesium	0.85
Oxygen	47.04
Silicon	20.83

The coordinate systems to which most of the data are referenced are also shown in Fig. 3.8.2. In each case the origin is at the center of the inside face of the shield.

Instrumentation

Gamma-ray dose rates were measured with an anthracene crystal scintillation dosimeter. The photomultiplier output current was read by a d-c integrator. Since the pulse output of the integrator was proportional to the current input, automatic plotting equipment, which requires a pulse signal, could be used. The dosimeter was calibrated against the known intensity from a Co^{60} source.

Fast-neutron dose rates were measured with a Hurst-type proportional counter. A Po-Be source was used for the daily calibrations of the counter. (Section 6.4 discusses calibration techniques and other details concerning this dosimeter.)

A BF_3-filled proportional counter was used for thermal-neutron flux measurements. Although the output from the counter more closely resembles neutron density than neutron flux, because of the nearly $1/v$ behavior of the $B^{10}(n,\alpha)$ cross section, the readings were normalized to cadmium-difference measurements made with bare and cadmium-covered gold foils in the radiation field from the reactor. Daily calibrations were made against a Po-Be source within a Lucite moderator.

A 3 by 3 in. NaI(Tl) scintillation spectrometer was used to measure gamma-ray pulse-height spectra. The output from its 3-in.-diam photomultiplier was analyzed by a 256-channel pulse-height analyzer. Energy calibrations were made against Cs^{137} and Co^{60} sources and the C^{12} decay gamma rays from a Po-Be source.

Results

Bunker Measurements. – In order to explore the effect of reactor height on the experimental results, the first series of measurements in the bunkers were for fixed counter positions and a variable reactor altitude. The resulting fast-neutron data are shown in Fig. 3.8.3. From these and gamma-ray measurements it was concluded that measurements at a single altitude would suffice for the present experiment. For the remainder of the experiments the reactor altitude was maintained at 100 ft, at which height a line from the reactor center to the center of the shield on the front bunker was perpendicular to the shield. The line from the reactor center to the center of the top shield struck the shield at a grazing angle of 9.5°.

Most of the later measurements in the bunkers were made as a function of one of the variables defined by the rectangular coordinate systems shown in Fig. 3.8.2. Unless otherwise specified, when measurements were made in one bunker, the

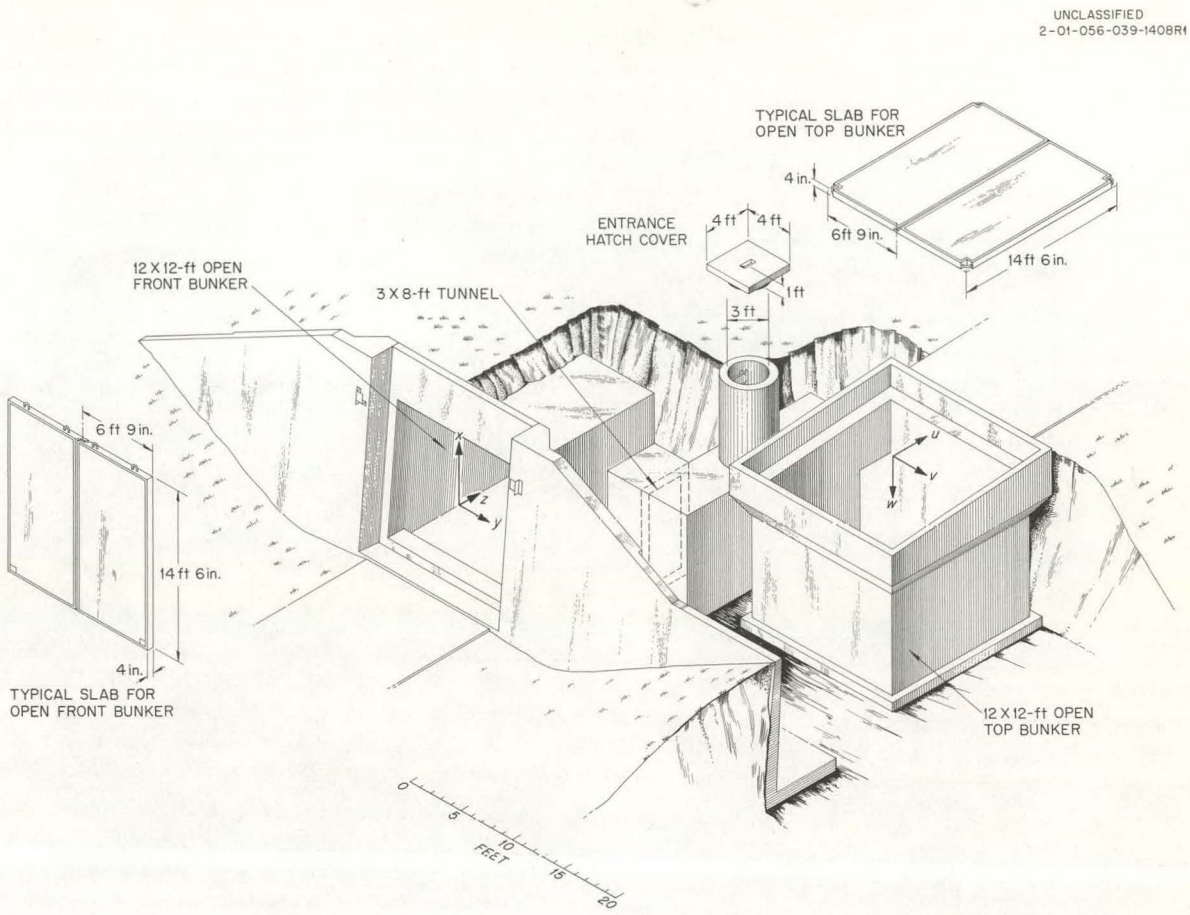

Fig. 3.8.2. Concrete Bunkers and Interconnecting Tunnel, Showing Coordinate Systems to Which Data Are Referenced.

other bunker was always shielded with a full 20 in. of concrete, although this precaution was later shown to be unnecessary.

Typical samples from the large quantity of fast-neutron and gamma-ray dose-rate and thermal-neutron flux traverses made along lines parallel to the coordinate axes for various shield configurations are shown in Figs. 3.8.4 and 3.8.5. Figure 3.8.4 presents gamma-ray dose rates as a function of distance along the z axis, and Fig. 3.8.5 shows fast-neutron dose rates along the w axis.

In an attempt to determine the relative contribution of each of the six walls of a bunker to the dose rate at its center, a shadow shield was used to block the detector's view of one or more of the walls. Since the interest was primarily in fast-neutron dose rate, the shadow shields were designed specifically for neutron attenuation. They were built of $4 \times 4 \times 8$ in. lithiated paraffin blocks (40 wt % natural lithium carbonate, 60 wt % paraffin), stacked so as to approximate a truncated pyramid. The base of the pyramid, facing and parallel to the wall being shielded, was 58 in. square; the truncated top was 22 in. square and faced the detector, which was positioned at the center of the bunker. The distance between the parallel planes of base and top was 20 in. Figure 3.8.6 shows fast-neutron dose-rate traverses made in the front bunker with various combinations of shadow shields, both with no shield on the front of the bunker and with a 4-in.-thick concrete shield on the bunker. The traverses were made in order

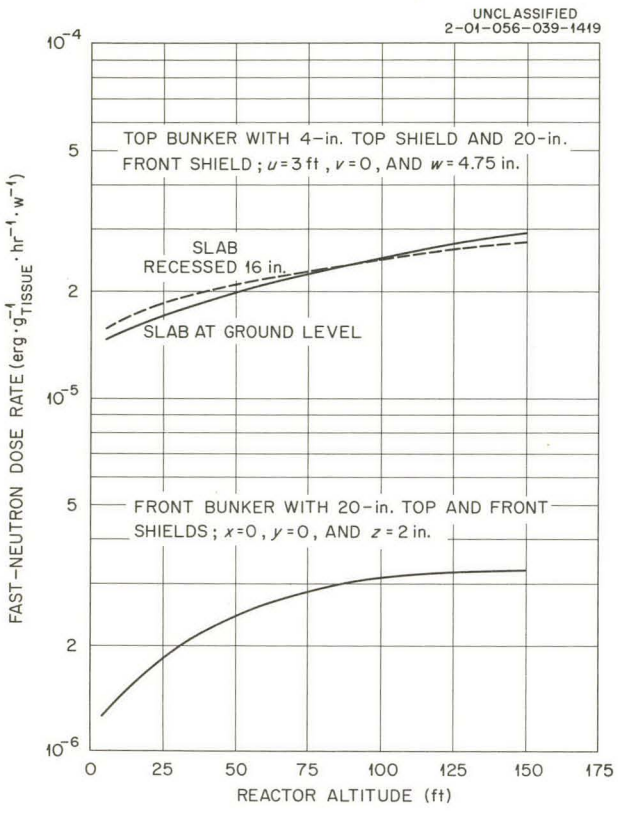

Fig. 3.8.3. Fast-Neutron Dose Rates in Front and Top Bunkers as a Function of Reactor Altitude.

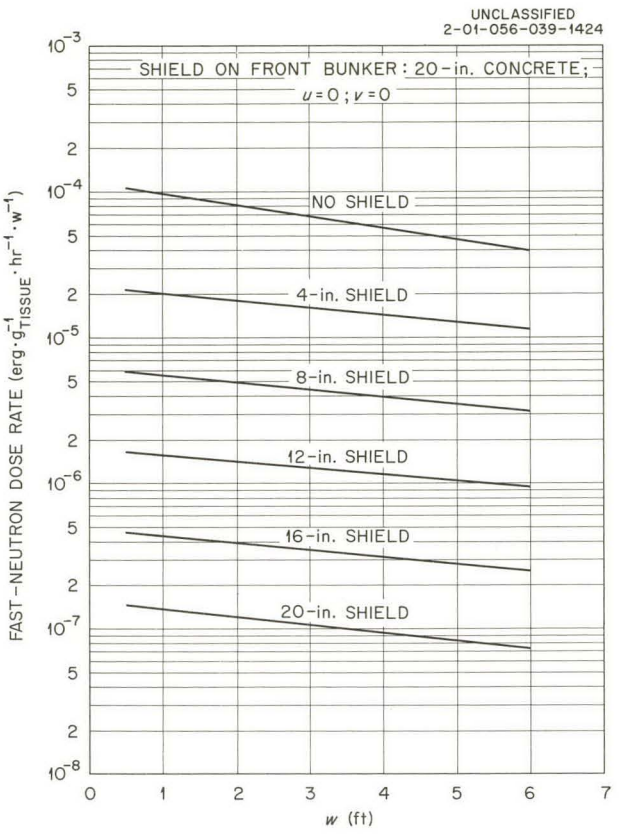

Fig. 3.8.5. Fast-Neutron Dose Rates as a Function of Distance Along w Axis, for Various Thicknesses of Concrete Shield on Top Bunker.

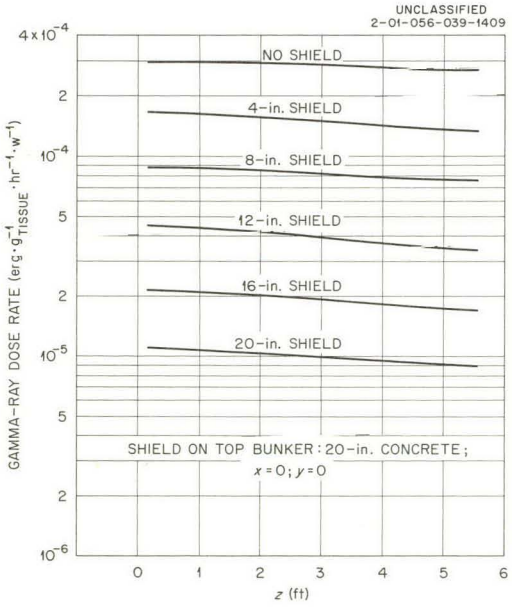

Fig. 3.8.4. Gamma-Ray Dose Rates as a Function of Distance Along z Axis, for Various Thicknesses of Concrete Shield on Front Bunker.

to obtain a normalization value at a point far enough from the shadow shield for the shield not to excessively perturb the reading. The normalization point was the average value at $y = 5$ ft. From the differences of the various measurements, it appears that when no shield is in place, ~77% of the fast-neutron dose rate comes from the front of the bunker, 7% from the rear, and 4% from each of the remaining walls. With 4 in. of concrete shielding, 75% of the observed dose rate appears to come from the front and 5% from each side and the rear.

Tunnel Measurements. – Figure 3.8.7 shows fast-neutron and gamma-ray dose-rate and thermal-neutron flux traverses along the center line of the tunnel connecting the two bunkers. During these measurements a 20-in.-thick concrete shield covered the open-top bunker, and the front bunker was open. The zero point of the traverse was the x,z plane of the front bunker.

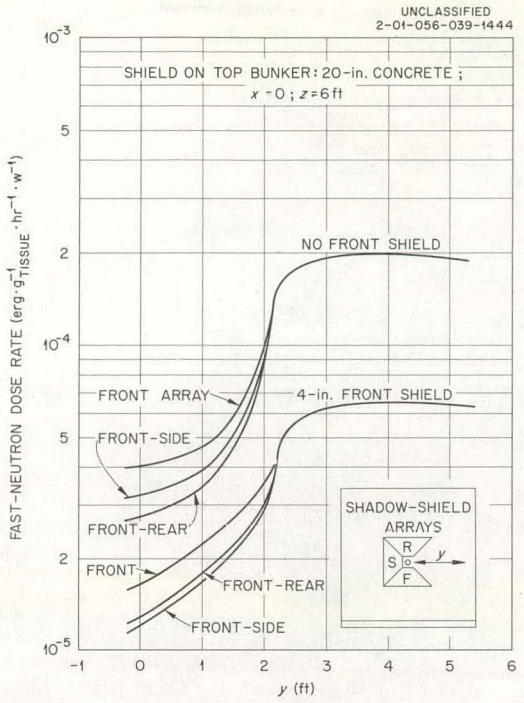

Fig. 3.8.6. Fast-Neutron Dose Rates in Front Bunker as a Function of Distance Along the y Axis, for Various Shadow-Shield Configurations.

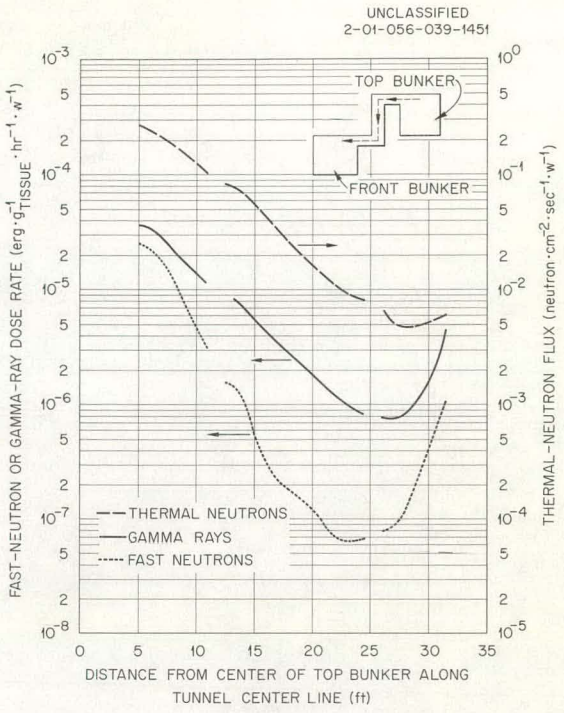

Fig. 3.8.8. Fast-Neutron and Gamma-Ray Dose Rates and Thermal-Neutron Fluxes Along the Center Line of the Tunnel, with a 20-in.-thick Concrete Shield on the Front Bunker and No Shield on the Top Bunker.

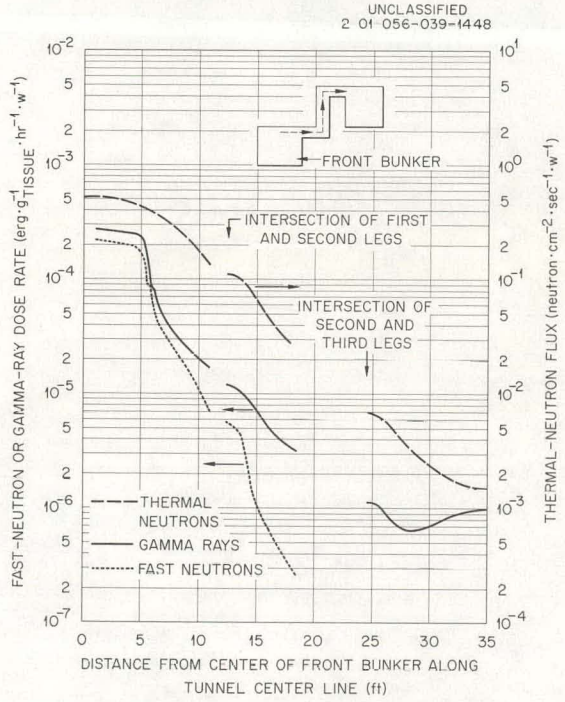

Fig. 3.8.7. Fast-Neutron and Gamma-Ray Dose Rates and Thermal-Neutron Fluxes Along the Center Line of the Tunnel, with a 20-in.-thick Concrete Shield on the Top Bunker and No Shield on the Front Bunker.

A similar set of traverses is shown in Fig. 3.8.8, but for the case of a 20-in.-thick concrete shield covering the front bunker and no shield on the top bunker. The zero point of these traverses is the w,u plane of the top bunker, and the traverses proceed toward the front bunker. Except for the regions close to the bunkers, the curves of Figs. 3.8.7 and 3.8.8 are quite similar in shape.

Gamma-Ray Spectra. – A number of gamma-ray pulse-height spectra were measured both in the center of the top bunker and in the center of the tunnel, with various configurations of the shield on the top bunker. A sample of these data is shown in Fig. 3.8.9, which shows the pulse-height spectra obtained in the tunnel with and without a boron shield over the crystal of the spectrometer. It is hoped that a future reduction of these and similar pulse-height spectra to incident gamma-ray spectra may aid in identifying the various sources of the gamma rays contributing to the observed dose rates.

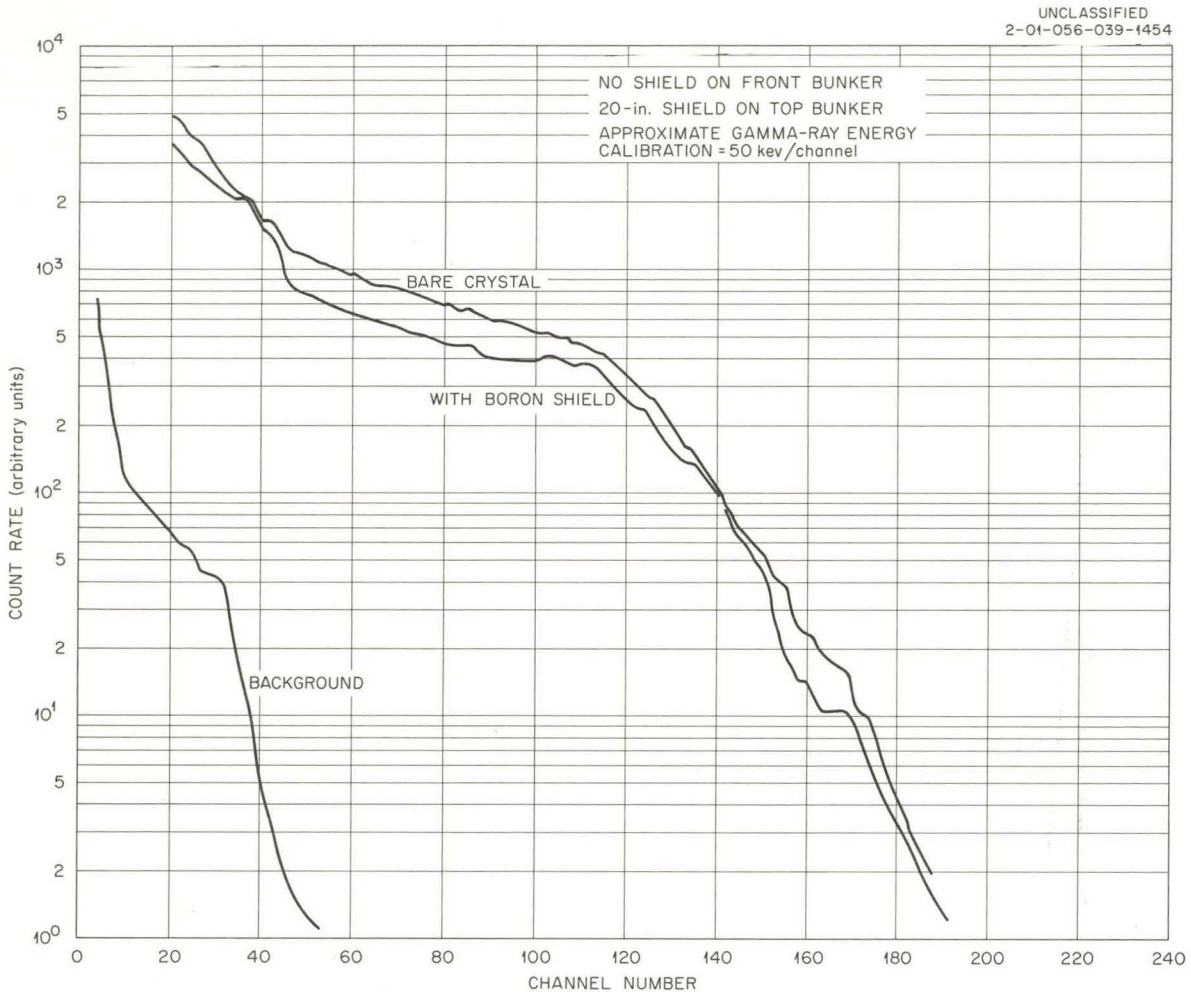

Fig. 3.8.9. Gamma-Ray Pulse-Height Spectra in Center of Tunnel, With and Without a Boron Shield on the Spectrometer Crystal.

3.9. CALCULATIONS OF THERMAL-NEUTRON FLUX DISTRIBUTIONS IN MULTILEGGED DUCTS USING AN ALBEDO MODEL WITH MONTE CARLO TECHNIQUES[1]

V. R. Cain

Introduction

Experimental data obtained at the Tower Shielding Facility in multilegged duct geometries (see Figs. 3.8.7 and 3.8.8 in preceding section) indicate that the gamma rays resulting from the capture of low-energy neutrons in the duct walls can be an important contribution to the total dose. An important problem in the calculation of this component is the determination of the spatial distribution of the low-energy neutrons, which involves the processes of the slowing down and transport of the higher energy neutrons and the transport of the low-energy neutrons themselves. The study reported in this section is concerned with the determination of the distributions of the low-energy neutrons in multilegged duct geometries.

The complexity of duct geometries, in general, precludes the use of many of the common neutron-transport calculational techniques. A full-scale Monte Carlo calculation would provide complete descriptions of fast-neutron and secondary gamma-ray dose rates by following all incident neutrons to their death but might be uneconomical because of requiring an excessive number of collisions to follow a neutron completely through the slowing-down and capture processes.

The procedure employed in the work summarized here utilizes the albedo, or reflection coefficient, model. The albedo may be obtained by studying a single wall-scattering process, possibly by experimental techniques or by detailed Monte Carlo calculations of the conventional type, in order to establish the validity of various assumptions and to establish the nature of the changes that must be made for different physical configurations. The combination of this detailed examination of a single wall-scattering process with a calculation which uses the albedo model in the correct geometry would certainly seem to be a more economical and versatile calculational technique than the full-scale Monte Carlo calculation. The albedo for low-energy neutrons, which is defined on the basis of number reflection, is high (on the order of 0.7 or 0.8), unlike the albedos for fast neutrons and gamma rays, which are defined on the basis of dose-rate reflection. Consequently, while the albedos for fast-neutron and gamma-ray dose rates give reasonable results by considering only one reflection, the albedo for low-energy neutrons requires consideration of orders of scatterings higher than the first in a calculation. If the albedo were low and the geometry simple, direct numerical integrations could be performed over all possible locations of each scatter point.[2] But when many scatterings must be considered and when the geometry becomes extremely complicated, these integrals become so complex that the solutions may be obtained more efficiently by the use of the random-sampling technique.[3] The technique ordinarily used in particle-transmission problems, the "random-walk" technique, rather than the technique of random sampling of the multiple integrals directly was selected for computing the thermal-neutron flux distributions reported in this study.

The Albedo – Random Walk Model

The problem of interest is that of predicting the thermal-neutron fluxes at various positions in a multilegged concrete-walled duct, which are due to a neutron radiation field incident on the mouth of the duct. It is assumed that this problem can be represented by the transport of particles down the duct according to an albedo model. When used for calculations of fast-neutron or gamma-ray doses, the differential albedo is defined as the fraction of the dose incident on a semi-infinite plane surface that is reflected into a particular solid-angle element. In general, the albedo must be a function of the incident direction and energy, the wall material, and the exit direction. Practical considerations of calculational complexity quite often lead to simplifying assumptions, such as the use

[1] Summary of ORNL-3507 (to be published).

[2] C. W. Terrell *et al.*, *Radiation Streaming in Shelter Entranceways*, ARF-1158A01-5 (July 1961).

[3] H. Kahn, *Nucleonics* 8, 28 (May 1950).

of an albedo which is an average of the differential albedo over the incident particle energy spectrum or the use of an albedo which has no dependence on the incident direction (and therefore no dependence on the exit azimuthal angle). For the problem considered here, both assumptions given above will be made; specifically, it will be assumed that the albedo is constant and that it is independent of the incident direction. In this case the albedo is defined on the basis of the number of particles reflected, rather than the fraction of dose reflected.

A computer code has been written to perform multiple albedo-scattering calculations in multilegged ducts. A description of the code is given in detail in ORNL-3507[4] and is summarized here.

A source plane from which all particles originate is defined as being located at the mouth of a duct which may have either a rectangular cross section or a cross section defined by the zeros of a general quadratic function: $ax^2 + by^2 + cxy + dx + ey + f$, with $a/b > 0$ and $a \neq 0$. The duct may have multiple right-angle bends when the rectangular cross section is used. The source may be either located at a point or uniformly distributed on the source plane. The angular distribution of the particles leaving the source plane may be specified (in terms of a probability density function) as a power series in the cosine of the polar angle of emission (the angle between the particle direction and the normal to the surface). The particle undergoing the random walk has no characteristics associated with it at any time other than its weight, which is unity upon emission from the source plane, its position, and its direction. When the particle collides with a wall surface, its weight is changed by a constant factor (corresponding to the albedo, or probability of reemission, associated with the actual wall and the physical particle whose behavior is being simulated). A direction of emission is then selected which is assumed to be independent of the incident direction. It is therefore not a function of the azimuthal angle and, as before, is selected from a probability density function expressed as a power series in the cosine of the polar angle of emission. Fluxes at various positions along the duct are computed from this random walk by one of two procedures. One technique, that of statistical estimation, involves an estimation at every scatter point, including the source point, of the flux contribution to a series of point detectors. The flux contribution is calculated by using the known probability of the particle reaching each of these detector locations from the wall scatter point. The other procedure is to add track lengths from the particle track which occur in each of a series of finite volume detectors. The flux in a particular detector is the sum of all such track lengths divided by the volume of the detector. The detector proving to be the most satisfactory for the problem under consideration is one that is thin in the dimension parallel to the duct center line and that occupies the entire cross section of the duct. The flux obtained from this detector is, of course, an average flux over the volume of the detector; but, since the flux does not vary rapidly along a plane normal to the center line, this average flux is a fairly good measure of the flux along the duct center line. The particles are followed until they completely traverse the duct, re-enter the source plane, or exceed a predetermined number of wall scatterings.

[4]Appendices A, B, and C.

Straight-Duct Calculations

The digital computer code, incorporating the albedo model described above, was used on both the Control Data Corporation (CDC) 1604A computer at ORNL and the International Business Machines (IBM) 7090 computer at ORGDP Central Data Processing Facility.

A large number of calculations performed with the computer code were for straight ducts, both circular and rectangular in cross section. A sample calculation, giving fluxes for a straight 1.9544-ft-diam cylindrical duct and an isotropic albedo of 0.8, is shown in Fig. 3.9.1. The results are presented as particle flux (particles/cm^2) along the center line of the duct normalized to an incoming current of 1 particle/cm^2 at the source plane. The flux was obtained by totaling the particle track lengths in each of a series of detectors occupying the entire cross section of the duct and having a thickness of 0.5 ft, and then dividing by the volume of the detector. The source was assumed to be uniform over the mouth of the duct and to have a distribution of angular current proportional to the cosine of the angle measured from the line normal to the source plane. (This

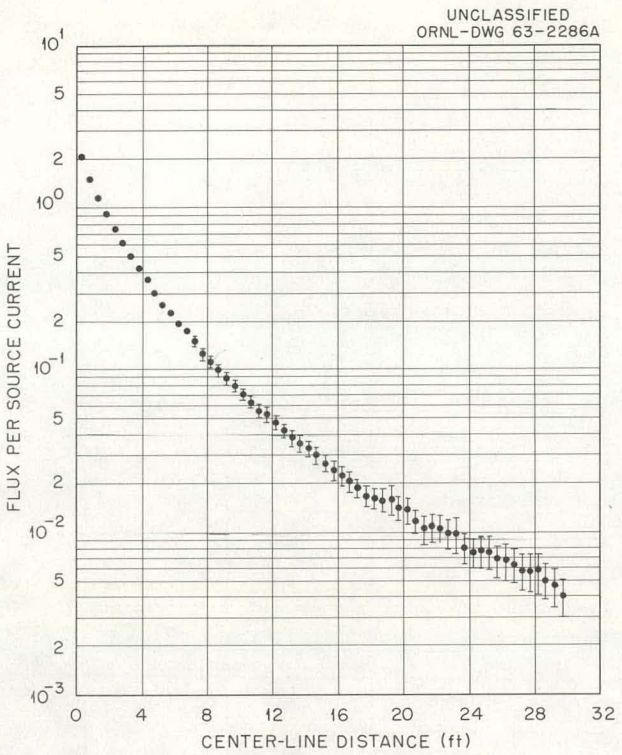

Fig. 3.9.1. Total Neutron Flux Calculated for 1.95441-ft-diam Cylindrical Duct Using an Isotropic Albedo of 0.8 (10,000 Histories).

corresponds to an isotropic flux outside the duct; that is, the number of neutrons per unit solid angle arriving at the duct mouth is constant for all directions.) The error bars shown in Fig. 3.9.1 and for all subsequent data from the computer code calculations represent $\pm 2\sigma$, where σ is the standard deviation, or square root of the variance.[5] It can be shown that there is a 95% probability that a new, independent calculation would be within the error bars. Calculations similar to those in Fig. 3.9.1 for various duct sizes and shapes (rectangular and cylindrical) and albedo representations were also performed.

Comparisons with an Analytic Approximation

One of the primary purposes in performing the straight-duct calculations was to enable comparisons with calculations based on an equation reported by Simon and Clifford.[6] The Simon-Clifford equation used for the comparison was derived for very long straight circular ducts with an azimuthally independent albedo expressed as a sum of isotropic and cosine distribution components as follows:

$$\alpha = \alpha'(A + 2B \cos \theta) , \qquad (1)$$

where

α = differential albedo (per unit cosine),

α' = total albedo,

A = fraction of albedo represented by an isotropic distribution,

B = fraction of albedo represented by a cosine distribution ($A + B = 1$),

θ = polar angle of emission, measured from the normal to the reflecting surface.

The albedo is an average over the incident neutron spectrum and therefore does not include an energy dependence. The Simon-Clifford equation using this albedo is

$$\phi = \phi_0 \left(1 + A \frac{\alpha'}{1 - \alpha'} + \frac{4B\delta}{l} \frac{\alpha'}{1 - \alpha'}\right), \qquad (2)$$

where

l = distance along the center line of the duct,

ϕ = neutron flux at l,

ϕ_0 = uncollided neutron flux at l,

δ = radius at the duct,

and α', A, and B are as described above. The equation was actually derived for a plane isotropic source at the duct mouth, but when given in the form of Eq. (2), it applies as well to the cosine source used for the calculations of this paper.

Scattered fluxes obtained with Eq. (2) for a 1-ft-diam cylindrical duct and isotropic and cosine albedos of magnitude 0.12 are compared with scattered fluxes from the Monte Carlo calculations in Fig. 3.9.2, in which all the data are normalized to unit particle flux from the source plane. For an isotropic albedo the two calculations (upper curve and triangular points) agree, within the 2σ limits of the Monte Carlo calculation, from about

[5] See Appendix A of ORNL-3507 for the definition of variance and methods for obtaining the estimate of the variance.

[6] A. Simon and C. E. Clifford, *Nucl. Sci. Eng.* 1, 156 (1956).

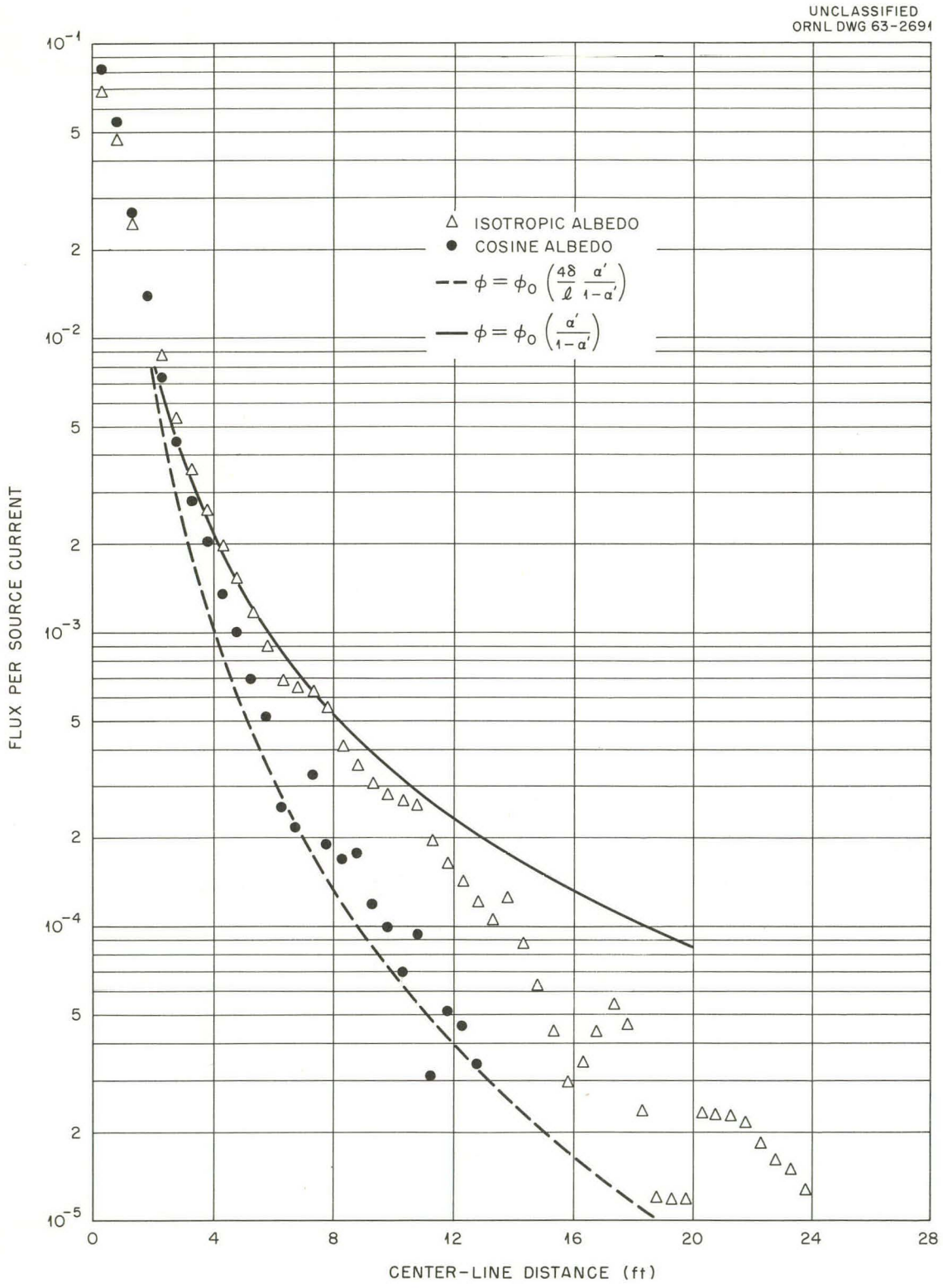

Fig. 3.9.2. Scattered Neutron Flux in a 1-ft-diam Cylindrical Duct: Comparison of Calculations Using Isotropic and Cosine Albedos of 0.12 with an Analytic Approximation.

3 to 12 ft. Beyond 12 ft the statistics of the Monte Carlo calculation are very poor and probably not meaningful. For a cosine albedo (lower curve and circular points), the agreement is within the 2σ limits beyond about 5 ft. Since the albedo is small, the unscattered flux accounts for most of the total flux (over 85% with the isotropic albedo and more than 85% with the cosine albedo), so that Eq. (2) may be expected to yield results that are correct to within about 5% beyond 2 ft (or 2 diameters from the source).

Figure 3.9.3 shows results of total flux calculations with an isotropic albedo of value 0.8 in two different geometries: a 3 by 1 ft rectangular duct and a 1.95441-ft-diam cylindrical duct. Also shown are the uncollided flux and the results of Eq. (2) for the cylindrical duct. The uncollided flux is not shown for the rectangular duct but is not too different from that for the cylindrical duct, especially at large distances, since the two ducts are of equal cross-sectional area. The ratios of the unscattered fluxes for the cylindrical duct to the unscattered fluxes for the rectangular duct are approximately 16, 4.5, 2, and 1.2% for distances of 2, 4, 6, and 8 ft, respectively. The Simon-Clifford equation gives an underestimate of the cylindrical duct results between about 2 and 8 diameters from the source. As will be seen, the rectangular duct results are lower than the cylindrical duct results and thereby are in better agreement with Eq. (2).

Figure 3.9.4 is comparable to Fig. 3.9.3 except that a cosine albedo distribution is used. Agreement with Eq. (2) is somewhat better, but this is partially because the scattered flux is not as large a fraction of the total flux as it is with the isotropic albedo.

Multibend-Duct Calculations

Most of the calculated results presented in this section were obtained for a three-legged 54-slab detector configuration. Duct heights of 1, 6, and 8 ft were used with the cross section shown in Fig. 3.9.5 (detectors 1 through 54 only). Two other configurations, resembling a room containing a source on one wall and having a two-legged duct extending from an adjacent wall, were also used by adding detectors 55 through 63 as shown in Fig. 3.9.5. The source is distributed uniformly on the plane at $x = 0$ from $z = 0$ to H (the duct height) and either from $y = 0$ to 3 ft in the case of the three-legged duct or from $y = 0$ to 7.5 ft in the case of the configuration consisting of a room and two legs.

All data presented here are plotted as particle flux due to a unit particle current source vs the distance along the center line of the duct. In Fig. 3.9.5 it can be seen that detectors 13, 14, and 15 and detectors 34, 35, and 36 are not located on the center line. The data from the detectors are plotted in numerical order, and so the points at 6.25, 6.75, 7.25, 16.75, 17.25, and 17.75 ft do not represent flux along the duct center line. As before, the horizontal bars above and below the plotted points represent 2σ or 2 standard deviations.

Figures 3.9.6 and 3.9.7, both for a cosine albedo of 0.8, compare the results of two different calculational techniques for a three-legged duct geometry with a 3×6 ft cross section. The data shown in Fig. 3.9.6 are from a calculation using the slab detectors given in Fig. 3.9.5, while the data given in Fig. 3.9.7 are from a calculation using statistical estimation of the flux to a series of point detectors along the duct center line. Exactly the same histories are used in both calculations. This pair of calculations demonstrates quite well that statistical estimation is not always desirable. In this case the machine time required for the statistical estimation calculation was longer by a factor of 12 (approximately 1 hr compared with 5 min). The calculation does reduce the variance for a given number of histories and would be preferable in most cases where the flux at only one or two points is required.

It should also be noted that the statistical estimation technique results in a much smoother curve. This is because the detector estimates are not statistically independent; estimates are made to each detector from every scatter point. An advantage of the statistical estimation calculation is that the answers are direct estimates of the flux as a function of distance down the duct center line. As mentioned previously, the particle flux obtained with the slab detectors is one which is an average over the volume of the detector, and, because of the way the geometry is set up, six of the detectors are not located on the duct center line. Comparison of the two figures indicates that the center-line flux is not much larger than the average flux; the 2σ limits of the two calculations overlap.

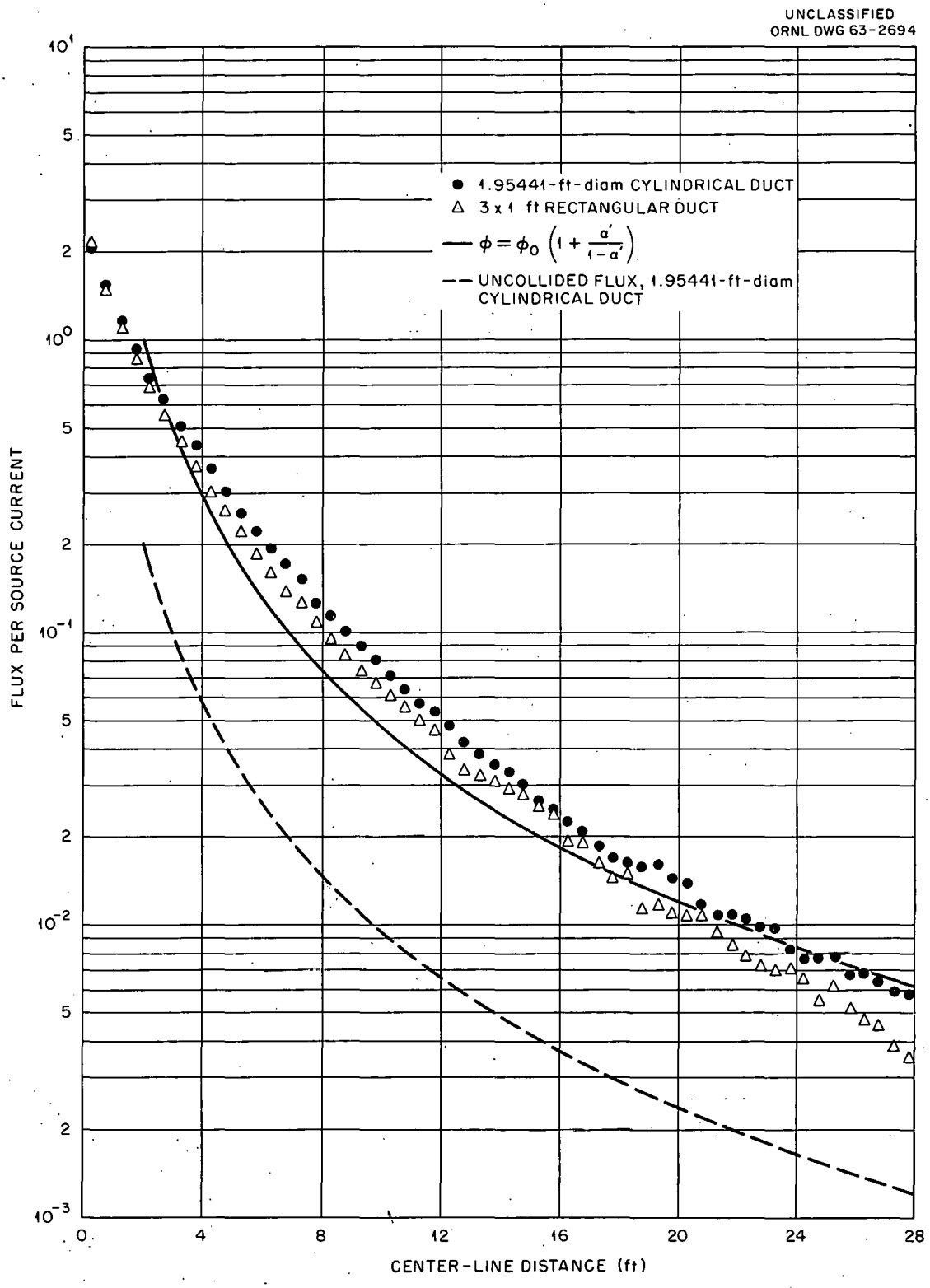

Fig. 3.9.3. Total Neutron Flux Using an Isotropic Albedo of 0.8: Comparison of Calculations for a 1.95441-ft-diam Cylindrical Duct, a 3 by 1 ft Rectangular Duct, and an Analytic Approximation.

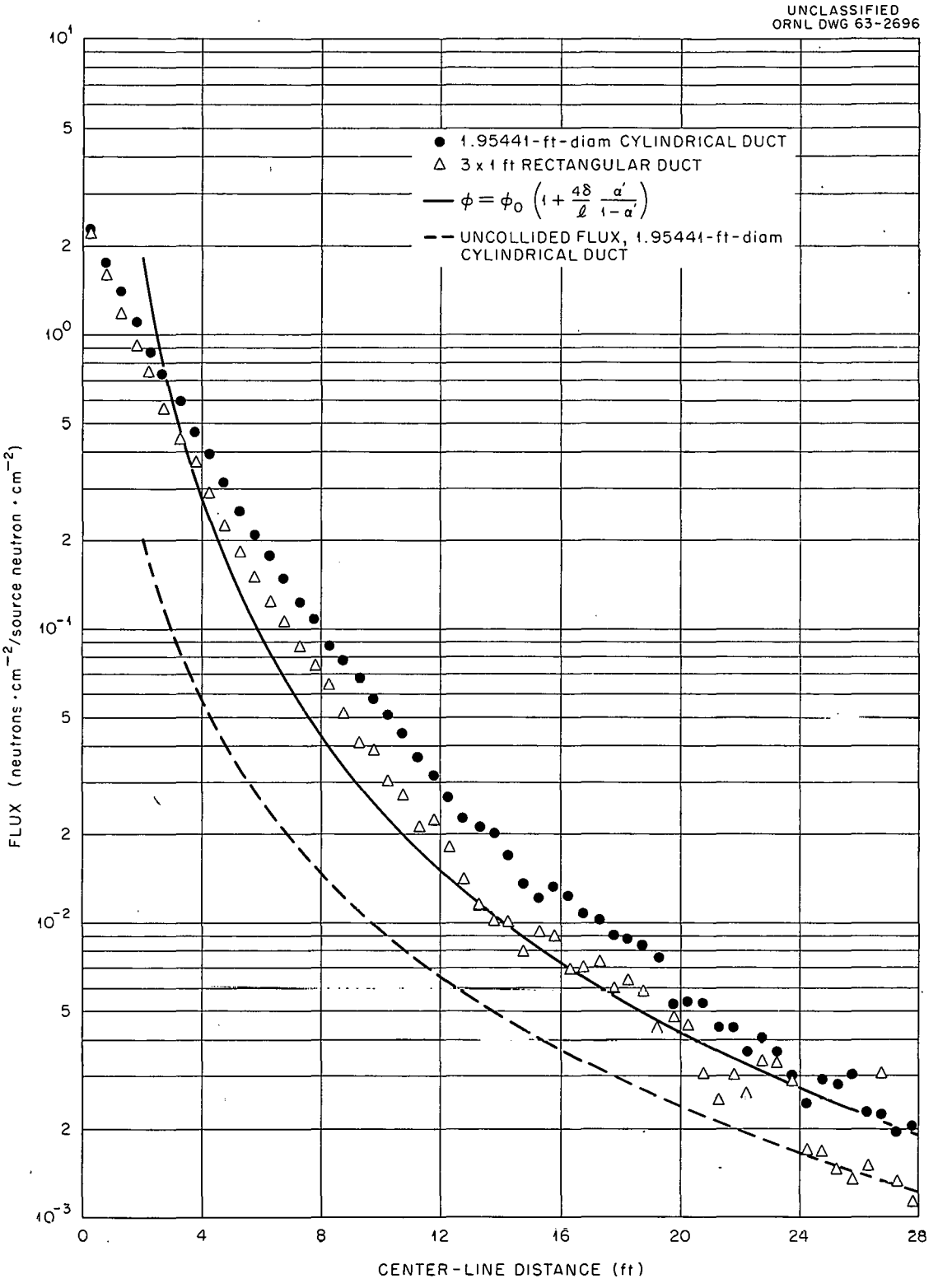

Fig. 3.9.4. Total Neutron Flux Using a Cosine Albedo of 0.8: Comparison of Calculations for a 1.95441-ft-diam Cylindrical Duct, a 3 by 1 ft Rectangular Duct, and an Analytic Approximation.

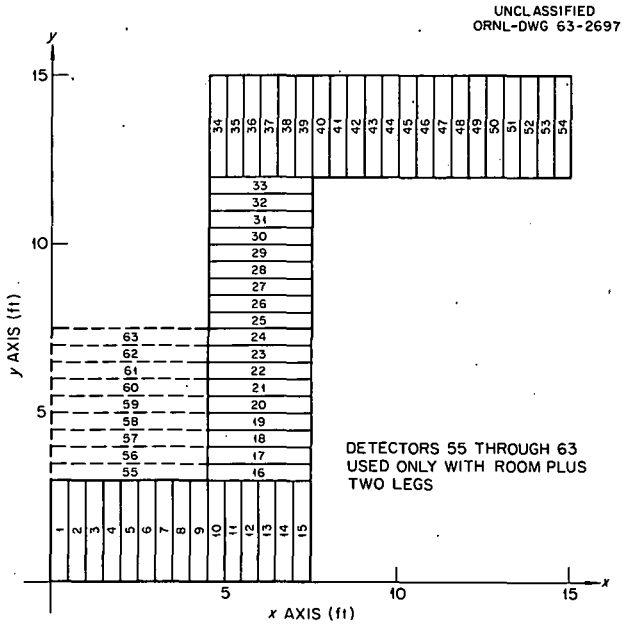

Fig. 3.9.5. Cross Section of x-y Plane Showing Detector Locations and Numbers for Three-Legged Duct Geometry and Room Plus Two-Legged Duct Geometry.

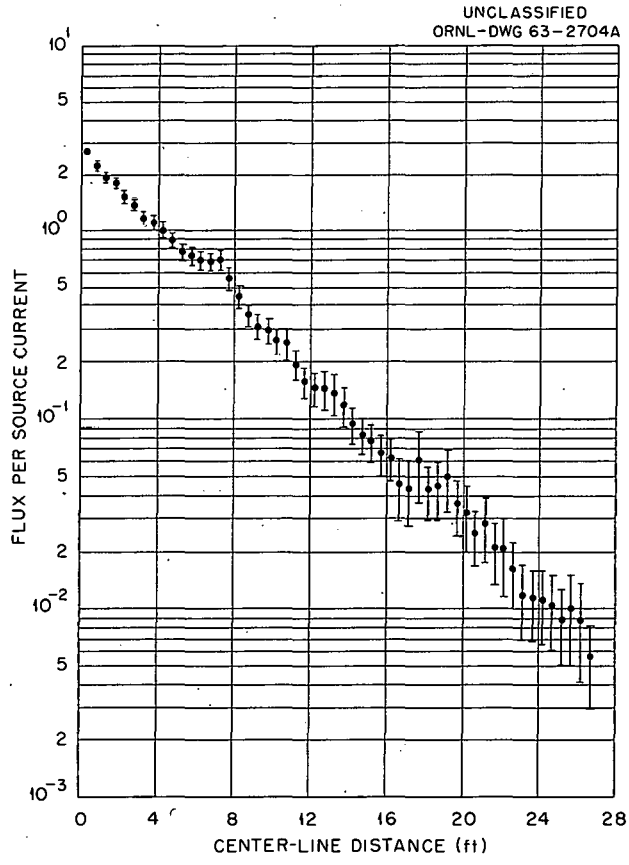

Fig. 3.9.6. Total Neutron Flux Calculated for Three-Legged 3 by 6 ft Rectangular Duct Using a Cosine Albedo of 0.8 (1000 Histories).

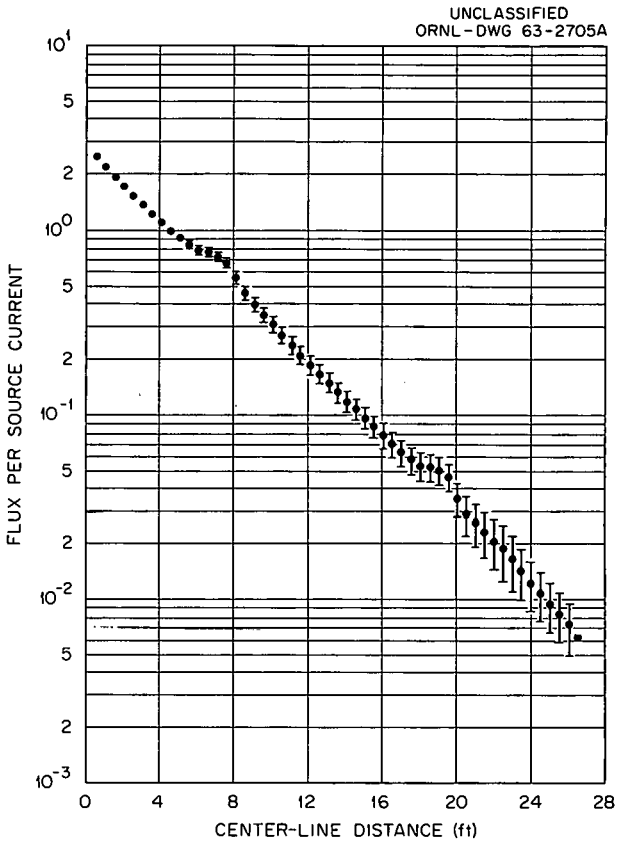

Fig. 3.9.7. Total Neutron Flux Calculated for Three-Legged 3 by 6 ft Rectangular Duct Using a Cosine Albedo of 0.8 (1000 Histories). Calculation based on statistical estimation.

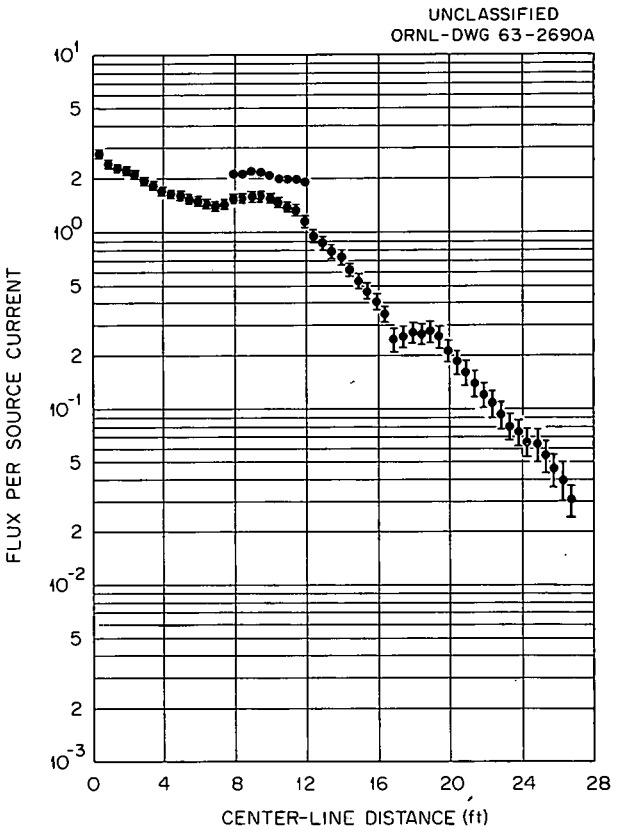

Fig. 3.9.8. Total Neutron Flux Calculated for Room (6 by 7.5 by 7.5 ft) and Two-Legged Duct (3 by 6 ft) Configuration (Shown in Fig. 3.9.5) Using a Cosine Albedo of 0.8 (4000 Histories). See text for explanation of geometrical configuration.

Figure 3.9.8 presents data from calculations using the nine additional detectors (55–63) shown in Fig. 3.9.5, which form a 7.5 by 7.5 ft room, with two legs of a duct leading from the room. The calculations used a cosine albedo of 0.8 and a duct height of 6 ft. The data for detectors 55 through 63 are plotted at the same center-line positions as detectors 16 through 24, respectively.

The thermal-neutron flux data from Figs. 3.8.7 and 3.8.8 (preceding section) were corrected for the contributions to the measurements from radiations penetrating the 20-in. concrete shield on the opposite bunker. The corrected data were then compared with calculated results as shown in Fig. 3.9.9. The circles on the figure are the results of two of the Monte Carlo calculations arbitrarily normalized. Both of the calculations used an albedo of 0.8 with a cosine distribution. One calculation, plotted from 1.8 to 19.2 ft along the center line, used a geometry mocking up the bunker and two legs of the tunnel. The other calculation, plotted from 6.8 to 32.6 ft along the center line, used a geometry representing the three legs of the tunnel.

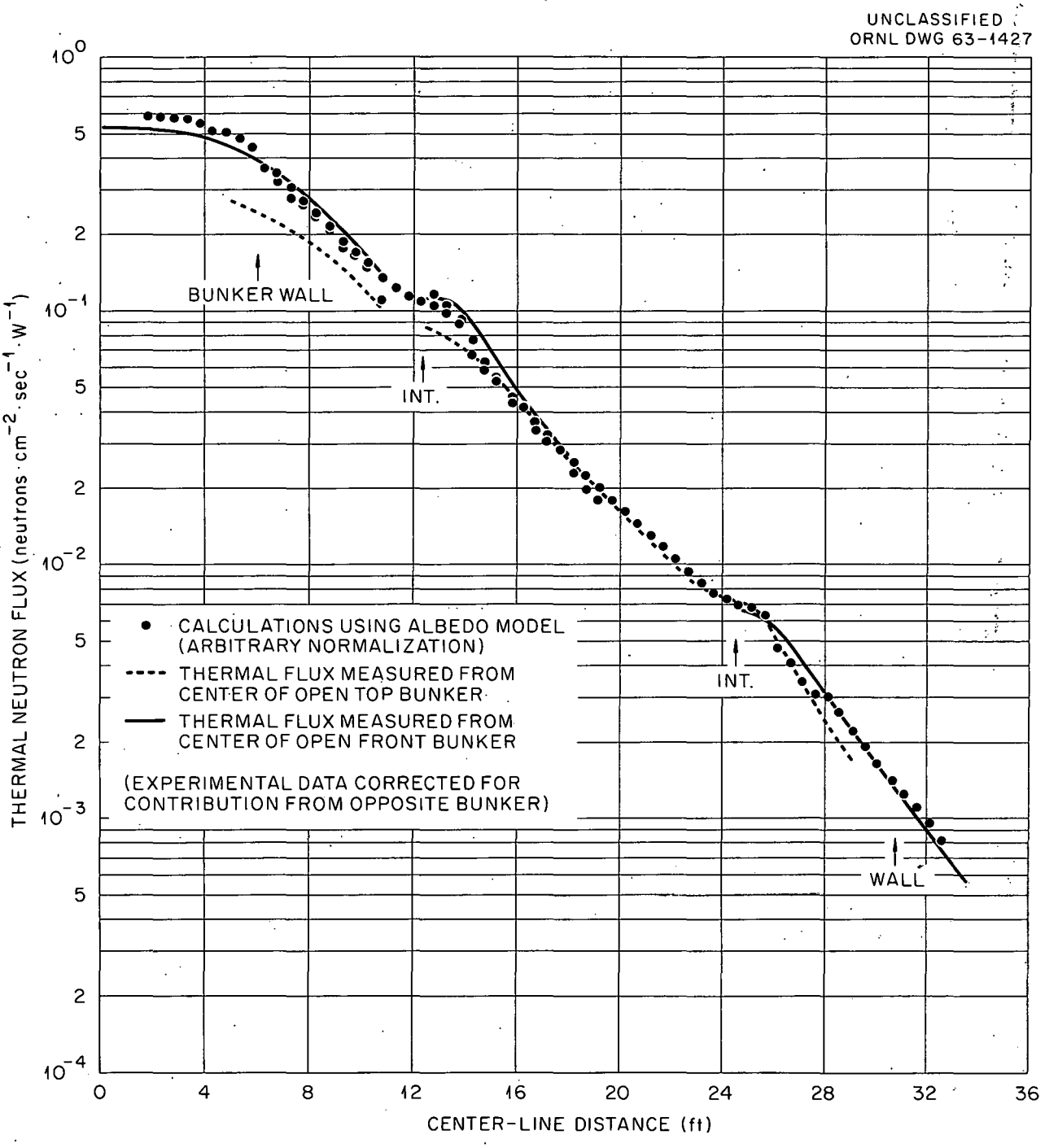

Fig. 3.9.9. Comparison of Calculations Using a Cosine Albedo of 0.8 with Thermal-Neutron Flux Measurements Along a Three-Legged Duct.

3.10. ANALYSIS OF TSR-II RADIATION DISTRIBUTION IN VERTICAL CONCRETE-LINED CYLINDRICAL HOLES AND AN ADJOINING TUNNEL[1]

M. B. Wells

Introduction

Typical results of a Tower Shielding Facility experiment in which measurements were made of fast-neutron and gamma-ray dose rates in cylindrical underground holes and an adjoining tunnel were reported previously.[2] The data, which have been compiled in detail for a topical report,[3] are now being analyzed to determine whether the effects of most (or all) of the parameter variations can be predicted independently of the measurements. Since the long-range objective of this and similar studies is the development of simplified techniques for predicting the penetration of initial weapons radiation into underground structures, the emphasis of the analysis is being placed on the derivation of simplified expressions for the important variables.

As described elsewhere,[2,3] the measurements were made in three 4-ft-diam concrete-lined holes dug in the ground at distances of 53, 161, and 435 ft from the TSF reactor pool and designated as Hole Nos. 1, 2, and 3, respectively. The uppermost 3 ft of each hole was recessed to a square cross section, 6 × 6 ft, to accommodate square covering shields of iron or concrete. The geometry of the experiment is shown in Fig. 3.10.1. In conformity with the presentation of the experimental results, the detector position in the analysis is described in units of l/D, where l is the distance between the ground level and the detector and D is the inside diameter of the hole. All calculations are for a detector located on the axis of the hole. The slant range from reactor to detector is called ρ, and γ is the reactor elevation angle.

The analysis of the unshielded cases is essentially complete, and the results are reported below. In general, the fast-neutron and gamma-ray dose rates are in good agreement with the experimental data, although the prediction of gamma-ray dose rates is complicated by the presence of secondary gamma rays resulting from thermal-neutron captures in the walls of the holes and in the instruments.

Prediction of Fast-Neutron Dose Rates

The prediction of the fast-neutron dose rates along the axes of the open holes is based on calculations of the various neutron fluxes contributing to the dose rate, including the direct-beam, air-scattered, and wall-scattered neutrons. A point-isotropic source emitting neutrons with energies

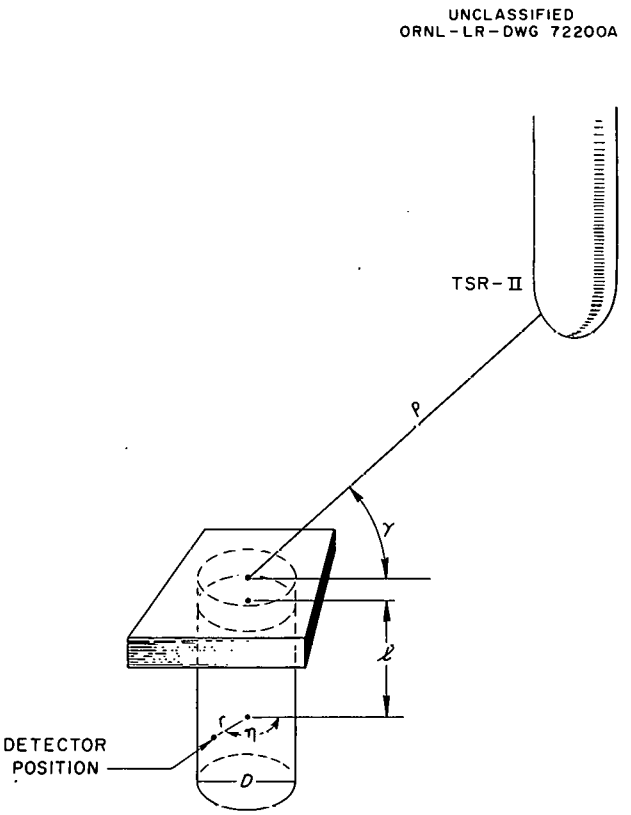

Fig. 3.10.1. Geometrical Parameters for TSF Measurements and Analysis.

[1] Work performed by Radiation Research Associates, Fort Worth, Texas, under Subcontract 2267.

[2] L. B. Holland *et al.*, *Neutron Phys. Div. Ann. Progr. Rept. Sept. 1, 1962*, ORNL-3360, p 122.

[3] L. B. Holland *et al.*, *Measurements of Radiation Intensities in Vertical Holes and an Adjoining Tunnel at the Tower Shielding Facility*, ORNL-3513 (in press).

defined by the measured COOL-I leakage spectrum[4] was assumed. The spatial distributions in air of the direct-beam and air-scattered fast-neutron dose rates from the shield were based on Monte Carlo calculations.[5,6] An air density at the TSF of 1.25×10^{-3} g/cm^3 was chosen. The calculated spatial distribution of the fast-neutron dose rate in air was normalized to the measured fast-neutron dose rate for reactor and detector heights of 116.5 ft at a range of 467 ft. The computed fast-neutron dose rates vs range are within 10% of the measured data[4] for reactor and detector heights of 116.5 ft for ranges of 100 to 800 ft.

The cumulative angular distribution of the air-scattered fast-neutron dose rate entering the holes is shown in Fig. 3.10.2 as a function of sin β, where 2β is the angle seen by the detector, for various values of γ and ρ. From the air-scattering calculations it was noted that for ρ = 100 ft the angular distribution of the air-scattered fast-neutron dose rate varies considerably with γ; however, the slopes of the curves for $\gamma = 15°$ at ρ = 100 and 450 ft are nearly identical.

The contribution to the fast-neutron dose rates by wall scattering of both the air-scattered and direct-beam fast neutrons was calculated for l/D = 0, 1, 2, and 3 in all three holes. The neutron albedo data were obtained by weighting the Monte Carlo results of Allen *et al.*[7] by the energy spectrum of fast neutrons incident upon the opening of Hole No. 1. The resulting dose-rate albedo was fitted by

$$\alpha(\theta_0,\theta) = 0.1105 \cos^{2/3}\theta_0 \cos\theta ,$$

where θ_0 and θ are the angles of incidence and reflection, respectively. For the wall scattering of the direct-beam fast neutrons, θ_0 was taken to be equal to γ. According to the calculations, a maximum in the total wall-scattered fast-neutron dose rate occurs at $\gamma = 82.5°$ for l/D = 2 and 3.

The total calculated fast-neutron dose rates in Hole No. 1 are compared in Fig. 3.10.3 with the measured dose rates. The greatest disagreement exists at l/D = 1 and is caused primarily by the use in the calculation of an insufficiently detailed description of the angular distribution of air-scattered neutrons incident on the hole wall between l/D = 0 and 1. The significant feature of the curves shown in Fig. 3.10.3 is the agreement between experimental and calculated values at l/D = 0 for all reactor angles. This agreement verifies the accuracy of the calculated radiation environment incident on the hole.

The experimentally observed maximum in the fast-neutron dose rate at $\gamma = 82.5°$ and l/D = 3 is confirmed by the calculations. Similar agreement exists between the experiment and calculations for Hole Nos. 2 and 3. The calculations for ρ = 100, 228, and 450 ft indicate no significant variation of the angular distribution of the air-scattered fast-neutron dose rate with distance, nor do they show any considerable effect of the air ground interface on the air-scattered fast-neutron dose rates entering the holes.

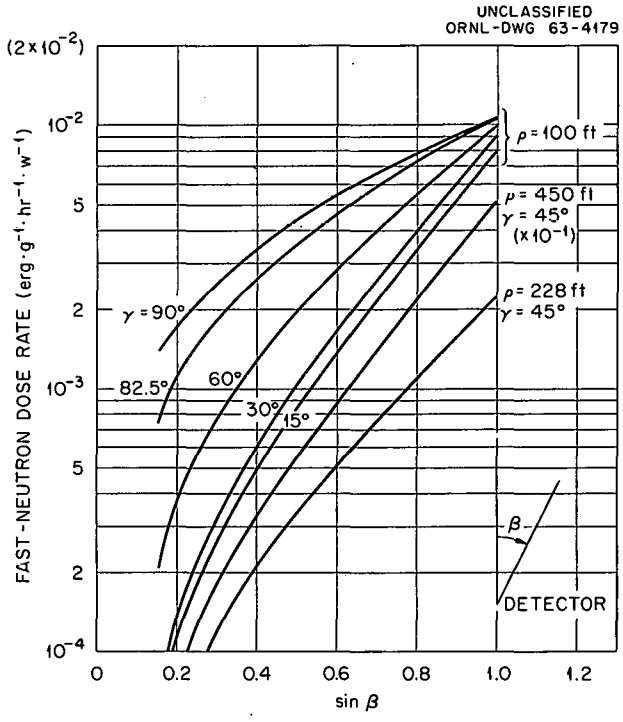

Fig. 3.10.2. Cumulative Angular Distribution of the Air-Scattered Fast-Neutron Dose Rate as a Function of the Solid Angle Seen by the Detector.

[4] F. J. Muckenthaler *et al.*, *In-Air Measurements in the Vicinity of the Tower Shielding Reactor-II*, ORNL-3288 (1963).

[5] M. B. Wells, *Monte Carlo Calculations of Fast-Neutron Scattering in Air*, vol. II, FZK-9-147 (August 1960).

[6] J. R. Stokes and W. C. Farries, FZK-132 (Classified).

[7] F. J. Allen *et al.*, *Neutron Reflection and Flux vs. Depth for Concrete*, BRL-1189 (1963).

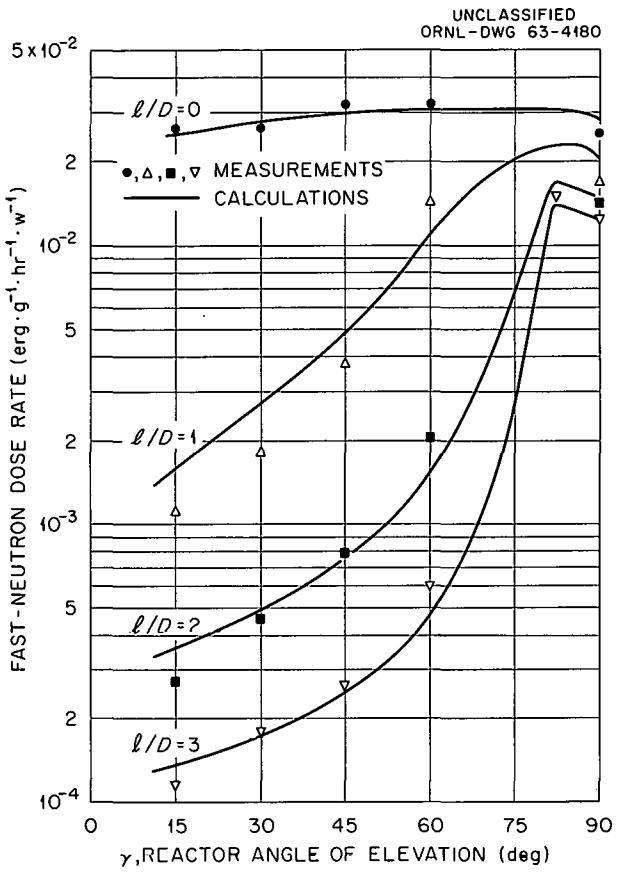

Fig. 3.10.3. Comparison of Calculated and Measured Fast-Neutron Dose Rates in Hole No. 1.

Prediction of Gamma-Ray Dose Rates

The prediction of the gamma-ray dose rates in the holes was based upon calculations of the several components contributing to the measured dose rate. These include (1) the direct-beam dose rate, (2) the air-scattered dose rate, (3) the dose rate resulting from air-captured thermal neutrons, (4) the dose rate resulting from wall-captured thermal neutrons, and (5) the dose rate resulting from wall scattering of direct-beam, air-scattered, and air-capture gamma rays.

Two corrections were made to the measured gamma-ray data to obtain the true dose rate. The first, a correction for the sensitivity of the gamma-ray dosimeter to fast neutrons, was taken to be 12.5% of the measured fast-neutron dose rate.[8] The second, a correction for thermal-neutron effects, was taken to be 6.3×10^{-5} erg·g^{-1}·hr^{-1}·w^{-1} per unit thermal-neutron flux.[8] The estimate of the thermal-neutron fluxes used in correcting the results for Hole No. 1 was obtained from measurements taken 40 in. above the hole and at depths of 12 and 15 ft along the axis of the hole for reactor angles of 15, 30, 60, and 90° (Fig. 3.10.4). Table 3.10.1 gives the corrected measured gamma-ray dose rates for Hole No. 1, with which the calculated dose rates can be compared.

A direct-beam gamma-ray dose rate of 1.43×10^{-2} erg·g^{-1}·hr^{-1}·w^{-1} was computed for a distance of 100 ft in air (density = 1.25×10^{-3} g/cm^3) by using a calculated gamma-ray leakage spectrum for the COOL-I shield.[6] A gamma-ray removal cross section of 0.065 cm^{-1} was used in computing the penetration of the direct-beam gamma-ray dose rate through the concrete lip of the holes. The calculation of the angular distribution of the air-scattered gamma-ray dose rate

[8] V. R. Cain, *A Study of the Radiation Shielding Characteristics of Basic Concrete Structures at the Tower Shielding Facility*, ORNL-3464 (in press).

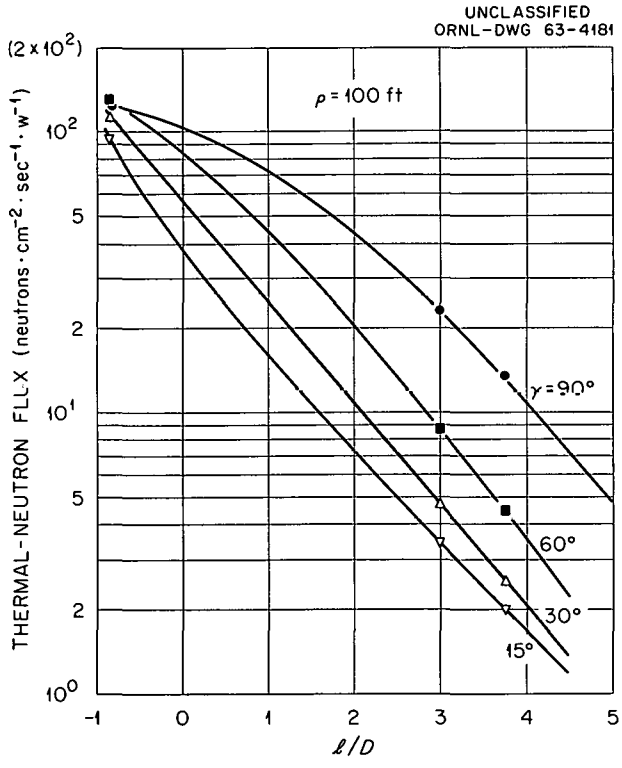

Fig. 3.10.4. Measured Thermal-Neutron Fluxes in Hole No. 1. Lines are drawn only to guide the eye.

Table 3.10.1. Corrected Experimental Gamma-Ray Dose Rates for Hole No. 1 (Unshielded)

l/D	Measured Gamma-Ray Dose Rate ($erg \cdot g^{-1} \cdot hr^{-1} \cdot w^{-1}$)	Fast-Neutron Correction ($erg \cdot g^{-1} \cdot hr^{-1} \cdot w^{-1}$)	Thermal-Neutron Correction ($erg^{-1} \cdot hr^{-1} \cdot w^{-1}$)	Corrected Gamma-Ray Dose Rate ($erg \cdot g^{-1} \cdot hr^{-1} \cdot w^{-1}$)
		$\gamma = 15°$		
0	2.20(−2)[a]	3.26(−3)	2.483(−3)	1.626(−2)
1	1.90(−3)	1.26(−4)	1.039(−3)	7.350(−4)
2	7.25(−4)	3.40(−5)	4.599(−4)	2.311(−4)
3	3.40(−4)	1.47(−5)	2.174(−4)	1.079(−4)
		$\gamma = 30°$		
0	2.15(−2)	3.31(−3)	3.528(−3)	1.466(−2)
1	2.85(−3)	2.28(−4)	1.544(−3)	1.078(−3)
2	1.00(−3)	5.74(−5)	6.678(−4)	2.747(−4)
3	4.50(−4)	2.25(−5)	2.961(−4)	1.314(−4)
		$\gamma = 60°$		
0	2.60(−2)	4.05(−3)	5.324(−3)	1.663(−2)
1	1.45(−2)	1.81(−3)	2.772(−3)	9.918(−3)
2	2.20(−3)	2.56(−4)	1.273(−3)	6.710(−4)
3	8.60(−4)	7.50(−5)	5.544(−4)	2.306(−4)
		$\gamma = 90°$		
0	3.10(−2)	3.19(−3)	6.426(−3)	2.138(−2)
1	2.26(−2)	2.12(−3)	4.536(−3)	1.594(−2)
2	1.96(−2)	1.77(−3)	2.709(−3)	1.513(−2)
3	1.61(−2)	1.56(−3)	1.449(−3)	1.309(−2)

[a]Numbers in parentheses are power-of-ten multipliers: $2.20(-2) \equiv 2.20 \times 10^{-2}$.

about the axis of Hole No. 1 was based on Monte Carlo air-scattering data of Lynch *et al.*[9]

The angular distribution of the air-capture gamma-ray dose rate about the axis of Hole No. 1 was computed from the air-scattering probabilities reported by Beissner[10] for neutrons in the energy interval 0 to 0.208 ev. An effective thermal-neutron source strength for the COOL-I shield of 2.43×10^9 neutrons$\cdot$sec$^{-1} \cdot$w^{-1} was determined from the measured thermal-neutron fluxes vs distance.[4] An examination showed that the angular distribution and magnitude of the air-scattered gamma-ray dose rate differed significantly from those of the air-capture gamma-ray dose rate.

The wall-capture gamma-ray dose rates along the axis of Hole No. 1 were computed by use of the thermal-neutron fluxes given in Fig. 3.10.4 and the capture-gamma-ray albedo data computed from the Monte Carlo data reported in ref 11. The capture-gamma-ray dose albedo for $\theta_0 = 0°$ is shown in Fig. 3.10.5 as a function of the angle of reflection, θ. The data for angles of incidence other than $\theta_0 = 0°$ are given by the relation

$$\beta(\theta_0,\theta) = \beta(\theta_0 = 0°,\theta) \cos \theta_0 .$$

The thermal-neutron flux at any depth l in the hole was assumed to be isotropic and to be constant over the radius of the hole. From the results

[9]R. E. Lynch *et al.*, *A Monte Carlo Calculation of Air-Scattered Gamma Rays*, ORNL-2292 (vol. 1) (1958).

[10]R. E. Beissner, *The Angular Distribution of Gamma Rays Resulting from Neutron Capture in Air*, FZK-9-151 (1961).

[11]M. B. Wells, *Gamma Dose Rates Resulting from Neutron Capture in Air and Concrete*, MR-N-238 (1959).

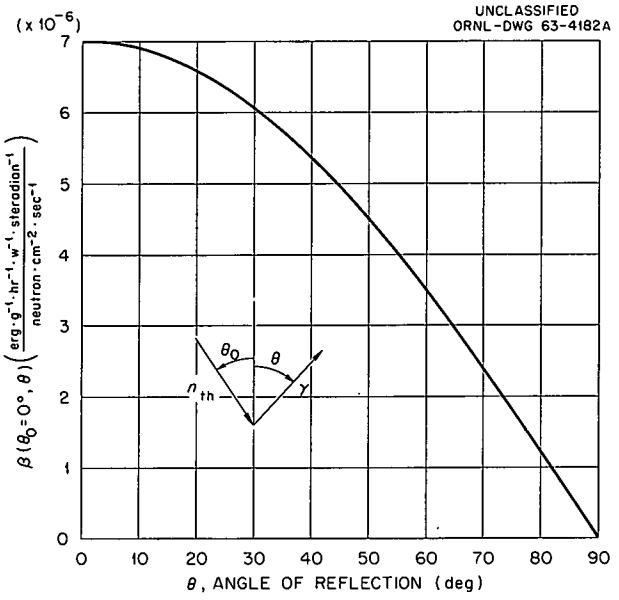

Fig. 3.10.5. Angular Distribution of Gamma-Ray Dose Rate Resulting from Thermal Neutrons Normally Incident upon Concrete.

of the calculation for the wall-capture gamma-ray dose rate along the axis of the hole it was noted that the maximum value of the wall-capture gamma-ray dose rate for each reactor angle considered occurred at an l/D value of ~ 1.

Additional components of the calculated gamma-ray dose rates, such as those resulting from wall scattering of the air-scattered direct-beam and air-capture gamma-ray dose rates, were investigated and found to be negligible; that is, their sum of a given value of l/D was less than 1% of the corrected measured gamma-ray dose rates.

The four important components of the calculated gamma-ray dose rates in Hole No. 1 are tabulated in Table 3.10.2, along with the total calculated gamma-ray dose rates and the ratio of the calculated dose rates to the corrected measured data. Except for the cases where $l/D = 0$, or where the detector can see the direct beam, the wall-capture gamma-ray dose rate is the most important component of the gamma-ray dose rates in Hole No. 1.

The ratios of the calculated total gamma-ray dose rates to the measured dose rates, as given in Table 3.10.2, reveal that the calculations are in fair agreement with the measurements, except at reactor angles of 15°, 30°, and 60° for $l/D = 1$. The poor agreement at these detector positions can probably be attributed to the shapes assumed for the thermal-neutron fluxes in the hole at l/D values of between 0 and 2. It is believed that the thermal-neutron fluxes in this region are underestimated by the curves shown in Fig. 3.10.4. Since the calculated gamma-ray dose rates at $l/D = 0$, 2, and 3 for all reactor angles are in reasonably good agreement with the corrected measured dose rates, it appears that the calculations of the direct-beam, air-scattered, and air-capture gamma-ray dose rates are accurate enough to define the radiation environment incident on the opening of the hole for shield penetration calculations.

Calculations were also performed to predict gamma-ray dose rates in a horizontal tunnel which was rectangular in cross section and was connected to Hole No. 1 10 ft below the ground level. The tunnel was 20 ft long and perpendicular to the vertical plane containing the hole axis and the reactor. Some thermal-neutron flux measurements in the hole and tunnel were available to define the detailed thermal-neutron flux distributions which were used in the wall-capture and detector-capture gamma-ray calculations. The angular distribution of the thermal-neutron flux incident on the walls was assumed to be isotropic, with the average angle of incidence taken as 60°. Results of a calculation for a reactor angle of 15° are compared in Fig. 3.10.6 with the measured data from a detector traversed along a line $5\frac{1}{2}$ in. off the floor and $8\frac{1}{4}$ in. off the wall of the tunnel. The correction applied to the measured gamma-ray dose rates to account for thermal-neutron capture in the gamma-ray dosimeter is indicated in Fig. 3.10.6. The dose rate resulting from thermal-neutron-capture gamma rays in the detector is approximately 50% of the total measured gamma-ray dose rate. It was observed that a change in the assumed average angle of incidence of the thermal-neutron flux from $\theta_0 = 60°$ to θ_0' would increase the magnitude of the calculated wall-capture dose rates shown in Fig. 3.10.6 by a factor of $2 \cos \theta_0'$, since the capture-gamma-ray albedo, $\beta(\theta_0,\theta)$, is dependent on the assumed angle of incidence. The iron reinforcing bars contained in the walls of the hole and tunnel also contributed to the increase in the wall-capture dose rate. According to the preliminary calculations, thermal-neutron capture in this iron would increase the calculated wall-capture gamma-ray dose rate at each detector position by approximately 25%.

Table 3.10.2. Calculated Gamma-Ray Dose Rates for Hole No. 1
(ρ = 100 ft)

l/D	Gamma-Ray Dose Rate ($erg \cdot g^{-1} \cdot hr^{-1} \cdot w^{-1}$)					Ratio: Calculated / Measured
	Direct-Beam	Air-Scattered	Air-Capture	Wall-Capture	Total	
			$\gamma = 15°$			
0	1.429(−2)[a]	1.640(−3)	4.045(−4)	2.937(−4)	1.663(−2)	1.023
1		4.119(−5)	2.441(−5)	3.571(−4)	4.227(−4)	0.575
2		1.197(−5)	7.268(−6)	1.946(−4)	2.792(−4)	1.208
3		5.456(−6)	3.426(−6)	9.878(−5)	1.077(−4)	0.998
			$\gamma = 30°$			
0	1.429(−2)	1.739(−2)	4.757(−4)	4.473(−4)	1.695(−2)	1.156
1		5.416(−5)	3.889(−5)	5.312(−4)	6.242(−4)	0.579
2		1.561(−5)	1.118(−5)	2.863(−4)	3.131(−4)	1.139
3		7.377(−6)	5.075(−6)	1.387(−4)	1.512(−4)	1.151
			$\gamma = 60°$			
0	1.429(−2)	1.871(−3)	5.695(−4)	7.296(−4)	1.746(−2)	1.050
1	6.362(−3)	3.399(−4)	1.024(−4)	9.259(−4)	7.730(−3)	0.779
2	1.237(−6)	6.527(−5)	3.665(−5)	5.232(−4)	6.264(−4)	0.934
3		3.035(−5)	1.866(−5)	2.575(−4)	3.065(−4)	1.329
			$\gamma = 90°$			
0	1.429(−2)	1.885(−3)	5.692(−4)	8.852(−4)	1.763(−2)	0.825
1	1.321(−2)	1.395(−3)	2.173(−4)	1.484(−3)	1.597(−2)	1.001
2	1.225(−2)	1.078(−3)	8.721(−5)	1.029(−3)	1.436(−2)	0.949
3	1.139(−2)	8.200(−4)	5.681(−5)	6.001(−4)	1.287(−2)	0.983

[a]Numbers in parentheses are power-of-ten multipliers: $1.429(-2) \equiv 1.429 \times 10^{-2}$.

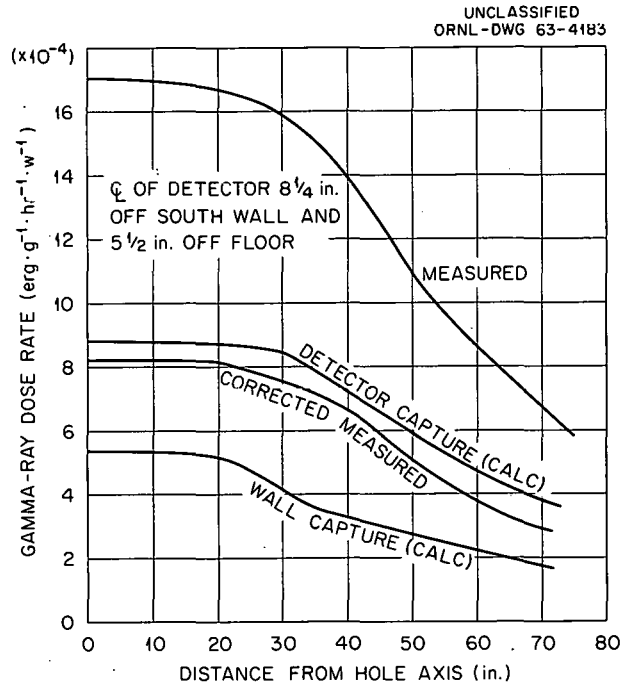

Fig. 3.10.6. Comparison of Measured and Calculated Gamma-Ray Dose Rates in Tunnel Off Hole No. 1.

3.11. ANALYSIS OF TSR-II RADIATION DISTRIBUTION IN UNDERGROUND CONCRETE BUNKERS[1]

R. L. French

The methods described in the preceding paper (Sec. 3.10) for analyzing the experimental data obtained in vertical concrete-lined cylindrical holes at the Tower Shielding Facility are also being used to analyze the experimental data obtained in underground bunkers (see Sec. 3.8). That portion of the analysis presented here considers only the fast neutron and gamma-ray distributions inside the open-top and open-front (i.e., unshielded) bunkers, the thermal-neutron distributions having been discussed elsewhere (Sec. 3.9).

The angular and energy distributions of the fast-neutron and gamma-ray fluxes incident on the bunkers approximately 700 ft from the TSR-II reactor in the COOL-I shield[2] were calculated from Monte Carlo data given in refs 3 and 4. These distributions were adjusted slightly to agree with the total fast-neutron and gamma-ray dose rates obtained by interpolating previously published "free-field" data[5] to correspond to the bunker location. Because no source-term measurements were made during the bunker experiment, considerable emphasis was placed on correlating measurements made just outside the bunkers to the free-field data.

Two positions in both the front bunker and the top bunker were selected for detailed analysis. The first position in each case is on the center line 0.5 ft from the center of the opening of the bunker. The second position is at the geometrical center of each bunker (see Fig. 3.8.2 in Sec. 3.8). Calculation of the dose-rate components at these positions involved: (1) solid-angle calculations to determine the fraction of the free-field fast-neutron and gamma-ray dose rates which pass through the bunker openings directly to the receiver positions, (2) calculation of fast-neutron scattering from the bunker walls to the receiver positions and, for the front bunker, fast-neutron scattering from the apron in front of the bunker, (3) calculation of gamma rays due to thermal-neutron captures in the concrete walls of the bunkers and in the apron, and (4) calculation of the gamma-ray dosimeter response to the thermal- and fast-neutron fluxes at all receiver positions. From the neutron concrete-scattering calculations it appeared that gamma-ray wall scattering would contribute only about 5% or less to the total gamma-ray dose rates; hence, gamma-ray scattering calculations were not performed.

The approach used in the solid-angle calculations was to divide the receiver angle, as measured from the line joining the source and receiver, into 10° increments and to compute the fraction of the solid angle in each increment not blacked out by the bunkers. These fractions were then multiplied by the free-field fast-neutron and gamma-ray dose rates in each angular increment and summed over all increments.

Fast-neutron scattering from the bunker walls and the apron was calculated by use of an analytical fit to a dose albedo, derived from the Monte Carlo reflection data of Allen *et al.*,[6] for air-scattered COOL-I fast neutrons incident on concrete. The albedo used was $0.1135 \cos^{2/3} \theta_0 \cos \theta$ (reflected dose per steradian per unit incident dose), where θ_0 and θ are the angles of incidence and reflection, respectively. Both angles were measured with respect to the normal to the concrete surface.

For the concrete-capture gamma-ray calculations, the measured thermal-neutron fluxes and the capture-gamma-ray albedo given in Fig. 3.10.4 were used. The measured thermal-neutron fluxes were assumed to be isotropically incident upon the concrete surfaces.

The calculated and measured data for fast neutrons and gamma rays are compared in Tables 3.11.1 and 3.11.2, respectively. The calculated fast-neutron dose rates for all receiver positions in both the front bunker and the top bunker agree with the measured dose rates within 10% except

---

[1] Work performed by Radiation Research Associates, Fort Worth, Texas, under Subcontract 2267.

[2] L. B. Holland *et al.*, *Neutron Phys. Div. Ann. Progr. Rept. Sept. 1, 1962*, ORNL-3360, p 122.

[3] J. R. Stokes and W. C. Farries, FZK-132 (Secret).

[4] W. C. Farries and J. R. Stokes, FZK-145 (1962) (Secret).

[5] F. J. Muckenthaler, *In-Air Measurements in the Vicinity of the Tower Shielding Reactor II*, ORNL-3288 (April 1963).

[6] F. J. Allen *et al.*, *Neutron Reflection and Flux Versus Depth for Concrete*, BRL-1189 (1963).

Table 3.11.1. Calculated and Measured Fast-Neutron Dose Rates in Unshielded Bunkers

(Refer to Fig. 3.8.2 in Sec. 3.8 for bunker coordinates)

Dose-Rate Component	Fast-Neutron Dose Rate ($erg \cdot g^{-1} \cdot hr^{-1} \cdot w^{-1}$)			
	Receiver in Open-Top Bunker, $u = v = 0$		Receiver in Open-Front Bunker, $x = y = 0$	
	Near Opening, $w = 0.5$	At Center, $w = 6.0$	Near Opening, $z = 0.5$	At Center, $z = 6.0$
	($\times 10^{-4}$)	($\times 10^{-4}$)	($\times 10^{-4}$)	($\times 10^{-4}$)
Calculated direct beam	None	None	0.520	0.520
Calculated air-scattered	1.05	0.377	1.56	1.00
Calculated wall-scattered	0.117	0.129	0.222	0.355
Calculated apron-scattered	None	None	0.582	0.265
Total calculated	1.17	0.506	2.88	2.14
Total measured	1.08	0.399	2.69	2.15
Ratio: calc/meas	1.08	1.27	1.07	0.995

Table 3.11.2. Calculated and Measured Gamma-Ray Dose Rates in Unshielded Bunkers

(Refer to Fig. 3.8.2 in Sec. 3.8 for bunker coordinates)

Dose-Rate Component	Gamma-Ray Dose Rate ($erg \cdot g^{-1} \cdot hr^{-1} \cdot w^{-1}$)			
	Receiver in Open-Top Bunker, $u = v = 0$		Receiver in Open-Front Bunker, $x = y = 0$	
	Near Opening, $w = 0.5$	At Center, $w = 6.0$	Near Opening, $z = 0.5$	At Center, $z = 6.0$
	($\times 10^{-5}$)	($\times 10^{-5}$)	($\times 10^{-4}$)	($\times 10^{-4}$)
Calculated incident[a]	5.71	1.05	2.80	2.61
Calculated wall-capture	0.362	0.554	0.0577	0.0883
Calculated apron-capture	None	None	0.0575	0.0394
Calculated fast-neutron response[b]	1.35	0.500	0.329	0.265
Calculated thermal-neutron response[c]	2.21	1.86	0.311	0.279
Total calculated	9.63	3.96	3.56	3.28
Total measured	8.75	4.75	2.95	2.70
Ratio: calc/meas	1.10	0.834	1.21	1.21

[a] Includes direct-beam, air-scattered, and air-capture gamma rays.

[b] Accounts for response of gamma-ray dosimeter to fast neutrons.

[c] Accounts for response of gamma-ray dosimeter to thermal neutrons.

for the center position in the top bunker, where the calculated dose rate exceeds the measured dose rate by 27%. Most of the dose rate at this position is due to air-scattered neutrons arriving through receiver angles between 40 and 120°. Hence the calculated result would be especially sensitive to small uncertainties in the calculated angular distribution of the fast neutrons.

The agreement between the calculated and measured gamma-ray dose rates in the bunkers is less satisfying, since the calculations are consistently high by approximately 10 to 20% except for the center position in the top bunker, where the calculated dose rate is low by approximately 15%. The reason for this discrepancy has not been resolved. However, the gamma-ray dose rate at the lower position is known to be especially sensitive to variations in the air-scattered gamma rays. Also, wall scattering of gamma rays should be more important for this position than for any other.

The generally close agreement between the calculated and measured dose rates in the bunkers illustrates that the radiation penetrating openings into underground structures can be predicted satisfactorily when the free-field radiation environment is known. It is emphasized that the calculations are completely independent of all measurements made during the bunker experiment, except for the use of measured thermal-neutron fluxes in the calculations of secondary gamma-ray production.

3.12. MEASUREMENTS OF DOSE RATES RESULTING FROM FAST-NEUTRON SCATTERING IN BERYLLIUM, CARBON, ALUMINUM, AND IRON

F. J. Muckenthaler, K. M. Henry, V. V. Verbinski, M. S. Bokhari,[1] J. J. Manning, J. L. Hull, and D. R. Ward

As was reported previously,[2] shielding research in direct support of the Space Nuclear Auxiliary Power (SNAP) program has been undertaken by the Neutron Physics Division. One of the major concerns of the program is the development of suitable methods for calculating doses at the payload which result from neutrons that are scattered around the reactor shadow shield by various components of a SNAP system. A theoretical program is under way at ORNL (see Sec. 3.13) and at Atomics International whose ultimate purpose is to provide the required calculational methods. In order to provide experimental data against which the calculations could be checked, an experiment was performed at the Tower Shielding Facility to measure scattered neutron doses from cylindrical samples of several materials. The materials used were beryllium, carbon, aluminum, and iron, all of which have reasonably well-known cross sections and some of which have been proposed for use in various components of the SNAP systems.

The general arrangement of the TSF experiment is shown in Fig. 3.12.1. The Tower Shielding Reactor II (TSR-II) was placed inside a spherical lead-water shield from which a neutron beam emerged through a 6-in.-diam air-filled collimator.[3] (Gamma-ray effects were reduced by a 2-in.-thick lead disk in the collimator adjacent to the reactor.) Each sample was supported at the center of the beam by very thin wires under tension so that the axis of the cylinder was in the vertical position. The supports for the wires were well

[1] On assignment from the Pakistan Atomic Energy Commission.

[2] C. E. Clifford, *Neutron Phys. Div. Ann. Progr. Rept. Sept. 1, 1962*, ORNL-3360, p 102.

[3] The reactor and shield are described elsewhere: L. B. Holland and C. E. Clifford, *Description of the Tower Shielding Reactor II and Proposed Preliminary Experiments*, ORNL-2747 (1959); L. B. Holland *et al.*, *Neutron Phys. Div. Ann. Progr. Rept. Sept. 1, 1959*, ORNL-2842, p 39.

above and below the beam. Location of the beam center line was obtained by mapping the dose rate at the sample position, 8 ft from the reactor shield, both vertically and horizontally, with a fast-neutron dosimeter.

The samples were all 6 in. long and their diameters were 6, 4, 2, and 1 in. The sample densities were 1.80 g/cc for beryllium, 2.25 g/cc for carbon, 2.70 g/cc for aluminum, and 7.85 g/cc for iron.

Fast neutrons scattered by the cylindrical samples were observed with a Hurst-type detector shielded and collimated as shown in Fig. 3.12.1. The shield consisted of a cylindrical tank with a hemispherical head containing water-filled compartments as shown in the figure. Approximately 10 in. of lead around the detectors reduced the gamma-ray background from the reactor. The tank head was penetrated by a cone-shaped air-filled collimator 32.75 in. long and tapered from

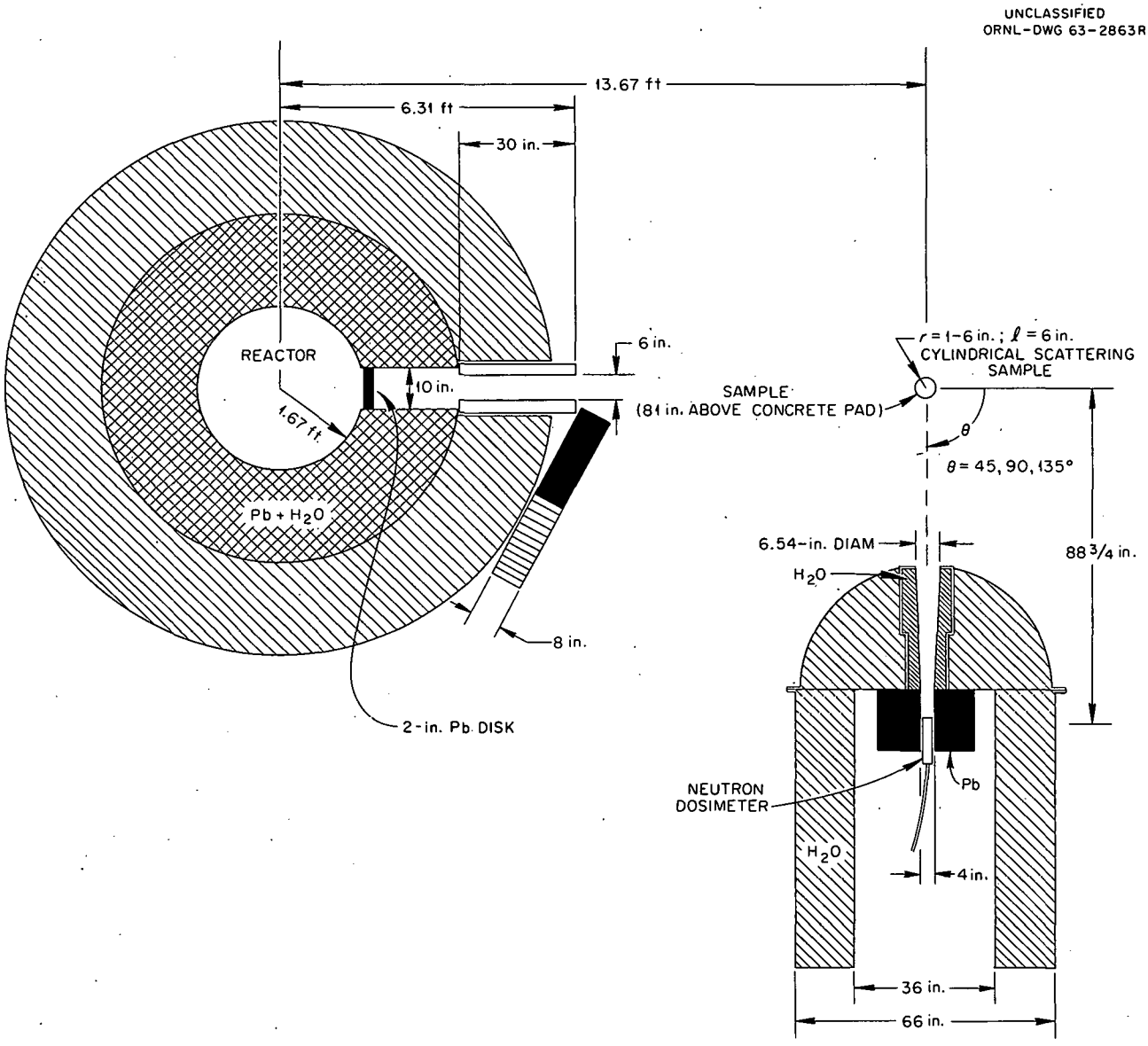

Fig. 3.12.1. Experimental Arrangement fro Measuring Scattered Neutron Dose from Cylindrical Samples in the TSR-II Beam.

6.54 in. at the outer end to 3.60 in. at the inner end. The detector-shield assembly was mounted on a three-wheeled carriage attached to a pivot point on the vertical center line of the sample. The assembly could thus be rotated about the sample while remaining a fixed distance from the sample position. The scattering angle θ was in the horizontal plane bisecting the sample and was defined by the center line of the neutron beam and a line between the center of the sample and the center of the detector.

The measured scattered fast-neutron dose rates for various sample materials and diameters at scattering angles of 45, 90, and 135° are given in Table 3.12.1. Background measurements (no sample in the beam) are included to indicate the degree to which air-scattered neutrons perturbed the experiment. Also included are ratios of the scattered dose rate to the direct-beam dose rate and ratios of the calculated scattered fractions to measured scattered fractions. The calculations were performed both by ORNL (see Sec. 3.13) and by Atomics International[4] for the experimentally determined neutron energy spectrum incident on the sample.

The energy spectrum of the direct beam at the sample position was measured with nuclear emulsions and also with an Li^6F Si-diode spectrometer. The results are presented in Fig. 3.12.2.

[4]K. Rooney, Atomics International, private communication.

Table 3.12.1. Measured Scattered Fast-Neutron Dose Rates and Comparison with Calculations[a]

Sample Diameter (in.)	Fast-Neutron Dose Rate ($erg \cdot g^{-1} \cdot hr^{-1} \cdot w^{-1}$)		$SF = \frac{\text{Scattered Dose Rate}}{\text{Direct-Beam Dose Rate}}$			SF_{calc}/SF_{meas}	
	Foreground	Background	Measured	AI Calculated[b]	ORNL Calculated	AI	ORNL
None	8.50(−2)[c]						
			Beryllium Sample: Scattering Angle = 45°				
1	4.85(−6)	1.40(−6)	4.22(−5)	3.85(−5)	3.80(−5)	0.91	0.90
2	1.07(−5)	1.40(−6)	1.11(−4)	1.07(−4)	1.01(−4)	0.96	0.91
4	1.93(−5)	1.40(−6)	2.13(−4)	2.03(−4)	1.99(−4)	0.95	0.93
			Beryllium Sample: Scattering Angle = 90°				
1	1.78(−6)	4.28(−7)	1.59(−5)	1.72(−5)	1.73(−5)	1.08	1.09
2	4.93(−6)	4.28(−7)	5.31(−5)	5.59(−5)	5.03(−5)	1.05	0.95
4	1.06(−5)	4.28(−7)	1.19(−4)	1.37(−4)	1.34(−4)	1.15	1.13
			Beryllium Sample: Scattering Angle = 135°				
1	2.12(−6)	7.80(−7)	1.58(−5)	1.83(−5)	1.82(−5)	1.16	1.15
2	5.25(−6)	7.80(−7)	5.26(−5)	6.10(−5)	5.56(−5)	1.16	1.06
4	1.25(−5)	7.80(−7)	1.39(−4)	1.63(−4)	1.58(−4)	1.17	1.14
			Carbon Sample: Scattering Angle = 45°				
1	3.33(−6)	1.26(−6)	2.43(−5)	1.98(−5)	1.95(−5)	0.81	0.80
2	7.96(−6)	1.26(−6)	7.87(−5)	6.48(−5)	6.23(−5)	0.82	0.79
4	1.77(−5)	1.26(−6)	1.94(−4)	1.69(−4)	1.66(−4)	0.87	0.86
6	2.52(−5)	1.26(−6)	2.82(−4)	2.42(−4)	2.38(−4)	0.86	0.84
			Carbon Sample: Scattering Angle = 90°				
1	1.56(−6)	4.28(−7)	1.34(−5)	1.19(−5)	1.14(−5)	0.89	0.85
2	4.27(−6)	4.28(−7)	4.53(−5)	4.17(−5)	3.99(−5)	0.92	0.88
4	1.22(−5)	4.28(−7)	1.39(−4)	1.23(−4)	1.20(−4)	0.88	0.88
6	1.91(−5)	4.28(−7)	2.19(−4)	2.02(−4)	1.91(−4)	0.92	0.87

Table 3.12.1 (continued)

Sample Diameter (in.)	Fast-Neutron Dose Rate ($erg \cdot g^{-1} \cdot hr^{-1} \cdot w^{-1}$)		$SF = \frac{\text{Scattered Dose Rate}}{\text{Direct-Beam Dose Rate}}$			$\frac{SF_{calc}}{SF_{meas}}$	
	Foreground	Background	Measured	AI Calculated[b]	ORNL Calculated	AI	ORNL
Carbon Sample: Scattering Angle = 135°							
1	2.04(–6)	7.80(–7)	1.48(–5)	1.52(–5)	1.51(–5)	1.03	1.02
2	5.12(–6)	7.80(–7)	5.11(–5)	5.30(–5)	5.02(–5)	1.04	0.98
4	1.37(–5)	7.80(–7)	1.52(–4)	1.58(–4)	1.54(–4)	1.04	1.01
6	2.30(–5)	7.80(–7)	2.62(–4)	2.78(–4)	2.61(–4)	1.06	1.00
Aluminum Sample: Scattering Angle = 45°							
1	3.66(–6)	1.13(–6)	2.99(–5)	2.73(–5)	2.72(–5)	0.91	0.91
2	9.29(–6)	1.13(–6)	9.60(–5)	8.70(–5)	8.99(–5)	0.91	0.94
4	2.25(–5)	1.13(–6)	2.52(–4)	2.25(–4)	2.24(–4)	0.89	0.89
6	2.89(–5)	1.13(–6)	3.27(–4)	3.34(–4)	3.22(–4)	1.02	0.98
Aluminum Sample: Scattering Angle = 90°							
1	1.49(–6)	3.79(–7)	1.31(–5)	1.22(–5)	1.21(–5)	0.93	0.92
2	4.43(–6)	3.79(–7)	4.76(–5)	4.37(–5)	4.28(–5)	0.92	0.90
4	1.24(–5)	3.79(–7)	1.41(–4)	1.32(–4)	1.31(–4)	0.94	0.93
6	2.06(–5)	3.79(–7)	2.38(–4)	2.28(–4)	2.20(–4)	0.96	0.92
Aluminum Sample: Scattering Angle = 135°							
1	1.51(–6)	7.01(–7)	9.58(–6)	9.28(–6)	8.98(–6)	0.98	0.95
2	3.56(–6)	7.01(–7)	3.36(–5)	3.53(–5)	3.34(–5)	1.05	0.99
4	1.01(–5)	7.01(–7)	1.10(–4)	1.17(–4)	1.12(–4)	1.06	1.02
6	1.87(–5)	7.80(–7)	2.12(–4)	2.16(–4)	2.07(–4)	1.02	0.98
Iron Sample: Scattering Angle = 45°							
1	4.48(–6)	1.26(–6)	3.79(–5)	3.31(–5)	3.04(–5)	0.87	0.80
2	1.03(–5)	1.26(–6)	1.06(–4)	9.75(–5)	9.16(–5)	0.92	0.86
4	2.05(–5)	1.26(–6)	2.27(–4)	2.17(–4)	2.00(–4)	0.96	0.88
6	2.72(–5)	1.26(–6)	3.05(–4)	2.77(–4)	2.79(–4)	0.91	0.91
Iron Sample: Scattering Angle = 90°							
1	1.62(–6)	4.28(–7)	1.41(–5)	1.46(–5)	1.27(–5)	1.04	0.90
2	4.69(–6)	4.28(–7)	5.01(–5)	4.95(–5)	4.43(–5)	0.99	0.88
4	1.18(–5)	4.28(–7)	1.33(–4)	1.36(–4)	1.26(–4)	1.02	0.95
6	1.82(–5)	4.28(–7)	2.09(–4)	2.20(–4)	2.12(–4)	1.05	1.01
Iron Sample: Scattering Angle = 135°							
1	2.05(–6)	7.80(–7)	1.49(–5)	1.65(–5)	1.49(–5)	1.11	1.00
2	5.18(–6)	7.80(–7)	5.18(–5)	5.57(–5)	5.20(–5)	1.08	1.00
4	1.47(–5)	7.80(–7)	1.45(–4)	1.63(–4)	1.49(–4)	1.12	1.03
6	2.41(–5)	7.80(–7)	2.49(–5)	2.75(–4)	2.56(–4)	1.10	1.03

[a]Digits in parentheses indicate power-of-ten multipliers; i.e., $8.50(-2) \equiv 8.50 \times 10^{-2}$.

[b]Private communication from K. Rooney, Atomics International.

[c]Direct-beam measurement at sample position.

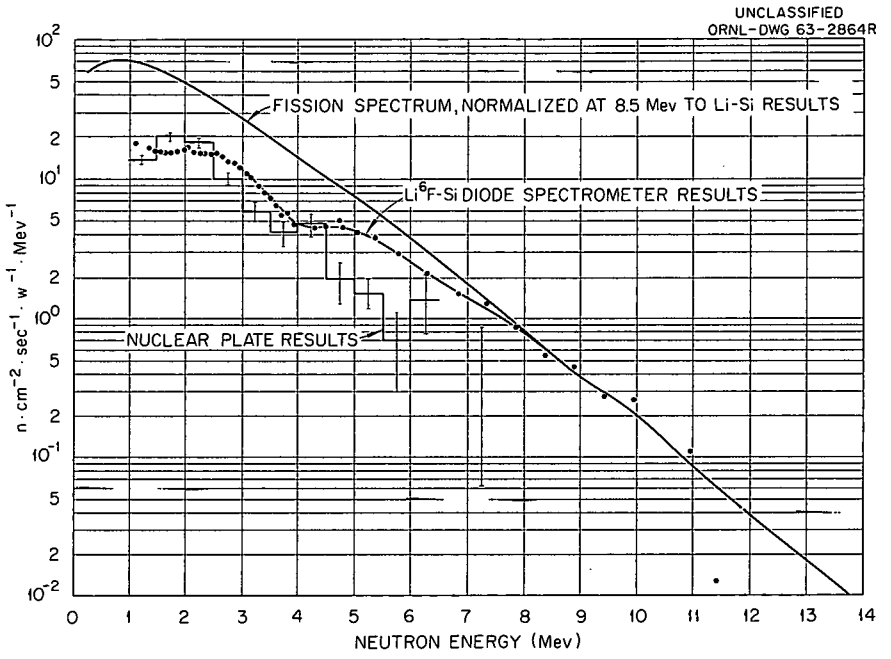

Fig. 3.12.2. Fast-Neutron Spectra at the Sample Position in the Collimated TSR-II Beam.

3.13. MONTE CARLO CALCULATIONS OF NEUTRON SCATTERING FROM CYLINDERS OF BERYLLIUM, CARBON, ALUMINUM, AND IRON

Be, C, Al, Fe

F. B. K. Kam, F. H. S. Clark, and J. G. LaTorre[1]

In the development of nuclear reactor power systems for space vehicles, the scattering of neutrons around the reactor shadow shield by various components of the system can contribute a major fraction of the radiation dose to the instrument payload. Therefore suitable methods for predicting scattered neutron doses for systems proposed in the Space Nuclear Auxiliary Power (SNAP) program must be developed. For some scattering agents, such as thin radiators, a single-scattering anaylsis may often be adequate, but for massive parts, such as control drum drives, the contribution to the dose by multiply scattered neutrons must be considered. This problem is now being attacked in a calculational program which has as its objectives (1) the computation by Monte Carlo techniques of a sufficient body of data to establish under what circumstances single-scattering methods can be successfully used and, hopefully, (2) the development of a means for estimating directional leakage fluxes to give rough predictions for scattering from massive components.

The calculations are being carried out by one of the variations of the 05R computer programs (see Sec. 5.6) for the geometry shown in Fig. 3.13.1. A parallel beam of neutrons is incident on a cylinder in a direction normal to the cylinder axis, and detector angles are measured from the direction of the incident beam in a plane perpen-

[1] Mathematics Division.

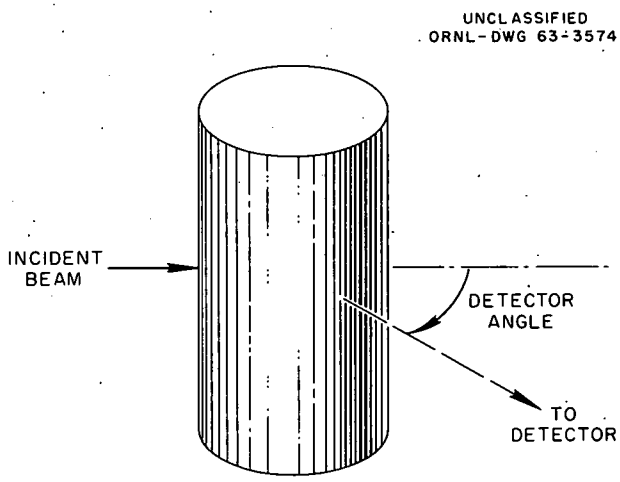

Fig. 3.13.1. Geometry for Neutron Scattering Calculations.

dicular to the cylinder axis. The cylinders are taken to be made of beryllium, carbon, aluminum, and iron, and the calculation is performed for the spectrum measured for the Tower Shielding Reactor II (see Sec. 3.12).

The mechanics of the calculation are entirely straightforward. No biasing is employed in computing the collision density in the cylinders, and the doses and fluxes at the detector are computed by statistical estimation from each collision point. It was found that a statistical error in the neighborhood of 4 or 5% could reasonably be achieved. In order to avoid a larger error from other sources, it is necessary to treat quite faithfully cross sections that might otherwise be dealt with roughly. The Be(n,2n) reaction is an example.

With the data obtained so far and with an arbitrary specification of what constitutes an acceptable accuracy, it should be possible to determine in many practical cases whether a single-scattering evaluation of dose is appropriate. The analysis of the data has not yet been carried to the point of achieving the second objective, that is, provision of an approximate angular scattering kernel for massive objects. More data will be required for this.

Some sensitivity to spectrum has been noted. Comparison of dose ratios for an incident fission spectrum with those for an incident TSR-II spectrum led to differences ranging from negligibly small to about 10% (with the greatest differences noted for the smallest cylinders); however, a considerable portion of these differences is statistical. In fact, for the larger cylinders, 4 and 6 in., where it is most important to have some multiple scattering estimation, the differences appear to be almost entirely statistical. The spectral dependence may therefore to some extent, but probably not too greatly, limit the generality of these results. The results of the calculations performed thus far are shown in Table 3.13.1. Comparisons with the experimental data, as well as comparisons with results from similar calculations performed at Atomics International, are included in Table 3.12.1 of Sec. 3.12.

Table 3.13.1. Calculated Dose and Flux Ratios for Scattered Neutrons

Material	Diameter (in.)	Detector Angle (deg)	Ratio: Scattered Dose / Incident Dose	Ratio: Singly Scattered Flux / Total Scattered Flux
Be	1	45	3.80×10^{-5}	0.68
		90	1.73×10^{-5}	0.42
		135	1.82×10^{-5}	0.55
	2	45	1.01×10^{-4}	0.53
		90	5.03×10^{-5}	0.37
		135	5.56×10^{-5}	0.41
	4	45	1.99×10^{-4}	0.38
		90	1.34×10^{-4}	0.25
		135	1.58×10^{-4}	0.29
	6	45	2.40×10^{-4}	0.35
		90	1.84×10^{-4}	0.23
		135	2.45×10^{-4}	0.28
C	1	45	1.95×10^{-5}	0.79
		90	1.14×10^{-5}	0.72
		135	1.51×10^{-5}	0.76
	2	45	6.23×10^{-5}	0.66
		90	3.99×10^{-5}	0.56
		135	5.02×10^{-5}	0.62
	4	45	1.66×10^{-4}	0.51
		90	1.20×10^{-4}	0.41
		135	1.54×10^{-4}	0.49
	6	45	2.38×10^{-4}	0.44
		90	1.91×10^{-4}	0.35
		135	2.61×10^{-4}	0.42
Al	1	45	2.72×10^{-5}	0.82
		90	1.21×10^{-5}	0.72
		135	8.98×10^{-6}	0.67
	2	45	8.99×10^{-5}	0.70
		90	4.28×10^{-5}	0.57
		135	3.34×10^{-5}	0.52
	4	45	2.24×10^{-4}	0.53
		90	1.31×10^{-4}	0.40
		135	1.12×10^{-4}	0.36
	6	45	3.22×10^{-4}	0.47
		90	2.20×10^{-4}	0.35
		135	2.07×10^{-4}	0.32
Fe	1	45	3.04×10^{-5}	0.78
		90	1.27×10^{-5}	0.66
		135	1.49×10^{-5}	0.69
	2	45	9.16×10^{-5}	0.62
		90	4.43×10^{-5}	0.48
		135	5.20×10^{-5}	0.52
	4	45	2.00×10^{-4}	0.41
		90	1.26×10^{-4}	0.31
		135	1.49×10^{-4}	0.38
	6	45	2.79×10^{-4}	0.34
		90	2.12×10^{-4}	0.24
		135	2.56×10^{-4}	0.32

THIS PAGE

WAS INTENTIONALLY

LEFT BLANK

4. Radiation Shielding Information Center

THIS PAGE

WAS INTENTIONALLY

LEFT BLANK

4.1. PROGRAM OF RADIATION SHIELDING INFORMATION CENTER (RSIC)

S. K. Penny, D. K. Trubey, and Betty F. Maskewitz

The Radiation Shielding Information Center (RSIC), an organization to collect, organize, evaluate, and disseminate information on radiation shielding, was established at ORNL in fiscal year 1963 by the U. S. Atomic Energy Commission. To date the emphasis of the Center has been on nuclear reactor and other low-energy radiations, but space and weapons radiations will be included in the near future.

The type of information which RSIC seeks falls into two classes: published literature, including reports issued by various nuclear-oriented organizations, and digital computer codes. The literature is examined, analyzed, and categorized in a sophisticated manner and then stored in an archival microfiche[1] file. The computer codes are examined for operability and ease of dissemination and to determine whether they produce the desired results. The literature concerning the use of the codes is kept separate from the main body of literature because of the relatively short life of computer codes.

When space radiations are included in the Center's activities, RSIC will seek a third class of information, which will consist of pertinent high-energy data not available in the literature, such as cross sections and flux-to-dose conversion factors. These data will be stored in a readily retrievable and duplicable form. (This class will be restricted to high-energy radiations since data of this type for low-energy radiations are collected by other centers.)

The services of RSIC are available to all organizations or individuals. The staff fulfills requests for (1) specific shielding information that can be supplied by telephone, by letter, or by conversation during a visit to the Center (appropriate security clearance will be necessary for access to the classified files), (2) bibliographies of shielding literature, either general or special in scope, (3) information concerning digital computer codes which have been written for shielding computations and made operable by the Center, and (4) copies of codes and associated software. In addition to specific requests, RSIC will publish a newsletter informing the shielding community of current research and development in the field of shielding and of the activities of the Center, publish bibliographies, and issue critical reviews, state-of-the-art reports, and compilations of generally useful shielding data.

The activities of the Center thus far have included the development of an information retrieval system using a digital computer (see Sec. 4.2). The system, which was used to produce the Center's first bibliography, described in Sec. 4.3, has the advantage that a current bibliography or literature search, satisfying any particular criteria, may be printed by machine at any time.

The Computer Code Section of RSIC has obtained a number of useful shielding codes and is presently checking them out on either the IBM-7090 or the CDC-1604A machine. The codes are also being prepared for routine dissemination through computer manufacturers.

Communication of RSIC with the shielding community is maintained through an international board of volunteer coordinators, who inform the Center of important shielding efforts in their organizations and make the Center aware of relevant needs of the shielding community in the area of information transmission.

Persons interested in RSIC should write S. K. Penny, Radiation Shielding Information Center, Oak Ridge National Laboratory, Post Office Box X, Oak Ridge, Tennessee 37831, or phone 615-483-8611, Ext. 6944.

[1] Unitized microfilm sheets, 3 × 5 in.

4.2. RSIC INFORMATION RETRIEVAL SYSTEM

S. K. Penny, D. K. Trubey, and M. B. Emmett[1]

An information retrieval system consisting of a set of programs for the IBM-7090 computer was developed by RSIC for storing bibliographic and indexing information on magnetic tapes and for producing literature searches and shielding bibliographies. In determining the type of system which should be used, it was judged that the amount of shielding literature being published is small enough to allow sophisticated indexing techniques yet large enough to require a machine system, as opposed to card handling or "peek-a-boo" techniques. While a number of information retrieval systems are available commercially, the RSIC staff decided against committing the Center to a particular system until it had gained experience in information retrieval. Since the staff members were already familiar with computer use and since a digital computer offers the advantage that both the programs and the input data can be easily revised, a computer was the machine selected for use in the retrieval system.

In preparing information for the computer each literature specimen is examined thoroughly for subject content, which is not always obvious from the title or the abstract, and then is indexed under as many subject categories as are necessary. A total of 118 subject categories are currently in use, each assigned a six-digit alphanumerical code number for machine searching and each a subcategory of the following basic list:

1. General Radiation Shielding References
2. Basic Nuclear and Atomic Information
3. Radiation Effects
4. Transport Theory
5. Experimental Techniques
6. Results of Radiation Transport Calculations and Experiments for Simple Geometries
7. Shield Design Techniques
8. Application of Calculational and Experimental Techniques to Complex Systems
9. Shielding Materials

In addition to a subject category number being assigned to each literature specimen, an emphasis role indicator number is assigned which gives a semiquantitative evaluation of the emphasis or relevance placed upon the category by the specimen. Where applicable, another role indicator is assigned which indicates whether the specimen describes or merely uses a given technique, theory, or device. Other indexes are built into the system for possible future use, one being the security classification. Thus far, however, only unclassified specimens have been placed in the system.

Three types of computer programs are used in the retrieval system, one which files information on tapes (updating), another which revises tapes (changes information already in the system that is in error or is obsolete due to revisions in the system), and a third which produces literature searches or bibliographies.

The information resulting from the first two programs is stored on tapes according to accession numbers, which represent the order of entry of the specimens into the system, to the author(s), and to the subject category number(s). Tape 1 is indexed by accession number and contains "permanent" bibliographic information such as title, document name and number, date of publication, author list, and classification. Tape 2, also indexed by accession number, contains the indexing information about the document; that is, it lists the category numbers and role indicators associated with each accession number. This tape is short and thus changes can be made at low cost. Tape 3 is indexed by category number and contains a list of accession numbers for each category; thus it is an inversion of Tape 2. Tape 4 is indexed by author and contains a list of accession numbers for each author (inversion of Tape 1). Tape 5 is indexed by author name and contains a list of authors in alphabetical order, each record containing the names of authors whose names begin with the same letter. Tape 5 is an aid to updating Tape 4. Alphabetizing is done partially by hand since the problems involved are too complicated to make complete machine alphabetizing worthwhile.

[1]Mathematics Division.

Once the information has been filed on the five tapes discussed above, the third computer program can be used for searching the system to locate specimens for an edit according to the criteria specified. At present the only edits produced are an accession list edit used by RSIC and the edit which is the first bibliography (see Sec. 4.3).

RSIC has obtained literature from various sources, for example, from staff members' files, from current documents in the ORNL Central Library, and from searching *Nuclear Science and Engineering* and *Nuclear Science Abstracts*. Other journals and abstract journals are being examined, and the various bibliographies obtained will be utilized. RSIC coordinators and others have supplied lists of relevant literature.

When a specimen is to be entered in the system, the analyst who reads the specimen logs the bibliographic information, writes comments to aid any future reanalysis, and records the appropriate category and role indicator code numbers. An eight-digit identifying number is also assigned to aid the subsequent handling of the information. The information, except for the comments, is then entered on forms for keypunching on cards. The cards are of four types, with one or more cards for each type. According to type, they contain (1) the document date, name, and number, and the page number in the document, (2) names of the authors (usually last name and initials only), (3) the title of the particular article in the document, if any, and (4) the security classification, category list with role indicators, and other indexes.

Various checks are made as the cards are read (via input tape) into the system. The identifying number, card type number, and card number are used to ensure that the cards are in the correct order, and the list of categories is compared with a master list to ensure that the list is reasonable. The information is simply added to Tapes 1 and 2, but, in general, the other tapes are completely rewritten.

4.3. COMPILATION OF SHIELDING BIBLIOGRAPHY

S. K. Penny and D. K. Trubey

The information retrieval system described in Sec. 4.2 was used to produce the first shielding bibliography published by RSIC [*Cumulative Bibliography of Literature Examined by the Radiation Shielding Information Center*, ORNL-RSIC-1 (April 1963)]. The bibliography represents a complete edit of the information tapes in the retrieval system. It differs from the usual bibliography in that it is in a "ready-searchable" form. It contains two parts: a list of documents by 118 subject categories and an author index. Each subject category lists all the documents dealing with that particular subject, the information being repeated under other categories when appropriate. The author index gives all relevant document accession numbers and subject category numbers for each author.

A distinctive feature of the bibliography is the inclusion with each literature specimen listed of the role indicators described in Sec. 4.2. Figures 4.3.1 and 4.3.2 are examples of the entries in the subject category section and author index, respectively.

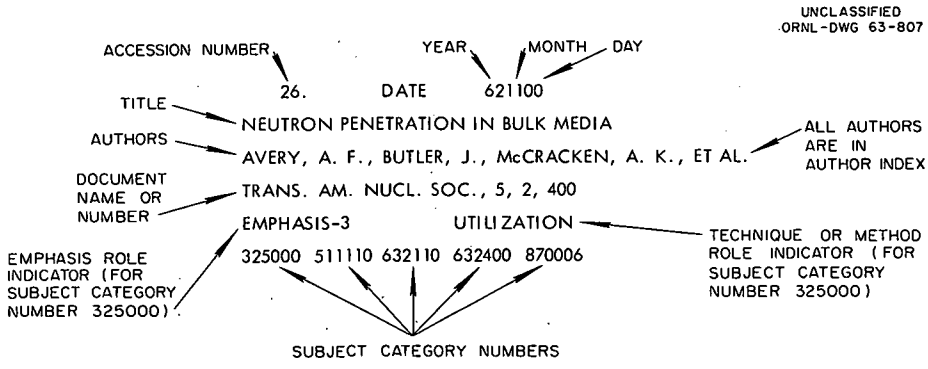

Fig. 4.3.1. Example of an Entry in the Subject Category Section of RSIC Bibliography.

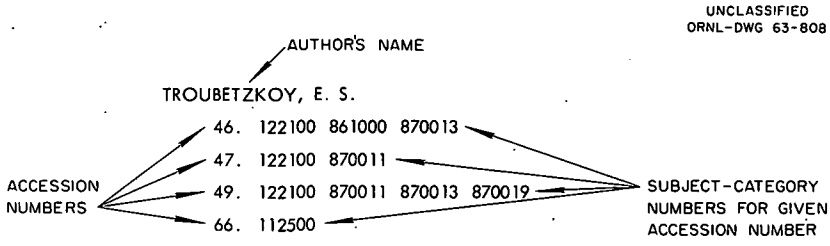

Fig. 4.3.2. Example of an Entry in the Author Index of RSIC Bibliography.

4.4. COLLECTION OF SHIELDING COMPUTER CODES

S. K. Penny, D. K. Trubey, and Betty F. Maskewitz

A special section has been formed in RSIC to collect and evaluate computer codes useful for shielding calculations. The main effort of the section is to accumulate experience with all computer codes relevant to shielding problems. The codes are examined as to operability, ease of dissemination, and production of the desired results.

The computer code section is also responsible for intercomparing various codes by means of simple standard problems. The comparisons will be made on the basis of accuracy, machine time required, ease of operation, ease of providing cross sections and other input data in the required format, etc.

A number of codes have been collected and most of them tested for operability. A comparison study is under development now and the results should be forthcoming soon.

Requests for codes, as well as for information concerning code usage, should be directed to the Center (see Sec. 4.1 for address).

5. Mathematics and Computer Programs

THIS PAGE

WAS INTENTIONALLY

LEFT BLANK

5.1. RECURSION RELATIONS AND SIMPLIFIED EXPRESSIONS FOR THE 6-*j* SYMBOLS[1]

C. D. Zerby

In the published report,[1] it is shown that the 144 symmetry properties of the 6-*j* symbols discovered by Regge can be displayed with a 4 × 4 array which is invariant to the ordering of three of the rows and all columns. The elements of the array are linear combinations of the quantum numbers. In addition, it is shown that a large set of three-term recursion relations exist. The recursion relations are used to deduce simplified expressions for the 6-*j* symbols in special cases.

[1]Published as ORNL-3440.

5.2. SOME SIMPLIFIED EXPRESSIONS FOR THE 3-*j* SYMBOLS[1]

C. D. Zerby and R. R. Coveyou

A general formalism has been developed for obtaining some simplified expressions for the 3-*j* symbol. The formalism is based on the notation introduced by Regge[2] which represents the 3-*j* symbol as a 3 × 3 square array in which each element is a linear combination of the quantum numbers having integral positive value. With the aid of the new formalism it was shown that the symbol can be expressed as a single algebraic term in certain ideal cases. In addition, it was shown that a recursion relation exists that leads to simplified expressions for the 3-*j* symbols when any one of the elements of the square array has a value of less than 3. The expressions have been published elsewhere.[1]

[1]Published as ORNL-TM-514.

[2]T. Regge, *Nuovo cimento* **10**, 544 (1958).

5.3. AN IBM-7090 SUBROUTINE PACKAGE FOR LANGRANGIAN INTERPOLATION[1]

S. K. Penny and M. B. Emmett[2]

When a computer code requires that the same type of calculation be performed repeatedly, it might be advantageous to perform the calculation once for the entire range of variables and store the resulting information in the machine in tabular form for future reference. The computing cost of a table lookup is usually much smaller than that of direct computation. Therefore in certain codes, where computational time is at a premium whereas storage area is not, this type of table generation is highly desirable.

A FORTRAN subroutine, LAGRAN, has been written for the purpose of generating a table of data by means of Lagrangian interpolation from a smaller table of data. The interpolation can be one of three types: linear, semilog, or log-log. The number of points to be used in the Lagrangian interpolation is optional. The values in the generated table correspond to values of the independent variable which are evenly spaced either in the variable itself or in its logarithm.

Details of the subroutine are given in ORNL-3428.[1]

[1]Published as ORNL-3428.

[2]Mathematics Division.

5.4. SUBROUTINE PACKAGES FOR MAKING LINEAR, LOGARITHMIC, AND SEMILOGARITHMIC GRAPHS USING THE CALCOMP PLOTTER

D. K. Trubey and M. B. Emmett[1]

A group of subroutine packages written in FORTRAN for the IBM-7090 and CDC-1604 computing machines to facilitate the plotting of curves and data points on the CALCOMP plotter are described in detail elsewhere.[2-4] The CALCOMP digital incremental plotter uses data placed on a magnetic tape by one of the computers mentioned above. The packages offer advantages over the more basic subroutines[5] of automatically drawing a grid with labeling, according to the user's specifications, and converting the plotting variables so that the programmer can use his own variables for coordinates rather than the inches required by the basic routines. The disadvantage is that, in the interest of simplicity, only certain options are permitted to the user.

The two FORTRAN codes are not interchangeable at the present time because the IBM-7090 version uses a basic package written in FAP and the CDC-1604 version uses a new and improved package written in CODAP. For this and other reasons, the CDC-1604 version is more flexible than the IBM-7090 version.

[1]Mathematics Division.

[2]D. K. Trubey and M. B. Emmett, *A CDC-1604 Subroutine Package for Making Linear, Logarithmic and Semilogarithmic Graphs Using the CALCOMP Plotter*, ORNL-3447 (June 10, 1963).

[3]D. K. Trubey and M. B. Emmett, *An IBM-7090 Subroutine Package for Making Logarithmic and Semilogarithmic Graphs Using the CALCOMP Plotter*, ORNL TM-430 (Dec. 12, 1962).

[4]D. K. Trubey and M. B. Emmett, *An IBM-7090 Subroutine for Making Linear Graphs Using the CALCOMP Plotter*, ORNL TM-430 Supplement (Feb. 27, 1963).

[5]D. K. Cavin, Mathematics Division, unpublished ORCID memorandums.

5.5. COMPARISON OF LEAST-SQUARES ALGORITHMS

D. Bogert and W. R. Burrus

When several computational methods are known which theoretically give the same answers, the choice of the best method for a particular computer is a question of strategy. For example, the conventional method for solving the least-squares problem, with $n \leq m$, finds the solution as $x = (\tilde{A}A)^{-1} \tilde{A} b$, but if $n = m$, this expression may be simplified to $x = A^{-1} b$. Thus, if $n = m$, ordinary matrix inversion is a much simpler method than the conventional least-squares method. Then the question arises as to whether the conventional least-squares method is the best method available for matrices in which $n < m$ or whether other least-squares methods exist which would yield better results. A short literature search revealed several different least-squares methods,[1-8] three of which have been compared with the conventional method (identified as ORDLS). The tentative results are presented here.

ORDLS: Ordinary Least-Squares Method

The least-squares problem is that of finding an approximate solution, $x = (x_1, x_2, \ldots x_n)$, to a set of overdetermined equations

$$Ax = b \tag{1}$$

so as to minimize the length of the residual vector, $Ax - b$, where $b = (b_1, b_2, \ldots b_m)$ is a vector of knowns and A is the matrix of coefficients A_{ij} relating the unknowns to the knowns. The least-squares problem is usually solved by finding the solution to the "normal equations" of least squares:

$$(\tilde{A}A)\, x = \tilde{A}\, b\,. \tag{2}$$

In ORDLS the solution is obtained as

$$x = (\tilde{A}A)^{-1}\, \tilde{A}\, b\,. \tag{3}$$

The matrix $(\tilde{A}A)^{-1}$ is known as the solution variance matrix and is useful for various statistical applications. The product $(\tilde{A}A)^{-1}\, \tilde{A}$, which relates the solution to the knowns, is called the "transformation matrix." Since several existing least-squares computer codes use double-precision arithmetic, ORDLS variants in both single and double precision were programmed. Also, since the matrix inversion of $(\tilde{A}A)$ had recently been emphasized,[9] two more variants of ORDLS were programmed, one which uses double precision for the computation of $(\tilde{A}A)$ and another which uses double precision for the inversion of $(\tilde{A}A)$. The importance of accuracy in inverting the matrix was therefore isolated.

ORTHO: Least Squares by Orthogonalization

If a square matrix U is found such that $Q = AU$ is orthogonal, then by substituting $A = QU^{-1}$ into the normal equations, (2),

$$\tilde{U}^{-1}\, \tilde{Q}Q\, U^{-1}\, x = \tilde{U}^{-1}\, \tilde{Q}\, b\,; \tag{4}$$

and since Q is orthogonal (i.e., $\tilde{Q}Q = I$),

$$x = U\, \tilde{Q}\, b \tag{5}$$

is obtained for the least-squares solution. The ORTHO code was programmed to obtain the upper

[1] H. Scheffe, *The Analysis of Variance*, Wiley, New York, 1959.

[2] P. Lauchli, *Numer. Math.* 3, 226–40 (June 1961).

[3] J. B. Rosen, *J. Soc. Ind. Appl. Math.* 8(1), 181–217 (1960).

[4] R. E. Von Holdt, p. 255–56 in *Proceedings of the Western Joint Computer Conference*, San Francisco, March 3–5, 1959, published by Institute of Radio Engineers, New York.

[5] T. N. E. Greville, *SIAM Review* 2(1), 15–22 (1960).

[6] P. J. Davis, Chap. 10 in *Survey of Numerical Analysis* (John Todd, ed.), McGraw-Hill, New York, 1962.

[7] P. J. Davis and P. Rabinowitz, p. 55–133 in *Advances in Computers* (F. L. Alt, ed.), Academic Press, New York, 1961.

[8] C. Lanczos, *Applied Analysis*, Prentice Hall, Englewood Cliffs, N. J., 1956.

[9] M. H. Lietzke, R. W. Stoughton, and M. P. Lietzke, *A Comparison of Several Methods for Inverting Large Symmetric Positive Definite Matrices*, ORNL-3430 (May 1963).

triangular matrix U by the recursive Gramm-Schmidt-Hilbert method. Several authors[6-8] warn against the gradual loss of orthogonality in the columns of Q due to the accumulation of numerical roundoff errors and suggest a progressive straightening technique to keep Q orthogonal. For this reason, a variant of the ORTHO method with progressive straightening was programmed.

Even if the matrix Q is not orthogonal, the solution is given by

$$x = U\,(\tilde{Q}Q)^{-1}\,\tilde{Q}\,b\,. \tag{6}$$

If the off-diagonal elements of $\tilde{Q}Q$ are small, then the solution, to first order, is

$$x = U(2I - \tilde{Q}Q)\,\tilde{Q}\,b\,. \tag{7}$$

It was found that the solution to Eq. (7) could be obtained by augmenting the orthonormalization algorithm with virtually no additional computation. The three algorithms are ORTHO, ORTHO-FIX, and ORTHO-AUG. The solution variance matrix is $U\tilde{U}$ and the transformation matrix is $U\tilde{Q}$.

VHOLDT: The Von Holdt Method

In our search for various least-squares methods, we found a recent decay analysis code that used a scheme due to Von Holdt. Von Holdt claims in his original paper[4] that the loss of significant figures is only half as large as with ORDLS. It is not clear whether Von Holdt is referring to a fixed-point computer or to a floating-point computer or whether he had actually tested his claim. Although the basic algorithm is quite similar to ORTHO (except that the matrix Q is not normalized), we decided to test it also.

TRILLS: Least Squares by Triangularization

Still another method is based on the observation that the replacement of A by (MA) and of b by (Mb), where M is any orthonormal m by m matrix, does not alter the solution to the normal equations, (2):

$$(\widetilde{MA})\,(MA)x = (\widetilde{MA})\,(Mb)\,. \tag{8}$$

If M is chosen such that MA is an upper triangular matrix in the upper n by n block and is zero in the remaining $(m - n)$ by n block, that is, that

$$(MA) = \begin{pmatrix} U \\ 0 \end{pmatrix}, \tag{9}$$

then the equations reduce to

$$Ux = b'\,, \tag{10}$$

where b' is the vector consisting of the first n elements of (Mb). The solution x may be obtained by solving Eq. (10) by back substitution or, since the inversion of a triangular matrix is simple,[8] by

$$x = U^{-1}\,b'. \tag{11}$$

A method was coded which gradually transforms A into U by performing a sequence of rotations in a two-dimensional subspace, each rotation reducing at least one lower triangular element to zero. By transforming the b vector at the same time, it is not necessary to save the sequence of rotations. Although this method of triangularization is used fairly often in matrix computations, we have not yet found a good reference to cite for its application to the least-squares problem. The solution variance matrix can be calculated as $U^{-1}\,\tilde{U}^{-1}$, and the transformation matrix as $U^{-1}\,\tilde{U}^{-1}\,\tilde{A}$. Use of the transformation matrix to obtain the solution $x = U^{-1}\,\tilde{U}^{-1}\,\tilde{A}b$, however, destroys most of the numerical advantages.

Numerical Test

In order to evaluate the various methods, we selected a sequence of test matrices of various orders. The matrices chosen were the cube of the n by n binomial matrix for various values of n from 3 to 45 so that

$$A = \begin{bmatrix} 0.50 & 0.25 & & & \\ 0.25 & 0.50 & 0.25 & & \\ & \ddots & \ddots & \ddots & \\ & & 0.25 & 0.50 & \end{bmatrix}^3 . \tag{12}$$

This test matrix has its largest elements near the diagonal and is of a type which frequently occurs in experimental physics, and its properties

(eigenvector and eigenvalues) are well known. Although the selection of test matrices with $n = m$ is atypical in ordinary least-squares problems, it is believed that the relative performance of the various algorithms is not affected significantly by the choice of the test matrix. The choice of a square matrix rather than a rectangular ($n < m$) matrix also allowed the solution to be obtained by ordinary matrix inversion, $x = A^{-1} b$. In order to eliminate the possibility that the simple structure of the elements of the test matrix could affect the numerical roundoff, we perturbed the elements of the test matrices with random normal deviates with a standard deviation of 2×10^{-7} of the value of the A_{ij} element. For example, the test matrix of order 5 was

$$A = \begin{pmatrix} 0.21875000 & 0.21874999 & 0.09375008 & 0.01562499 & 0.00000000 \\ 0.21874985 & 0.31250018 & 0.23437499 & 0.09374992 & 0.01562501 \\ 0.09375001 & 0.23437501 & 0.31249975 & 0.23437497 & 0.09375000 \\ 0.01562501 & 0.09374999 & 0.23437491 & 0.31249997 & 0.21875000 \\ 0.00000000 & 0.01562502 & 0.09375008 & 0.21874997 & 0.21874993 \end{pmatrix} .$$

The effect of the random perturbations is large enough to change the elements of $(\tilde{A}\tilde{A})^{-1}$ for the larger cases ($n = 45$) by an order of magnitude. The right-hand side, b, of Eq. (1) was then constructed from the perturbed matrix by combining columns so that the exact solution to the perturbed system is 1000 for all x_i except for the central x_i, which is 10,000.

Preliminary Numerical Results

The criterion used for evaluation of the results was the average magnitude of the error. Qualitatively, the results of all methods tested fall into one of four general groups as shown on Fig. 5.5.1. Single-precision ORDLS, VHOLDT, and ORTHO became useless (i.e., the errors were as large as the solution) beyond $n = 7$. ORTHO-FIX and ORTHO-AUG fell into the same general group as TRILLS and ordinary matrix inversion. These methods give useful results up to and beyond $n = 45$. Double-precision ordinary matrix inversion and double-precision TRILLS are accurate to the full eight figures printed out. However, double-precision ORDLS started out with all eight figures accurate but rapidly degenerated until only about two of the eight figures were accurate at $n = 35$. About three more significant figures were obtained with the least-squares algorithm of NLLS.[10] This algorithm is hand-coded to carry about 19 decimal digits of precision in its arithmetic, as compared with 16 decimal digits in the FORTRAN double-precision arithmetic. Performing only the product $(\tilde{A}\tilde{A})$ in double precision or the inversion only in

[10] These calculations were done by P. B. Wood, Central Computer Section, ORGDP, using the algorithm from NLLS, Share Distribution No. 837.

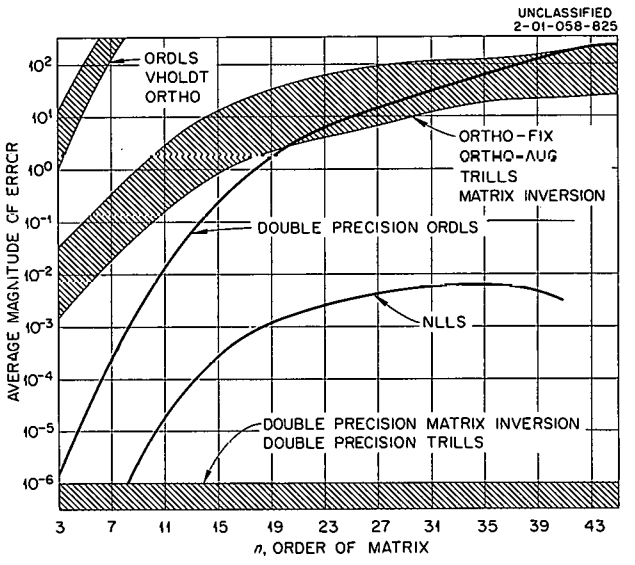

Fig. 5.5.1. Average Magnitude of Error vs Order n of Test Matrix for Various Least-Squares Methods.

double precision gave no substantial improvement over single-precision ORDLS. Apparently both the product and the inversion have to be done in double precision for any benefit to be effected.

No comparisons of computing speeds have yet been made, but the computation time should be approximately proportional to the number of multiplications involved. Table 5.5.1 gives the number of multiplications, not including numbers of the order of $n \times m$ or less. FORTRAN double precision increased the running time by a factor of 5 to 10, depending upon the amount of input-output. Surprisingly, the NLLS-ORDLS algorithm appears to be similar in speed to the comparable FORTRAN double-precision ORDLS. Although all results are shown for unweighted least squares, nonequal weighting can be included in all the methods with only $n \times m$ additional multiplications.

Conclusions

ORDLS is not the best method with respect to accuracy, but it might be the best on the basis of speed for highly overdetermined systems ($n << m$) if a loss of significant figures is not serious. TRILLS and the ORTHO variants appear to be about comparable. VHOLDT is almost as poor as ORDLS, although it can undoubtedly be "fixed" by either a straightening technique or a first-order correction scheme. TRILLS is the simplest code, and it is also the fastest if many of the elements below the diagonal are initially zero since the rotations can be skipped for these elements.

The FORTRAN algorithms can be obtained from the authors.

Table 5.5.1. Approximate Number of Floating-Point Multiplications for Various Methods

Method	Number of Multiplications		
	Solution Vector	Variance Matrix	Transformation Matrix
ORDLS	$n^2\left(\frac{1}{2}m + n\right)$	0	n^2m
TRILLS	$n^2\left(2m - \frac{2}{3}n\right)$	$\frac{1}{2}n^3$	n^2m
ORTHO	$n^2\left(m + \frac{1}{2}n\right)$	$\frac{1}{2}n^3$	n^2m
ORTHO-FIX	$n^2(2m + n)$	$\frac{1}{2}m^3$	n^2m
ORTHO-AUG	$n^2\left(m + \frac{1}{2}n\right)$	$\frac{1}{2}n^2(n + m)$	$n^2\left(\frac{3}{2}m + n\right)$

5.6. MODIFICATIONS TO THE O5R COMPUTER CODE

D. Irving

The O5R (Oak Ridge Random Research Reactor Routine[1]), a general-purpose Monte Carlo code for the generation of neutron histories below 50 Mev, is being revised so that future changes in the code can be made more easily. Although the code was designed originally for reactor problems, it may also be used for shielding calculations. It can handle problems involving several scatterers and several media in a general complex geometry. Cross sections may be given at as many as 10^4 energy values and scattering may be done up to a P_8 approximation. So that the code will have general applications, no analysis is done by O5R; instead, neutron histories are generated on tape, and specific analysis routines are written for each problem.

Two versions of the code, one written in FORTRAN and the other in CDC-1604A machine language, are being completed. If, as is intended, the two versions are compatible, subroutine by subroutine, a working version of O5R can be assembled by combining the FORTRAN versions of some of the subroutines with the machine language versions of the remaining subroutines. This combines ease of making changes with efficiency in running time. Any subroutines which are to be changed, either to adapt the code to a particular problem or to introduce new features into the program, can be used in their FORTRAN version with the more efficient machine language versions of unaltered subroutines.

A complete writeup containing a flow chart and description of each subroutine is being prepared. Also being completed is an operator's manual describing the input for O5R, the specification of a source, the format of a collision tape, and so forth. Upon completion of the FORTRAN code and writeup, O5R will be available for distribution to other installations.

In addition to O5R itself, two other programs, GEOM and XSECT, are being prepared with a full writeup, operator's manual, and FORTRAN code. GEOM is a general geometry subroutine which is used by O5R but which may be detached and used separately in analysis routines. XSECT is a cross-section handling routine and is needed to prepare cross-section tapes for O5R.

A subroutine for the handling of thermal neutrons in O5R has been completed and is being tested. The routine is based on a free-gas model for the motion of the nuclei. It can handle many media and many elements in a general geometry and may be used either for purely thermal problems or for problems that also use the slowing-down portions of O5R.

---

[1] R. R. Coveyou, J. G. Sullivan, and H. P. Carter, *The O5R Code: A General Purpose Monte Carlo Reactor Code for the IBM-704 Computer*, a paper presented at the Symposium on Codes for Reactor Computations, Vienna, Austria, 1961; see also R. R. Coveyou, J. G. Sullivan, and H. P. Carter, *Neutron Phys. Div. Ann. Progr. Rept. Sept. 1, 1958*, ORNL-2609, p 87.

THIS PAGE

WAS INTENTIONALLY

LEFT BLANK

6. Radiation Detector Studies (I)

THIS PAGE

WAS INTENTIONALLY

LEFT BLANK

6.1. A SHIELDED-DIODE FAST-NEUTRON SPECTROMETER

V. V. Verbinski, M. S. Bokhari,[1] and H. A. Todd[2]

Efforts at developing a fast-neutron spectrometer capable of measuring neutron spectra in the intense gamma-ray fields characteristic of nuclear reactors have, in general, met with only limited success, despite the fact that in the high neutron flux of a reactor the spectrometer need not be very efficient, even for measurements behind thick shields (see Sec. 3.2). The approach used by Love and Murray,[3,4] who constructed a neutron-sensitive detector consisting of an Li^6F layer sandwiched between two silicon surface-barrier diodes, was the most promising. In their detector the alpha particle and the triton emitted in opposite directions in the $Li^6(n,\alpha)T$ reaction were separately detected in the diodes, and the sum of their energies gave the energy of the incident neutron plus the Q value of the reaction. The closed-sandwich geometry of their counter worked fairly well for neutrons having energies $\lesssim 5$ Mev. Above this energy, however, the determination of the background due to neutron interactions in the silicon of the diodes became difficult. The evaluation of the background by the use of another pair of diodes, essentially identical to the first but without the Li^6F layer, was not accurate because of the difficulties associated with matching the sensitive areas of two pairs of diodes and their capacitances and depletion depths by adjustment of the bias voltages and amplifier gains.

As a way of improving the counting efficiency of a diode spectrometer, Dearnaley *et al.*[5] proposed the substitution of He^3 gas for the Li^6F layer. With such an arrangement the measurement of the background associated with (n, charged-particle) reactions in the silicon is easily accomplished by evacuating the gas, if the energy loss in the gas is ignored. However, the lower Q value of the $He^3(n,p)T$ reaction – only 0.75 Mev compared with 4.78 Mev available from the $Li^6(n,\alpha)T$ reaction – does not allow adequate discrimination against background from gamma-ray pileup, even with the use of fast coincidence circuits. In addition, the forward peaking of the reaction particles from He^3 restricts the permissible diode separation, and thus the effective shielding against gamma radiation and very fast neutrons.

In the spectrometer described below the difficulties associated with accurate background subtraction and gamma-ray pileup have been overcome, and the range of neutron energies over which the spectrometer can successfully be used has been extended to include practically the entire spectrum of reactor neutrons.[6]

Spectrometer Design

The present spectrometer[7] differs from the earlier version[3,4] in that (1) the Li^6F that was deposited on a face of one of the closely spaced ($\sim$0.001-in.) diodes in the original design is now independently supported between more widely spaced diodes and can be replaced by an Li^7F layer for background determinations; and (2) the region between the diodes previously occupied by a thin film of air is now evacuated. A diagram of the revised arrangement is shown in Fig. 6.1.1.

[1]U.S. Agency for International Development Fellow, on loan from the Pakistan Atomic Energy Commission.

[2]Instrumentation and Controls Division.

[3]T. A. Love and R. B. Murray, *IRE Trans. Nucl. Sci.* 8(1), 91 (1961).

[4]T. A. Love and K. M. Henry, *Neutron Phys. Div. Ann. Progr. Rept. Sept. 1, 1961*, ORNL-3193, p 116.

[5]G. Dearnaley, A. T. G. Ferguson, and G. C. Morrison, *IRE Trans. Nucl. Sci.* 9(3), 174 (1962).

[6]The authors are indebted to T. A. Love for helpful discussions.

[7]Fabricated by R. E. Zedler, Instrumentation and Controls Division.

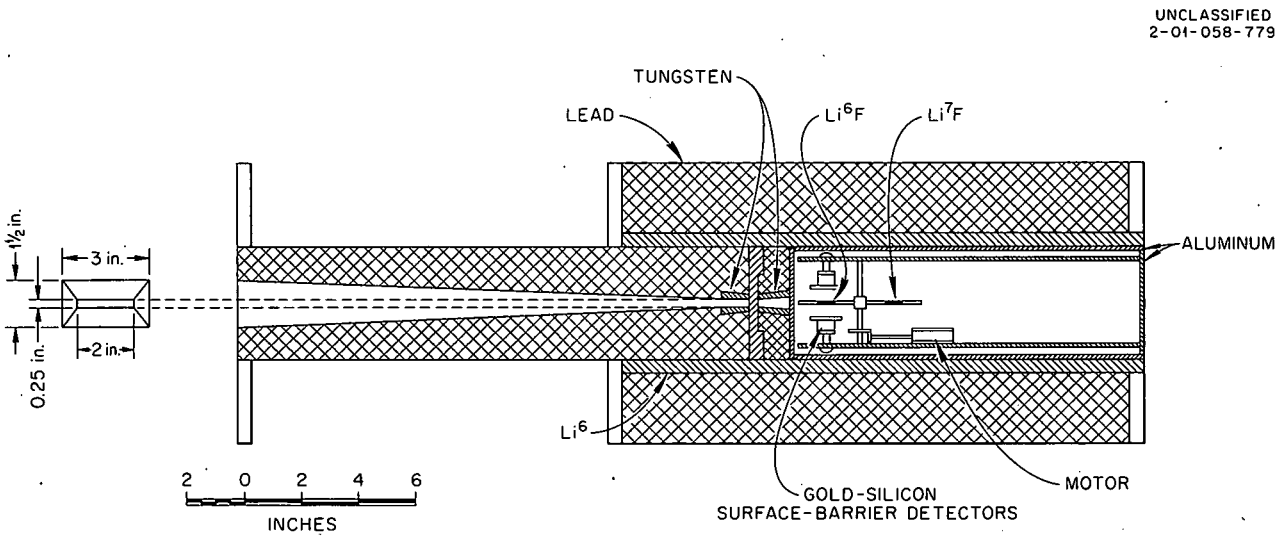

Fig. 6.1.1. Cross Section of the Shielded-Diode Fast-Neutron Spectrometer.

To shield the diodes against intense gamma-ray fields and very fast neutrons, a lead shield and a tungsten-lined lead collimator are used. By further shielding against thermal neutrons with Li^6 on all sides, the spectrometer has been successfully used to measure the spectrum of the directed fast-neutron flux within the Bulk Shielding Reactor I, both at its face and as far away as 60 cm in water (see Sec. 3.2).

A neutron, after passing through the collimator, impinges on the Li^6F layer and produces an alpha particle and a triton which share between them the energy of the incoming neutron, E_n, plus 4.78 Mev, the Q value of the $Li^6(n,\alpha)T$ reaction. The output pulse, which is obtained by summing up the energies deposited by the alpha particle and the triton in the diodes, corresponds, however, to an energy that is less than $(E_n + Q)$. This is because the particle pair is subject to energy losses in the 580-μg/cm^2 layer of Li^6F, the 100-μg/cm^2 layer of gold on each diode, and the 50-μg/cm^2 layer of Formvar backing on which the Li^6F has been vacuum-evaporated before reaching the sensitive volume of the silicon. The energy loss is variable, depending not only on the angles of emission of the alpha particle and triton but also on the point at which the $Li^6(n,\alpha)T$ reaction takes place in the Li^6F layer. This variable energy loss governs the width of the peak resulting from monoenergetic neutrons, while the average energy loss controls the position of this peak on the pulse height vs energy plot. For the counter with a 580-μg/cm^2 Li^6F layer, the full-width at half maximum is 18% for thermal neutrons, 8.2% for 3-Mev neutrons, and 1.1% for 14.7-Mev neutrons. The average energy loss observed is 0.84 Mev.

Both the Li^6F layer and the almost equally thick Li^7F layer that is used for background determinations are mounted on a thin aluminum wheel driven by a small remotely controlled electric motor which is mounted inside the vacuum-tight aluminum cylinder that houses the diode assembly.

Electronics

Figure 6.1.2 shows a block diagram of the electronics associated with the spectrometer. The signal from each diode is first fed into its respective preamplifier, which in turn feeds a DD-2 double-delay-line amplifier[8] having a 0.7-μsec clipping time. The pulse from each of the DD-2 amplifiers, A and B, is fed into a discriminator circuit biased to reject all pulses which represent an energy less than the minimum energy deposited in either diode by alpha particles ejected in the reaction $Li^6(n,\alpha)T$ by thermal neutrons. A coincidence circuit further rejects all pulses separated in time by more than 75 nsec.

[8]E. Fairstein, *Rev. Sci. Instr.* 27(7), 475 (1956).

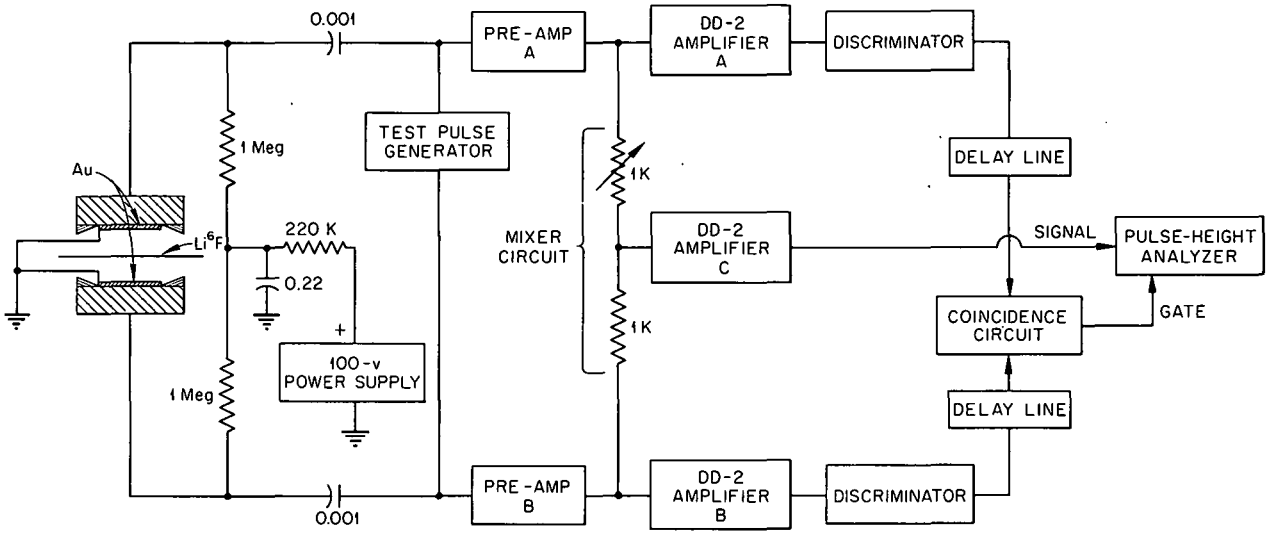

Fig. 6.1.2. Block Diagram of Shielded-Diode Spectrometer Electronics.

The pulses from the preamplifiers are summed in the mixer circuit, which in turn feeds the DD-2 amplifier C. The output pulse from the amplifier C is finally displayed on the analyzer only when the analyzer is simultaneously triggered by an output pulse from the coincidence circuit.

Detector Efficiency. – The detector efficiency depends on the differential reaction cross section per steradian, the thickness of the Li^6F layer, and the geometry of the diode arrangement. If σ is the differential reaction cross section per steradian, N the number of Li^6 nuclei, and ω the solid angle between a point on the Li^6F layer and the diodes, then the efficiency per unit area at this point is given by $\sigma N \omega$.

The differential cross sections per steradian for the reaction $Li^6(n,\alpha)T$ are known for neutrons of energies from 0.150 to 2.15 Mev and at 14 Mev.[9] The lack of information on differential reaction cross sections for neutron energies between 2.15 and 14 Mev may make calculations of efficiency in this region rather uncertain. The total cross sections for this reaction are known, however, up to 14-Mev neutron energy. If the known differential reaction cross section per steradian (averaged about 90° in the center-of-mass system over all angles of emission of alpha or triton accepted by the diode geometry) is plotted as a function of neutron energy, a curve results which is similar in shape to that for the total reaction cross section. From the $1/E$ nature of the reaction cross section above 2.15 Mev, there being no resonances, it is reasonable to use the total reaction cross section and divide it by 13.33, the ratio of the total reaction cross section to the average differential cross section obtained from the above plot.

As discussed earlier, the alpha particle and the triton are emitted in opposite directions in the center-of-mass system, and in actual counting coincidence is demanded between pulses from the two diodes. This places a "constraint" on the solid-angle calculation which requires elliptical integrals for points on the Li^6F that are away from the center of the Li^6F layer. It was therefore found convenient to compute the solid angle numerically from point to point. Figure 6.1.3 shows a plot of solid angle vs radial distance from the center of the Li^6F layer for the geometry of the present spectrometer. The average solid angle $\bar{\omega}$, calculated by weighting contributions from concentric rings of Li^6, is 1.35 steradians.

[9] D. J. Hughes and R. S. Carter, *Neutron Cross Sections: Angular Distributions*, pp 3, 6, 8, BNL-400, 2d ed., vol I (October 1962).

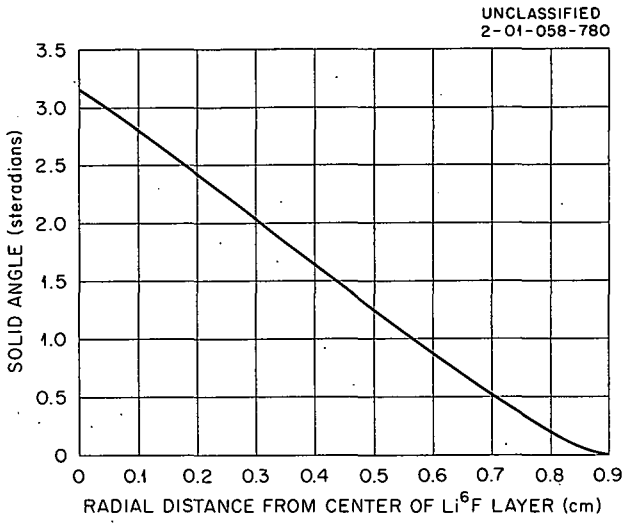

Fig. 6.1.3. Solid Angle Between Li^6F and a Diode, as a Function of Radial Distance from the Center of the Li^6F Layer.

A diode separation of 1.79 cm was used in the present spectrometer.

The Li^6F layer is 580 $\mu g/cm^2$ thick, and its diameter is 3.75 cm. However, its effective diameter is limited by the diameter, D, of the diodes and the separation between them, because of the coincidence requirement. The value of the effective diameter is $0.943D$ (D = 1.8 cm), obtained from Fig. 6.1.3, and the effective number of Li^6 nuclei is 1.37×10^{19}. From the average differential reaction cross section, the average solid angle, and the total number of Li^6 nuclei, the counter efficiency was calculated to be $\sim 3.2 \times 10^{-3}$, which agrees with experimentally determined values for thermal neutrons within 10%. The theoretical calculation of efficiency, however, did not take into account the uncertainties in the thickness of the Li^6F layer, the separation distance of the diodes, the active area of the diodes and their alignment, losses due to Coulomb scattering, or the finite thickness of the wire grid supporting the Li^6F layer. The last four factors tend to decrease the efficiency, but by not more than a few percent each.

For determinations of absolute flux, the value of $N\bar{\omega}$ was calculated from the experimentally measured[10] efficiency, $\sim 3.5 \times 10^{-3}$ (±10%), for thermal neutrons. For these measurements the spectrometer was exposed in the ORNL Graphite Reactor thermal column, and the number of counts under the thermal peak was obtained. A gold monitor foil was used for this exposure and for an exposure in which the Li^6F film was replaced by a 1-mil-thick gold foil of the same diameter. The neutron absorption for the Li^6F was nearly the same as that for the gold foil, and hence the uncertainties due to flux depression in the gold foils were canceled out. The flux determination was finally made by punching out disks of decreasing size from the center of the large gold foil and measuring the activation of these disks. The flux was flat in the "effective" region of the Li^6F layer.

Further checks of the spectrometer efficiency for fast neutrons are in progress. However, on the basis of $N\bar{\omega}$, as calculated above, the efficiency for 3-Mev neutrons is estimated to be $\sim 5.2 \times 10^{-7}$ (see Sec. 3.3).

The loss of alpha particles would make it impossible to accurately calculate the spectrometer efficiency as a function of energy. Some care is required, therefore, in selecting safe discriminator bias settings. The proper procedure for biasing the present spectrometer below the alpha pulses is to first record the response of individual diodes to thermal neutrons without discrimination (Fig. 6.1.4) and then to raise the bias level for one of the diode amplifiers so that only triton pulses can come through. Finally, these triton pulses are used to gate the multichannel analyzer, while the pulses from the unbiased diode are displayed on the analyzer. These pulses will be the stripped distribution of alpha-particle pulses, with gamma rays and other undesirable pulses removed, from which the highest safe bias level can be ascertained.

Detector Response to Monoenergetic Neutrons

Response of the spectrometer to thermal, 3-Mev, and 14.7-Mev neutrons has been measured without the use of the collimator and shielding shown in Fig. 6.1.1. Thermal neutrons were obtained from the ORNL Graphite Reactor thermal column, and 3- and 14.7-Mev neutrons were produced in the reactions $D(d,n)He^3$ and $T(d,n)He^4$, respectively, by using an electrostatic accelerator. Figure 6.1.5 demonstrates the linearity of the detector

[10] T. V. Blosser, private communication.

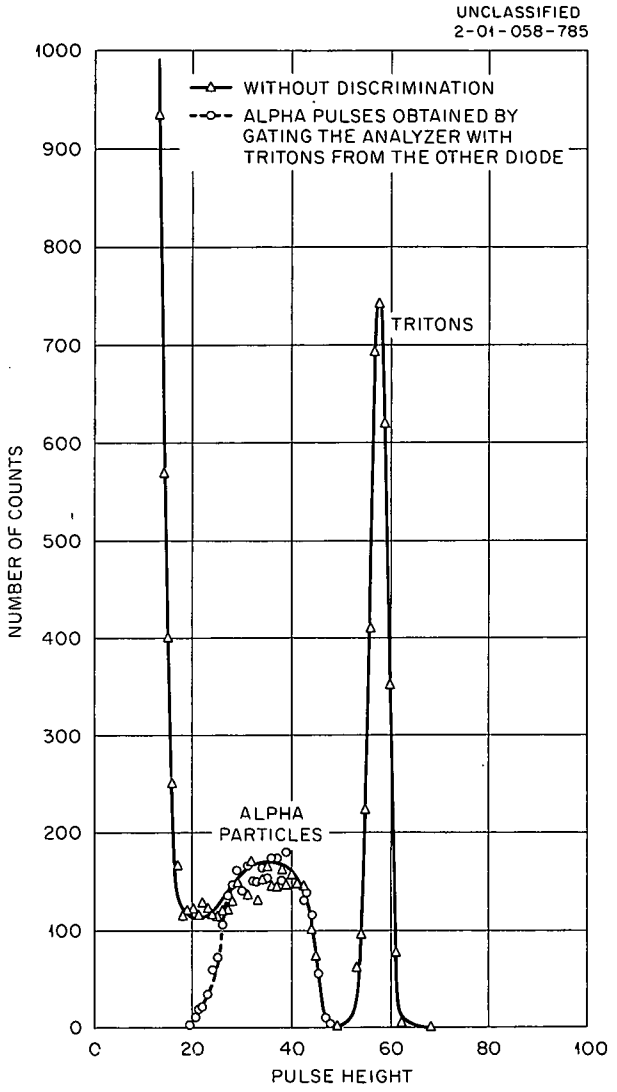

Fig. 6.1.4. Response of a Single Diode to Thermal Neutrons.

over the neutron energy range from 0 to 14.7 Mev, in that the points fall on a straight line. This line extrapolates to a value of 0.84 Mev below the Q value of 4.78 Mev, which is in agreement with an approximate calculation of the average energy loss for thermal neutrons. This means that the average energy loss of the particle pair is roughly constant for neutrons of all energies. Because of the forward inclination of the alpha particle and the triton, which increases with the neutron energy, the mean absorption thickness, $\overline{\Delta x}$, increases. This partially compensates for a decrease of dE/dx with the increasing energy of the particle pair, so that the average energy loss, $\overline{\Delta E}$ $(= dE/dx\overline{\Delta x})$, is approximately constant.

The pulse-height distribution resulting from exposure of the unshielded and uncollimated spectrometer to thermal neutrons is shown in Fig. 6.1.6. Similar curves for 3- and 14.7-Mev monoenergetic sources are shown in Figs. 6.1.7 and 6.1.8, respectively. All three curves represent net foreground only. In the cases of thermal and 3-Mev sources, no background was observed because the threshold energy for the (n, charged-particle) reaction in silicon, which is responsible for any background, is too high. In the case of the 14.7-Mev source, however, the background was very high but was well separated from the peak and could be accurately reproduced by substituting the Li^7F layer for the Li^6F layer. With the use of a collimator and shielding, the background will be much lower, and background subtraction should be all the more accurate.

The shape of the peaks is symmetrical in all cases, because the individual alpha and triton pulse-shape distributions are symmetrical (simple addition). If, however, the alpha particles leaving at shallow angles are accepted, as is the case with a closed-sandwich diode, then the individual pulse shape distributions can be asymmetric, both having a low-pulse-height tail. The sum-pulse

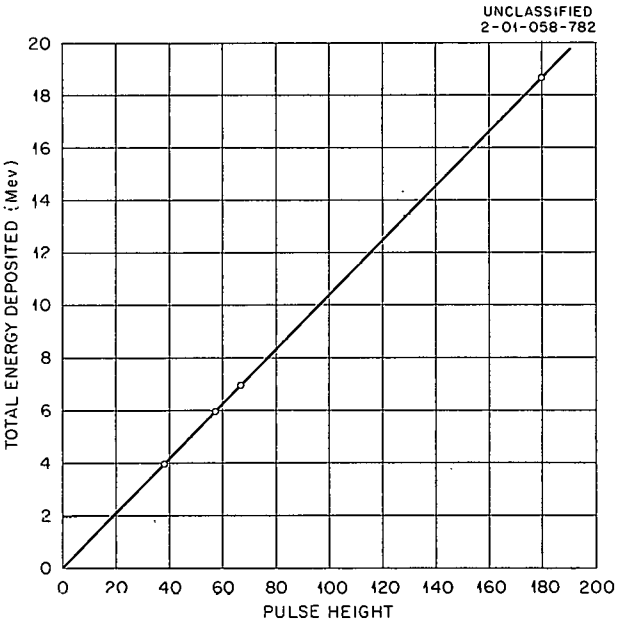

Fig. 6.1.5. Total Energy Deposited in Diode as a Function of Pulse Height.

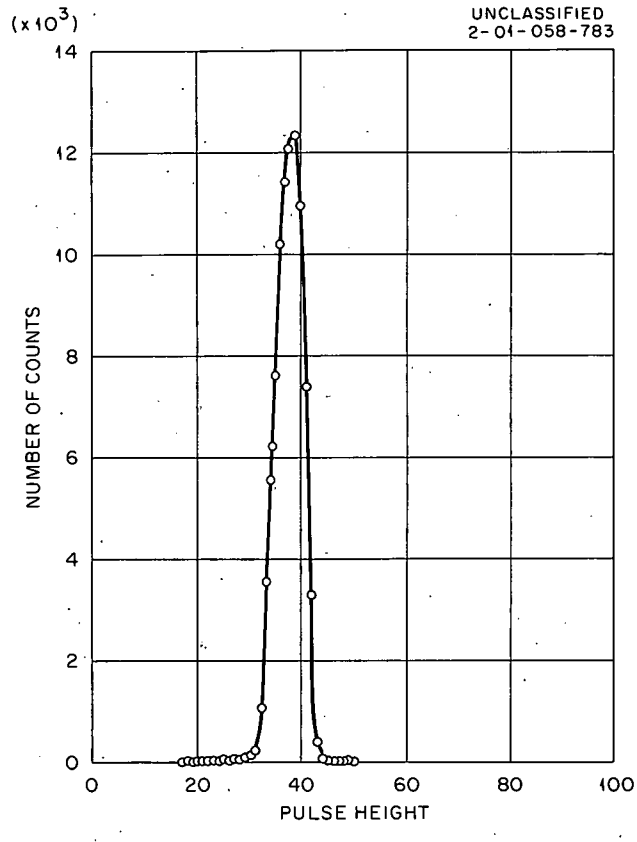

Fig. 6.1.6. Pulse-Height Spectrum from Thermal Neutrons.

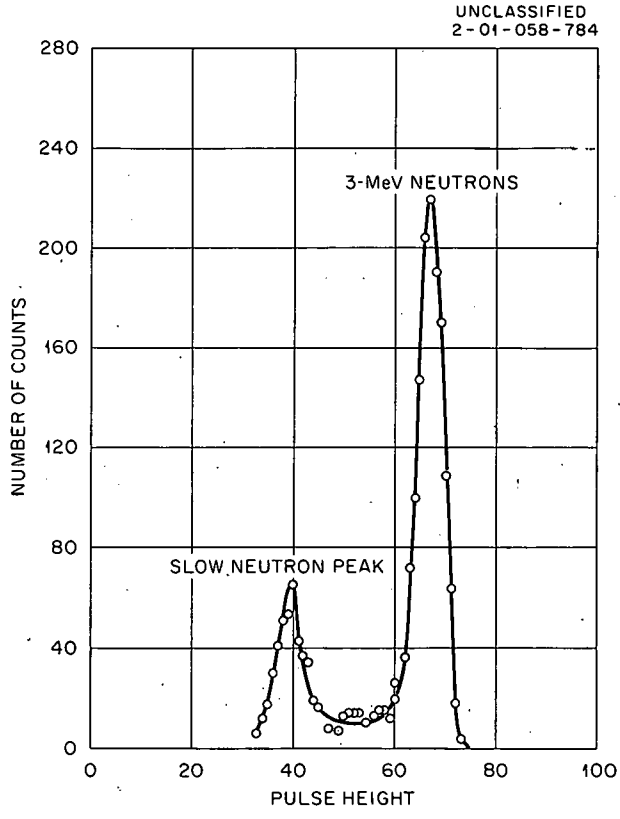

Fig. 6.1.7. Pulse-Height Spectrum from 3-Mev $D(d,n)He^3$ Neutrons.

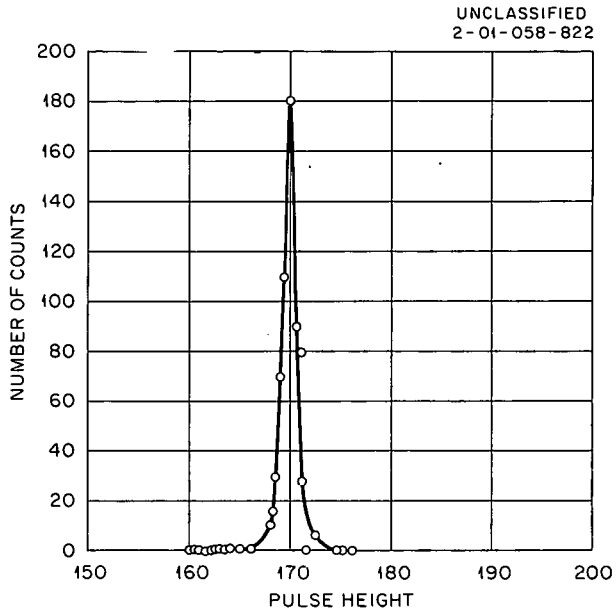

Fig. 6.1.8. Pulse-Height Spectrum from 14.7-Mev $T(d,n)He^4$ Neutrons.

can then be asymmetric because of the larger pulse-height spread of the alpha particles.

Application

A typical application of the spectrometer to the measurement of a reactor spectrum is shown in Fig. 6.1.9. The data were taken with the collimator and shielding surrounding the diodes. The spectrum is characterized by an epithermal peak perched on the fission neutron spectrum.

When the spectrometer was tested without the lead collimator, gamma-ray pileup completely masked the neutron counts due to the high gamma-ray buildup in the reactor. Even with the shielding in place, at high reactor powers gamma-ray pileup not only broadens the epithermal peak but at a distance of 60 cm in water, where the gamma-ray-to-neutron ratio is extremely high (see Sec. 3.2), also causes a shift in the analyzer base line. It is therefore necessary to use a pulse generator under actual running conditions to determine the broadening as well as the energy shift.

Conclusions

It has been shown that the spectrometer with the "shielded diode" design is suitable for measuring a reactor spectrum amidst intense gamma-ray and fast-neutron background. The detection efficiency, which is $\sim 3.5 \times 10^{-3}$ for thermal neutrons, can be increased by an order of magnitude by using a matrix of diodes with a preamplifier for each element. For a given diode separation, the spectrometer efficiency is not proportional to diode area but increases much more rapidly. Also, the use of metallic Li^6 in place of the fluoride would more than double the spectrometer efficiency for the same energy resolution.

The method of detection of neutrons described here can be extended by a small modification of the counter to measure the differential reaction cross section $\sigma(\theta_\alpha,\theta_T)$ for $Li^6(n,\alpha)T$ for which no data exist between 2 Mev $< E <$ 14 Mev.

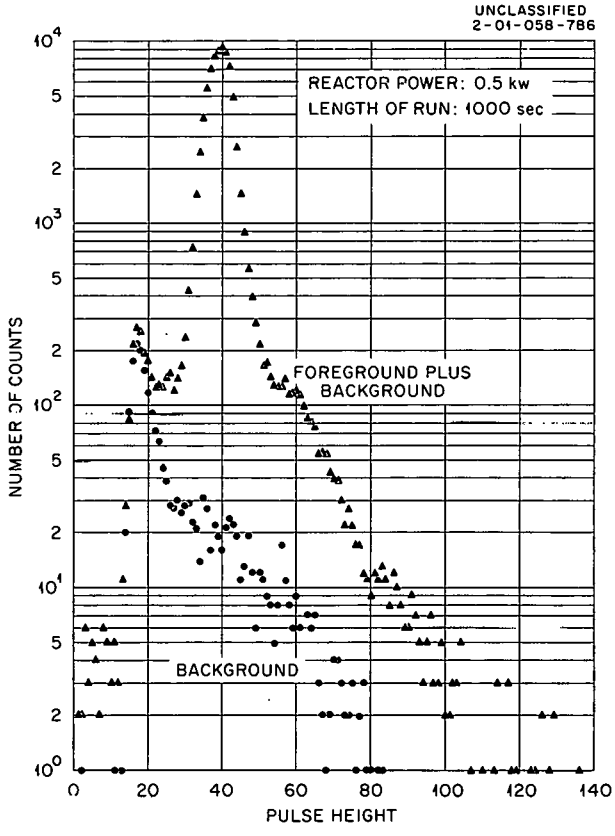

Fig. 6.1.9. Typical Reactor Spectrum (Unprocessed Data) Obtained with the Shielded-Diode Spectrometer.

6.2. A METHOD OF CORRECTING GAMMA-RAY SPECTRAL MEASUREMENTS FOR COLLIMATOR EFFECTS

G. T. Chapman

When measuring a gamma-ray spectrum with a system in which the photons are collimated through a shield, it is essential to have some estimate of the effectiveness of the collimator in order to correctly evaluate the data. No known shielding material is absolutely opaque to gamma rays. Consequently, penetration of gamma rays through small thicknesses of the material at the entrance and exit apertures, even if the shield is thick enough to stop the gamma rays, will effectively increase the solid angle of the collimator and give rise to an apparent error in the measured count rate. In addition, gamma rays may be scattered by the collimator walls before reaching the detector. Since scattering degrades the energy of the gamma rays, a disproportionate number of counts may then appear in the "tail" of the measured pulse-height distribution which could be misinterpreted as a reduced efficiency (defined as the ratio of the area under the total absorption peak to the total area of the distribution for monoenergetic photons) for the crystal.

Neither of the above effects is easy to measure with precision. Therefore, one must rely on intuition, experience, and the available computations in order to get a reasonable approximation for the required data corrections. Mather[1] investigated the problem analytically, and various experimenters[2-4] have obtained results which apparently substantiate his conclusions. A less sophisticated method, which is based on a curve published by Mather,[5] has been used to obtain an approximation for the collimator response of the Model IV gamma-ray spectrometer[6] used to measure the gamma-ray spectrum of the stainless steel reactor (see Sec. 3.1).

The primary difference between the method used for the stainless steel reactor measurement and the method presented by Mather lies in interpretation. Mather suggests that to a first approximation the effect of penetration is the same as reducing the collimator length by 1 mean free path of the collimator material at each end (and, consequently, by implication, the same as reducing the shield thickness), whereas the interpretation presented here obtains approximately the same results by a slight energy-dependent increase in the radii at the entrance and exit apertures of the collimator and no reduction of the collimator length. It is believed that this interpretation affords a simpler method for calculating the collimator response than that described by Mather.[1]

Figure 6.2.1 shows a shield containing a collimation hole with a geometric radius of r cm.

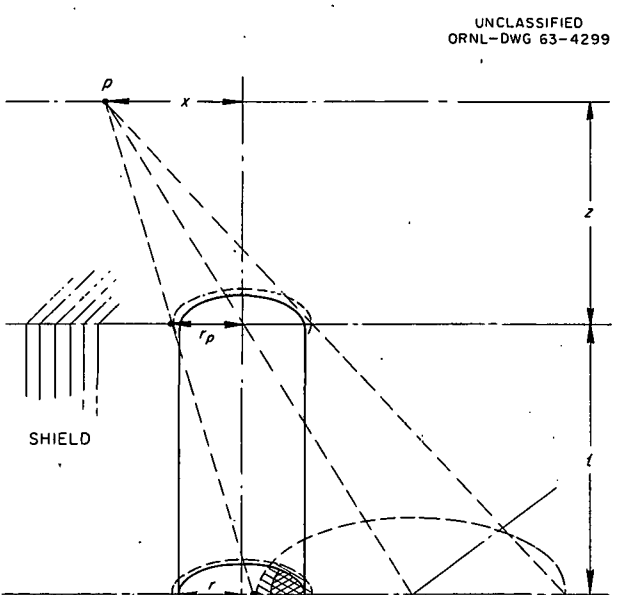

Fig. 6.2.1. Conceptual Change in the Collimator Geometry Due to Penetrating Radiation. Note a slight beveling at the ends; the double-cross-hatched area represents the illuminated area due to a point isotropic source of nonpenetrating (optical) radiation; the single-cross-hatched area represents the additional illuminated area due to penetrating radiation.

[1] R. L. Mather, *J. Appl. Phys.* **28**, 1200 (1957).

[2] R. A. Hefferlin and W. E. Kreger, *Nucl. Instr.* **3**, 149 (1958).

[3] F. M. Tamnovic and R. L. Mather, *J. Appl. Phys.* **28**, 1208 (1957).

[4] L. C. Thompson, *Nucl. Instr. Methods* **9**, 175 (1960).

[5] R. L. Mather, *J. Appl. Phys.* **28**, Fig. 9 (1957).

[6] G. T. Chapman *et al.*, *Neutron Phys. Div. Ann. Progr. Rept. Sept. 1, 1962*, ORNL-3360, p 3.

Gamma rays from the point source at P are required to pass through the unobstructed opening before being seen by the detector. If the collimator is assumed to be "optical," the gamma rays which pass through the double-cross-hatched area are the only ones that will be seen when P is displaced from the collimator center line by an amount $x > r$, since all other gamma rays will intercept a surface of the collimator. If $d\sigma$ is an element of this illuminated area, the solid angle subtended by the area $A(x)$ is

$$\omega(x) = \int_{A(x)} \frac{\mathbf{n}\cdot\mathbf{l}_\sigma}{|l_\sigma|}\frac{d\sigma}{l_\sigma^2}, \qquad x \geqq r, \quad (1)$$

where $\mathbf{n} \equiv$ a unit vector normal to $d\sigma$ and pointing away from the source, and $\mathbf{l}_\sigma = \mathbf{l}_\sigma(x,z) =$ distance from P to $d\sigma$. If the length of the collimator is large compared with the radius, then $\mathbf{l}_\sigma \cong \mathbf{l}_s$, where $\mathbf{l}_s$ is the distance from the source to the center of the illuminated area $A(x)$, and $\mathbf{n}\cdot\mathbf{l}_\sigma \cong l_s \cos\theta \cong l_s$. Therefore

$$\omega(x) \cong 1/l_s^2 \int_{A(x)} d\sigma = A(x)/l_s^2 . \quad (2)$$

The illuminated area, $A(x)$, is simply defined by the intersection of the collimator opening at the exit and the projection of the entrance opening on the same plane. Thus it is obvious that

$$A(x \leqq r) = \pi r^2 , \quad (3)$$

and it may be shown that

$$A(x > r) = \frac{\pi}{2} r^2(1+\beta^2) - (\beta-1)\beta x r(1-f_1^2)^{1/2} - r^2(\beta^2\phi_1 + \phi_2) , \quad (4)$$

where

$$\beta = 1 - \frac{l}{z},$$

$$f_1 \equiv \frac{(\beta+1)x^2 + (\beta-1)r^2}{2\beta r x},$$

$$\phi_1 \equiv \arcsin f_1,$$

$$\phi_2 \equiv \arcsin\left[\frac{(\beta+1)x^2 - (\beta-1)r^2}{2rx}\right],$$

and r, x, l, and z are defined in Fig. 6.2.1.

If, however, the gamma rays are allowed to penetrate the edges of the collimator, the radius at each end of the collimator hole is assumed to be increased to r_p cm, as shown by the dashed lines of Fig. 6.2.1. The amount of the energy-dependent increase is derived from Fig. 9 of Mather's paper,[5] in which the ratio of the penetration area to the geometric area is given vs the collimator length in mean free paths of material. It will then be noticed that the illuminated area is increased by the amount shown with the single cross-hatching. Substituting the new energy-dependent radius into Eq. (4), an estimate of the solid angle for a given gamma-ray energy may be obtained from

$$\omega(x,E) = \frac{A(x,E)}{l_s^2}. \quad (5)$$

Figure 6.2.2 shows $A(x,E)$ for 0.662-Mev gamma rays plotted against source location as the source was moved away from the collimator axis. The dimensions and materials of the collimator used in the calculations corresponded to those of the Model IV spectrometer,[6] and the source was assumed to be at a distance z equal to the length of the spectrometer cone. The integrated count

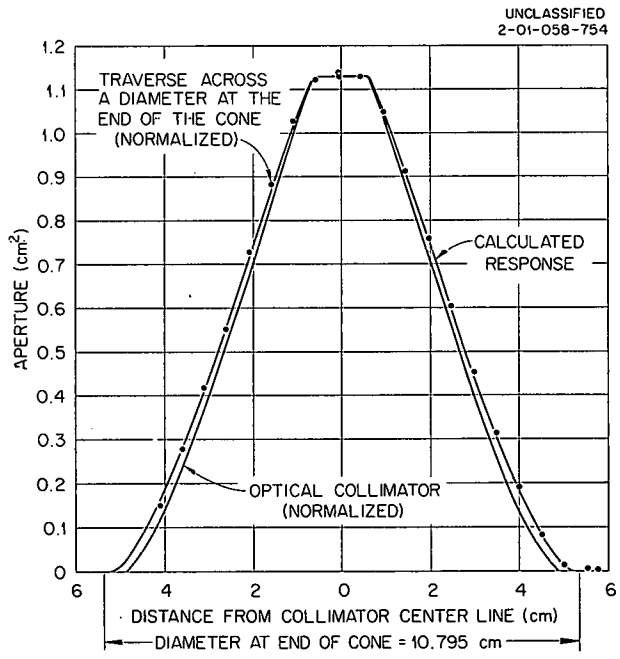

Fig. 6.2.2. Collimator Response for 0.662-Mev Gamma Rays.

rate as a function of position x obtained by moving a small source of 0.662-Mev gamma rays (Cs^{137}) diametrically across the end of the cone is shown normalized to the calculated value at the collimator center line. The agreement is obvious, even with the effects of scattering neglected in the calculation. The normalized response for an "optical" collimator is shown on the same figure to emphasize the error that may exist if penetration is not considered.

6.3. SOME FORTRAN CODES USED IN THE INITIAL REDUCTION OF DATA TAKEN WITH MULTICHANNEL PULSE-HEIGHT ANALYZERS[1]

J. D. Jarrard and G. T. Chapman

Numerous computer programs have been written in support of the gamma-ray spectral measurements of a stainless steel reactor recently concluded at the Bulk Shielding Facility (see Sec. 3.1), and several have applications beyond their use in the data reduction of this particular experiment. Three of these programs, identified as PREPARE, BIFIT, and ADJUST, are discussed below.

PREPARE

In many types of nuclear counting experiments the result is often a histogram of counts (y) vs some independent variable (x) containing one or more regions where the count distribution is assumed to be Gaussian in nature with respect to the independent variable. In order to make a Gaussian fit to these data by means of a least-squares technique, it is generally necessary to estimate an initial set of parameters. The computer program entitled PREPARE has been written for the IBM-7090 to generate the first estimates of Gaussian-fit parameters. The output of PREPARE is on punched cards ready for submission to a nonlinear least-squares program.[2] Utilization of this program was found to eliminate much of the time-consuming work required in estimating the parameters by hand and preparing the data for the iterative fit.

PREPARE computes an estimate of the following five parameters (see Fig. 6.3.1):

$P_1 \equiv$ the $x = 0$ intercept of the base line,

$P_2 \equiv$ the slope of the base line,

$P_3 \equiv$ the area under the Gaussian portion of the distribution,

$P_4 \equiv$ the half width of the Gaussian distribution at y_{max}/e, where y_{max} is the net amplitude of the Gaussian portion of the distribution,

$P_5 \equiv$ the mean center of the Gaussian distribution.

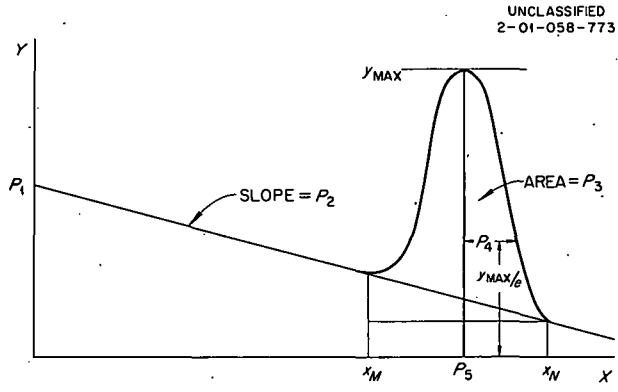

Fig. 6.3.1. Parameters Estimated by PREPARE.

[1] To be published as ORNL TM-659.

[2] W. R. Busing and H. A. Levy, *OR GLS, A General Fortran Least Squares Program*, ORNL TM-271 (June 1962).

The parameter P_5 is determined first by taking the first moment about $x = 0$:

$$P_5 = \frac{\sum_{i=M}^{N} x_i y_i}{\sum_{i=M}^{N} y_i}, \quad (1)$$

where the range of the summation is over the base of the Gaussian distribution (Fig. 6.3.1). This range is determined by inspection and is provided to the program as input data along with the measured distribution.

The parameter P_2 is computed from the equation

$$P_2 = \frac{y_N - y_M}{x_N - x_M}. \quad (2)$$

Then, with P_2 and P_1 known, the zero intercept may be computed as

$$P_1 = y_M - P_2 x_M. \quad (3)$$

The area under the Gaussian portion of the curve, P_3, is computed as the difference between the total area under the curve, as determined by a direct application of Simpson's rule over the range $i = M, N$, and the trapezoidal area at the base of the Gaussian distribution:

$$P_3 = \frac{1}{3}(y_N - y_M) + 4 \sum_{i(\text{odd})} y_i + 2 \sum_{i(\text{even})} y_i - \frac{1}{2}[(y_M - y_N)(x_N - x_M)] - [y_N(x_N - x_M)]. \quad (4)$$

The properties of the Gaussian distribution enable the calculation of P_4. Since $P_4 = \sigma\sqrt{2}$, where σ is the standard deviation of the Gaussian distribution, and $P_3 = [2\pi]^{1/2} y_{\max} \sigma$,

$$P_4 = \frac{[\pi]^{-1/2} P_3}{y_{\max}}, \quad (5)$$

where $y_{\max}$ is obtained from the equation

$$y_{\max} = y(P_5) + \frac{y(P_5 - 1) + y(P_5 + 1)}{8[2y(P_5) - y(P_5 - 1) - y(P_5 + 1)]} - (P_1 + P_2 P_5). \quad (6)$$

The parameters supplied by PREPARE are strictly estimates of the true parameters. Table 6.3.1 indicates the relative agreement between these estimates and the final parameter values obtained by a nonlinear least-squares fit[2] over two experimental distributions.

Table 6.3.1. Comparison of Gaussian Parameters Estimated by PREPARE and Those Obtained from a Nonlinear Least-Squares Fit

Parameter	PREPARE	Least-Squares Fit
	Sample 1	
P_1	1.6×10^3	1.4×10^3
P_2	-1.6×10^1	-1.4×10^1
P_3	2.3×10^3	2.7×10^3
P_4	2.8×10^0	3.0×10^0
P_5	8.5×10^1	8.6×10^1
	Sample 2	
P_1	4.2×10^3	4.5×10^3
P_2	-1.8×10^2	-2.0×10^2
P_3	5.1×10^4	4.9×10^4
P_4	1.2×10^0	1.1×10^0
P_5	1.7×10^1	1.8×10^1

BIFIT

The program entitled BIFIT performs a power-series polynomial least-squares fit to a set of data by taking into consideration uncertainties in both the x and y components of each data point. This is accomplished by using the method described by Deming[3] that is based on a development by Lagrange multipliers.

The selection of a polynomial of suitable degree defines the condition equation

$$F(x_i, y_i, a, b, c, \ldots) = 0, \quad i = 1, 2, \ldots n, \quad (7)$$

[3] W. E. Deming, *Statistical Adjustment of Data*, Wiley, New York, 1944.

to be approached by the least-squares fit. In this case the condition equation can be considered as

$$F = (y_i - a - bx_i - cx_i^2 \ldots) = 0 , \qquad (8)$$

where y_i and x_i are the adjusted data points and a, b, c, ... are the adjusted parameters.

With the actual data available and with a set of estimated parameters α, β, γ, ... , the approximation to the condition equation is

$$F^h(X_h, Y_h, \alpha, \beta, \gamma, \ldots) = F_0^h , \qquad (9)$$
$$h = 1, 2, 3, \ldots n,$$

which, in this case, becomes

$$F_0^h = (Y_h - \alpha - \beta X_h - \gamma X_h^2 \ldots) , \qquad (10)$$
$$h = 1, 2, 3, \ldots n,$$

and is the amount by which the condition $F = 0$ fails to be satisfied. This residual can be described to the first order in terms of the component residuals and parameter corrections

$$\begin{aligned} V_{xh} &= X_{xh} - x , \\ V_{yh} &= Y_{yh} - y , \\ A &= \alpha - a , \\ B &= \beta - b , \\ C &= \gamma - c , \end{aligned} \qquad (11)$$

as

$$F_0^h \cong \sum_x \frac{\partial F^h}{\partial x} V_x + \sum_y \frac{\partial F^h}{\partial y} V_{yh} + \frac{\partial F^h}{\partial a} A + \frac{\partial F^h}{\partial b} B + \frac{\partial F^h}{\partial c} C , \quad h = 1, 2, \ldots n. \qquad (12)$$

The above condition is combined with the least-squares equation

$$S = \sum_h \frac{(V_{xh})^2}{(\sigma_x^h)^2} + \frac{(V_{yh})^2}{(\sigma_y^h)^2} , \qquad (13)$$

in which σ_x^h and σ_y^h are the estimated standard deviations of the x_h and y_h components of an observed data point.

This combination with suitable manipulation[4] yields a set of normal equations from which the parameter corrections A, B, C, ... can be determined by solving for p in the matrix equation:

$$Z^T W Z p = Z^T W F_0 , \qquad (14)$$

where

$$W = \begin{vmatrix} \frac{1}{(\sigma_F^1)^2} & \cdot & \cdot & \cdot \\ & \frac{1}{(\sigma_F^2)^2} & & \\ & & \ddots & \\ & & & \frac{1}{(\sigma_F^n)^2} \end{vmatrix} , \qquad (15)$$

in which

$$(\sigma_F^h)^2 = \left(\frac{\partial F}{\partial x}\right)^2 \sigma_{x_h}^2 + \left(\frac{\partial F}{\partial y}\right)^2 \sigma_{y_h}^2 ,$$
$$h = 1, 2, \ldots n;$$

$$Z = \begin{vmatrix} \frac{\partial F^1}{\partial a} & \frac{\partial F^1}{\partial b} & \cdots\cdots & \frac{\partial F^1}{\partial k} \\ \frac{\partial F^2}{\partial a} & \frac{\partial F^2}{\partial b} & \cdots\cdots & \frac{\partial F^2}{\partial k} \\ \vdots & & & \end{vmatrix} ; \qquad (16)$$

and

$$p = \begin{vmatrix} A \\ B \\ C \\ \vdots \end{vmatrix} . \qquad (17)$$

The term F_0 in Eq. (10) is the data vector

$$F_0 = \begin{vmatrix} F_0^1 \\ F_0^2 \\ \\ F_0^3 \\ \vdots \\ F_0^n \end{vmatrix} . \qquad (18)$$

[4] *Ibid.*, p 53.

Solving Eq. (11) for p by the usual matrix inversion techniques, the adjusted parameters can be computed as:

$$\begin{aligned} a &= A + \alpha \\ b &= B + \beta \\ c &= C + \gamma \\ &\vdots \quad \vdots \quad \vdots \end{aligned} \tag{19}$$

This program, written for the IBM-7090 in FORTRAN, includes the additional feature that the initial parameter estimates, α, β, γ, . . . , are automatically determined by performing a preliminary unweighted least-squares fit on the data utilizing a subroutine POLFIT.[5] Although a power series polynomial was used in this case, the method described above is equally applicable to various other linear and nonlinear functions in that the parameter corrections are determined from the evaluated partial derivatives and residuals are computed from the initial parameter estimates.

ADJUST

The program ADJUST[6] performs a numerical redistribution of pulse-height spectra for the correction of gain and/or zero shifts occurring between spectral measurements. The program will operate on and redistribute a pulse-height spectrum as if it had been measured at virtually any reasonable gain and zero setting.

Internally the program generates a table of polynomial coefficients resulting from quadratic least-squares fits to the contents of consecutive and overlapping groups of three channels of the original pulse-height spectrum. These coefficients are stored as a function of the invariant relating the gain curves of the original and redistributed spectra; that is, if the gain were in channels/volt, the curves would be stored as a function of volts. A new channel width based on the desired new gain and zero is computed. The contents of the new channel are then determined by selecting a curve from the stored table as a function of a value of the invariant (e.g., voltage) corresponding to the location of a new channel and integrating it over the new channel width.

Since this program assumes that the original spectrum has been assigned the correct gain and zero parameters, the redistributed spectrum will have no greater accuracy in this respect than the original. The area of the original pulse-height spectrum has been found to be conserved in the redistributed spectrum to within $\sim 0.1\%$ unless a large zero shift is encountered. The program also generates a set of pseudo-count-rate statistics based on the channel contents of the redistributed spectrum. A Cs^{137} spectrum that has been numerically redistributed by means of ADJUST is shown in Fig. 6.3.2.

The least-squares-fit technique used in ADJUST has also been useful in the interpolation of data. The table of least-squares fits is generated by utilizing the known data points, and the interpolated values are obtained by the selection and evaluation of the quadratic fits.

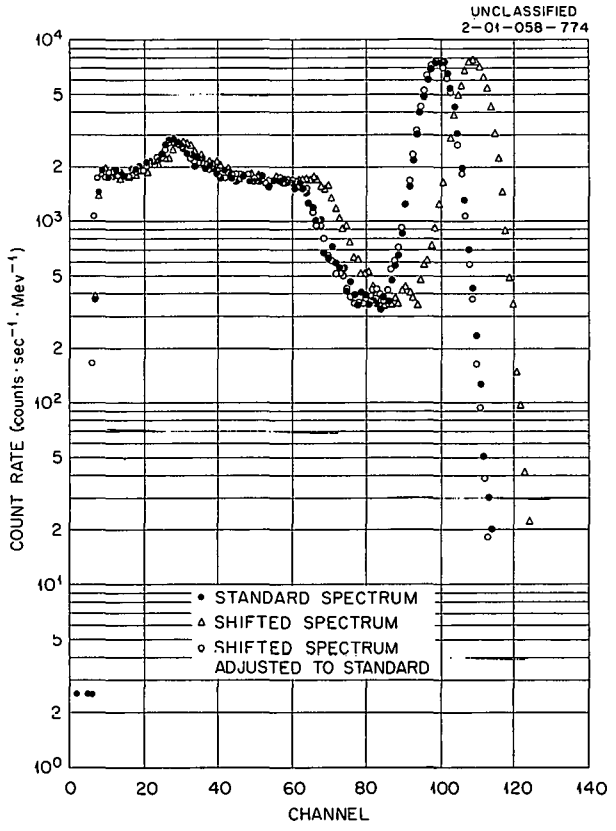

Fig. 6.3.2. Numerical Redistribution by ADJUST of Cs^{137} Spectrum.

[5] M. P. Lietzke, *POLFIT II, An IBM 7090 Program for Polynomial Least Squares Fitting*, ORNL-3132 (Apr. 24, 1961).

[6] J. D. Jarrard, "ADJUST," accepted for publication in *Nuclear Science and Engineering*.

6.4. TEMPERATURE COEFFICIENT OF HURST-TYPE FAST-NEUTRON DOSIMETERS

R. E. Wright

An experiment was performed to determine the effects of temperature on a Hurst-type fast-neutron dosimeter. The detector consisted of an ethylene-filled polyethylene-walled proportional counter and a transistor preamplifier mounted in a common aluminum housing. The pulses from the preamplifier were fed into an A-1 linear amplifier which included a transistorized pulse-height integrator.

The detector calibration consisted of first setting the system gain so that a 2-r/hr field of Co^{60} gamma rays at the center of the detector would produce a linear amplifier output of 40 pulses per minute that were larger than 6 [referred to as an "integral pulse-height setting (PHS) count rate"]. A PHS curve (count rate vs PHS) was then taken with the detector in a neutron field from a Po-Be source in order to check neutron response.

The cooling and heating arrangement shown in Fig. 6.4.1 was used to vary the temperature of the system from −80°F to 150°F. Cooling was accomplished by dry nitrogen gas flowing through copper tubing, which was first passed through a liquid-nitrogen bath and then around the detector. Heating was provided by a Variac-controlled strip heater surrounding the detector housing. The temperature was monitored by two thermocouples, one in the air space adjacent to the chamber and the other in the air space surrounding the preamplifier. The entire detector assembly was mounted in a Styrofoam (expanded polystyrene) box to provide insulation.

During the experiment the Po-Be source was placed outside the Styrofoam box at an arbitrary distance to provide approximately 6000 counts/min at a PHS of 6. The integrator count rate was approximately 3500 counts/min, with a spread of ±4% caused by system noise. (This count rate is approximately proportional to the area under the PHS curve, which is in turn proportional to the ionization produced in the detector.) Periodically a precisely known pulse from a pulse generator was fed through the preamplifier and A-1 amplifier to monitor the system gain.

The general procedure of the experiment consisted in obtaining an integral pulse-height curve at room temperature and then measuring the integrator count rate at intervals as the detector temperature was decreased at a rate of 2°F per minute until it reached −3°F. Heat was then applied, and points were taken at intervals as

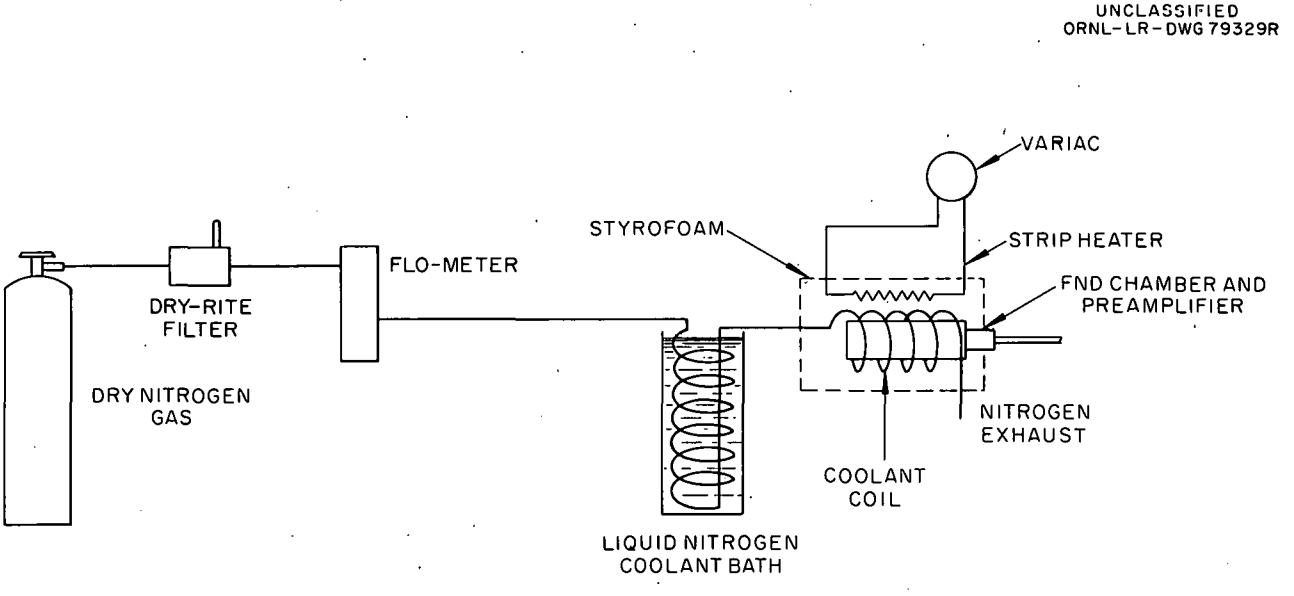

Fig. 6.4.1. Cooling and Heating Arrangement for Preamplifier and/or Chamber.

the temperature was increased. PHS curves were obtained at stabilized temperatures of −3, 80, and 135°F. A system gain check was recorded at intervals with the integrated fixed points. All tests were repeated several times for confirmation of results.

With the chamber and preamplifier both placed in the Styrofoam box, the temperature was varied from −32°F to 135°F and points were recorded at intervals of approximately 10°F. The variation in the integrator count rate (dose rate) from −32°F to 120°F was within the statistics of the count rate (see Fig. 6.4.2). If the statistics had been better, a minor change due to the gain of the preamplifier increasing with temperature would have been observed. As the temperature was increased above 120°F, the chamber sensitivity decreased rapidly, there being a decrease of 6% in the integrator count rate between 120 and 135°F.

The preamplifier gain was monitored separately during the experiment to determine whether it was affected by temperature variations. The preamplifier gain increased 0.035% per °F at a linear rate proportional to the temperature. (Since the temperature coefficients of the components in the preamplifier which caused this change are probably not reproducible, other supposedly identical preamplifiers may not exhibit this same temperature coefficient.)

As an additional check, the chamber and the preamplifier were separated so that only the temperature of the chamber was varied. The chamber was subjected to a more extreme temperature range than had been used previously, and the results (Fig. 6.4.3) showed that there was a tolerable change in counting rate from −77°F to 100°F but that the chamber lost sensitivity more rapidly above 100°F; the counting rate decreased by 11% at 150°F. The difference in the count rates observed for increasing and decreasing temperatures is due to the temperature of the ethylene gas in the chamber changing more slowly than did the temperature of the adjacent air (the measured temperature shown in Fig. 6.4.3 is the air temperature).

When the chamber and preamplifier are at the same temperature, a minor compensation occurs

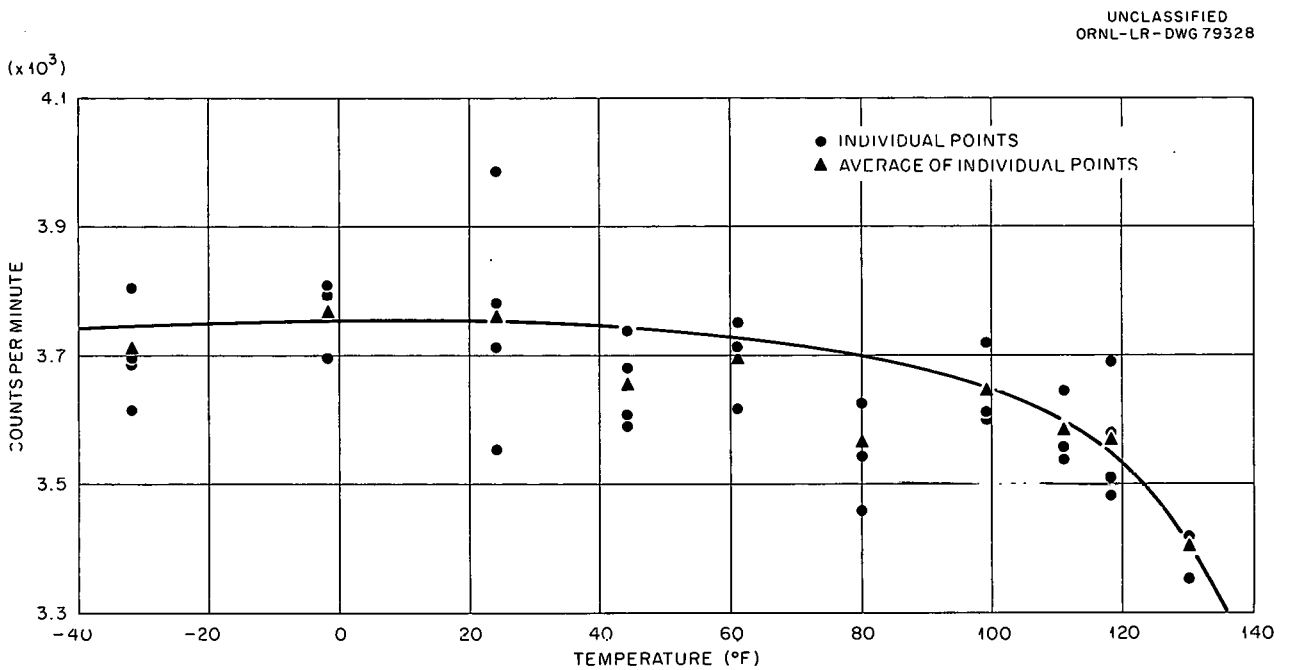

Fig. 6.4.2. Integrator Count Rate as a Function of Chamber-Preamplifier Temperature.

between 100 and 120°F owing to the preamplifier gain increasing while the chamber sensitivity is decreasing. Although the degree of compensation might vary with different preamplifiers, with the unit used in this experiment the compensation extends the operating temperature to 120°F with reasonable variation due to temperature excursions.

In summary, the Hurst-type fast-neutron dosimeter can be used over the temperature range of −80°F to 100°F with a reasonable sensitivity change (4.5%). Above 100°F a change of 0.22% per °F can be expected up to 150°F. If the transistor preamplifier is used in the same environment, the upper end of the operating range of the fast-neutron dosimeter may be extended to 120°F.

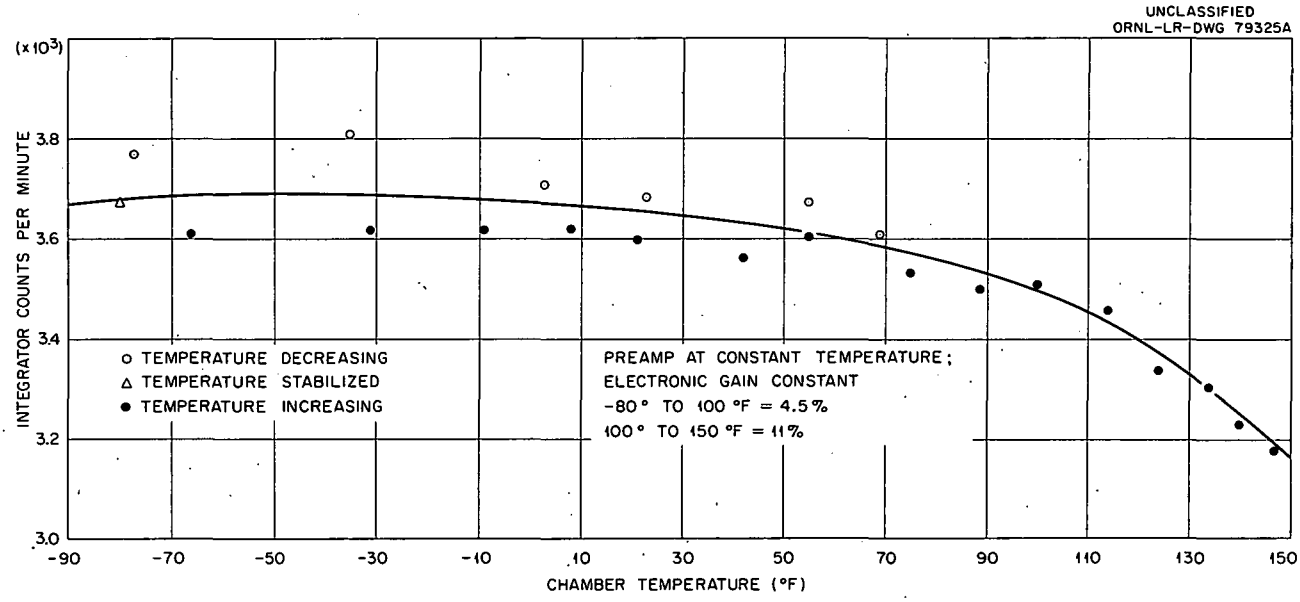

Fig. 6.4.3. Integrator Counting Rate as a Function of Chamber Temperature.

7. Water Desalination Studies — Theoretical

THIS PAGE

WAS INTENTIONALLY

LEFT BLANK

7.1. A VARIATIONAL PRINCIPLE FOR THE POISSON-BOLTZMANN EQUATION – ACTIVITY COEFFICIENT OF A SALT IN A CHARGED MICROCAPILLARY[1,2]

Lawrence Dresner

The Poisson-Boltzmann equation has been used to describe many phenomena in electrochemistry,[3–5] solution chemistry,[6] colloid chemistry[7] and the chemistry of polyelectrolytes[8,9] and ion-exchange materials.[10,11] Because of the complexity created by its nonlinearity, only a few exact solutions to the Poisson-Boltzmann equation are known.[3,4,8,9,12] In general, the powerful methods of solution developed for linear partial differential equations, such as separation of variables, expansion in orthogonal functions, use of Fourier and other transformations, etc., cannot be applied to the Poisson-Boltzmann equation.[13] However, one of the well-known approximate methods of solution developed for linear problems, the variational method,[14] can be applied to the nonlinear Poisson-Boltzmann equation. The published paper will give a functional that is a minimum for solutions of the Poisson-Boltzmann equation and whose minimum value is related to the electrostatic part of the free energy of the system. With the help of this functional and a simple trial function, the electrostatic contribution to the mean activity coefficient of a 1:1 electrolyte invading a small, surface-charged microcapillary will be estimated as an illustration.

[1]Work performed at ORNL for the Office of Saline Water, U. S. Department of the Interior.

[2]Accepted for publication in the *Journal of Physical Chemistry*.

[3]G. Gouy, *J. Phys.* 9(4), 357 (1910); *Ann. Physik* 7(9), 129 (1917).

[4]D. L. Chapman, *Phil. Mag.* 25(6), 475 (1913).

[5]O. Stern, *Z. Elektrochem.* **30**, 508 (1924).

[6]P. Debye and E. Huckel, *Physik. Z.* **24**, 185, 305 (1923).

[7]E. J. W. Verwey and J. T. G. Overbeek, *Theory of Stability of Lyopho-Colloids*, Elsevier, New York, 1948.

[8]R. M. Fuoss, A. Katchalsky, and S. Lifson, *Proc. Nat. Acad. Sci.* **37**, 579 (1951).

[9]T. Alfrey, P. W. Berg, and H. Morawetz, *J. Polymer Sci.* **7**, 543 (1951).

[10]L. Lazare, B. R. Sundheim, and H. P. Gregor, *J. Phys. Chem.* **60**, 641 (1956).

[11]L. Dresner and K. A. Kraus, *J. Phys. Chem.* **67**, 990 (1963).

[12]The solution independently found by Fuoss *et al.*[8] and by Alfrey *et al.*[9] has also been given by H. Lemke [*J. für die Reine und Angewandte Mathematik* **142**, No. 2, 118 (1913)] and by G. W. Walker [*Proc. Roy. Soc. (London)* **A41**, 410 (1915)]. It is a special case of a very general two-dimensional solution to the equation $\nabla^2 u = e^u$ due to J. Liouville [*J. de Mathem.* (1) **18**, 71 (1853); see also H. T. Davis, *Introduction to Nonlinear Differential Integral Equations*, GPO, Washington, 1960].

[13]Interestingly enough, in a certain special case conformal mapping is applicable; see M. v. Laue, *Jahrb. Radioaktivität Elektronik* **15**(3), 206 (1918).

[14]The possible use of the variational method in the Debye-Hückel case was mentioned in a footnote by S. Levine, *J. Chem. Phys.* **7**, 836 (1939).

7.2. THERMODYNAMIC EQUILIBRIA OF ELECTROLYTE SOLUTIONS IN CONTACT WITH CHARGED MICROPOROUS SOLIDS[1,2]

Lawrence Dresner

If a charged microporous body is allowed to come to equilibrium with an external electrolyte solution, the ionic concentrations in the pore liquid will generally be different from the ionic concentrations in the external solution. These concentration differences are caused by electric charge being fixed to the walls of the micropores. Together with the mobile ions in the pore liquid, this charge creates a highly nonuniform electric potential, which in turn affects the ionic population of the pore. The ionic concentrations and the electric potential are connected by the Poisson-Boltzmann equation; solution of this equation and the use of some thermodynamic formulas allow the calculation of the electrolyte distribution coefficients. A simple tractable model of a charged microporous body for which the Poisson-Boltzmann equation can be solved and the distribution coefficients calculated is that of independent cylindrical microcapillaries on whose inner surface a fixed, homogeneous electric charge resides, and it is this model which is analyzed in the present work.

When only two distinct ions are present and the capillary radius is sufficiently small, the surface charge sufficiently large, or the external electrolyte sufficiently dilute, the external electrolyte will be strongly excluded from the capillary interior (Donnan exclusion, distribution coefficient < 1). As the three conditions above are relaxed, the electrolyte concentration in the capillary liquid rises so that in the limit of large capillary radius, small surface charge, or high external concentration, the distribution coefficient approaches unity.

When only two distinct ions are present in macroscopic quantities but other ions are present in trace quantities, the ions of the macrosalt behave as described above, that is, as if the trace ions were absent. This simply reflects the fact that only the ions of the macrosalt are influential in determining the equilibrium electric potential. The trace ions behave in the following way: Those of the same sign as the fixed charge (co-ions) behave similarly to the macrosalt, while those of the opposite sign (counter-ions) have distribution coefficients which fall toward unity as one moves out of the region of good exclusion of the macrosalt.

In the interest of brevity, no case has been reported in which more than one macrosalt is present in the external solution. The method by which the present computations have been done (see Sec. 7.1) is nonetheless applicable to all cases. The cases considered are (1) monovalent co- and counter-ions, (2) divalent co-ions and monovalent counter-ions, and (3) monovalent co-ions and divalent counter-ions. For each type of macrosalt, the distribution coefficients of six trace ions with valences ± 1, ± 2, and ± 3 have been calculated. The distribution coefficient of a macroion is the same as that of a trace ion of the same valence.

The study of the thermodynamic equilibria of charged microporous bodies in contact with electrolyte solutions has obvious importance to the problems of water desalination. In fact, it has already been suggested that a "salt filter" could be constructed from a charged microporous solid operating in the good exclusion range.[3] Other applications of the work reported may be to soil chemistry, to ion-exchange chemistry, and to polyelectrolyte chemistry.

---

[1]Work performed at ORNL for the Office of Saline Water, U. S. Department of the Interior.

[2]To be published in *Journal of Physical Chemistry*.

[3]L. Dresner and K. A. Kraus, *J. Phys. Chem.* **67**, 990 (1963).

PUBLICATIONS

Alsmiller, F. S., R. G. Alsmiller, Jr., and J. E. Murphy,* "Nuclear-Meson Cascade Calculations," *Am. Phys. Soc. Bull.* **8**, Ser. II, 366 (1963).

Alsmiller, F. S., R. G. Alsmiller, Jr., and D. K. Trubey, "Comparison of Primary Proton Dose with the Dose from Gamma Rays Produced by Inelastic Scattering of Solar Flare Protons," p 718 in *Proceedings of the Symposium on the Protection Against Radiation Hazards in Space, Gatlinburg, Tennessee, November 5–7, 1962,* TID-7652, Book 2.

Alsmiller, R. G., Jr., *Ionization of Lithium by Electrons and Protons,* ORNL CF-63-2-46 (Feb. 18, 1963).

Alsmiller, R. G., Jr., and F. S. Alsmiller, *A Perturbation Method for Solving the Angle Dependent Nucleon-Meson Cascade Equations,* ORNL-3467 (July 16, 1963).

Alsmiller, R. G., Jr., F. S. Alsmiller, and J. E. Murphy,* "Nucleon-Meson Cascade Calculations in the Straight-Ahead Approximation," p 698 in *Proceedings of the Symposium on the Protection Against Radiation Hazards in Space, Gatlinburg, Tennessee, November 5–7, 1962,* TID-7652, Book 2.

Alsmiller, R. G., Jr., F. S. Alsmiller, and J. E. Murphy,* *Nucleon-Meson Cascade Calculations: Transverse Shielding for a 45-Gev Electron Accelerator (Part I),* ORNL-3289 (Dec. 28, 1962).

Alsmiller, R. G., Jr., F. S. Alsmiller, and J. E. Murphy,* *Nucleon-Meson Cascade Calculations: Transverse Shielding for a 45-Gev Electron Accelerator (Part II),* ORNL-3365 (Feb. 13, 1963).

Alsmiller, R. G., Jr., F. S. Alsmiller, and J. E. Murphy,* *Nucleon-Meson Cascade Calculations: Transverse Shielding for a 45-Gev Electron Accelerator (Part III),* ORNL-3412 (Mar. 14, 1963).

Alsmiller, R. G., Jr., and J. E. Murphy,* *Space Vehicle Shielding Studies: Calculations of the Attenuation of a Model Solar Flare and Monoenergetic Proton Beams by Aluminum Shields,* ORNL-3317 (Jan. 8, 1963).

Alsmiller, R. G., Jr., and J. E. Murphy,* *Nucleon-Meson Cascade Calculations: Shielding Against an 800-Mev Proton Beam,* ORNL-3406 (Feb. 7, 1963).

Alsmiller, R. G., Jr., and J. E. Murphy,* *Nucleon-Meson Cascade Calculations: The Star Density Produced by a 24-Gev Proton Beam in Heavy Concrete,* ORNL-3367 (Jan. 7, 1963).

Auerbach,* E. H., and F. G. Perey, *Optical Model Neutron Transmission Coefficients, 0.1 to 5.0 Mev,* BNL-785 (April 1963).

Bertini, H. W., "Monte Carlo Calculations for Intranuclear Cascades," p 433 in *Proceedings of the Symposium on the Protection Against Radiation Hazards in Space, Gatlinburg, Tennessee, November 5–7, 1962,* TID-7652, Book 2; also issued as ORNL-3383 (Apr. 23, 1963).

Bertini, H. W., "Intranuclear Cascade Calculation," *Am. Phys. Soc. Bull.* **8**, Ser. II, 316 (1963).

Bertini, H. W., "Low-Energy Intranuclear Cascade Calculation," *Phys. Rev.* **131**, 1801 (1963).

Bertini, H. W., *Description of Printed Output from Intranuclear Cascade Calculation,* ORNL TM-480 (Feb. 5, 1963); also issued as ORNL-3433 (May 1963).

*Non-Division personnel.

Bertini, H. W., *A Literature Survey of Nonelastic Reactions for Nucleons and Pions Incident on Complex Nuclei at Energies Between 20 Mev and 33 Gev,* ORNL-3455 (Aug. 9, 1963).

Blizard, E. P., *Analytical Methods of Shield Design,* and *Shield Optimization with Respect to Weight,* chaps. 11 and 14 in "Shielding," vol III, part B, of *Reactor Handbook,* 2d ed., revised, Interscience, New York, 1962.

Blizard, E. P., "Shielding of Man in Space," p 339–364 in *Lectures in Aerospace Medicine 4–8 February 1963,* USAF School of Aerospace Medicine, Aerospace Medical Division, Brooks Air Force Base, Texas.

Blizard, E. P., A. D. Callihan, and F. C. Maienschein, *Neutron Physics Division Annual Progress Report for Period Ending September 1, 1962,* ORNL-3360.

Blizard, E. P., and L. S. Abbott, editors, "Shielding," vol III, part B, of *Reactor Handbook,* 2d ed., revised, Interscience, New York, 1962.

Blosser, T. V., and R. M. Freestone, Jr., "The ORNL Mobile Radiation Measurement Laboratory," *Nucleonics* **21**(2), 56 (1963).

Buck, B., "Calculation of Elastic and Inelastic Proton Scattering with a Generalized Optical Model," *Phys. Rev.* **130**, 712 (1963).

Burrus, W. R., "Inequality Method of Unfolding for Nuclear Spectroscopy," *Trans. Am. Nucl. Soc.* **6**(1), 173 (1963).

Burrus, W. R., and D. Bogert, "A Study of the Errors Associated with Spectral Analysis Methods," p 127 in *Applications of Computers to Nuclear and Radiochemistry,* NAS-NS-3107 (n.d.).

Cain, V. R., "Thermal Neutron Flux Distribution in Multilegged Entranceways," *Trans. Am. Nucl. Soc.* **6**(1), 191 (1963).

Cain, V. R., L. B. Holland, and J. R. Wilson, ORNL-3414 (Apr. 15, 1963) (classified).

Callihan, A. D., "Accidental Nuclear Excursion in Recuplex Operation at Hanford in April 1962," *Nucl. Safety* 4(4), 136 (1963).

Callihan, A. D., and Critical Experiments Facility Staff, *A Safety Review of the Oak Ridge Critical Experiments Facility,* ORNL TM-349 (Dec. 10, 1962).

Chapman, G. T., K. M. Henry, J. D. Jarrard, and R. L. Cowperthwaite, "Preliminary Report on the Measured Gamma-Ray Spectra from a Stainless Steel Reactor," *Trans. Am. Nucl. Soc.* **6**(1), 176 (1963).

Chester,* R. O., F. C. Maienschein, and R. W. Peelle, "Nonlinear Least-Squares Fitting Applied to Gamma-Ray Scintillation Detector Response Functions," p 201 in *Applications of Computers to Nuclear and Radiochemistry,* NAS-NS-3107 (n.d.).

Clark, F. H. S., and W. E. Kinney, Li^6(n,dn)α, Li^7(n,tn)α, and Li^7(n,n') *Neutron Treatment in O5R,* ORNL CF-63-5-33 (May 20, 1963).

Dresner, L., "Electrokinetic Phenomena in Charged Microcapillaries," *J. Phys. Chem.* **67**, 1635 (1963).

Dresner, L., *A Remark on the Second Fundamental Theorem in One-Velocity Transport Theory,* ORNL-3330 (Oct. 17, 1962).

Dresner, L., and K. A. Kraus,* "Ion Exclusion and Salt Filtering with Porous Ion-Exchange Materials," *J. Phys. Chem.* **67**, 990 (1963).

Dresner, L., and A. M. Weinberg,* "Recent Developments in the Theory and Technology of Chain Reactors," *Rev. Mod. Phys.* **34**, 747 (1962).

Fox, J. K., L. W. Gilley, and D. W. Magnuson, *Preliminary Solution Critical Experiments for the High-Flux Isotope Reactor,* ORNL-3359 (May 28, 1963).

*Non-Division personnel.

Gibson, W. A., *Energy Removed from Primary Proton and Neutron Beams by Tissue,* ORNL-3260 (September 1962).

Gwin, R., and R. B. Murray,* "Emission Spectra of CsI(Tl) Crystals and the Possible Role of Self-Trapped Holes," *Am. Phys. Soc. Bull.* **7**, Ser. II, 543 (1962).

Gwin, R., and R. B. Murray,* *Studies of the Scintillation Process in CsI(Tl),* ORNL-3354 (Oct. 22, 1962).

Gwin, R., and R. B. Murray,* "Scintillation Process in CsI(Tl). I. Comparison with Activator Saturation Model," *Phys. Rev.* **131**, 501 (1963).

Gwin, R., and R. B. Murray,* "Scintillation Process in CsI(Tl). II. Emission Spectra and the Possible Role of Self-Trapped Holes," *Phys. Rev.* **131**, 508 (1963).

Harvey,* J. A., and F. C. Maienschein, *Comparison of Pulsed-Neutron Sources for Time-of-Flight Neutron Spectroscopy,* ORNL TM-582 (May 29, 1963).

Henry, K. M., J. D. Kington, and F. C. Maienschein, *Operating Procedure for the Bulk Shielding Reactor (Fifth Edition),* ORNL TM-616 (Aug. 15, 1963).

Holland, L. B., *Report of Action Taken on Recommendations of the Tower Shielding Reactor II Design Review Committee,* ORNL CF-63-4-68 (Apr. 25, 1963).

Johnson, E. B., and R. K. Reedy, Jr., *Neutron Multiplication by Experimental Gas Cooled Reactor Fuel Assemblies,* ORNL TM-433 (Nov. 27, 1962).

Kinney, W. E., R. R. Coveyou, and C. D. Zerby, "A Series of Monte Carlo Codes to Transport Nucleons Through Matter," p 608 in *Proceedings of the Symposium on the Protection Against Radiation Hazards in Space, Gatlinburg, Tennessee, November 5–7, 1962,* TID-7652, Book 2.

Kinney, W. E., and C. D. Zerby, "Calculation of Nucleon Transport Below 400 Mev," *Am. Phys. Soc. Bull.* **8**, Ser. II, 316 (1963).

LeBerre,* F., and R. E. Maerker, *Comparison of Several Mathematical Methods for Calculating the Slowing Down Density in a Heavy Medium,* DEP/SEPP 263/63, Centre d'Etudes Nucleaires de Fontenay-aux-Roses (June 1963).

Maerker, R. E., F. J. Muckenthaler, and L. B. Holland, *In-Air Radiation Measurements in the Vicinity of the Tower Shielding Reactor II,* ORNL-3288 (Mar. 25, 1963).

Magnuson, D. W., *High Flux Isotope Reactor Critical Experiment No. 2, Part VIII,* ORNL CF-62-10-105 (Nov. 13, 1962).

Magnuson, D. W., *High Flux Isotope Reactor No. 2. Part VII, Reactivity and Power Distribution Measurements with Two-Section Control Plates,* ORNL CF-62-9-75 (Oct. 8, 1962).

Maienschein, F. C., and T. V. Blosser, "The Depth-Dose Distribution Produced in a Spherical Water-Filled Phantom by the Interactions of a 160-Mev Proton Beam," *Trans. Am. Nucl. Soc.* **6**(1), 195 (1963); also issued as ORNL-3457 (June 7, 1963).

Maienschein, F. C., T. V. Blosser, W. R. Burrus, W. A. Gibson, T. A. Love, R. W. Peelle, R. T. Santoro, and W. Zobel, "Experimental Techniques for the Measurement of Nuclear Secondaries from the Interactions of Protons of a Few Hundred Mev," p 523 in *Proceedings of the Symposium on the Protection Against Radiation Hazards in Space, Gatlinburg, Tennessee, November 5–7, 1962,* TID-7652, Book 2.

Maienschein, F. C., and C. D. Zerby, *Neutron Physics Division Space Radiation Shielding Research Annual Progress Report for Period Ending August 31, 1962,* ORNL CF-62-10-29 Rev. (Nov. 1. 1962).

Mihalczo, J. T., "Prompt-Neutron Lifetime in Hydrogen-Moderated 3%–U^{235}-Enriched Uranium Critical Assemblies," *Trans. Am. Nucl. Soc.* **5**(2), 387 (1962).

*Non-Division personnel.

Mihalczo, J. T., "Superprompt-Critical Behavior of an Unmoderated, Unreflected Uranium-Molybdenum Alloy Reactor," *Nucl. Sci. Eng.* **16**(3), 291 (1963).

Mihalczo, J. T., "Prompt-Neutron Decay in a Two-Component Enriched-Uranium-Metal Critical Assembly," *Trans. Am. Nucl. Soc.* **6**(1), 60(1963).

Mihalczo, J. T., ORNL TM-450 (Jan. 10, 1963) (classified).

Mihalczo, J. T., ORNL TM-561 (Apr. 10, 1963) (classified).

Muckenthaler, F. J., ORNL-3395 (Mar. 22, 1963) (classified).

Nichols,* J. P., E. D. Arnold,* and D. K. Trubey, "Evaluation of Shielding and Hazards in the Transuranium Processing Facility," *Trans. Am. Nucl. Soc.* **5**(2), 297 (1962).

Penny, S. K., and M. B. Emmett,* *An IBM-7090 Subroutine Package for Lagrangian Interpolation,* ORNL-3428 (Mar. 1, 1963).

Penny, S. K., and D. K. Trubey, ORNL CF-63-1-5 (Feb. 5, 1963) (classified).

Penny, S. K., and D. K. Trubey, *Cumulative Bibliography of Literature Examined by the Radiation Shielding Information Center,* ORNL RSIC-1 (May 13, 1963).

Penny, S. K., D. K. Trubey, and B. F. Maskewitz, *r.s.i.c. newsletter,* No. 1, June 1, 1963.

Perey, F. G., "Optical Model Analysis of Proton Elastic Scattering in the Range of 9 to 22 Mev," *Phys. Rev.* **131**, 745 (1963).

Perey, F. G., *A Fortran Program for Calculating the Scattering of Nucleons from a Nonlocal Optical Potential,* ORNL-3429 (June 26, 1963).

Perey, F. G., and G. R. Satchler,* "Validity of the DWBA for Inelastic Scattering from Nuclei," *Phys. Letters* **5**(3), 212 (1963).

Perey, F. G., R. J. Silva,* and G. R. Satchler,* "Excited-Core Model of Odd-A Nuclei and the Cu^{63} (p,p′) Reactions," *Phys. Letters* **4**, 25 (1963).

Silver, E. G., *Source-Strength and Long-Counter-Response Calibrations at the BSF 300-kev Accelerator,* ORNL TM-550 (Apr. 8, 1963).

Thomas, J. T., "Studies of Critical Cubic Arrays of Fissile Materials," *Trans. Am. Nucl. Soc.* **6**(1), 169 (1963).

Thomas, J. T., J. K. Fox, and E. B. Johnson, *Critical Mass Studies – Part XIII. Borosilicate Glass Raschig Rings in Aqueous Uranyl Nitrate Solutions,* ORNL TM-499 (Feb. 26, 1963).

Thomas, J. T., J. K. Fox, and E. B. Johnson, "The Effect of Borosilicate Glass Raschig Rings on the Criticality of Aqueous Uranyl Nitrate Solutions," *Trans. Am. Nucl. Soc.* **6**(1), 169 (1963).

Trubey, D. K., *Tabulated Values of Scattered Gamma-Ray Fluxes in Water Interpolated from Moments Method Calculations,* ORNL-3466 (July 15, 1963).

Trubey, D. K., *A Calculation of Radiation Penetration of Cylindrical Duct Walls,* ORNL CF-63-2-64 (Feb. 28, 1963).

Trubey, D. K., and M. B. Emmett,* *A CDC-1604 Subroutine Package for Making Linear, Logarithmic, and Semilogarithmic Graphs Using the CALCOMP Plotter,* ORNL-3447 (June 10, 1963).

Trubey, D. K., and M. B. Emmett,* *An IBM-7090 Subroutine Package for Making Logarithmic and Semilogarithmic Graphs Using the CALCOMP Plotter,* ORNL TM-430 (Dec. 12, 1962).

Trubey, D. K., and M. B. Emmett,* *An IBM-7090 Subroutine for Making Linear Graphs Using the CALCOMP Plotter,* ORNL TM-430 Supplement (Feb. 27, 1963).

*Non-Division personnel.

Trubey, D. K., and S. K. Penny, "Transfusion – A Numerical Method for Computing Low-Energy Neutron Spatial Distributions," *Trans. Am. Nucl. Soc.* **5**(2), 409 (1962).

Trubey, D. K., S. K. Penny, and M. B. Emmett,* *OGRE-P2, A Monte Carlo Program for Computing Gamma-Ray Leakage from Laminated Slabs with a Distributed Source,* ORNL TM-237 (Oct. 3, 1962).

Turner,* J. E., J. L. Feuerbacher,* C. D. Zerby, W. E. Kinney, J. Neufeld,* W. S. Snyder,* and R. L. Woodyard,* "The Calculation of Radiation Dose in Tissue from High-Energy Protons," p 619 in *Proceedings of the Symposium on the Protection Against Radiation Hazards in Space, Gatlinburg, Tennessee, November 5–7, 1962,* TID-7652, Book 2.

Verbinski, V. V., "Fast-Neutron Transport in LiH," *Trans. Am. Nucl. Soc.* **6**(1), 190 (1963).

Zobel, W., *Experimental Determination of Corrections to the Neutron Activation of Gold Foils Exposed in Water,* ORNL-3407 (Mar. 21, 1963).

Zerby, C. D., "Theoretical Studies on the Transport of High Energy Radiation Through Shielding Materials," p 57 in *Premier Colloque International sur la Protection Aupres des Grands Accelerateurs,* Presses Universitaires de France, Paris, 1962.

Zerby, C. D., *Gamma-Ray Attenuation,* chap. 10 in "Shielding," vol III, part B, of *Reactor Handbook,* 2d ed., revised, Interscience, New York, 1962.

Zerby, C. D., *Recursion Relations and Simplified Expressions for the 6-j Symbols,* ORNL-3440 (May 2, 1963).

Zerby, C. D., *Material Requirements for Shielding Against Space Radiations,* ORNL TM-552 (May 21, 1963).

Zerby, C. D., "A Monte Carlo Calculation of the Response of Gamma-Ray Scintillation Counters," p 89 in *Methods in Computational Physics,* vol I, Academic Press, New York, 1963.

Zerby, C. D., and R. R. Coveyou, *Some Simplified Expressions for the 3-j Symbols,* ORNL TM-514 (Mar. 15, 1963).

Zerby, C. D., and H. S. Moran, *A Collimator Study for a 5-Gev Electron Beam,* ORNL TM-423 (Dec. 7, 1962).

Zerby, C. D., and H. S. Moran, *A Monte Carlo Calculation of the Three-Dimensional Development of High-Energy Electron-Photon Cascade Showers,* ORNL TM-422 (Dec. 3, 1962).

Zerby, C. D., and H. S. Moran, "Studies of the Longitudinal Development of Electron-Proton Cascade Showers," *J. Appl. Phys.* **34**(8), 2445 (1963).

Zerby, C. D., and H. S. Moran, "Calculations of the 3-Dimensional Development of Electron-Photon Cascade Showers," *Am. Phys. Soc. Bull.* **8**, Ser. II, 365 (1963).

*Non-Division personnel.

THIS PAGE

WAS INTENTIONALLY

LEFT BLANK

ORNL-3499, Vol I
UC-34 – Physics
TID-4500 (23rd ed.)

INTERNAL DISTRIBUTION

1. L. S. Abbott
2. F. S. Alsmiller
3. R. G. Alsmiller, Jr.
4. H. W. Bertini
5. N. A. Betz
6–30. E. P. Blizard
31. T. V. Blosser
32. M. S. Bokhari
33. W. R. Burrus
34. V. R. Cain
35. A. D. Callihan
36. G. T. Chapman
37. F. H. Clark
38. C. E. Clifford
39. J. C. Courtney
40. R. R. Coveyou
41. G. deSaussure
42. J. K. Dickens
43. L. Dresner
44. M. B. Emmett
45. R. M. Freestone, Jr.
46. W. A. Gibson
47. L. W. Gilley
48. R. Gwin
49. J. A. Harvey
50. K. M. Henry, Jr.
51. N. W. Hill
52. L. B. Holland
53. J. L. Hull
54. D. Irving
55. E. B. Johnson
56. W. H. Jordan
57. L. Jung
58. F. B. K. Kam
59. J. D. Kington
60. W. E. Kinney
61. C. E. Larson
62. H. Maier-Leitnitz
63. T. A. Love
64. R. E. Maerker
65. D. W. Magnuson
66. F. C. Maienschein
67. J. J. Manning
68. Betty F. Maskewitz
69. J. T. Mihalczo
70. J. M. Miller
71. H. S. Moran
72. F. J. Muckenthaler
73. J. E. Murphy (K-25)
74. R. B. Parker
75. R. W. Peelle
76. S. K. Penny
77. C. M. Perey
78. F. J. Perey
79. G. R. Satchler
80. R. T. Santoro
81. R. J. Scroggs
82. R. J. Silva
83. E. G. Silver
84. M. J. Skinner
85. G. G. Slaughter
86. R. D. Smiddie
87. J. A. Swartout
88. T. Tamura
89. J. T. Thomas
90. H. A. Todd
91. D. K. Trubey
92. V. V. Verbinski
93. J. Wachter
94. D. R. Ward
95. A. M. Weinberg
96. L. W. Weston
97. G. C. Williams
98. R. E. Wright
99. Gale Young
100. W. Zobel
101. R. A. Charpie (consultant)
102. P. F. Gast (consultant)
103. R. F. Taschek (consultant)
104. T. J. Thompson (consultant)
105. M. L. Goldberger (consultant)
106. Radiation Shielding Information Center
107. Biology Library
108–110. Central Research Library
111. Reactor Division Library
112–113. ORNL–Y-12 Technical Library, Document Reference Section
114–161. Laboratory Records Department
162. Laboratory Records, ORNL R.C.

EXTERNAL DISTRIBUTION

163. J. E. Russell, Rensselaer Polytechnic Institute, Troy, New York
164. R. W. Hockenbury, Rensselaer Polytechnic Institute, Troy, New York
165. E. Haddad, General Atomic, San Diego, California
166. W. M. Lopez, General Atomic, San Diego, California
167. J. R. Bird, U.K. Atomic Energy Research Establishment, Harwell, England
168. J. K. Fox, Phillips Petroleum, Idaho Falls, Idaho
169. M. B. Wells, Radiation Research Associates, Fort Worth, Texas
170. R. L. French, Radiation Research Associates, Fort Worth, Texas
171. J. Kirkbride, General Atomic, San Diego, California
172. P. Phillips, General Atomic, San Diego, California
173. H. Goldstein, Division of Nuclear Science and Engineering, Columbia University, New York City
174. R. L. Childers, University of South Carolina, Department of Physics, Columbia, South Carolina
175. C. D. Zerby, Union Carbide Research Institute, P. O. Box 278, Tarrytown, New York
176. H. E. Stern, NASA, Huntsville, Alabama
177. S. P. Shen, New York University, Department of Physics, New York 53, New York
178. R. Aronson, Radioptics, Inc., 28 Pilgrim Avenue, Yonkers, New York
179. V. D. Bogert, 62 Brixton Road, Garden City, Long Island, New York
180. I. H. Usmani, Chairman, Pakistan Atomic Energy Commission, P. O. Box 3112, Karachi, Pakistan
181. K. F. Orton, Head, Instrumentation Section, Berkeley Nuclear Laboratories, Berkeley, Gloucestershire, England
182. Robert K. Hunter, Jr., The Marquardt Corporation, Nuclear Systems Division, P. O. Box 2013, Van Nuys, California
183. Bernard Hildebrand, Worcester Polytechnic Institute, Department of Physics, Worcester, Massachusetts
184. Francois de Vathaire, C.E.N. de Saclay, Direction de la Physique et des Piles Atomiques, B.P. No. 2, a Gif sur Yvette, Seine et Oise, France
185. M. J. Saepen, Communate Europeenne de l'Energie Atomique, Bureau Central de Mesures Nucleaires, Steenweg op Retie, Geel, Belgium
186. Kaman Shure, Westinghouse Electric Corporation, Bettis Atomic Power Division, Bettis Site, P. O. Box 1468, Pittsburgh 30, Pennsylvania
187. J. R. Beyster, General Atomic, San Diego, California
188. D. F. Cronin, National Lead Company of Ohio, Nuclear Safety Department, Cincinnati 39, Ohio
189. F. L. Keller, The Aerospace Corporation, 2400 East El Segundo Boulevard, El Segundo, California
190. Leon Katz, University of Saskatchewan, Saskatoon, Saskatchewan, Canada
191. James D. King, Assistant Professor of Physics, University of Saskatchewan, Saskatoon, Saskatchewan, Canada
192. R. L. Mather, Code 945, U.S. Naval Radiological Defense Laboratory, San Francisco 24, California
193. J. Persiani, Argonne National Laboratory, 9700 South Cass Avenue, Argonne, Illinois
194. Ed Bennett, Argonne National Laboratory, 9700 South Cass Avenue, Argonne, Illinois
195. Noel Ethridge, Ballistic Research Laboratory, Aberdeen Proving Ground, Aberdeen, Maryland
196. W. E. Wilson, Jr., Assistant Reactor Supervisor, N.W. Nuclear Reactor, University of Washington, College of Engineering, Seattle, Washington
197. Maj. Fort A. Verser, Cm1C, USA, Defense Atomic Support Agency, Department of Defense, Washington 25, D.C.
198. Jerome L. Shapiro, Division of Engineering and Applied Science, California Institute of Technology, Pasadena, California

199. E. A. Warman, Nuclear Analysis Department, Nuclear Operations – REON, Aerojet-General Corporation, Azusa, California
200. Walter Lowen, Department of Mechanical Engineering, Union College, Schenectady 8, New York
201–202. J. L. Symonds, Chief, Division of Physics, Australian Atomic Energy Research Establishment, Sutherland, N.S.W., Australia
203. J. Butler, Acting Head of Shielding Group, Atomic Energy Research Establishment, Harwell, Didcot, Berkshire, England
204. Rafael Perez-Belles, Department of Nuclear Engineering, University of Florida, Gainesville, Florida
205. G. Denielou, C.E.N., Chemin des Martyrs, Grenoble, France
206. R. Joly, C.E.N., de Saclay, B.P. No. 2, Gif sur Yvette (S et O), France
207. P. Lafore, C.E.N., Centre de Fontenay-aux-Roses, Paris 6, France
208. W. L. Gill, Manned Spacecraft Center, Life Systems Division, 2002 Wayside Drive, Houston, Texas
209. B. J. Moyer, University of California, Radiation Laboratory, Berkeley, California
210. J. Rastoin, C.E.N., Centre de Fontenay-aux-Roses, Paris 6, France
211. S. Szawlewicz, Chief, Reactor Safety Branch, Division of Reactor Development, U.S. Atomic Energy Commission, Washington, D.C.
212. T. F. Arcoleo, The Beryllium Corporation, P. O. Box 1462, Reading, Pennsylvania
213. R. L. Cowperthwaite, 1928 Highland Avenue, Knoxville, Tennessee
214. J. D. Jarrard, 103 Meadowbrook, Clinton, Tennessee
215. C. F. Johnson, General Dynamics, Fort Worth, Texas
216. Martin Leimdorfer, Oxenstiernsgatan 31, Stockholm NO, Sweden
217. J. Braun, Aktiebolaget Atomenergi, Reactor Development Division, Drottning Kristinas Vag 47, Stockholm O, Sweden
218. V. B. Bhanot, Physics Department, Punjab University, Chandigarh 3, India
219. R. W. McNamee, Union Carbide Corporation, New York
220. Research and Development Division, AEC, ORO
221–860. Given distribution as shown in TID-4500 (23rd ed.) under Physics category (75 copies – OTS)